Title
Functionalization and Multi-Dimensional Structure Fabrication using Ultrafast Laser Direct Writing (FS-LDW)

Author
Koo, Sangmo

Publication Date
2016

Peer reviewed|Thesis/dissertation

Functionalization and Multi-Dimensional Structure Fabrication using Ultrafast Laser Direct Writing (FS-LDW)

by

Sangmo Koo

A dissertation submitted in partial satisfaction of the

requirements for the degree of

Doctor of Philosophy

in

Engineering – Mechanical Engineering

in the

Graduate Division

of the

University of California, Berkeley

Committee in charge:

Professor Costas P. Grigoropoulos, Chair
Professor Liwei Lin
Professor Seung-Wuk Lee

Spring 2016

Functionalization and Multi-Dimensional Structure Fabrication
using Ultrafast Laser Direct Writing (FS-LDW)

By

Sangmo Koo

Abstract

Functionalization and Multi-Dimensional Structure Fabrication
using Ultrafast Laser Direct Writing (FS-LDW)

by

Sangmo Koo

Doctor of Philosophy in Engineering - Mechanical Engineering

University of California, Berkeley

Professor Costas P. Grigoropoulos, Chair

Femtosecond laser-direct writing (FS-LDW) can functionalize the surface of diverse device components, including cell culture plates and medical implants. Since FS-LDW is in essence a non-contact fabrication method, it allows the surface patterning and micro-/nano-machining of material with minimal mechanical/thermal deformation. Hence, micro-/nanofabrication and material processing by femtosecond laser has attracted intense interest.

Ultrafast laser ablation using far-field optics in a tight focusing configuration offers substantial advantages for the direct, maskless and arbitrary patterning of various materials and curved surfaces, while maintaining high feature resolution. Patterned surfaces with nanoscale craters or ablated pattern on electrospinning fibrous scaffolds can control and direct the cell migration. Control of topographical features in the cellular microenvironment can be achieved by combining FS-LDW with new materials. Direct laser writing by multi-photon polymerization is a nonlinear optical technique that allows the fabrication of 3D structures with resolution beyond the diffraction limit (~100nm). Incorporation of self-assembled block-copolymer nanomaterials into such structure fabricated by two-photon polymerization and, produced mesoscale structures endowed with guided nanoscale patterns (~10nm). This new capability can be used in many applications, including advanced optical metamaterials as well as for efficient photovoltaic energy conversion. In contrast, using low numerical aperture objective lens, fast fibrous structure (high aspect ratio) fabrication is possible. Well-organized fibrous structure can be used for patient-/disease-specific drug testing platform.

Femtosecond laser direct writing is promising technique that can induce surface (*e.g.*, via ablation) or volumetric patterning in a serial fashion (multi-photon polymerization). We applied these techniques to design and control multi-functional platform fabrication. As a result, FS-LDW fabricated structures exhibit higher resolution fabrication, and efficient functionality (*e.g.*, in controlling the migration on 2D and 3D structure / tuning of mechanical stiffness of structure / directed self-assembly of block copolymer / enhancement of fluidic mixing.

Dedication

To my family members,

Thank you for all of your support,
and I love you

Table of Contents

List of figures

Nomenclature

A	Area
$a(x,y)$	Spatial shape
a	Distance between for parallel rods of woodpile structure
a_f	Force deflection position
a_{xy}	Lateral resolution
a_z	Axial resolution
a_z	Distance between for adjacent layer of woodpile structure
$b(z)$	Attenuation term
$\vec{B}$	Magnetic induction field and
C	Heat capacities of lattice subsystems
C_e	Heat capacity of electron
C_M	Speed of the refraction wave
c_{heat}	Heat capacity coefficient
c	Speed of light
c_p	Specific heat at constant pressure
D	Thermal diffusivity
$\vec{D}$	Electrical displacement vector
D_{abl}	Ablated crater diameter
D_c	Conjugate diameter of nucleus
D_e	Thermal diffusivity of electrons
D_f	Diameter of fiber
D_Q	Diffusion coefficient of the quencher
D_t	Transverse diameter of nucleus
d_c	Displacement of the tipless AFM cantilever
d_f	Relative deflection of the fiber
E	Intensity of electric field
$\vec{E}$	Electric dipole moment
E_F	Fermi energy
E_F	Area energy
E_f	Young's modulus
E_g	Bandgap energy
E_L	Line energy
e	Charge of electron
F	Fluence
F_{point}	Individual fiber point force
F_{th}	Threshold Fluence
F_{tissue}	Generated force by the cardiac microtissues
f	Volume fraction of one block of block copolymer
f_{dist}	Distributed forces
$\vec{H}$	Magnetic field
ΔH_v	Enthalpy

h	Convection heat transfer coefficient
h_s	Hatch spacing
I	Laser intensity
I_0	Laser beam intensity at the central axis in the focus plane
J	Free current density vector
K_0	Modified Bessel function
K_c	Spring constants of tip-less AFM cantilever
k	Thermal conductivity
k_B	Boltzmann constant
k_e	Thermal conductivity of the material
k_g	Thermal conductivity of the air
k_p	Propagation constant
k_s	Thermal conductivity of the solid
k_{tQ}	Reaction rate
L_0	Domain spacing of block copolymer
L_e	Electron energy transfer depth
L_f	Fiber total length
L_p	Optical penetration depth
$l_d(l_T)$	Thermal diffusion length
l_f	Fiber length
l_{pd}	Effective penetration depth
M_0	Initial number of monomer
m_e	Effective mass of electron
N	Total number of repeating units
N_c	Characteristic plasma density
N_{ED}	Electron density
n	Refractive index
n_0	Linear refraction index
$\vec{P}$	Polarization vector
P_{cr}	Critical power for self-focusing
P_L	Laser power
p	Polymerization rate
Q	Volumetric heating rate
Q_0	Initial quencher number density
q	Internal heat
q_m	Average heat flux on the laser spot
R	Laser spot size
R_{NP}	Radius of nanoparticle
R_p	Pulse repetition rate
r	Radial distance
r_0	Radius of laser beam
r_1	Radius of the quencher-free domain
S	Source
T	Cardiac tissue thickness
T	Temperature

T_{ab}	Ambient temperature
T_e	Temperature (electron)
T_F	Fermi temperature
T_g	Glass transient temperature
T_m	Melting temperature point
T_0	Initial temperature of substrate
ΔT_{max}	Required temperature for nanoparticle melting
t_{diff}	Diffusion timescale
$t(t)$	Temporal shape
$U(\boldsymbol{x}, t)$	Phase change (*i.e.* latent heat) or chemical reactions
$\boldsymbol{v}_s$	Velocity of the substrate relative to the heat source (scan speed)
W	Cardiac tissue width
$\boldsymbol{x}$	Position tensor

α	Absroption coefficient
α_{av}	Valance ionization coefficient
α_{diff}	Half angle of the light cone
γ_{Ke}	Keldysh parameter
Γ_{e-ph}	Electron-phonon coupling strength
δ_f	Fiber deflection
δ_R	Effective two-photon cross-section for radical generation
ε_0	Electric permittivity
ε_θ	Thermal radiation coefficient
η_{av}	Avalanche ionization rate
λ	Wavelength
μ	Magnetic permeability
μ	Solid fraction ($= \rho/\rho_s$)
μ_0	Magnetic permeability in the vacuum
ρ	Density
ρ_R	Density of radicals
σ	Stefan-Boltzamnn constant
τ	Pulse duration
τ_e	Characteristic time for cooling of the hot electron
τ_M	Mechanical relaxation time
Φ	Empirical coefficient.
ϕ_{th}	Threshold energy for ablation
χ	Flory-Huggins segmental interaction parameter
χ_{abl}	Depth of ablated crater
$\chi^{(n)}$	Susceptibility
ω	Frequency of laser pulse
ω_0	Gaussian beam waist
ω_2	Angular frequency of an incoming photon
$\hbar$	Planck constant

1PA	Single-photon absorption
1PP	One-photon polymerization
2D	Two-dimensional
2D FFT	2D Fast Flourier transform
2PA	Two-photon absorption
2PP	Two-photon polymerization
3D	Three-dimensional
3PA	Three-photon absorption
3PP	Three-photon polymerization
AAO	Anodic aluminum oxide
AFM	Atomic force microscopy
AR	Aspect ratio
BCP	Block copolymer
BD	Beating duration
BF	Beating frequency
BIS	4,4'-bis(diethylamino) benzophenone
BNP	Brain natriuretic peptide
BSA	Bovine serum albumin
CMs	Cardiomyocytes
CT	Critical threshold for ablation
CW	Continuous wave
cTnT	Cardiac Troponin T
DADs	Delayed after depolarizations
DCM	Dilated cardiomyopathy
DI	Deionized
DMAEMA	2-(dimethylamino) ethyl methacrylate
DMEM	Dulbecco's Modified Eagle Medium
DMSO	Dimethyl sulfoxide
DOT	Disorder-to-order transition
DSA	Direct self-assembly
EADs	Early after depolarizations
EBL	Electron beam lithography
ECG	Electrocardiography
ECM	Extracellular matrix
EDX	Energy-dispersive X-ray spectroscopy
ETS	Electron transfer system
F-actin	Filamentous actin
FBS	Fetal bovine serum
FEM	Finite element method
FIB	Focused ion beam
FPA	Field potential amplitude
FPD	Field potential duration
FS-DLW	Femtosecond laser direct writing

FWHM	Full width half maximum
GFP	Green fluorescent protein
HAZ	Heat-affected zone
HBSS	Hanks' balanced salt solution
HCM	Hypertrophic cardiomyopathies
HFIP	Hexafluoroisopropanol
hBNP	Nesiritide
hiPS	Human induced pluripotent stem
KO	Knockout
LBO	Lithium triborate
L-ETRS	Laser induced electron transfer for direct reduction and sintering
LQT3	Long QT syndrome type 3
MAA	Methacrylic acid
MAD	Median absolute difference
MAPTMS	3-[(methacryloyloxy)propyl]trimethoxysilane
MAZPO	(Methacryloyloxy)tripropoxy-zirconium
MCV	Maximal contraction velocity
MEA	Multielectrode array
MEM-NEAA	MEM non-essential amino acids
MEMS	Microelectromechanical systems
MPA	Multiphoton absorption
MRV	Maximal relaxation velocity
MYBPC	Myosin binding protein C
NA	Numerical aperture
ND	Neutral density
NP	Nanoparticles
OCT	Optimal cutting temperature
ODT	Order-to-disorder transition
P2VP	Poly(2-vinylpyridine)
P4VP	Poly(4-vinylpyridine)
PBS	Polarizing beam splitter
PBS	Phosphate buffered saline
PDMS	Polydimethylsiloxane
PCR	Polymerase chain reaction
PEO	Poly(ethylene oxide)
PFA	Paraformaldehyde
PI	Photoinitiator
PLCL	Poly(L-lactide-co-carprolactone)
PLLA	Poly(L-lactic acid)
PMMA	Poly(methyl methacrylate)
ps	picosecond
PS II	Photosystem II
PVDF	Polyvinylidene Fluoride syringe filter
QCM-D	Quartz Crystal Microbalance with Dissipation
RGD	Arginine-Glycine-Aspartic acid
RIE	Reactive ion etching

RT-qPCR	Reverse transcription-q polymerase chain reaction
SEM	Scanning electron microscopy
SLS/SLM	Selective laser sintering/melting
SORP	Self-organized precipitation
SPR	Surface plasmon resonance
SR	Sarcoplasmic reticulum
STED	Stimulated-emission-depletion
SVA	Solvent vapor annealing
TA	Thermal annealing
TALEN	Transcription activator-like effector nuclease
TCPS	Tissue culture polystyrene
TEM	Transmission electron microscopy
TFM	Traction force microscopy
THF	Tetrahydrofuran
TRP	Tryptophan
TTL	Transistor-Transistor-Logic
TTM	Two-temperature model
TYR	Tyrosine
UV	Ultraviolet
WT	Wild type
ZPO	Zirconium propoxide
β-MHC	β-myosin heavy chain

Chapter 1 Introduction

Major advantages of surface treatment by laser include high processing speeds, precise hardening depth control, minimization of structural distortion and cracking, elimination of separate quenching medium, and the ability to selective-site hardening with small size at where hard to reach areas (*e.g.*, inside surface of small holes). Especially, femtosecond laser direct writing (FS-DLW) has been considered as a promising nanofabrication tool for diverse materials. Micro-/nano- fabrication and material processing by femtosecond laser has become important in recent years for many fields such as electronics[1-5], optics[6], chemistry[7] and biomedical[8] engineering. Due to the non-contact fabrication nature, laser ablation allows micromachining and surface patterning of materials with minimal mechanical and thermal deformation[9, 10]. The advantage of femtosecond laser fabrication compares to the other laser (*e.g.,* nanosecond laser) lies in its ability to deposit energy into a material in a very short time period, before thermal diffusion can occur. As a result, the heat-affected zone (HAZ), where melting and solidification occur, is significantly reduced, leading to structural features that are smaller in size and have higher resolution. Rapid heating of the surface can be achieved with little thermal penetration. [10, 11]

First of all, FS-DLW can be used for the manipulation of biomaterials for tissue engineering[12]. Tissue engineering is defined as the discipline which applies the principles of engineering and life sciences toward the development of biological substitutes that restore, maintain, or improve tissue function or a whole organ. Creating an engineered tissue requires imitating the extracellular matrix (ECM)[13]; this entails finding a material suitable for the fabrication of a scaffold for a specific tissue engineering application, fabricating the scaffold, and seeding it with cells for cell culturing *in vitro* or *in vivo*. Micro- and nano-topography have been found to influence cell adhesion[14], proliferation[15] and differentiation[16]; this is the one reason why the use of FS-DLW in scaffold fabrication has found explosive increase over the last few years. Cells adhere to surfaces and form anchorages of a variety of forms in different tissues of micro-/nano and mesoscale patterns[17]. In particular, the nanoscale patterning has received much attention since most surfaces in or on the natural tissues are in nanometer length scale[18].

Nanoscale modifications in topographical and chemical patterns elicit diverse cell behavior, ranging from adhesion, cytoskeletal organization, nucleus orientation and directional migration. Controlling of spatial biomolecules arrangement is critical for focal adhesion formation/distribution for cell fate and functions[14, 19, 20]. Thus scale and type of patterns (symmetry, spatial distribution) shows different effect on cell behavior. Biocompatible three-dimensional (3D) scaffolds play a pivotal role in tissue engineering.[21-26] These scaffolds are fabricated with controlled mechanical and biological properties so that they can support new tissue formation by providing physical

and chemical cues that promote various cellular responses such as differentiation, proliferation and migration. Specifically, the architecture of tissue-engineered scaffolds is designed to mimic the organized structure and biological function of native ECM. Thus, a favorable ECM-like microenvironment for cells is crucial for achieving the desirable scaffold integration, cell–material interactions and tissue ingrowth[27]. Electrospinning is a popular technique used to fabricate ECM-like scaffolds. Electrospun scaffolds have great potential in that their structures, especially in nanoscale networks, not only resemble natural ECM but also exhibit high surface-area-to-volume ratios favorable for attachment of cells and bioactive molecules to fiber surfaces[28-33]. Fabrication on this electrospun fibers is possible by focused femtosecond laser beam to reduce the denaturation of materials.

Direct laser writing by multi-photon polymerization is a nonlinear optical technique which allows the 3D structures fabrication with a high resolution beyond the diffraction limit[10]. The polymerization process is initiated when the ultrafast laser beam is focused into the volume of a transparent, photo-curable material and multi-photon absorption takes place within the focal volume[34]. By moving the focused laser beam in arbitrary direction (x-y-z direction), polymerized 3D structures can be fabricated[35-37]. The materials used in this work are photo-curable organic-inorganic hybrid materials, prepared by the sol-gel process. Focused laser beam induce the π-bond generation with nearby double bond of molecules, this propagation makes it possible to fabricate 3D structure[38-43].

Combination of self-assembly property of block copolymer (BCP) and high precision 3D structure by multi-photon polymerization, advanced 3D mesoscale structure fabrication was possible. Self-assembly of BCP is broadly considered an attractive means of generating nanoscale structures and patterns over large areas with nanoscale domain sizes.[44] However, the spontaneous formation of equilibrium nanostructures in response to temperature and solvent concentration changes must be guided to yield the long range order and orientation. Direct self-assembly (DSA) of BCP with 3D confinement is also important for diverse applications such as optics[45, 46], electronics and photovoltaics.[45, 47]

We have shown some of the versatile capabilities of laser processing for

1. Modification the surface properties of materials in order to enhance their performance (Ablation)
2. 3D complex structure fabrication with nanoscale resolution for diverse platforms with functionalities (Multi-photon polymerization)

Furthermore, these techniques can be combined with other materials such as BCPs for realizing unique functionality. The laser is a flexible tool that allows precise deposition of energy into the material at a confined area. A variety of different material responses can be achieved depending on the material and the laser parameters. It is allowed to design and optimize to alter the material's surface chemistry, morphology to get the desired function, and features which expand their applications. Material modifications can occur over many different length scales, adding complexity to the surface and a new dimension to surface optimization. Laser surface processing has been a key element in a number of operations and will continue to improve the performance of

materials in existing applications opening open the door to new materials and novel device concepts[10, 11].

Chapter 2: In this chapter, I will give an introduction of the femtosecond laser direct writing technique.

Chapter 3 : In this chapter, I will explain about the surface modification and functionalization (*via* Ablation). Multiphoton ablation-based nanoscale surface patterning with various aspect ratios and pitches not only altered the cells' focal adhesion size and distribution[48], but also affected cell morphology, migration and ultimately localization. As a result, nanocrater pitch can disrupt the formation of mature focal adhesions to favor the migration of cells toward higher-pitched regions, which present increased planar area for the formation of stable focal adhesions. Moreover, by designing surfaces with variable pitch but constant nanocrater dimensions (diameter / depth), we were able to create diverse cellular patterns. Our surface-patterning approach that does not involve chemical treatments and can be applied to various materials represents a simple method to control cell behavior on surfaces. Advanced nanofabrication methods have led to creating superb resolution of the patterns, allowing more precise quantitative experimentation. Addition to femtosecond laser ablation can be used to increase cell infiltration into nanofibrous scaffolds[49]. Laser ablation can not only create desired features in micrometer length scale but also presents a new approach in the fabrication of three-dimensional porous constructs for tissue engineering.

Chapter 4 : In this chapter, we used the two-photon polymerization(2PP) technique to create a cohort of 3D filamentous matrices to regulate the structural organization of cardiomyocytes and their functions[50, 51]. We successfully created fibrous matrices with different fiber diameters and spacing, and found that fiber spacing predominantly determined the formation of 3D tissue and cardiomyocyte alignment. Cardiomyocyte alignment is associated with the cardiomyocyte contractile function and dysfunction in the cardiac tissue. The parallel registration of sarcomeric Z-line and calcium metabolism was strongly correlated with the range of cardiomyocyte shapes, and cytoskeleton and sarcomeres play an important role in modulating ion channel kinetics and calcium transient. The spatial alignment of cardiomyocytes enhanced the parallel coupling of myofibrils to maintain the polarity of cardiomyocytes and intracellular network which is responsible for the spatio-temporal coordination of cellular contractility. Compared to 2D substrates, these 3D matrices showed much stronger similarity to the topographic complexity *in vivo*. In particular, our matrices could be fabricated over a wide range of dimensions, and bending stiffness also can be tuned. Since these fibers were rhythmically deformed by the beating cardiac microtissues, we could quantitatively evaluate the contraction forces on this platform. And we also established an *in vitro* model of 3D human cardiac tissue by populating synthetic filamentous matrices with healthy wildtype and patient-specific disease type. Our studies highlighted the possibility of exploiting the mechanical load to the cardiac tissue, which will hopefully lead to a more comprehensive understanding of the role of mechanical equilibrium in cardiac tissue homeostasis and pathogenesis. This model is also a pioneering testbed for assessing drug efficacy for

patients with rare genetic disorders, moving drug discovery and development into the era of personalized medicine.

Chapter 5 : A wide variety of high performance and functional materials have been developed for applications in electronics, photonics, and biomaterials. Scalability is perhaps the biggest challenge within BCP DSA for applications in nanotechnology. There has been greater emphasis on advanced instruments are required to scale-up existing methods and develop new technologies that are inherently more scalable by design. In this chapter, we review laser-based nanoscale fabrication technique(2PP) and self-assembled polymeric morphologies (frustrated phases) of BCP in the 3D confined structure with nanoscale, which is distinctly different from those in the bulk phase.

Chapter 6 : Nature provides cues for configuring bio-mimetic systems. In this chapter, I will show conductive pattern fabrication using concept of electron transfer system (ETS) in nature[52, 53]. Especially, on the leaf, there are unique ETS for photosynthesis which is composed by amino acid with aromatic ring that can transfer the electron adjacent molecule by the photon. Ultraviolet light irradiated into a thin film of precursor solution consisting of tyrosine based mixture with silver ion can efficiently generate and transport free electrons and large amount of silver nanoparticles. This patterning process is promising for environmental-friendly conductive patterning technique, because non-sintered pattern can be removed easily by water without any other toxic organic solvents.

Chapter 2 Fundamental of Femtosecond Laser Direct Writing (FS-LDW)

Fundamental studies of material processing by femtosecond laser have revealed the time-dependent dynamics of ultrafast electron excitation and energy transfer to the lattice system[10, 11]. For femtosecond laser pulses, the electrons and the lattice are driven far out of equilibrium, and induce lattice disorder. During the interaction of an ultrashort pulse with a transparent material, the laser energy is first deposited into the electrons and transferred to the lattice, via electron excitation and relaxation. In contrast to this, laser pulses of nanoseconds duration can be used to anneal the lattice by thermal processing. Due to the nonlinear nature of multi-photon absorption, tightly focused femtosecond laser beam can be strongly absorbed. The interaction between laser pulse and material occurs only near the focal volume where the peak intensity is sufficiently high to induce multiphoton absorption. This is fundamentally different to the possible avalanche ionization process that can induce breakdown in the case of interaction of longer laser pulses[10, 11]. For long pulses, avalanche ionization mainly caused by impurities and dislocations in the focal volume. Therefore, it occurs stochastically and is irreproducible. In contrast, the multiphoton absorption dominated process induced by femtosecond lasers is only seeded by multiphoton/tunnel ionization, allowing reproducible and controllable processing.

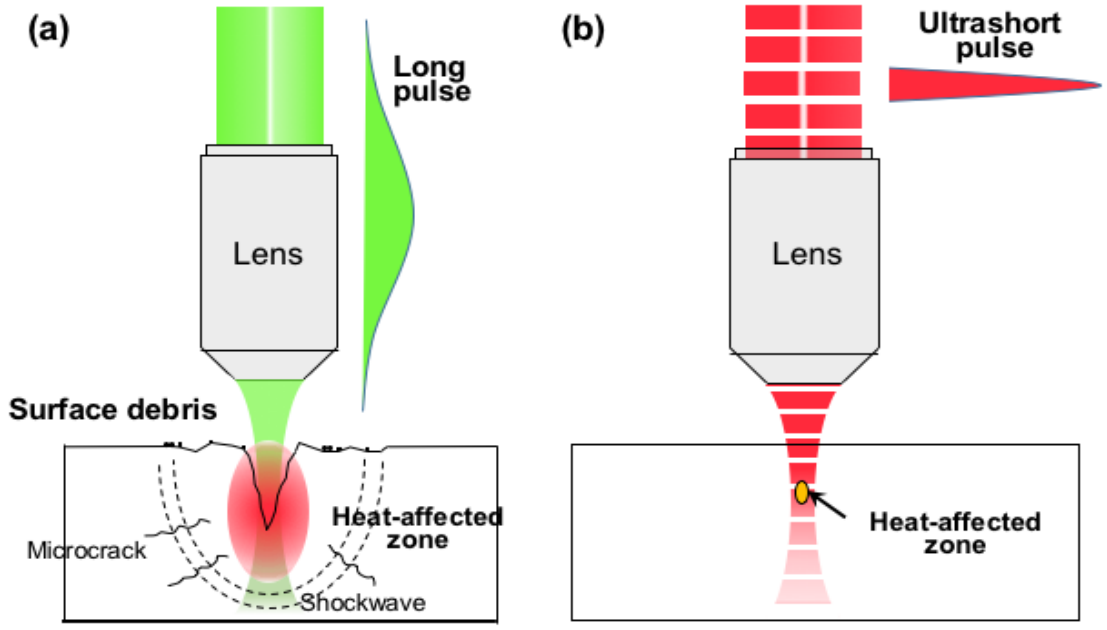

Figure 2.1. Schematic of interaction between laser pulse and transparent materials (a) long laser pulse, (b) ultrashort laser pulse

2.1 Reduction of thermal effect

Femtosecond laser processing has several advantages. First of all is the minimization of thermal diffusion that can significantly reduce thermal effects during material processing[10, 11]. An important scaling quantity is the thermal diffusion length (l_T)

$$l_T \approx \sqrt{D\tau}$$

where $D = \kappa/\rho c_p$ is the thermal diffusivity of the material, and τ is pulse duration. The thermal diffusion length characterizes the distance wherein temperature changes propagate in some characteristic time(τ). Typically, τ is considered to be the laser beam dwell time or temporal pulse width. Hence, thermal diffusion length considered as a measurement of how far the energy spreads during the laser irradiation. Following this initial interaction, further thermal propagation leads to elevated temperatures at distances beyond this length. The spread in energy during the laser pulse combined with that of after the pulse can lead to changes in the material properties. The region over which these changes occur is denoted the heat affected zone (HAZ). For femtosecond laser pulses, the energy deposition is much shorter than the mechanical relaxation time (τ_M) defined as

$$\tau_M \sim \frac{(L_p + L_e)}{C_M}$$

where L_p is the optical penetration depth, L_e is the electron energy transfer depth and C_M is the speed of the rarefaction wave in the solid target. In other words, the pulse duration is shorter than the time needed to initiate a collective motion of the atoms within the absorbed volume. Very fast heating of the near surface region of the target (top layer of the solid), the energy absorption is so high that vaporization occurs. And rapid "atomization" following the rupture of the atomic cohesion in the solid due to extreme absorbed energy. Such process leads to the expansion of a plume composed of atoms and ions along the normal of the target with very low angular aperture and with velocities.

2.2 Heat transfer modeling

Thermal effect on the material can be explained as a result of temperature change. The temporal and spatial temperature field of a material are governed by the heat equation. The heat equation is derived from the conservation of energy and Fourier's law of heat conduction with fixed laser beam. The heat equation can be written as :

$$\rho(\boldsymbol{x},T)c_p(\boldsymbol{x},T)\frac{\partial T(\boldsymbol{x},T)}{\partial t}-\nabla[k(\boldsymbol{x},T)\nabla T(\boldsymbol{x},T)]+\rho(\boldsymbol{x},T)c_p(\boldsymbol{x},T)\boldsymbol{v}_s\nabla T(\boldsymbol{x},T)=Q(\boldsymbol{x},T)$$

where ρ is the mass density, c_p is the specific heat at constant pressure, k is the thermal conductivity, and $\boldsymbol{v}_s$ is the velocity of the substrate relative to the heat source. The left side of equation describes the effects of thermal conduction and material convection. The right side, incorporates the contribution of heat sources and sinks through the volumetric heating rate ($Q(\boldsymbol{x},T)$). However, for the case of shallow surface absorption, this contribution can approximately be separated into a spatial shape $a(x,y)$ determined by the profile of beam, attenuation term $b(z)$ and temporal shape $t(t)$, which could be a constant for continuous wave, or quantify the temporal distribution of an isolated pulse and even a train of pulses. Phase change (*i.e.* latent heat) or chemical reactions (*i.e.* released or consumed energy) can be accounted for by the term $U(\boldsymbol{x},t)$ and the volumetric heating term becomes as

$$Q(\boldsymbol{x},t)=a(x,y)b(z)t(t)+U(\boldsymbol{x},t)$$

In some cases of extremely rapid material heating or very small material dimensions, the continuum assumptions of heat equation may not appropriate during the initial laser-material interaction and requires alternative modeling including molecular dynamic simulations and even ab-initio modeling of the fundamental energy transport. However, in most cases, right after the initial interaction, the heat equation remains valid. In certain cases, there are simplifying assumptions that can be applied to enable analytic solutions, such as treating material properties as constants, incorporating laser heating through the boundary conditions for the case of surface absorption, or treating the laser shape term as a delta function for the case of a tightly focused laser spot.

2.3 Two-temperature model

Most of the pulse energy is deposited into electrons before being transferred to the lattice when the pulse duration is shorter than the electron-phonon coupling time (generally, electron-photon coupling time ~tens ps)[10, 11]. The free-electron temperature increases rapidly and becomes much higher than the lattice temperature, a process that can be characterized by a two-temperature model (TTM). Thermalization between the electron subsystem and the lattice is usually much longer (1~100 ps), depends on the electron-phonon coupling strength (Γ_{e-ph}). Thus, ultrafast laser excitation generates a hot electron gas that is highly not in equilibrium with the lattice. Typically, the electron-phonon coupling is also much faster than the heat diffusion. Hence, the melting or ablation depth is determined by the maximum of the optical and ballistic electron heat penetration depth. The transient non-equilibrium between the hot electrons and the lattice can be described

by two temperatures T_e and T, which can be calculated from the corresponding heat equations. The (coupled) nonlinear equations for T_e and T can be written as

$$C_e(T_e)\frac{\partial T_e}{\partial t} = \nabla[k_e(T_e,T)\nabla T_e] - \Gamma_{e-ph}(T_e)[T_e - T] + Q(z,t)$$

and

$$C(T)\frac{\partial T}{\partial t} = \nabla[k(T)\nabla \mathrm{T}] + \Gamma_{e-ph}(T_e)[T_e - T]$$

where C_e is the heat capacity of electron and C is heat capacities of lattice subsystems. In a 1D approximation the source term can be written as

$$Q(z,t) = \alpha A I(t)\exp(-\alpha z)$$

With femtosecond pulses, heat conduction within the lattice subsystem, $\nabla[k(T)\nabla \mathrm{T}]$ term can be ignored. Heat conduction occurs much rapidly through the free electron gas than via phonons. For medium levels of excitation $C_e \ll C$ and the electrons can be heated to very high transient temperatures. If T_e is much lower than the Fermi temperature ($T_F \equiv E_F/k_B$), the heat capacity of electrons can be approximated by $C_e = C_0 T_e$ where $C_0 = \pi^2 N_e k_B/2T_F$ is constant where E_F is Fermi energy and k_B is Boltzmann constant. C can be assumed to be constant for temperature above the Debye temperature. For the femtosecond pulse regime, the pulse duration is shorter than the characteristic time for cooling of the hot electron gas due to energy exchange with the lattice:

$$\tau_l \ll \tau_e \equiv \frac{C_e}{\Gamma_{e-ph}}$$

For $t \ll \tau_e$, $\Gamma_{e-ph}T_e \ll C_e T_e/t$, the electron-phonon coupling can be ignored. If we also ignore heat conduction by electrons, which is a reasonable approximation with $D_e\tau_{e-ph} < \alpha^{-2}$ where $D_e = k_e/C_e$ is the thermal diffusivity of electrons, and can be derived as

$$\frac{1}{2}C_0\frac{\partial {T_e}^2}{\partial t} = \alpha I_a exp(-\alpha z)$$

$$T_e(t) = \left[{T_0}^2 + \frac{2\alpha\phi_a(t)}{C_0}exp(-\alpha z)\right]^{1/2}$$

where $\phi_a(t) = \int_0^t I_a(t')dt'$, T_0 is the initial temperature. At the end of the pulse, $t = \tau_l$

$$T_e(\tau_l) \approx \left(\frac{2\alpha\phi_a}{C_0}\right)^{1/2} \exp\left(-\frac{\alpha z}{2}\right)$$

The evolution of the temperature for times , $t \geq \tau_l$ is described by nonlinear equation with $Q = 0$. In this regime, T_e rapidly decreased due to the electron energy transfer to the lattice. As heat conduction can be ignored, lattice temperature describes as

$$T \approx \frac{\alpha \phi_a}{C} exp(-\alpha z)$$

by employing the energy balance

$$CT = \int_0^{T_e} C_e(T_e{}')dT_e{}'$$

$$T_e(\tau_l) \approx \left(\frac{2\alpha\phi_a}{C_0}\right)^{1/2} \exp\left(-\frac{\alpha z}{2}\right)$$

If $CT = \rho c_p T \approx \Delta H_v$, ablation occurs. This approximation can be employed as long as $T_e \ll E_F/k_B$. And we can get the ablated depth as

$$\Delta h = \frac{1}{\alpha} ln \frac{\phi}{\phi_{th}}$$

with $\phi_{th} = \Delta H_v/\alpha A$.

Material in the laser interaction region is then ejected in a very short time in the form of hot dense plasma, leaving the local lattice still cold. This effect is obvious for femtosecond lasers with a low repetition rate (a few kHz or less). This process can effectively suppress the formation of a heat-affected zone enabling micro/nanoscale fine structure fabrication. On the other hand, for laser pulse duration significantly longer than the electron-phonon coupling time, although the radiation energy is first transferred to the electrons, the electrons transfer it to the lattice before the pulse has terminated. This allows the electrons and the lattice to reach an equilibrium state, and the laser simply heats the solid to its melting temperature within the duration of the pulse. This gives rise to significant thermal diffusion and consequently a reduction in fabrication quality and resolution.

2.4 Multiphoton absorption

Since multiphoton absorption only occurs in the beam focal volume, where the light intensity is high another important benefit of femtosecond laser direct writing is the capability of machining transparent materials in a 3D space-selective manner. For

nanosecond laser, because single photon absorption is involved, modification always begins at the surface and then moves inward. Even if a nanosecond laser with wavelength sufficiently long for the material to be transparent is used, 3D processing still has difficulties, because radiation intensity sufficiently high to induce multiphoton absorption will also lead to strong thermal effects such as cracking.[48, 54-57] The ability to create arbitrary 3D structures within transparent substrates by the use of femtosecond lasers enables the production of novel device architectures with enhanced functionality and improved compactness. Hence, the multi-photon absorption makes it possible to fabricate high-resolution structure with sub-diffraction limit. The effective processing profile of a femtosecond laser beam can be much narrower than its Gaussian intensity profile. This is because the distribution of absorbed energy for n-photon absorption is proportional to the n^{th} power of the laser intensity (n is the number of photons simultaneously absorbed by the material to transmit the electron from valance band to conduction band). Suppression of the heat-affected zone restricts the laser-modified region to within a few nanometers of the volume where the laser fluence is above the threshold for inducing multiphoton absorption. This makes it easy to achieve a fabrication resolution far beyond the optical diffraction limit by adjusting the intensity at the center of the Gaussian beam profile as close as possible to the threshold intensity for modification[10, 58]. As a result, it is possible to modify precisely or change the physical and/or chemical properties of the material in a spatially selective manner including surface (2D) and bulk (3D) micro/nanofabrication (machining) [2, 49, 59, 60], ablation, multi-photon polymerization[51, 61-65], selective metallization can be achieved by FS-LDW, which enables multifunctional integration in a single substrate.

2.5 Ablation

Laser ablation is the removal of material from a substrate by direct absorption of laser energy. Typically, laser ablation occurs by the pulse laser irradiation (ablation is also possible with intense continuous laser irradiation). The onset of ablation occurs above a threshold fluence, which depends on the absorption mechanism, material, substrate properties (morphology, micro-/nanostructure, presence of defects) and laser pulse properties (pulse duration and wavelength). With multiple pulses, the ablation thresholds decrease due to defect accumulation. Above the ablation threshold, the depth or volume of material removed per pulse typically shows logarithmic linear relationship[66].
At low fluences, photo-thermal mechanisms for ablation include material evaporation and sublimation. For multicomponent systems, the more volatile species may be depleted more rapidly, changing the chemical composition of the remaining material. With higher fluence, heterogeneous nucleation of vapor bubbles leads to normal boiling. If material heating is sufficiently rapid for the material to approach its thermodynamic critical temperature, rapid homogeneous nucleation and expansion of vapor bubbles lead to explosive boiling (phase explosion) carrying off solid and liquid material fragments. When the excitation time is shorter than the thermalization time in the material, non-thermal, photochemical ablation mechanisms can occur[10, 58].

The temporal pulse length of laser significantly affects the dynamics of the ablation. As the pulse length is shortened, energy is more rapidly deposited into the material leading to fast material ejection. The volume of material that is directly excited by the laser has less time to transfer energy to the surrounding material before being ejected. Therefore, the ablated volume becomes more precisely defined by the laser spatial profile, optical penetration depth, and the remaining material has less residual energy, which reduces the heat affected zone. The effect of short pulses (femto to picosecond) is most apparent in the ablation. In contrast, materials of large thermal diffusivity and relatively low melting points will exhibit extended heat affected zones and deep molten regions when ablated with nanosecond laser pulses.
The ablation threshold fluence for a material reduces at shorter pulse lengths and becomes more sharply defined. However, even for these ultrashort pulses, there is excess energy remaining in the material that can still cause thermal effects in the surrounding material after the pulse has ended. Additionally, femtosecond pulses can cause optical breakdown, which reduces the optical absorption depth and can even cause strong absorption in otherwise transparent wide-bandgap materials. Another distinction of femtosecond and picosecond ablation is that the laser–material interaction is separated in time from material response and ejection. In contrast to this, during nanosecond ablation, shielding of the surface by the ejected ablation plume can reduce the amount of energy absorbed by the material.

2.6 Multi-photon photo-polymerization

The thresholding characteristics observed extensively in various materials are the most important factors contributing to spatial resolution improvement in femtosecond laser direct writing. In the particular case of photopolymerization of resins, the unpolymerized monomer or photoinitiator molecules or molecular segments are removable from the polymer network. The combined action of optical, chemical and material nonlinearities makes it possible to achieve reproducible fabrication resolution of tens of nanometers that is much smaller than the optical diffraction limit. Theoretically, voxels may be further reduced in size only if the laser pulse energy is regulated closer to but still above the threshold level. However, this is tough to experimentally confirm since individual voxels produced by low exposure are mechanically too weak to resist the rinsing necessary for removal of the unexposed portion and survive electron beam exposure. The femtosecond laser direct writing fabrication accuracy is generally determined by the smallest achievable voxel sizes. More details will be given in Section 4.2.[37, 61, 65, 67-69]

Chapter 3 Surface Patterning and Functionalization by Femtosecond Laser Direct Writing (Ablation)

3.1 Introduction

3.1.1 Conventional surface patterning

Micro-/nanofabrication techniques enable us design the diverse functionalized platform or substrate. Generally, most micro-/nanofabrication techniques are based on photolithography and soft lithography. Photo-curable material (*i.e.*, Photoresist) can be cured by the illumination of light with specific wavelength. The cured structure can be used for fabricating master mold for soft lithography.
Microscale patterned surfaces were widely used for efficient functionalization, although applications maybe limited due to low resolution. Hence, nanoscale patterning on the substrate with precision has been attracting increasing interest. Several techniques have been employed for nanoscale structure formation, including electron beam lithography[70], microcontact printing and electrospinning.

3.1.1.1 Electron beam lithography

Electron beam lithography (EBL) is a direct patterning method. Taking advantage of the development of scanning electron microscopy (SEM), it has also been possible to advance the high-resolution patterning technique using electron beam. This method has enabled fabrication of high precision photomasks for photolithography, and is also used for physical/chemical patterning. However, patterning using EBL must meet requirements such as conductive plate, stable and ultra-high vacuum condition. However, this fabrication process takes long time, and the cost is also high.

3.1.1.2 Micro-/Nano-contact printing

Micro-/nano-contact printing is a convenient and widely used soft lithography technique. Using micro- and nano-scaled patterned elastomer stamps[20, 71, 72], target material can be transferred and printed on the recipient substrate. Advantages of this technique are the high throughput and ease of use. However, pattern on the mold should have high precision resolution chemical patterning. For mold fabrication, other lithography techniques are generally used such as dip-pen lithography, EBL and focused ion beam (FIB) lithography[30, 32, 33, 73-77]. This method also costs high and is slow. Furthermore, this technique is subject to deformation of the mold.

3.1.1.3 Electrospinning

The electrospinning technique can generate nanoscale fibrous structures with high strength and large surface area. High surface area to volume ratio of those electrospun matrices can be beneficial with respect to the diffusion and delivery of material molecules due to the mesh-like structures with micro- or nanosize pore structure[28, 29, 75, 78, 79]. This backbone structure can be used in diverse applications for biological structure and efficient energy system. Especially these structures mimic the native extracellular matrices (ECM) and can be applied to enhancement of 3D tissue formation[59, 78-82].

3.1.2 Cell migration

The migration of cells has been described as a multistep process. For cells to migrate, actin polymerization at the leading edge pushes the plasma membrane forward and forms new regions of actin cortex. New points of anchorage are formed between the actin filaments and the surface filopodia. Contraction at the rear of the cell then draws the body of the cell forward. Old anchorage points are released at the back as the cell crawls forward. This multistep process is repeated for cell migration.
In the real tissue, cells are in the environment with diverse mechanical, physical and chemical stimulations *etc*. The cells can sense and respond to those stimulations. Stiffness differences also effect on the migration (durotaxis). Directional mechanical force (mechanotaxis), and chemical gradient (chemotaxis) also affect directional migration. Cell migration can be effected by outer biomolecules that react with ECM, and the gradient of density of ECM protein would enhance the migration (haptotaxis). Controlling the cell migration is important to figure the mechanism of biofilm formation. Formation of biofilm on the medical devices (aggregation of cell cluster) induces additional medical cost. Cataract of after artificial lens implant surgery is one of the unwanted cell migration. Cell migration is an essential cellular response for a variety of physiological and pathological phenomena[83-90]. For example, leukocytes migration mediates immune responses. Migration of fibroblasts, vascular endothelial cells, and osteoblasts contributes to wound healing, tissue regeneration, and metastasis. In contrast to this, it also can lead to implant failure of percutaneous devices due to epithelial down-growth on the implant surface as migration is dependent on cell-materials interactions[91-93].

3.1.2.1 Cell migration by mechanical(physical) condition

3.1.2.1.1 Topography

Cell can sense the surface topography upto few nanometer scales. Generally, it is known that cell filopodia sense the topography and accordingly react. Controlling cell adhesion, orientation and migration is possible using microscale topography structures. For

example, cell sense the groove/ridge topography structure, they are aligned along groove structure and migrate in this direction. Deeper and narrower structures are more effective on the controlling the alignment and migration[94-96].

3.1.2.1.2 Mechanical force

Other factors controlling the cell migration and alignment are mechanical forces. Mechanical stress and strain are able to regulate the cell behavior. The shear stress by external flows enhances the cell migration toward to shear stress direction. For example, mechanical strain in a vascular wall is anisotropic in its circumferential direction, and cell also aligned by the cyclic uniaxial strain. In a cardiovascular system, shear stress induced by blood flow regulates endothelial cell migration[18, 97-100]. They migrate toward the lower shear stress region, and also change their shape for efficient reduction of stresses. This also affects gene expression (transcription and translation) to react in response to these external stimulations. Turning cell behavior into stem cell broadens the possibility of application into regenerative medicine.

3.1.2.1.3 Rigidity

Cells also sense the rigidity or stiffness of substrates, as there is a diverse rigidity range from soft (brain (~1kPa)) to rigid (bone (~100kPa)) in the body. After sensing the substrate stiffness, focal adhesion and intracellular cytoskeleton structure formed according to outer environments. On the softer substrate, stable and mature focal adhesion is formed. Cells exert less tension on softer surface and consequentially crawl faster. Hence, cells tend to migrate to a stiffer substrate owing to the stronger traction force between the cells and the substrate[101-104].

3.1.2.2 Cell migration by chemical condition

Chemical gradient is another important factor for directional cell migration toward to favorable region (chemotaxis)[105-107]. In the presence of a spatial chemical gradient, intracellular sensory systems impose a bias on cells random walk behavior in a manner that yields net migration toward a preferred direction. In contrast to this uniform chemical condition, cell motility can be controlled without directional migration (chemokinesis)[86, 108]. For immune system, inflammatory response, white blood cell intrusion into infected region with high concentration of interleukin. This is representative example of chemotaxis.

3.2 Ablation for surface functionalization using femtosecond laser direct writing

FS-LDW is applied to functionalized surface fabrication. There is increasing demand for developing new techniques for nanometer length scale patterning. In this chapter, we will

discuss how a femtosecond laser can be used to modify and pattern the material (particularly transparent material). We recall the basic principles that govern the interaction of femtosecond laser pulses with transparent materials[34]. A femtosecond laser pulse has extremely high peak power and intensity due to ultrashort pulse width. When highly intense ultrashort laser pulses are focused into transparent dielectric material, only the localized region within the focal volume absorbs the laser energy by nonlinear absorption processes such as multiphoton initiated avalanche ionization. There is no or minimal heat exchange during femtosecond laser pulse irradiation, which results in minimizing thermal stress and distortion of materials. The nonlinear optical characteristics and minimized heat and shock effects are particularly beneficial to fabrication stable high-resolution [10, 11].

3.2.1 Principles and characteristics of femtosecond laser processing

3.2.1.1 Non-thermal processing

In contrast to processing by nanosecond and longer pulses for which thermal processes dominate, femtosecond laser pulses enable non-thermal processing, allowing high-precision material processing [10, 11]. This characteristic is attributed to rapid energy deposition in the material. It takes a few hundred femtoseconds to a few picoseconds for the electron distribution to reach thermal equilibrium after femtosecond laser irradiation. In contrast, the time to transfer energy from the electron subsystem to the lattice, which induces thermalization, is of the order of 1-100 ps (depending on the electron–phonon coupling strength of the material). Thus, femtosecond lasers can efficiently cause electron heating and generate a hot electron gas, which is far from equilibrium with the lattice. Consequently, only a very small fraction of the laser pulse energy is converted into heat, resulting in non-thermal processing that enables high-quality microfabrication to be performed.

3.2.1.2 Minimization of heat-affected zone

Even though femtosecond laser pulses mainly induce non-thermal processes, they may still generate heat [10, 11]. However, femtosecond laser pulses suppress the formation of a heat affected zone due to their extremely short pulse widths. This permits high-quality microfabrication, even for metals with high thermal conductivities.

When the laser pulse width is shorter than the electron–phonon coupling time in laser–matter interactions, thermal diffusion to the interior of the material can be almost ignored. Most metals have an electron–phonon coupling time of the order of picoseconds, which is sufficiently long compared with the pulse width of femtosecond lasers. In this regime, when the material is heated to near the melting point T_m by femtosecond laser irradiation, the thermal diffusion length l_d is given by

$$l_d = \left[\frac{128}{\pi}\right]^{1/8} \left[\frac{kC}{T_m \Gamma_{e-ph}{}^2 C_e{}'}\right]^{1/4}$$

where k is the thermal conductivity, C is the lattice heat capacity, Γ_{e-ph} is the electron-phonon coupling constant, $C_e{}'$ is defined as $C_e{}' = C_e/T_e$. C_e is the electron heat capacity and T_e is the electron temperature. On the other hand, when the laser pulse width τ is much longer than the electron-phonon coupling time, l_d can be approximately estimated using $l_d = \sqrt{D\tau}$ where D is the thermal diffusivity. Hence, femtosecond laser processing can clearly reduce the thermal diffusion length, reducing heat affected zone formation in the processed region.

3.2.2 Interaction between transparent material and femtosecond laser pulse

High intensity of laser light can initiate an ablative material removal. Laser ablation encompasses several mechanisms such as photo-thermal, photo-chemical, hydrodynamic, and exfoliation ablation mechanism. [10,11]
The photo-thermal ablation occurs via bond breaking of atoms by the lattice vibrational energy that is transferred from irradiating laser light. In contrast, the photo-chemical ablation occurs via bond breaking of atoms by laser-induced electronic excitations. Both mechanisms enhance the liberation of atomic materials. On the other hand, hydrodynamic and exfoliation mechanisms enhance the liberation of bulk materials. The hydrodynamic ablation occurs via fluidic motion of micrometer scale droplets by laser-induced melting of material and the exfoliation ablation is mediated via separation of flakes from the surface by energy-absorbing defects.
For the femtosecond laser ablation, photochemical ablation process predominantly occurs since the pulse duration of femtosecond laser is shorter than the electron-phonon relaxation time. (*i.e*. heat exchange between irradiating laser pulses and the material barely occurs during the femtosecond laser material interaction.) Therefore, we can diminish the thermal effect and fabricate precise structures on the material.

Femtosecond laser irradiation induces electron excitation and relaxation processes in transparent material with wide bandgap (Figure 3.1). Electrons are initially excited from the valence band to the conduction band by multiphoton absorption or tunneling ionization. [10,11]
For relatively low laser intensities of the incident femtosecond laser beam, generated free electrons contribute to photo-chemical reactions (*e.g.*, photo-reduction of ions) and excited electrons can sequentially absorb several photons in the same laser pulse so that they are excited to higher energy states which free carrier absorption is efficient. This sequential excitation is termed electron heating and it results in non-thermal bond breaking.

At sufficiently high laser intensities, excited electrons are accelerated by the intense electric field of the ultrafast laser beam and collide with surrounding atoms, generating secondary electrons (avalanche ionization), which cause Coulomb explosion and eventually non-thermal ablation. Some of the generated free electrons relax to localize the energy stored in electron-hole pairs, which form self-trapped excitons (STEs). This relaxation often commences within 1 ps after laser irradiation. Some self-trapped excitons relax to form permanent defects within a few hundred ps. Glass heating occurs a few tens of picoseconds after laser irradiation due to free electron relaxation and the irradiated area returns to room temperature after several tens of microseconds, causing modification or damage.

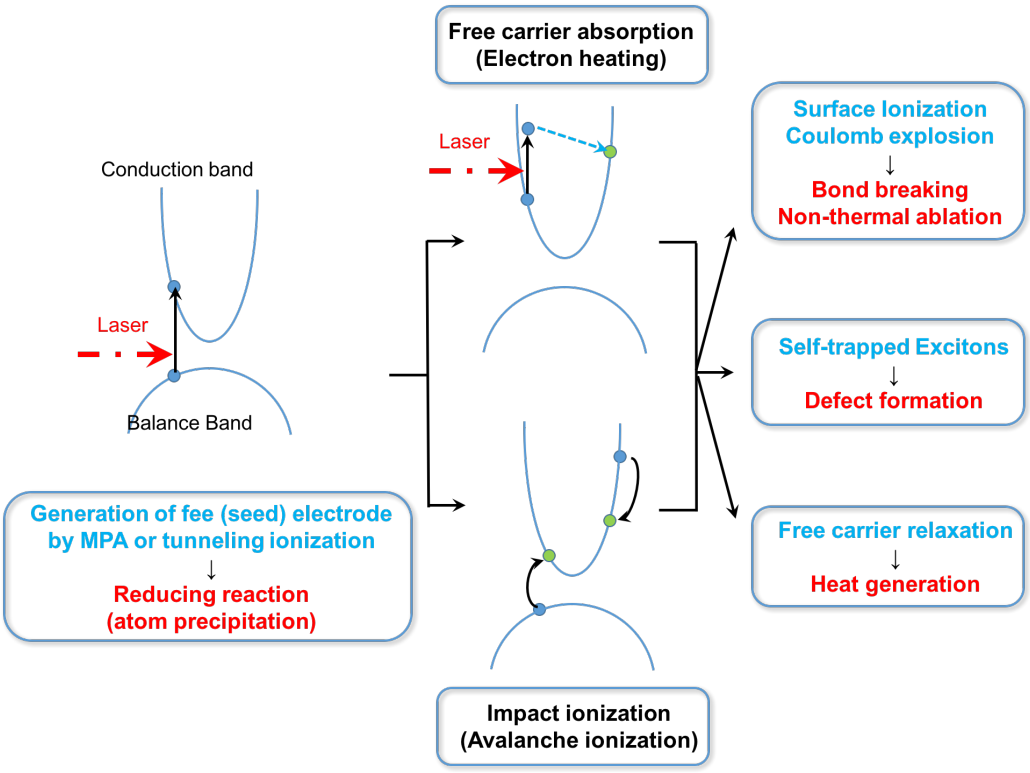

Figure 3.1. Interaction between transparent material and ultrafast laser pulse

3.2.2.1 Multiphoton absorption

For single photon absorption, the laser applies the energy into the material by generating electron-hole plasma. However, for wide bandgap material (*i.e.* dielectric), the cross section of the linear absorption is relatively small. In contrast to this, non-linear absorption (multiphoton absorption, tunnel ionization and avalanche ionization) can be dominant by creation of free carrier in the materials under irradiation of intense femtosecond laser pulses. [10,11]

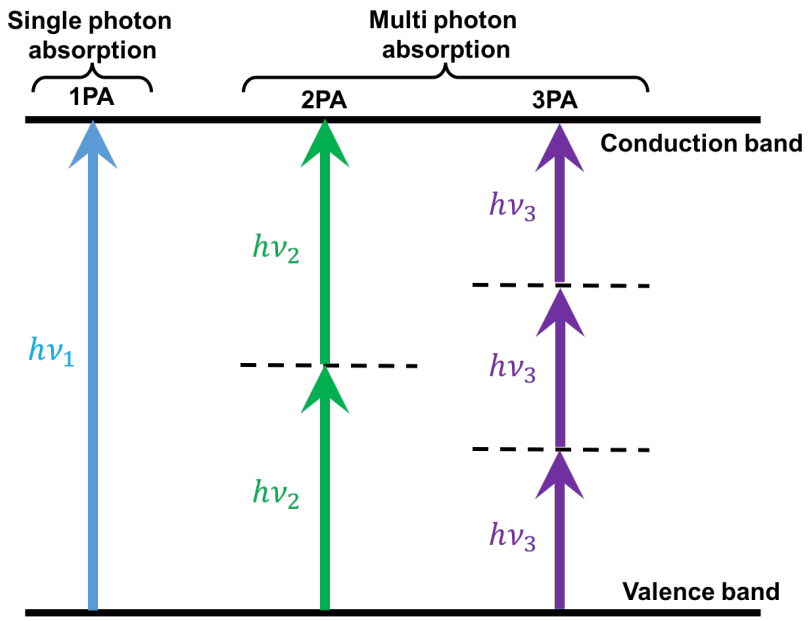

Figure 3.2. Single- (1PA) and multi-photon absorption (2PA and 3PA)

Single-photon absorption occurs when the single photon energy ($\hbar\omega$) of laser pulse is bigger bandgap energy (E_g) of material. For the wide bandgap materials, absorbed energy by single photon absorption of the femtosecond laser pulses with wavelength near the visible is not sufficient to excite an electron from the valence band to the conduction band.

Contrast to this, multiphoton absorption occurs when the photon energy ($\hbar\omega$) of laser pulse is smaller than bandgap (E_g). Simultaneous absorption of multiple photons must be involved in excitation of valence band electrons depending on laser intensity. Thus, the laser absorption occurs only within a focal volume, where the intensity exceeds the multiphoton absorption thresholds. The rate of multi-photon absorption can be expressed as

$$P(I)_{MPA} = \sigma^{(n)} I^m$$

where I is the laser intensity, $\sigma^{(n)}$ is the cross section of n-photon absorption, and m is the smallest number of photon to satisfy the relation as

$$m(\hbar\omega) > E_g$$

3.2.2.2 Interaction between femtosecond laser and polymer

With ultrafast laser pulses, direct ionization and dense electron-hole plasmas formation can lead to non-thermal phase transformations, direct bond-breaking, and explosive

disintegration of the lattice through electronic repulsion (Coulomb explosion). In certain nonmetals such as polymers and with relatively long thermalization times, photochemical ablation can still occur with short wavelength nanosecond lasers, producing well defined ablated regions with small heat affected zones.

In all cases, material removal is accompanied by a highly directed plume ejected from the irradiated regime. The dense vapor plume may contain solid and liquid clusters of material. At high intensities, a significant fraction of the species may become ionized, producing a plasma. Also, with pulses longer than ps, interaction of the laser light with the plume may be significant. The plume can absorb and scatter radiation, changing the actual flux received by the surface. Recoil from the plume can generate shockwaves in the material, causing plastic deformation and workpiece hardening. The recoil can also cause further expulsion of any remaining molten material as well as initiate shock waves. Resolidification of expelled liquid and condensation of plume material into thin films and clusters of nanoparticles can alter the topography at the rim and surrounding areas of the ablated region.

3.2.2.3 Tunneling ionization and Keldysh parameter

The tunneling ionization can be enhanced with extremely intensive femtosecond laser pulse irradiation into wide bandgap materials. Under this condition, the laser pulse energy induce periodic distortion of binding atomic potential (Figure 3.3), which allows direct tunneling of electrons from valence band to conduction band in a shorter than the laser pulse period. The crossover between multi-photon and tunneling ionization can be determined by Keldysh parameter (γ_{Ke}) as

$$\gamma_{Ke} = \frac{\omega\sqrt{2m_e E_g}}{eE}$$

where m_e is effective mass of electron, e is the charge of electron and E is intensity of electric field oscillating at frequency of laser pulse (ω).

Multi-photon process is dominant : $\gamma_{Ke} > 1.5$
Tunneling process is dominant : $\gamma_{Ke} < 1.5$
Coexist of the multi-photon and tunneling processes : $\gamma_{Ke} \sim 1.5$

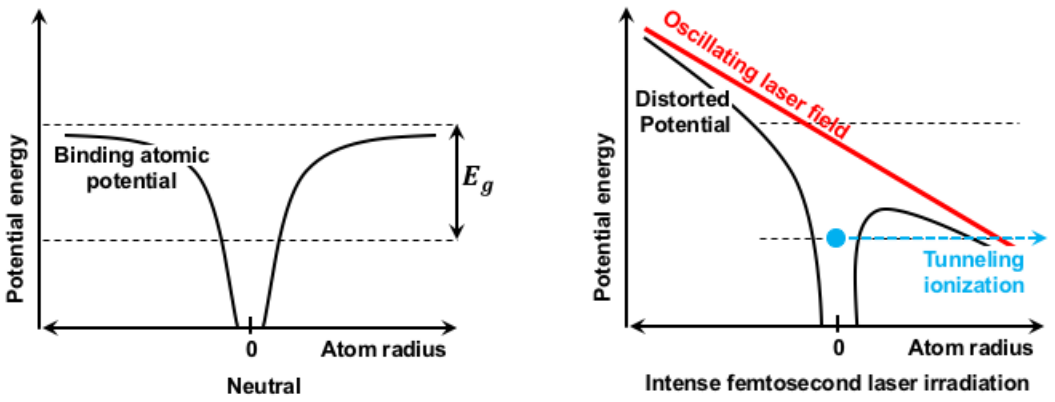

Figure 3.3. Tunneling ionization. (Left) natural behavior of atoms (Right) the tunneling ionization initiated by laser pulse energy induced distortion of binding atomic potential.

3.2.2.4 Avalanche ionization

The avalanche ionization involves free-carrier absorption followed by impact ionization. For this successive process, it requires seed electrons which is already present in the conduction band. This can be provided by photo-ionization, thermally excited carriers, or ionized impurity. Electrons in the high energy state can linearly absorb more photons sequentially, ionizing electrons from the valence band. Once the photon energy by the sequential absorption of n photons exceeds the band gap energy ($n(\hbar\omega) > E_g$), they impact more valence-band electrons by collisional ionization. If laser field is present and intense enough, the conduction band population grows by the avalanche process [10,11]. The electrons experience the intra-band transitions within the conduction band. The kinetic energy of the intra-band transit electrons can be transferred to electrons in valance band. If the transferred energy is greater than bandgap of material ($E_e > E_g$), the electrons are excited to conduction band (avalanche ionization). The electron density (N_{ED}) in the conduction band can be described by the following rate equation as

$$\frac{dN_{ED}}{dt} = \eta_{av} N_{ED} = \alpha_{av} I N_{ED}$$

where η_{av} is the avalanche ionization rate, α_{av} is the valance ionization coefficient, and the avalanche rate depends on the laser intensity as :

$$\eta_{av} = \alpha_{av} I$$

Combining with multi-photon ionization, above equation can be extended as :

$$\frac{dN_{ED}}{dt} = \alpha_{av} I N_{ED} + \sigma^{(m)} N_{ED} I^m$$

Note that electron population in conduction band depends on laser intensity (I).

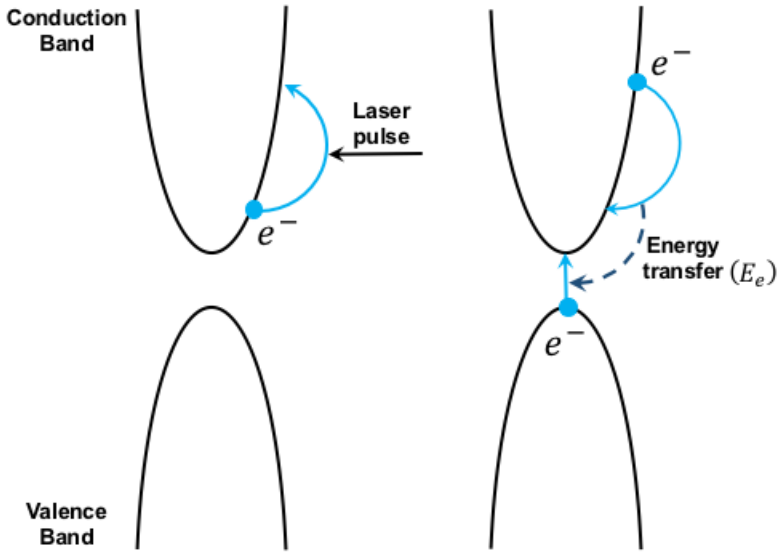

Figure 3.4. Avalanche ionization. (Left) absorption of irradiating laser energy by excited electrons, (Right) kinetic energy transfer from excited electrons to valance band electrons (E_e: kinetic energy of excited electrons in conduction band)

3.2.2.5 Ablation threshold of material

The femtosecond laser processing induces regular structures on materials due to aforementioned characteristics. There is minimum pulse energy fluence (J/cm^2) to initiate the material removal of ablation process [10,11]. Ablation threshold (F_{th}) is one of the useful parameters for laser processing. Gaussian beam waist (ω_0) can be determined from relation between the square of ablated crater diameter (${D_{abl}}^2$) and logarithm of pulse energy fluence (lnF) [66]as

$$ {D_{abl}}^2 = 2{\omega_0}^2 ln\left(\frac{F_0}{F_{th}}\right) $$

For the multi-photon absorption and relatively high pulse energy fluence, the effective penetration depth should be considered to determine the ablation threshold of material.

$$ \chi_{abl} \approx l_{pd} \times ln\left(\frac{F}{F_{th}}\right) $$

where χ_{abl} is the depth of ablated crater and l_{pd} is the effective penetration depth. The effective penetration depth can be affected by intensity of laser pulse. The ablation threshold can be a guideline for effect surface patterning fabrication.

3.2.2.6 Optical breakdown in dielectric materials

The femtosecond laser-induced damage in dielectric materials is known as a nonlinear process [10,11]. The damage in pure wide bandgap materials is associated with rapid buildup of conduction electrons. The mechanism of the optical breakdown can be explained by understanding the relative roles of various ionization and relaxation channels, particularly near the damage threshold. Once a dense electron-hole plasma has been generated in a bulk of dielectric materials by femtosecond laser irradiation, several mechanisms can be anticipated such as melting or vaporization of the solid, following strong phonon emission as well as generation and accumulation of intrinsic defects. The majority of previous studies for determining the damage mechanisms has focused on damage thresholds depending on laser pulse duration according to a $\sqrt{t_{pulse}}$ scaling. It is well known that thermal diffusion is dominant by 10 ps or longer laser pulse duration. In contrast, laser processing using femtosecond lasers, the pulse duration is much shorter than the characteristic time of thermal diffusion, and the damage threshold deviates from the square root scaling.

3.3 Experimental

3.3.1 Material preparation

3.3.1.1 Sample (Quartz and Polystyrene) preparation for ablated pattern

Fused silica (fused quartz ; 0.5-mm thick 4-in diameter) and tissue culture polystyrene (TCPS) were used for this experiment. For quartz, square pieces with 8 mm by 8 mm dimensions were prepared by dicing. For the cleaning, we cleaned the quartz samples ultrasonically with acetone for 1 hour before and after ablation processing and with methanol for 1 hour additionally after the processing. For TCPS, this material can be deformed by acetone easily, to reduce the change of material, we put the sample in the ethanol for sonication for 1 hour before and after ablation processing. TCPS samples were sonicated in DI water for 30 min after patterning, subsequently exposed to 70% ethanol for 1hr under UV light, and finally dried in 60°C oven for 30 min prior to cell seeding[48].

3.3.1.2 Nanofibrous scaffold fabrication

Electrospun scaffolds were fabricated using a customized electrospinning setup. Poly(L-lactide-co-carprolactone)/Poly(ethylene oxide) (PLCL/PEO)[109, 110] and Poly(L-lactic acid)/Poly(ethylene oxide) (PLLA/PEO) [111-113]scaffolds were electrospun as membranes on a rotating collector substrate. PLCL and PLLA were dissolved in hexafluoroisopropanol (HFIP) at 15% and 1% w/v concentrations, respectively. PEO was dissolved in 90% ethanol. PLCL/PEO and PLLA/PEO scaffolds were electrospun as dual fiber formulations by electrospinning separate jets of PEO and PLCL/PLLA solutions at a

single rotating substrate. The salt sodium acetate was added to all polymer solutions to aid in electrospinning. Controlling the quantity of precursor, we used the programmable syringe pump. Precursor loaded syringe was connected with flexible and long silicon tubing. And end of this tubing, the stainless needle with 1.5 in long and 500 µm diameter was connected. A high-voltage supply was used to apply a 15 kV voltage to the needle. The distances between needle end and collector plate was controlled by linear stage. For this experiment, we set the distance as 8.5 cm. PLLA/PEO and PLCL/PEO fibers with diameters ranging from 200-nm to 3-µm were ejected from the charged needle towards the grounded collector surface. The PLLA solution was delivered with a 1ml/hr flow rate by automated syringe pump. To get the approximately 150-µm thickness nanofibrous scaffold, we run this experiment for 45 min. And thickness of nanofibrous scaffold was measured by thickness gauge (Mitutoyo America, Aurora). After whole process, for removal of solvent (HFIP) in the electrospun sheets, we placed this scaffold into vacuum oven overnight with room temperature to remove any residual HFIP solution.

3.3.1.3 Microscale resonator platform fabrication

This process performed by Professor David Horsley's group of the University of California at Davis. The process flow is shown in Figure 3.5, where steps (a-d) were performed in the Sandia National Labs AlN MEMS fabrication process and steps (e) were performed at the UC Berkeley Marvell Nano Lab. This process incorporates a sacrificial polysilicon release pit that precisely defines the PMUT diameter, thereby enabling a small device size (25 µm and even smaller) with close spacing (5 µm) and eliminating the need for through-wafer etching. The sacrificial polysilicon is etched by vapor phase XeF_2, releasing the PMUT membranes as shown in step (e). The etch holes must be small to enable them to be sealed without filling the cavity beneath the PMUT membrane. Dense arrays having etch holes as small as 2 µm x 4 µm were successfully released. Reducing the density to 155 transducers/mm^2 allowed successful release using smaller 1-µm diameter etch holes, suggesting that XeF_2 depletion occurs during the release of dense arrays.

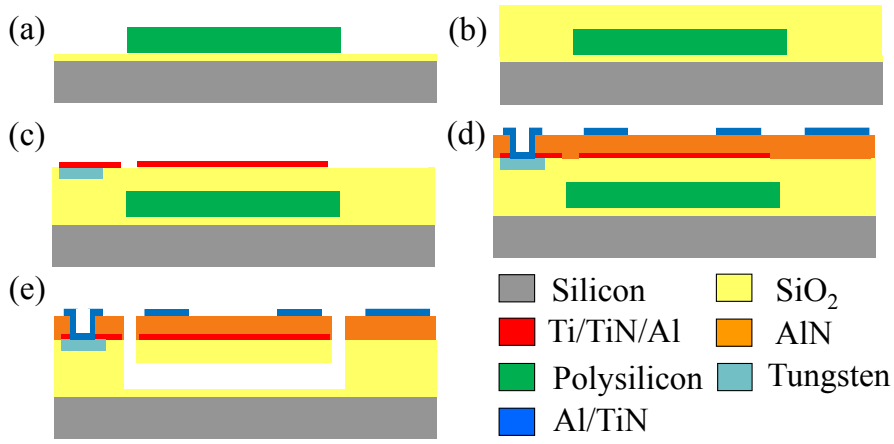

Figure 3.5. Fabrication process of microscale resonator platform

3.3.2 Diverse ablation pattern fabrication

3.3.2.1 Nanoscale crater fabrication

We fabricated nanoscale topographical patterns by exploiting the optical breakdown of dielectric materials induced by femtosecond laser pulses. We used a Ti:Sapphire regeneration amplifier system (Spectra-Physics, US; with 100 fs pulse length [at full width half maximum (FWHM)] and fundamental wavelength of ~800 nm), and a wavelength of ~400 nm was obtained by frequency-doubling using a nonlinear crystal. Patterned nanoscale features by user-designed rastering of the sample across the beam path. And laser pulses emission was synchronized with the sample translation. The experimental apparatus is shown in Figure 3.6. We adjusted the laser fluence with an attenuator comprised of a half wave plate ($\lambda/2$) and a polarizing beam splitter (PBS). As the laser pulse energy required to ablate high-resolution features is extremely low, we inserted a neutral density (ND) filter into the beam path. To generate user-designed patterns, we loaded samples on a precise 2D motorized stage (ANT130, Aerotech Inc., US) with a synchronized laser firing system controlled by a programmable computer. The stage was driven by its own driver (NDrive ML) and software (A3200, Aerotech Inc., US) controlled by a computer. The driver has digital input and output ports that can generate TTL signal configured by the software. The sample was precisely aligned perpendicular to the incident laser beam by adjusting the tilting angle of the sample. To fabricate various nanocrater features, we used long working distance objective lenses with three different numerical aperture sizes: 20x objective lens (Mitutoyo M Plan Apo, NA= 0.45), 50x objective lens (Mitutoyo M Plan Apo, NA= 0.55) and 100x objective lens (Nikon CFI 60 LU Plan Epi ELWD Infinity-Corrected, NA= 0.8). We ablated bare quartz samples with single pulses using the computer-controlled system[48].

Since the interaction of the laser with TCPS is significantly different from that on quartz, we conducted an independent parametric analysis on TCPS to optimize the laser parameters for fabrication of the nanocraters for this new material. We optimized the laser ablation parameters by changing the laser power and number of laser pulses. For TCPS ablation, the required power for a single laser pulse is significantly lower than for quartz. We used a 50x objective lens (Mitutoyo M Plan Apo, NA = 0.55) to fabricate the small diameter craters on TCPS[48].

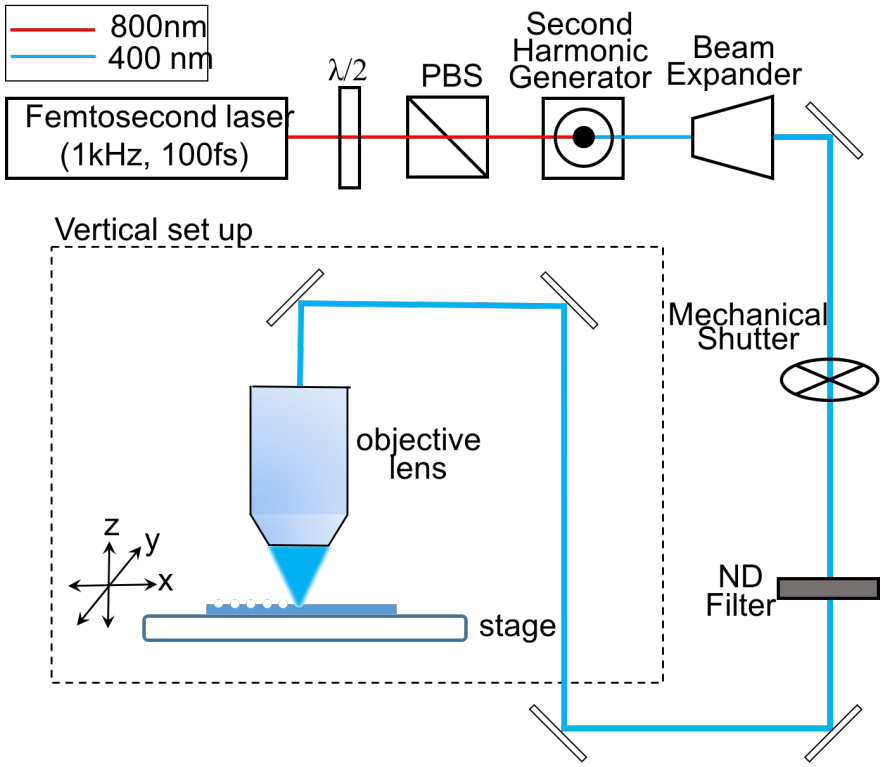

Figure 3.6. Schematic of femtosecond laser direct writing for ablation patterning

The present study was performed to investigate cell morphology and motility on microscale anisotropic ablated pattern different aspect ratios (1: 3-5-7-9). Hypothesis is this research is that anisometric pattern also effect on the focal adhesion distribution and cell migration directionality. We also prepared an anisotropic pattern with different aspect ratio. To fabricate the different ratio pattern, overlapped patterning method was used. Number of laser shot was determined by aspect ratio (AR) as 'Number of laser shot = (2 x AR) + 1' (Figure 3.7). Addition to this, 'enhance' and 'hinder' pattern fabricated the structure between guiding pattern with parallel (enhance) and perpendicular (hinder) direction.

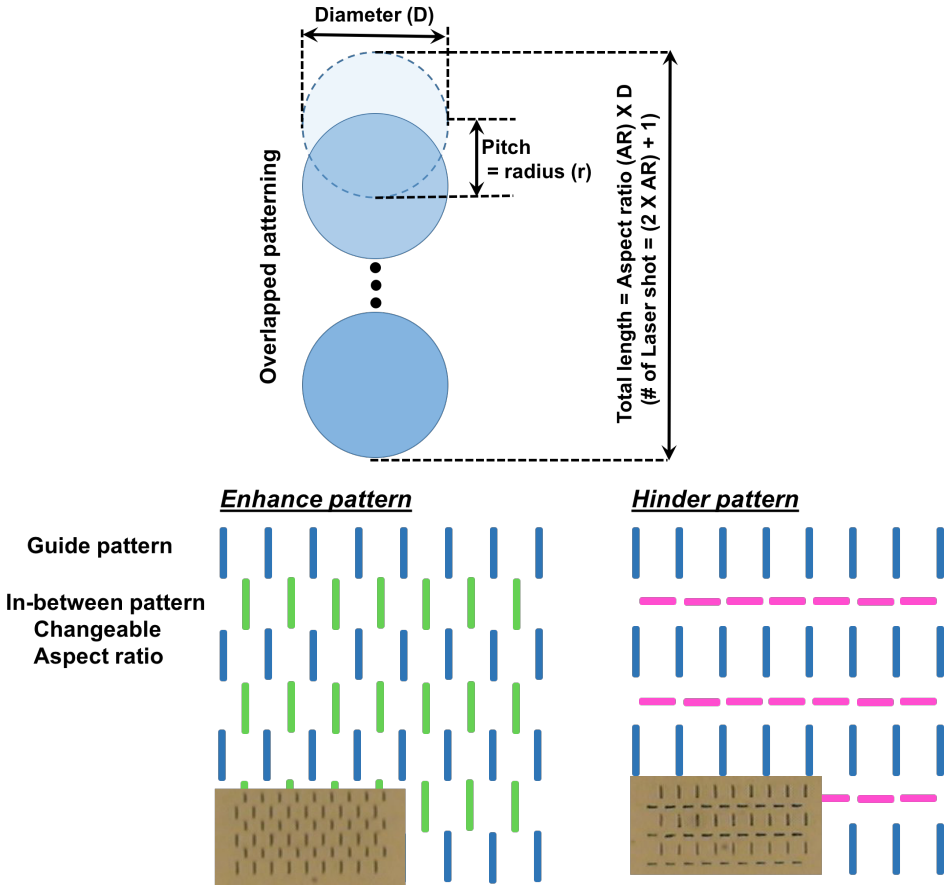

Figure 3.7. Schematic of anisotropic pattern fabrication. Enhance and hinder anisotropic pattern

3.3.2.2 Line ablated pattern fabrication on electrospun nanofibrious scaffold

The ablation characteristics of the PLCL-based scaffolds were first evaluated, using the procedure previously described for poly(L-lactide) (PLLA)-based scaffolds, to determine optimal parameters for generating the desired ablation patterns. A Ti:sapphire amplified laser system (Spitfire, Spectra Physics, Irvine, CA) and 5x objective lens (Mitutoyo M Plan Apo, NA= 0.14) was used to perform femtosecond laser ablation. Briefly, single discrete pulses of varying laser energy (ranging from 7 μJ–91μJ) were shot onto the scaffolds to first observe how pore size generated varied with laser energy. Next, pulse number was varied (1-9 times) at 2 constant pulse energies (28μJ and 49μJ) to determine resulting change in depth with increasing number of pulses. Finally, stage migration parameters were varied to determine degree of overlap between pulses required to produce a uniform channel. Using data derived from the ablation characterization, ablation channels of approximately 50 μm pore diameter were fabricated on one side of each scaffold using pulses of 49 μJ laser energy.

3.3.2.3 Laser trimming on microscale resonator platform

Due to the thin thickness of piezoelectric layer, minimization of thermal accumulation is important for this experiment. Minimizes thermal effects occurring within the short pulse duration (~100fs), reducing the thermal stress and damage to the piezoelectric layer during the trimming process. Trimming was conducted using an automated system with computer control over stage motion and laser pulse firing. We applied 12.7nJ laser pulse energy with 50x objective lens (Mitutoyo M Plan Apo, NA= 0.55).

3.3.3 Cell culture and imaging

NIH-3T3 cells were maintained in Dulbecco's Modified Eagle Medium (DMEM) (Gibco Invitrogen), with 10% fetal bovine serum (FBS) (Gibco Invitrogen) and 100 units/ml penicillin and streptomycin (Gibco Invitrogen) in 75-cm^2 culturing T-flask (Corning) at 37°C and 5% CO_2 culture incubator. Before experiments, samples were coated with fibronectin (Sigma Aldrich) with 20μg/ml concentration in phosphate buffered saline (PBS) (Gibco, Invitrogen) to enhance the adhesion between quartz substrate and cells for 1 hours. The samples were then rinsed with PBS for several times. Confluent cells were detached from the flask through treatment with 0.05% Trypsin-EDTA (Gibco Invitrogen) and seeded onto the patterned substrate in sterile polystyrene well plates with CO_2-independent media (Gibco Invitrogen), 10% FBS, 100 units/ml penicillin, and 1% GlutaMAX (Gibco Invitrogen) and placed on an inverted fluorescence microscope (IX71, Olympus) that was covered by a chamber to maintain temperature and humidity. Phase-contrast images were taken every 5 minutes with a digital CCD camera (Retiga 2000R cooled, Qimaging) for about 2-3 days [48].

3.3.4 Immunofluorescence staining

For visualizing vinculin, F-actin, and nucleus, fibroblast cells plated on patterned surfaces and a flat surface for 15 hours were washed with pre-warmed PBS. Samples were fixed 1 hour and 12 hours post seeding with 4% paraformaldehyde (Santa Cruz Biotech) for 15 minutes. Cell were permeablized using 0.2% TritonX (Sigma) in dPBS. Blocking and fixation were done with a solution of 2% bovine serum albumin (Sigma), 0.3 M glycine (Sigma), 0.2% Tween-20 (Sigma) in dPBS for at least 30 minutes. Samples were incubated with a primary mouse-anti-vinculin antibody (1:200) (Sigma) overnight at 4°C then washed. Anti-mouse 633 secondary (1:100) (molecular probes) and Actistain-555 (1:500) (Cytoskeleton, Inc.) were incubated for 1.5 hours at room temperature then washed. The nucleus was stained with 300nM DAPI (Molecular Probes) for 5 minutes and washed. Samples were kept in PBS and turned over for the inspection by an upright fluorescent microscope (AxioImager M1, Zeiss). Samples were inverted onto coverslips

just before imaging. Images were acquired using the Zeiss 710 Axio-Observer with 40x oil immersion objective. For immunofluorescence imaging of fibroblast cells on TCPS ablation patterns, a 40x water immersion objective was used [48].

3.3.5 Talin overexpression

Overexpression of the first 405-amino-acid sequence of the globular N terminus of Talin-1 was accomplished using the Lonza Nucleofector 2B. GFP/Talin-1(1-405) plasmids included the entire FERM domain and were shown to over-activate the $\alpha_5\beta_1$ and $\alpha_5\beta_3$ integrins in transfected cells. For each transfection, approximately 10 million cells were suspended in 100 µl of Nucleofector 2 Solution R with 8 µg of plasmid and transfected using program U-030. Immediately after transfection, 500 µl of DMEM (ATCC) supplemented with 10% fetal calf serum (ATCC) was added to the cell solution. The sample was then incubated at 37ºC for 15 min. Cells were gently transferred into culture flasks and seeded at ~90% confluency in normal growth medium. After 24 h, transfected cells were sorted using flow cytometry for GFP fluorescence. Cells were seeded on patterned samples 48 h after transfection [48].

3.3.6 Blebbistatin treatment

To explore the effect of cell migration on cell patterning, cells were treated with 50 µM blebbistatin, which inhibits the binding of myosin II to actin and therefore interferes with myosin II contractility and cell migration. Treatment solutions were prepared by suspending (-)-blebbistatin (Sigma) in dimethyl sulfoxide (DMSO; Sigma). This solution was added to the cell media immediately after cell seeding [48].

3.3.7 RGD (Arg-Gly-Asp) peptide coating

A number of combinations of albumin blocking, media conditions, and avidin derivatives were deposited onto ablated surface in an attempt to minimize non-specific cell adhesion. Biotinylated bovine serum albumin (BSA) and avidin derived proteins were adsorbed from PBS (pH 7.2) at 0.1 mg/mL for 1hr. Biotin-containing molecules were conjugated to the avidin derivatives for 1 hour at 0.05 to 0.1 mg/mL in PBS, and rinsed three times. Surfaces were kept bathed in PBS until cell seeding. (RGD sequence: 15 amino acid peptide containing the sequence RGD ; biotin-CGGNGEP**RGD**TYRAY-NH_2)[114].

3.3.8 Quartz Crystal Microbalance with Dissipation

The adsorption kinetics of fibronectin (bovine, Sigma Aldrich) to TCPS and SiO_2 sensor crystals was characterized using the standard flow module of a Q-Sense E1 QCM-D (Biolin Scientific, Sweden). To create the TCPS interfaces, polystyrene sensor crystals were activated by an oxygen plasma treatment (Plasmatic Systems) at 1 Torr and 150 W for 1 min. Adsorption to both SiO_2 and TCPS surfaces was determined by recording the frequency shift of the fifth and seventh overtone at 23°C for a fixed time interval (50min). The QCM-D was set up and calibrated in buffer (1X PBS, pH 7.4, flow rate = 100 µl/min). After obtaining a stable signal ($\Delta f = 0$), the peristaltic pump was stopped and the protein sample (20 µg/ml in DMEM) was introduced (flow rate = 100 µl/min). 50 min after injection, the sensor was rinsed with 1xPBS for 10 minutes to remove non-specifically-bound protein [48].

3.3.9 Characterization of electrospun scaffolds

Top-down and transverse cross-sectional views of the ablated scaffolds were imaged using a scanning electron microscope to visualize changes in resultant fiber morphology, as well as pore diameter and pore depth generated by femtosecond laser ablation treatment. All images were captured at various magnifications with an accelerating voltage of 10kV. Images were processed and analyzed using the open source software ImageJ (National Institutes of Health, MD, USA).

3.3.10 *In vivo* Subcutaneous Implantation

The biological performance of the various ablated electrospun scaffolds was assessed using a rat subcutaneous implant model at sub-chronic time points. All animal study procedures were approved by the Institutional Animal Care and Use Committee at the University of California, Berkeley. Adult male Sprague-Dawley rats were anesthetized with 1.5% isoflurane in 70% N_2O / 30% O_2. Incisions were made on the left and right lower abdominal regions and 3x7mm samples of each ablated scaffold (n=3) were implanted subcutaneously and secured to the fascia using non-resorbable 8-0 nylon stay sutures. The wound was closed using resorbable 4-0 nylon sutures. All animals were given Buprenorphine post-surgery. The animals were sacrificed at 2-week sub-chronic time points and the samples were explanted and processed as described below.

3.3.11 Histology & Immunofluorescent Staining

Upon explantation of the samples and prior to cryosectioning, tissue samples were embedded and frozen in optimal cutting temperature compound (OCT). Sectioning was then conducted using a Leica cryotome. All tissue sections were taken in the transverse plane with respect to the long axis of the implanted sample. Masson's trichrome staining was performed to assess cell penetration and tissue integration.
Immunostaining was used to identify cell types present in the sections. Images were processed and analyzed using the open source software ImageJ (National Institute of Health, MD, USA). The samples were immunofluorescently stained for the following cell markers: vimentin (Abcam), CD68 (ABD Serotec) and CD31 (Abcam). Fluorescence images were obtained with a Zeiss Axoiscope epifluorescent microscopy and Axiovision software. Images were analyzed using ImageJ software.

3.3.12 Characterization of ablated pattern

3.3.12.1 Atomic force microscopy (AFM)
The ablation craters were examined by atomic force microscopy (AFM, Nanoscope IIIa, Bruker) with high aspect ratio tips (Nanosensors, AR5-NCHR, Aspect ratio ≥ 5:1) in tapping mode. To analyze the relationship between the ablated crater dimensions and the laser energy, we generated craters with various energies and scanned a 3x3 μm^2 area of the substrate with the AFM. The cross-section profiles of ablation pattern were obtained via the AFM software (Nanoscope analysis; Bruker) [48].

3.3.12.2 FEI-Scanning electron microscopy (FEI-SEM)
The craters were also analyzed using FEI-scanning electron microscopy (FEI-SEM; Zeiss). To reduce the charging effect, 10-nm thickeness gold layer was coated [48].

3.3.12.3 Measurement of mechanical properties of electrospun fibrous scaffold
To determine the mechanical property of the nanofibrous scaffolds, scaffolds were first cut into pieces approximately 0.5 cm 1 cm and subjected to uniaxial tensile testing in the lon- gitudinal direction using an Instron 5544 tester (Instron, Canton, MA). Prior to testing, three thickness measurements along the length of each sample were taken with the thickness gauge and averaged; likewise, three width measurements were acquired using a digital caliper and averaged. After placing the sample in between the grips, the gauge length was measured with a digital caliper. Each sample was extended until failure at a rate of 0.1 mm/s, and the applied force and deformation were recorded every 1 s via Bluehill software (Instron). The elastic modulus was calculated by determining the slope based on the applied load and scaffold deformation in the linear region of the stress–strain curve and the dimensions (thickness and width) of the samples

3.4 Results and discussion

Attempts to control cell behavior at cell-material interfaces have employed chemical and physical properties of surface, such as surface chemistry, topography, stiffness, and combinations of these properties. Regarding topographical cues, it is well known that interfaces with micro/nanoscale topographical features strongly modulate cell behavior such as adhesion, migration, proliferation and differentiation. Although topographical cues on the microscale have been shown to be powerful to control cell behavior, they are limited by the inability to independently control physical inputs to cells on the length scale of focal contacts (*e.g.*, ~ 100-200 nm depending on maturity).
The present study uses multiphoton ablation lithography (via ablation) to create nanocrater patterned with different topography (diameter and depth) and distribution (spacing) interfaces that control focal adhesion formation and migration, rendering surfaces cell repellant under specific conditions. Intense femtosecond laser pulses can damage in transparent dielectrics through nonlinear absorption such as multiphoton initiated avalanche ionization. Ablation process by femtosecond is stable and reproducible, since there is no heat exchange during the femtosecond laser pulse irradiation, minimizing thermal stress and collateral damage.
Although laser machining is an attractive approach for many biomedical applications, a major concern using this process biomaterial scaffolds has the potential for thermal effects. However, femtosecond lasers are considered promising tools to rapidly process and create complex structures on electrospun scaffold due to minimal thermal and physical stress. Femtosecond laser processing superior to other laser machining process lie primarily in its very rapid creation of vapor and plasma phases that lead to negligible heat conduction and the absence of liquid phase. Thus, femtosecond lasers processing offers the possibility of precise material processing with clean surfaces and reduced thermal damage. The diameter and depth of fabricated pattern can be controlled precisely using FS-DLW [48].

3.4.1 Characterization of patterned surface

3.4.1.1 Nanascale crater pattern

We fabricated nanoscale features in quartz with various shapes (depth versus diameter) by adjusting the pulse energies and focusing with objective lenses of different numerical apertures (NA). For quartz samples, there was no evidence of melting or capillarity assisted material movement around the crater, and we checked by SEM. The thermal exposure was minimized during the short pulse regime, and this attribute allowed us to fabricate nanocraters in quartz without the addition of a lip structure at peripheral of the ablated areas. Minimization of positive topography is critical this research to eliminate roughness effects on their cell behavior [48].

To demonstrate the generality of our observations, we also evaluated the directional cell migration with another substrate that is widely used for cell culture, tissue culture polystyrene (TCPS). Using the same fabrication technique as for quartz, similar nanocraters were fabricated on polymer (polystyrene). The polymer-laser interactions, however, complicated thermal absorption processes. Atomic force microscopy (AFM) revealed a rim of ablated material surrounding the craters that was not formed on quartz substrates. Although we did minimize the rim dimensions, it was not possible to prevent entirely their formation, leading to some deviations of the cell behavior compared to quartz. However, we were able to successfully reproduce the cell repellant effect on the patterned TCPS[48].

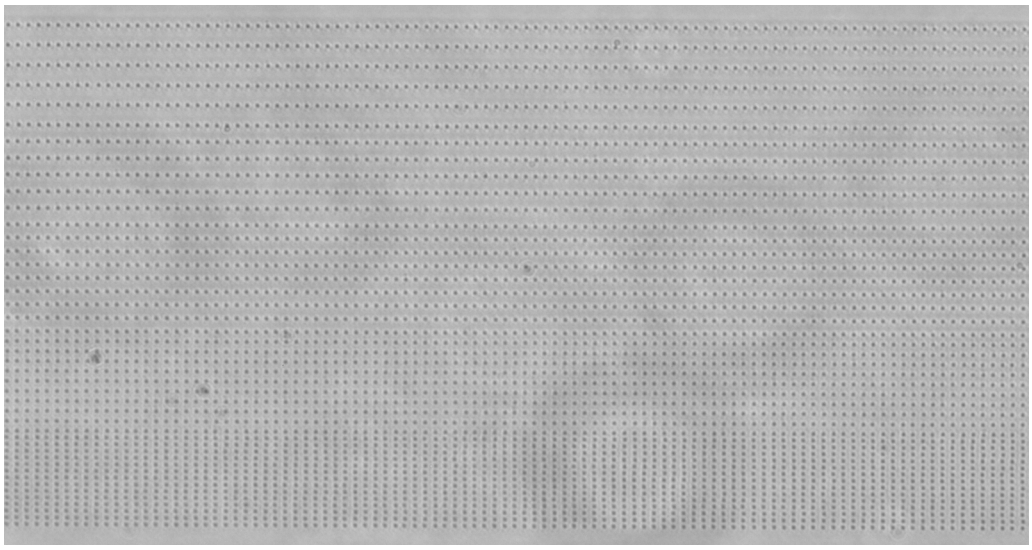

Figure 3.8. Optical microscopy image of ablated pattern on the quartz

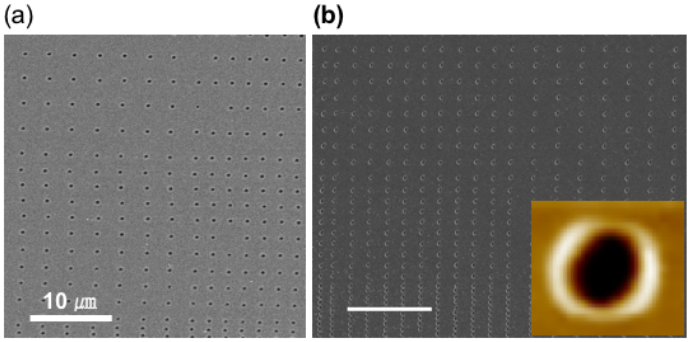

Figure 3.9. SEM image of the ablated pattern (a) Quartz and (b) Polystyrene (scale bar : 10μm)

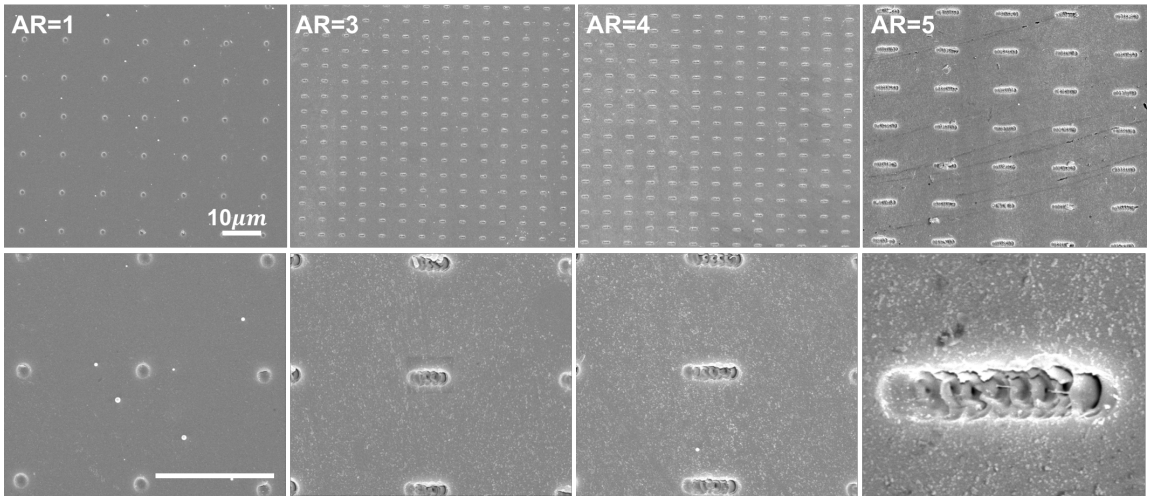

Figure 3.10. SEM image of the anisotropic ablated pattern with aspect ratio = 1, 3, 4 and 5 (scale bar : 10μm)

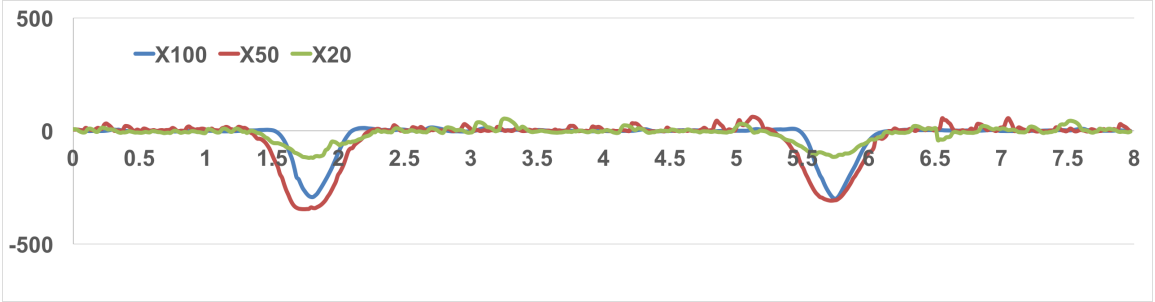

Figure 3.11. AFM contour scans presenting cross sectional images for three different nanocrater dimensions (depth and diameter) (on the quartz) fabricated by x100x, x50, and x20 objective lenses

Diameter (nm)	Depth (nm)	Area of crater bottom (μm^2)	Laser power (nJ)	Objective lens
1000	350	0.96	30	50x
1000	100	0.80	35	20x
1000	30	0.79	30	20x
600	350	0.43	25	100x
600	110	0.30	25	50x
500	45	0.20	20	50x

Table 3.1. Dimensions of nanocraters for creating ablated patterns on quartz surface

For characterization of the 'lip' features adjacent to the crater of ablated pattern on polystyrene, we measured their height and FWHM. We observed wider (larger FWHM) and taller lips as the laser power increased. And similarly, with increasing number of laser shots, it also shows the deeper ablated pattern and higher FWHM of lip feature. To generate nanocraters matching the size on quartz, we used single laser pulses with 3 nJ via 50x objective lens. Thereby, the width and height of the lip was kept relatively small compared to the diameter, depth, and pitch of the craters. We created patterns in TCPS similar to those in the previously studied quartz substrates [48].

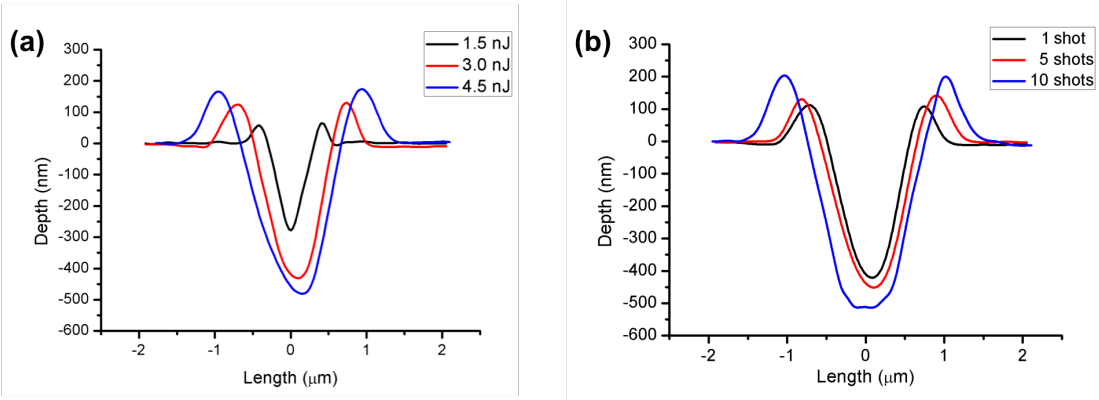

Figure 3.12. Cross sectional profiles at the center-line of the ablated nanocraters (on the polystyrene) depending on (a) pulse energies and (b) laser shot number with 3nJ using the x50 objective lens

Diameter (nm)	Depth (nm)	Height of margin (nm)	FWHM of margin (nm)	Laser power (nJ)	Number of Laser pulses	Objective Lens
690	250	30	82	1.5	1	50x
1100	420	120	140	3	1	50x
1500	480	150	400	4.5	1	50x
1230	450	140	275	3	5	50x
1500	500	200	470	3	10	50x

Table 3.2. Dimensions of nanocraters for creating ablated patterns on polystyrene surface

3.4.1.2 Line ablated pattern on electrospun nanofibrous scaffold

Electrospun scaffolds are used extensively in tissue engineering applications due to ECM-like microenvironment. However, one major limitation is the poor infiltration due to dense fibers, small pore size. Small pore size of electrospun scaffolds results from the dense network of fibers, and this hinders cell infiltration, reduces their use in replacing large tissues that require ample vascularization and nutrient diffusion. The various techniques to overcome limitations have been investigated, introducing the incorporation of sacrificial fibers and porogens, modification of fiber diameter, and photopatterning

processing by UV radiation treatment to increase pore size and overall porosity. Here, we employ a femtosecond laser ablation method to create microscale groove (line) features on electrospun PLLA/PEO and PLCL/PEO nanofibrous scaffolds. To characterize the ablation of electrospun PLLA/PEO and PLCL/PEO scaffolds, the effects of varying laser energy and pulse number on ablated pore size and depth, respectively, were examined. Our plots show that the diameter of ablated pores increased linearly as laser energy increased, and the resulting depth was linearly proportional to the pulse number. For PLLA/PEO, with single laser pulse the average diameter of ablated pores increased from about 30 to 110 μm as the laser power before objective lens was increased from 8 to 96 μJ. And with a 18 μJ femtosecond laser, the average depths of ablated pores increased from about 30 to 275 μm as the number of pulses was increased from 1 to 9, with complete through-holes achieved beyond 10 pulses. For PLCL/PEO, with single laser pulse the average diameter of ablated pores increased from about 20 to 40 μm as the laser power before objective lens was increased from 8 to 96 μJ. And with a 28 μJ femtosecond laser, the average depths of ablated pores increased from about 23 to 125 μm as the number of pulses was increased from 1 to 9, with complete through-holes achieved beyond 10 pulses. And with a 49 μJ femtosecond laser, the average depths of ablated pores increased from about 26 to 162 μm as the number of pulses was increased from 1 to 9. We demonstrated that the scaffold material could be removed controllably layer by layer and that well-defined pore size and spacing could be easily produced in a rapid format.

Our SEM visualization confirmed that femtosecond laser ablation of electrospun scaffold resulted in minimal thermal stress and collateral damage. The PLLA/PEO and PLCL/PEO fiber architecture, especially in regions immediately adjacent to the ablation site, did not reveal molten morphology. The ablated scaffolds maintained an overall intact fibrous structure and provided a more porous structure, not only because of the patterned arrays of holes, but more importantly due to the relatively larger pore sizes on the post-ablation edge compared to the pores on the scaffold surface. Thus, our findings suggest that the process of femtosecond laser ablation can impart beneficial features in addition to patterned holes to electrospun scaffolds in order to increase not only pore size and improve bulk porosity but also to provide the path for cell infiltration between layers of electrospun fibers.

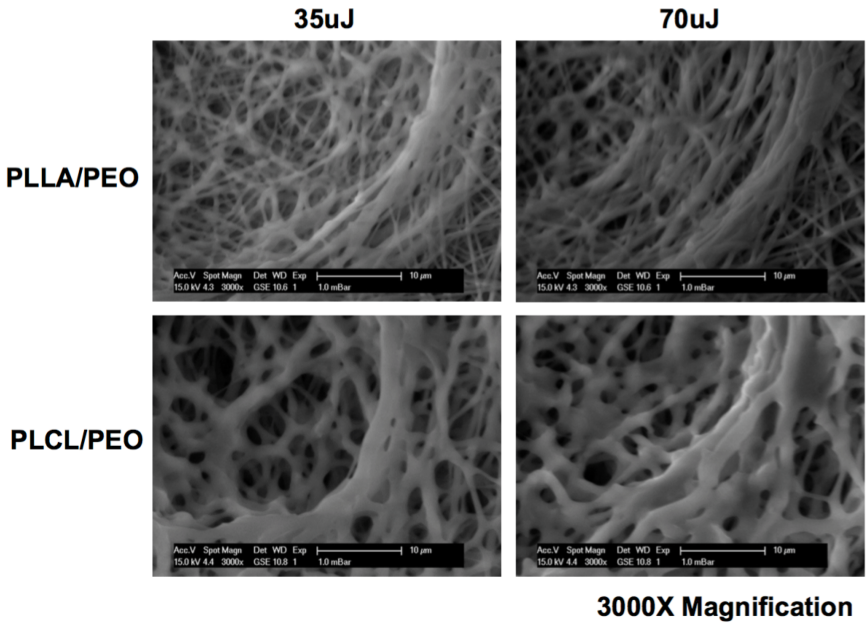

Figure 3.13. SEM image of the patterned craters on the electrospun nanofibrious scaffold (PLLA/PEO and PLCL/PEO) with single laser shot

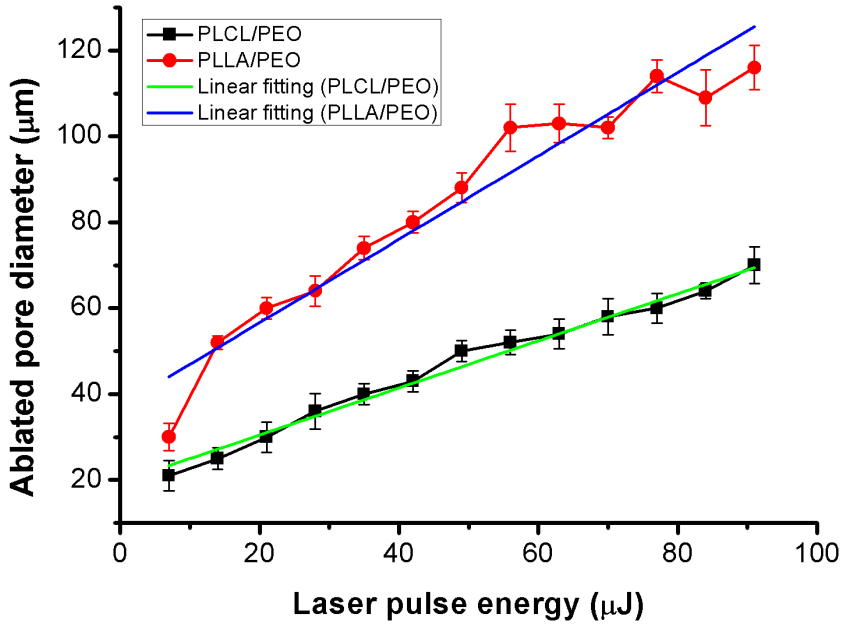

Figure 3.14. Relation between laser pulse energy and ablated pore diameter of the electrospun nanofibrious scaffold (PLLA/PEO and PLCL/PEO) and fitting line

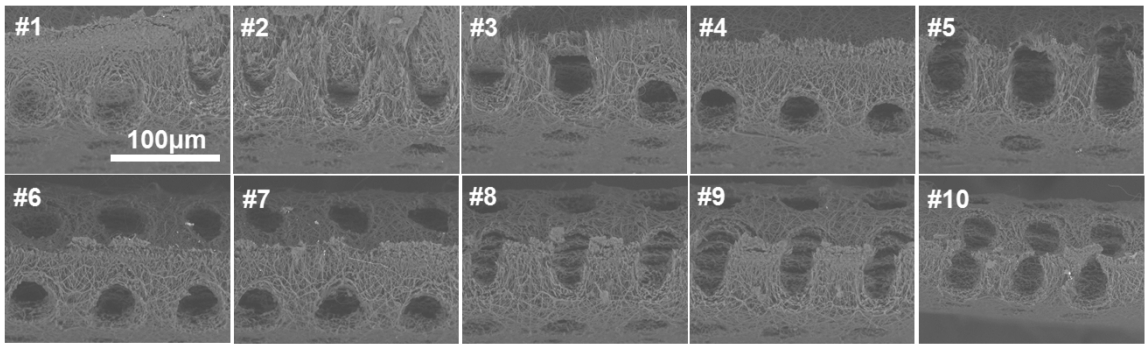

Figure 3.15. SEM image of the patterned craters on the electrospun nanofibrious scaffold (PLCL/PEO) with multiple laser shot using x5 objective lens

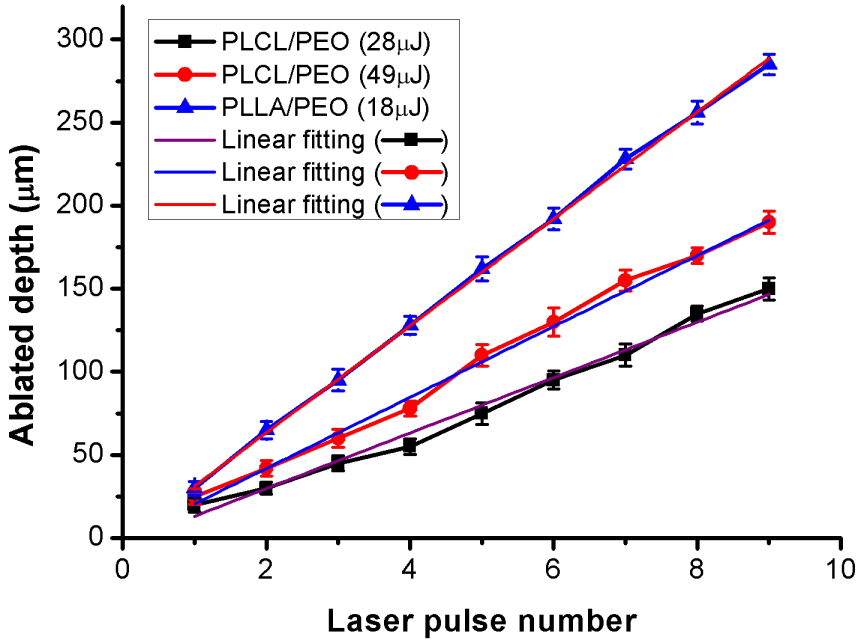

Figure 3.16. Relation between laser pulse number and ablated pore diameter of the electrospun nanofibrious scaffold (PLLA/PEO and PLCL/PEO) with different laser pulse energy and fitting lines

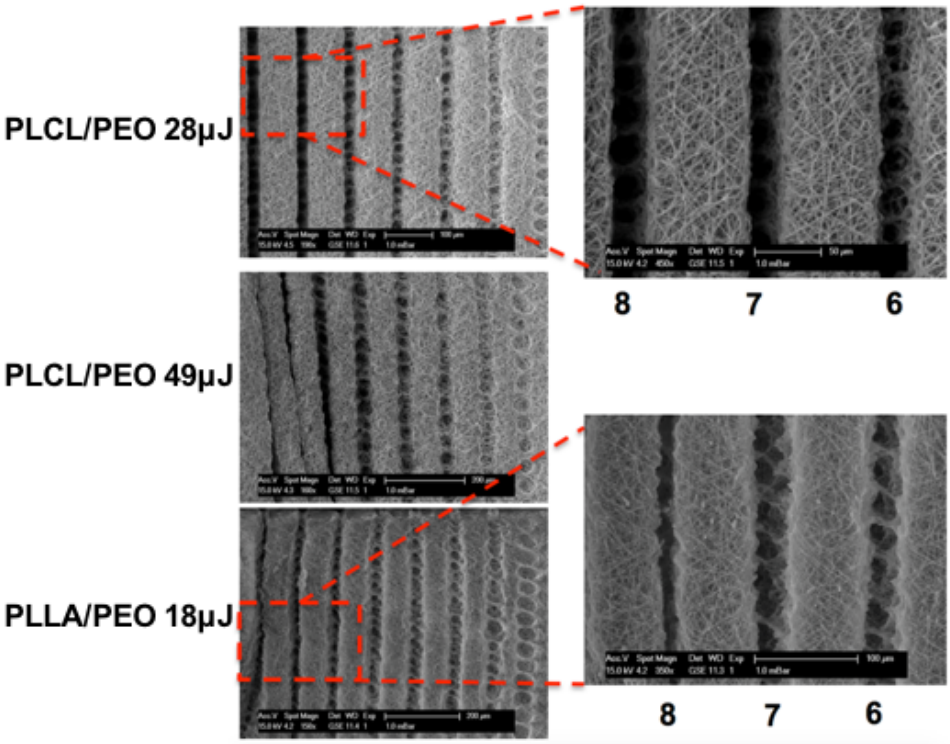

Figure 3.17. SEM image of the ablated pattern with line pattern on the electrospun nanofibrious scaffold (PLCL/PEO and PLLA/PEO) with different pulse energy (Left) and overlapped pulse number (Right)

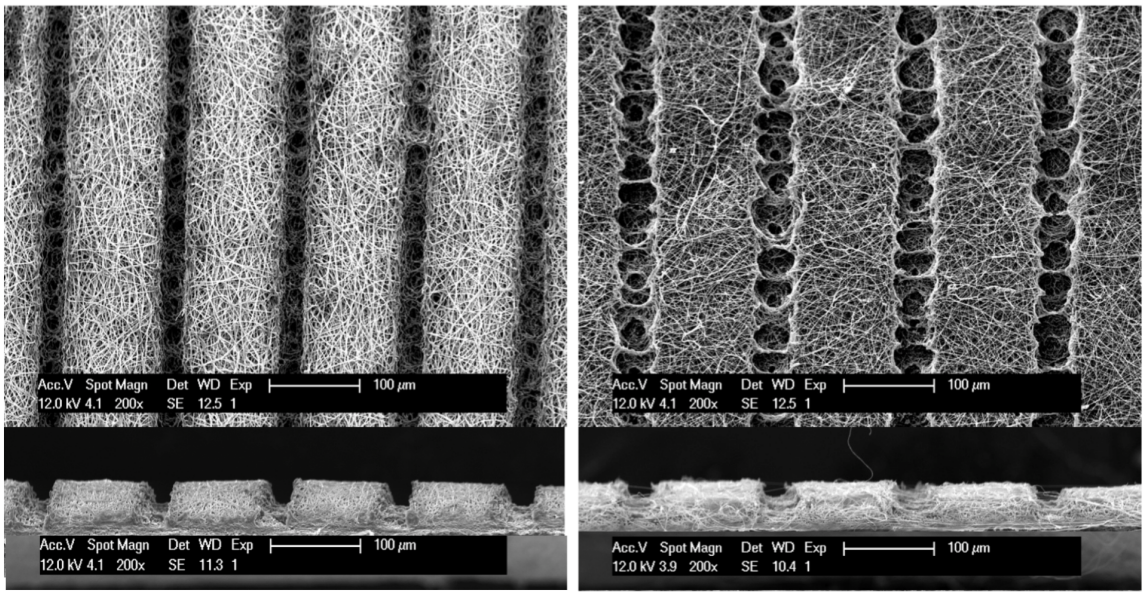

Figure 3.18. SEM image of the ablated line pattern and cross-sectional on the electrospun nanofibrious scaffold: (Left) PLCL/PEO, (Right) PLLA/PEO

3.4.2 Interaction between nanoscale ablated pattern and cell

Features and spatial distribution of the nanoscale craters in quartz affected cell adhesion, morphology, migration, and spatial organization. We observed cellular (NIH-3T3 ; fibroblast cells) adhesion and spreading on isometric patterned surfaces with same craters (1 μm in diameter, 350 nm in depth), and different nanocrater distribution (2, 4 and 8 μm pitch). After cells were allowed time to migrate, areas of low pitch (2 and 4 μm) exhibit smaller cell densities than larger pitched (8 μm) nanocrater surfaces or unablated areas. Cells on the smaller pitched surfaces also appeared refractile and weakly attached. Furthermore, the morphology and focal adhesion distribution of cells were also altered depending on pattern pitch. Cells on surfaces with the smaller pitches had decreased and less pronounced focal adhesions that were primarily distributed at either the leading or trail edge of the cell (Figure 3.38). These cells also appeared to have a greater degree of polarization and fewer multiaxial protrusions [48].

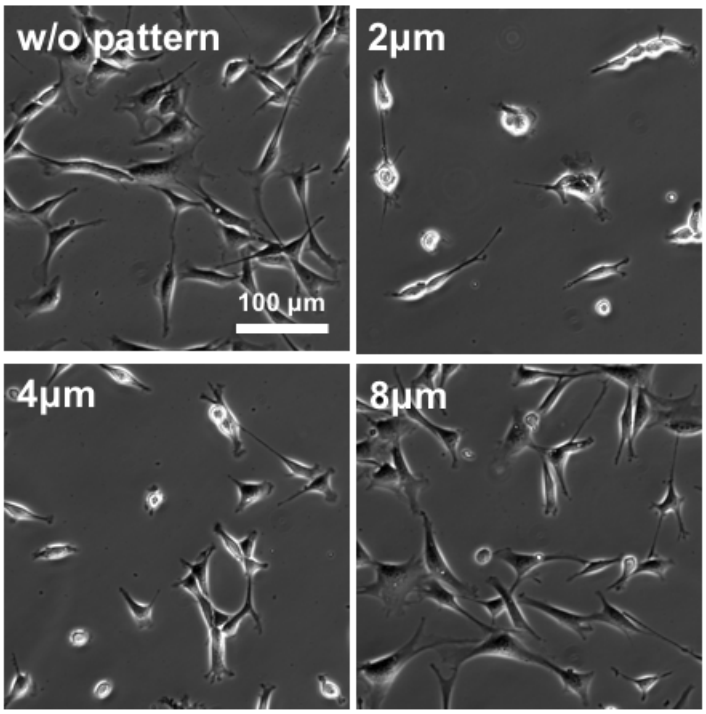

Figure 3.19. The nanocrater pattern spacing alters cell adhesion and morphology. Cells were plated on the nanocrater-patterned quartz surfaces in serum-containing medium for 15 hours on the pattern (1 μm in diameter, 350 nm in depth)

We further quantify and compare the repellant efficiency of the isometric patterns with a constant (2 and 4 μm pitched isometric pattern) and with a gradient spacing (from 2 to 4 μm with constant increase). When cells were cultured on nanoscale topographical patterns (800 nm in diameter and 300 nm in depth), they moved away from the patterned

surfaces and migrated towards non-ablated areas, and forming line patterns of cell clusters between the patterned areas. Our hypothesis is that the cells sensed the non-ablated surface, they tended to migrate toward to non-ablated region for easiness for focal adhesion [48].

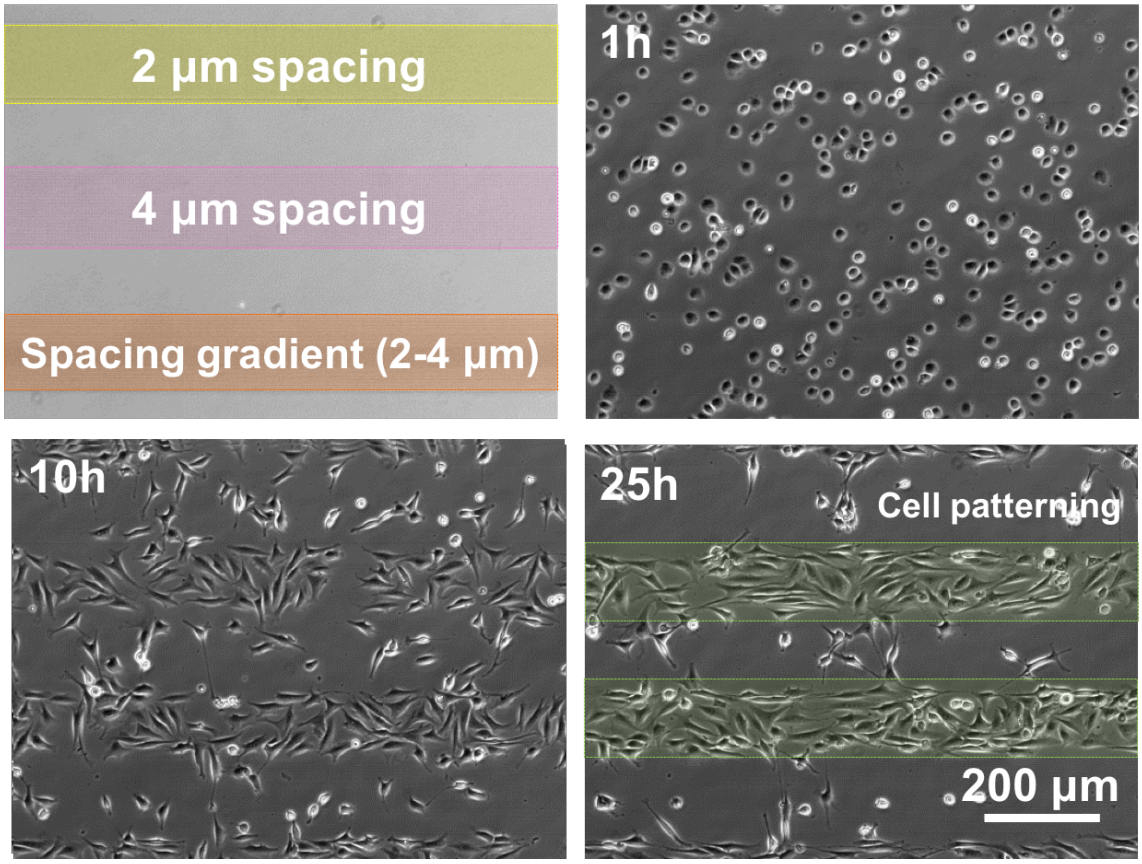

Figure 3.20. Time-lapse phase-contrast images of NIH-3T3 cells cultured on isometric pitch (2 and 4 μm) and a spacing gradient (from 2 to 4 μm) pattern (800 nm in diameter, 300 nm in depth nanocraters)

Due to the polymer-laser interaction, nanocraters in TCPS were surrounded by a lip, which prevented the fabrication of pattern with pitches less than 2 μm. We prepared patterned samples with isometric pitches of 2, 4, 6, and 8 μm. On the 2 μm spacing area, a trend of cell migration is similar to the one on quartz was observed as cells migrated away from the ablated region. In contrast, on the wider spacing pattern (4, 6 and 8 μm) area, there was no significant directional migration or repellent effect, which we attribute to the increased roughness due to the lip and thereby enlarged available area for focal adhesions [48].

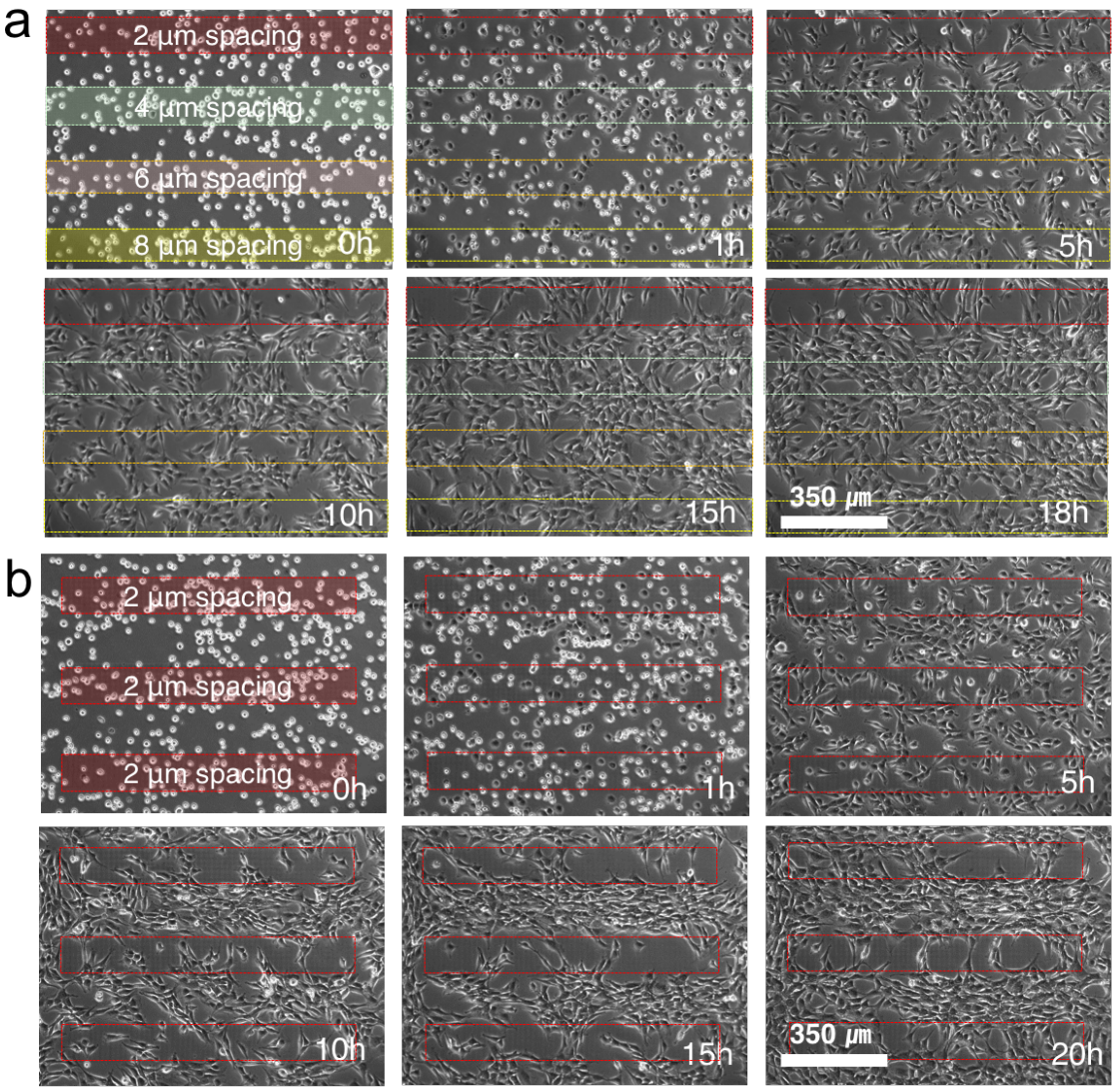

Figure 3.21. Time-lapse phase-contrast images of NIH-3T3 cells cultured on (a) isometric pitch (2-4-6-8 μm), and isometric pitch (2-2-2 μm) patterns (on TCPS) (1100 nm in diameter, 420 nm in depth nanocraters)

3.4.2.1 Normalized cell number density on the isometric pattern

The number of cells in a surface (160 μm x 2000 μm) was counted from three independently repeated experiments. For every hour, we calculated the normalized cell number (the number of currently residual cells / the number of initially attached cells). Subsequently, ten or more cells, spatially isolated from each other, were randomly selected for quantitative analysis. After 25 hours from the cell seeding, the normalized cell numbers are 0.43±0.08 (mean of normalized value ± SD) for 2 μm spacing pattern, 0.45±0.10 for 4-μm spacing pattern and 0.25±0.03 for spacing-gradient pattern,

respectively. Cells on the spacing gradient pattern shows higher tendency to migrate toward to favorable region (non-ablated region) [48].

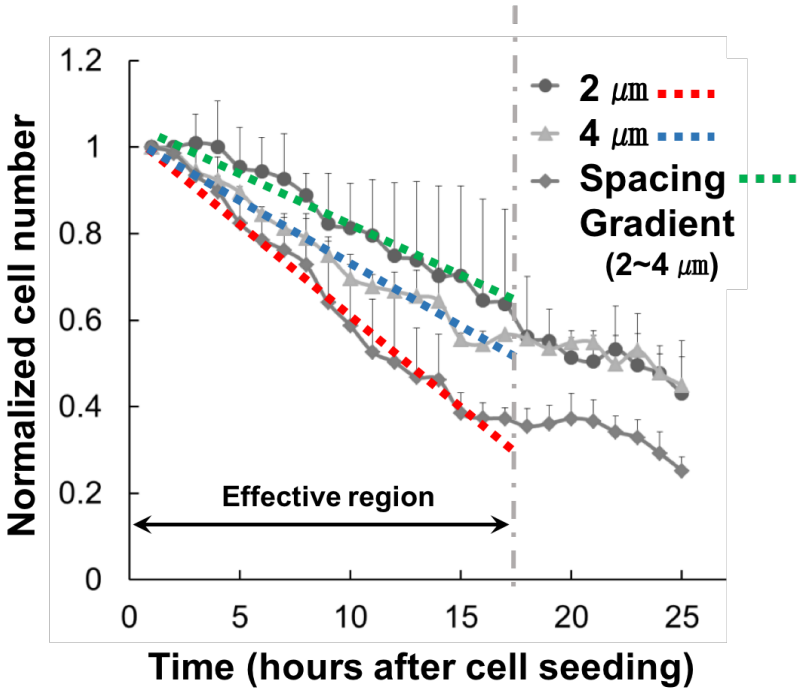

Figure 3.22. A plot of normalized cell number (the number of currently residual cells / the number of initially attached cells) on the quartz with time shows the repellent effect on the isometric pattern (2 and 4-μm spacing) and spacing-gradient patterned area (from 2~4 μm with constant increase pitch)

Figure 3.23. A plot of normalized cell number (the number of currently residual cells / the number of initially attached cells) shows the repellent effect of each pattern after 25h from the cell seeding on TCPS ablated pattern. The pattern with 2 μm spacing, we could see significant migration trend and generating the line pattern with cell colonies. In contrast, cells on the 4-6-8 μm spacing pattern, cells were adhering on the substrate and spread, didn't migrate. After 10 hours later of cell seeding, number of cell increased dramatically. After 15 hours, the normalized cell numbers are 0.46±0.09 (normalized value ± SD) for 2-μm spacing pattern, and keep increasing with time passage. Cells on the 4-6-8-μm spacing pattern shows increase of normalized cell number (upto 1.35±0.06 after 20 hrs) with time, and cell migration trend is not distinguishable [48].

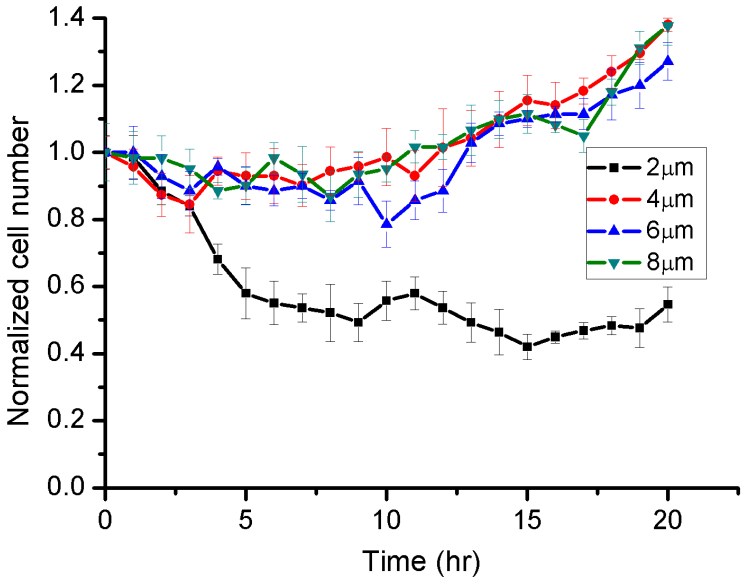

Figure 3.23. A plot of normalized cell number (the number of currently residual cells / the number of initially attached cells) on the polystyrene with time shows the repellent effect on the isometric pattern (2-4-6-8μm spacing).

3.4.3 Enhancement of directional migration on gradient pattern

We next prepared a different spacing-gradient pattern along x-y axis of nanoscale craters in quartz, and observed cell morphology after adhesion, migration, and spatial organization patterning. The spacing between nanocraters varied between 1 and 10 μm, and each patterned area with the same pitch was approximately 20~40-μm wide [48]. Hence, attached cells can spread and sense the neighboring crater features with differential pitch. The spacing-gradient pattern effectively guided cell migration and created cell repellant interfaces. By spatially defining nanocrater patterns over a large substrate area, cells migrated to avoid areas of the surface with high nanocrater density (small pitch region). High densities of the nanocraters perturbed the coordination of leading edge protrusion, cell body translocation, and trailing edge retraction during migration. Cells on the small pitch regions therefore migrate to regions of the surface where normal 2D coordination of these events can occur [48].

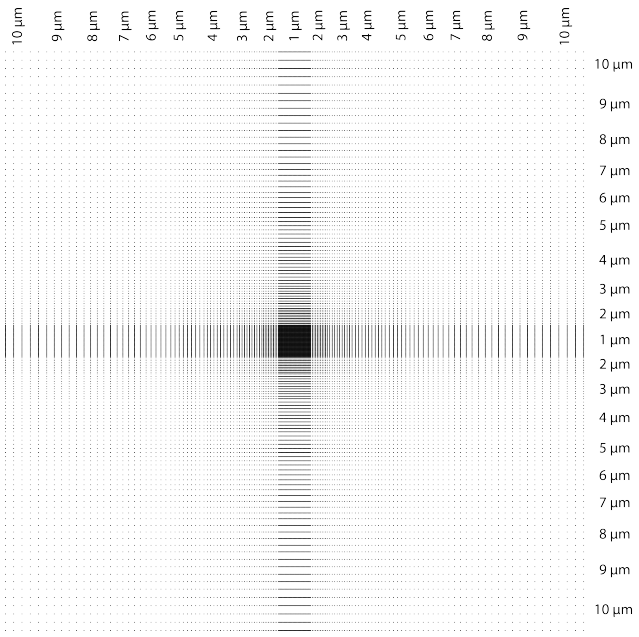

Figure 3.24. Schematic diagram of full pattern design representing the pitch gradient. The spacing between nanocraters varied between 1 and 10 µm, and each patterned area with the same pitch was approximately 20~40-µm wide

On the gradient patterns, the cell-repelling effect was more pronounced. Since the cells migrated towards larger pitch areas, (*i.e.* from the center to the periphery of the gradient pattern), which provided the cells greater probability to contact the "nanocrater-free" surface. Most of the cells on the gradient pattern migrated towards borders without dramatically with time [48].

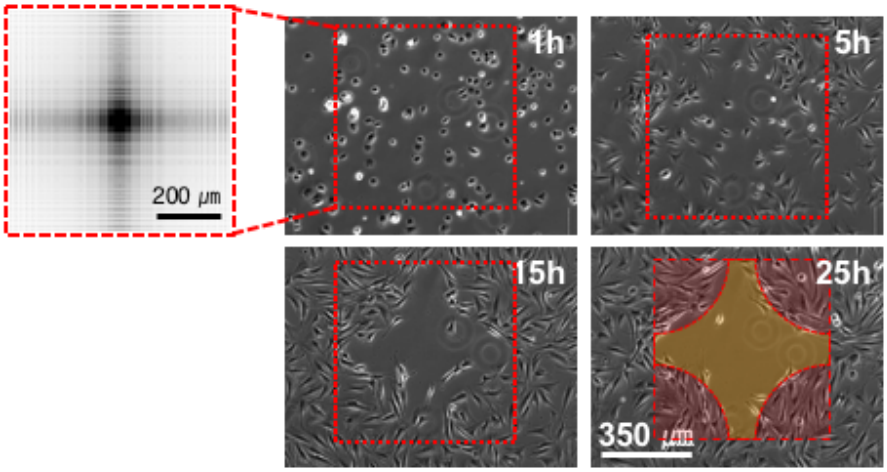

Figure 3.25 Time-lapse phase-contrast images of NIH-3T3 cells cultured on a gradient pattern as shown Figure 3.24 (1,000 nm in diameter, 350 nm in depth nanocrater).

For the anisotropic pattern, at the overlapped region, double laser pulse applied in the same spot. To get the same shape of ablated pattern with single laser pulse, we had to decrease the laser pulse energy. On the anisotropic patterns (1 μm in diameter and 350nm in depth) with different aspect ratio, compare to the normal isometric pattern, the cell-repelling effect was more pronounced. When cells were cultured on the different aspect ratio pattern, they moved away from the patterned surfaces and migrated towards non-ablated areas within shorter time than single laser shot pattern (aspect ratio = 1). Our hypothesis is that anisotropic patterns enhance the directionality. To verify this, we took the immunofluorescence image for visualization of focal adhesion, and calculated the directionality relatively to direction of anisotropic pattern using nucleus image (DAPI).

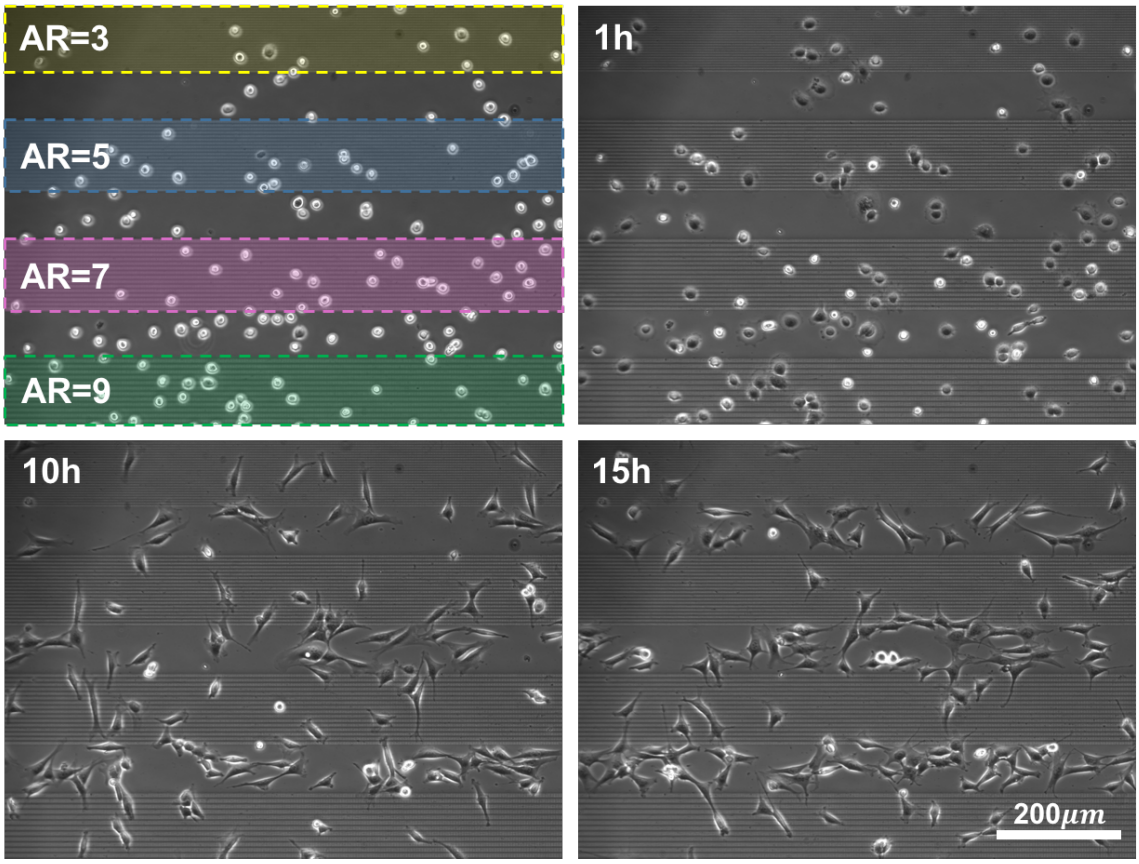

Figure 3.26 Time-lapse phase-contrast images of NIH-3T3 cells cultured on an anisotropic pattern (Aspect ratio = 3-5-7-9) (1,000 nm in diameter, 350 nm in depth nanocrater)

Same Surface Area index, we could see the similar trend on the cell adhesion. To quantify the effect of anisotropy of pattern on migration, normalized cell number was calculated. Comparison with isometric pattern (without anisotropy), cell migrate faster on anisotropic pattern(AR=5) than dot pattern (AR=1).

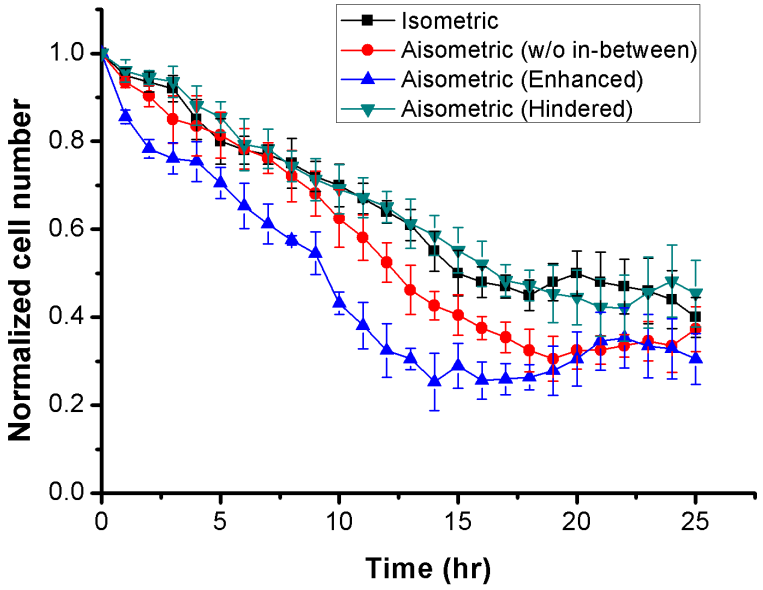

Figure 3.27. A plot of normalized cell number (the number of currently residual cells / the number of initially attached cells) on the quartz with time shows the repellent effect on the anisometric pattern (without in-between pattern) and pattern win in-between pattern (enhanced and hindered pattern)

3.4.3.1 Effect of nanocrater morphology

To understand how the nanoscale interface affects cell patterning, we fabricated six different nanoscale topographical (diameter and depth) patterns using 100x, 50x and 20x objective lenses. At the early stage (within 1~2 hours after cell seeding) of cell spreading, no significant migration was observed between patterned and the non-patterned surfaces. However, they showed the different adhesion trend depending on the location of pattern (i.e. different pitch of ablated pattern). Cells at the center of spacing-gradient patterns did not spread compared to cells at the perimeter. Approximately 5 hours after cell seeding, the cell density at the center of the pattern decreased, an observation that was most pronounced for the larger diameter nanocraters (1000 nm in diameter and 350 nm in depth). After 10 hours, cells clearly migrated from the highest density of nanocraters, small pitch toward the lower density of nanocraters, creating a region on the surface that repelled cell colonization. After 25 hours, the formed boundary lines of the repellent region did not show significant changes. After this point, cells were spread on the substrate, doesn't not migrate. (Figure 3.25).

As a result, the depth and diameter of nanocraters affected the area of the cell repellent zone (Figure 3.28) : the area increased with larger craters and decreased with the smaller features. Guided migration, and ultimately cell repellence, was not observed for the smallest patterns of 500/45 nm in diameter/depth.

For quantitative analysis, we defined a non-adherent zone ratio (non-adhesion ratio) representing the area of cell repelling zone (A_N) to the total area of spacing-gradient

patterns (A_T). The non-adherent zone ratio decreased with decreasing depth and diameter. Within nanocraters of constant diameter, the deeper craters had significantly greater areas of the surface that repelled cells [48].

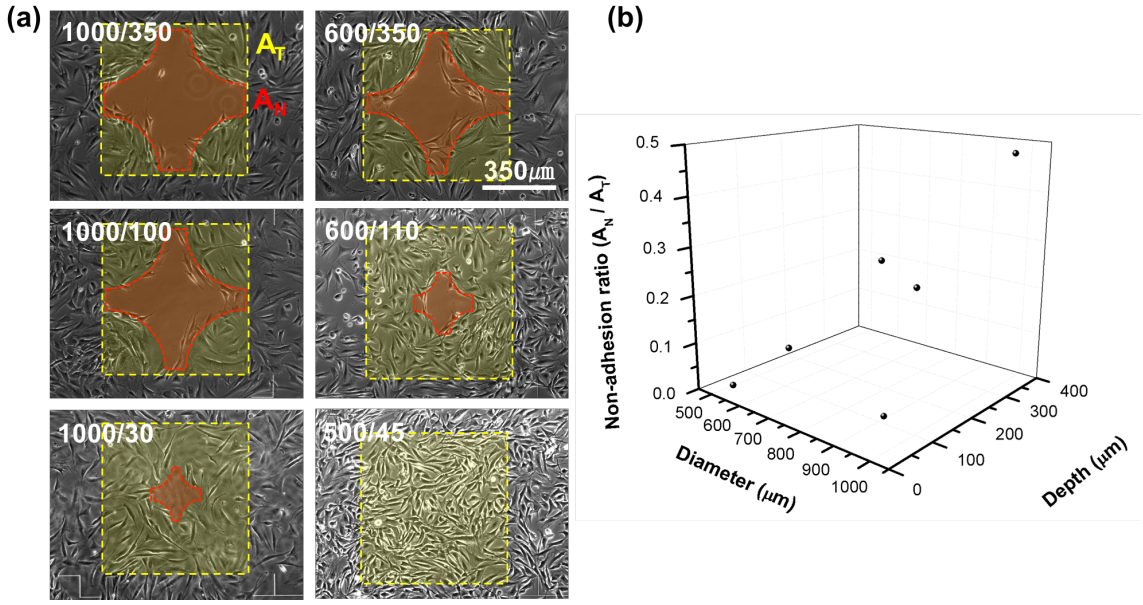

Figure 3.28. Effect of nanocrater topographies (diameter and depth) on cell migration and formation of a cell-repellent zone. (a) Phase-contrast images of cell migration 25 h after cell seeding on spacing-gradient patterns with 6 different nanocrater dimensions (diameter nm/depth unit [nm]) and (b) The non-adhesion ratio was defined as the area of repelling zone (A_N) / the total area of patterned surface (A_T). The non-adherent zone ratio decreased with decreasing nanocrater diameter and depth

On the polystyrene surface, the depth and diameter of nanocraters also affected the area of the cell repellent zone (Figure 3.29) : the area increased with larger craters and decreased with the smaller features. Guided migration, and ultimately cell repellence, was not observed for the smallest patterns of 400/120 nm in diameter/depth. For quantitative analysis, we defined a “non-adherent zone ratio” representing the area of cell repelling zone (A_N) to the total area of spacing-gradient patterns (A_T). The non-adherent zone ratio decreased with decreasing depth and diameter (Figure 3.29 (s)). Within nanocraters of bigger in diameter and deeper craters had significantly greater areas of the surface that repelled cells [48].

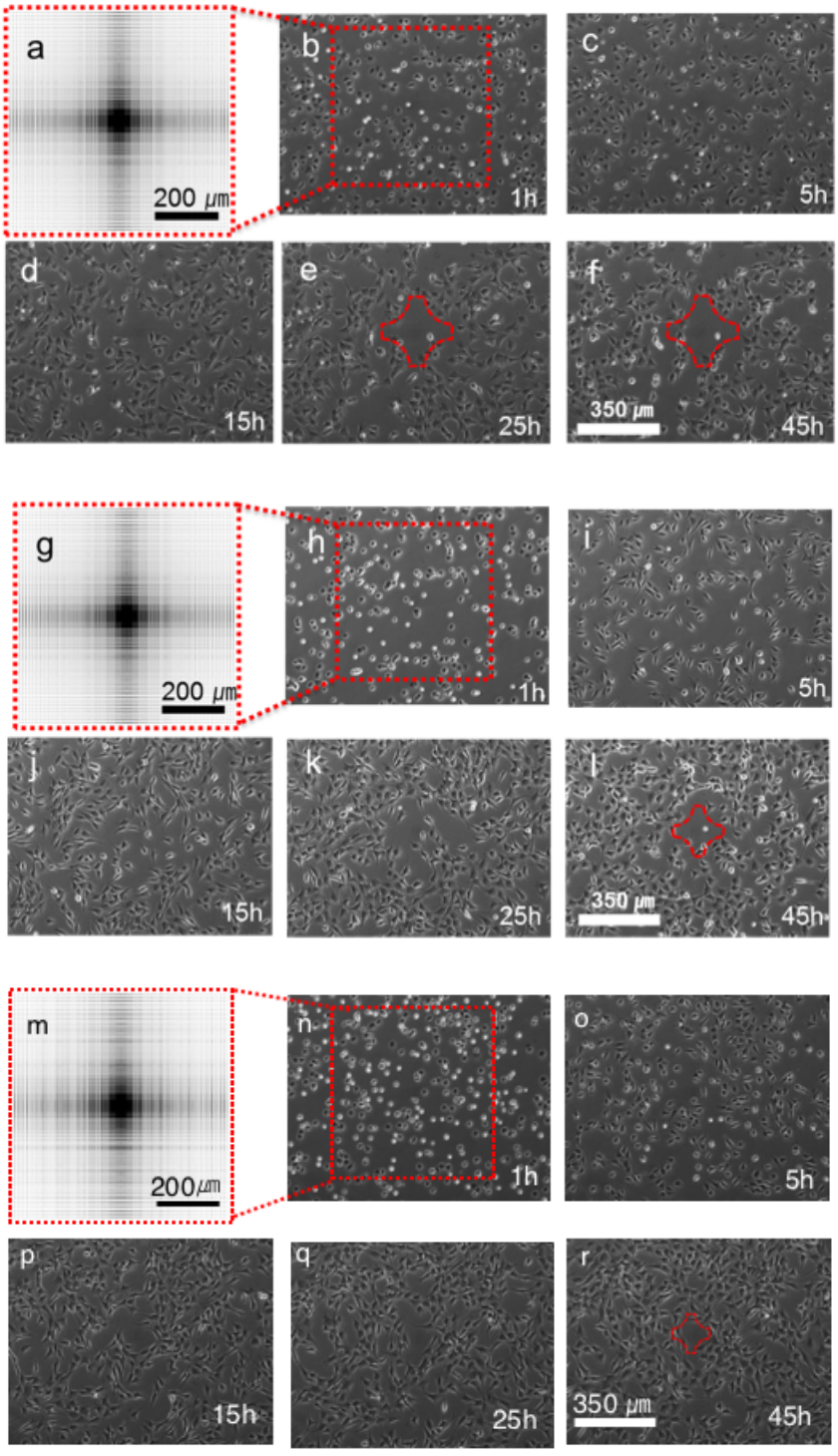
a
200 μm
b
1h
c
5h
d
15h
e
25h
f
350 μm
45h
g
200 μm
h
1h
i
5h
j
15h
k
25h
l
350 μm
45h
m
200μm
n
1h
o
5h
p
15h
q
25h
r
350 μm
45h

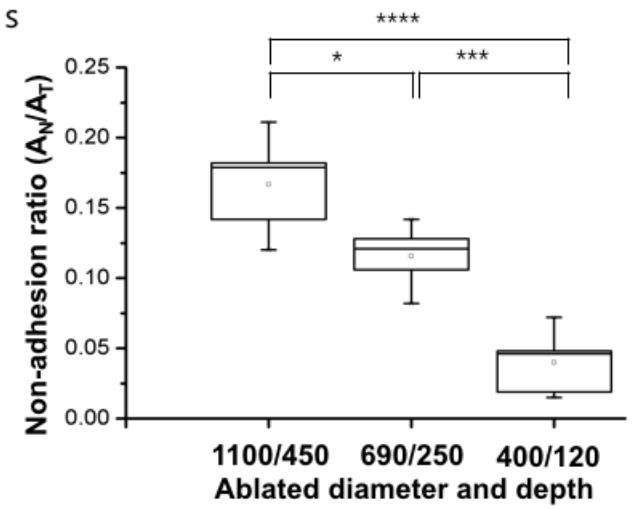

Figure 3.29. Time-lapse phase-contrast image of NIH-3T3 cells cultured on a patterned TCPS depending on different ablated diameter and depth. (a-f) Cells on the patterned TCPS in media containing 1100 nm / 450 nm (diameter / depth) (g-l) 690 nm / 250 nm. (m-r) 400 nm / 120 nm. (s) Non-adhesion ratio (the area of repelling zone (A_N) / total area of patterned surface (A_T)) decreased. (*p≤ 0.05, **p≤ 0.01, ***p≤0.001, ****p≤0.0001 (Kruskal- Wallis))

3.4.3.2 Quantification of ablated pattern density

To determine the effect of the nanocrater dimension on the cell repellant region of the spacing-gradient patterns, we also defined a "Surface Area Index" (SAI) as the ratio of crater area versus exposed surface area [48]

$$SAI = \frac{A_c}{A_p - A_c + A_s}$$

where area of a nanocrater opening (A_c), area of a unit plane surface(A_p) and surface area inside of nanocrater (A_s). For calculation of surface area of inside of nanoscater, we assumed that it's shape is conical shape based on measured diameter and depth. Even though its real shape is not conical shape, rather part of sphere, we used this assumption for easiness of calculation. According to the result of previous section result, the boundary line of the repelling zone resembles an arc. Along this arc, the ratios of planar surface versus nanocraters area are constant, which shows that the repelling effect from the nanocraters is independent of the distribution of the planar surface. However, considering the depth effect, the SAIs at the repellent boundary depends on the depth of the craters, suggesting a critical depth for the bottom of the crater to be inaccessible for cellular interrogation. These observations support the hypothesis craters of a critical depth, *i.e.* ~100 nm in this study, prevent cells from reaching the crater bottom to form stable focal adhesions [48]. This result is consistent to the real experiment (Figure 3.28 and 3.29).

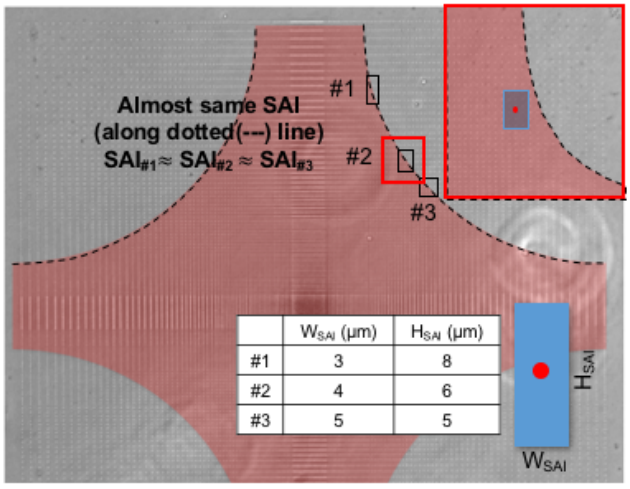

Figure 3.30. (a) Cell repelling zone (red colored area) and boundary lines (black dashed lines) are overlaid an image of the gradient pattern. The same Surface Area Index (SAI) applies to cells along the boundary lines

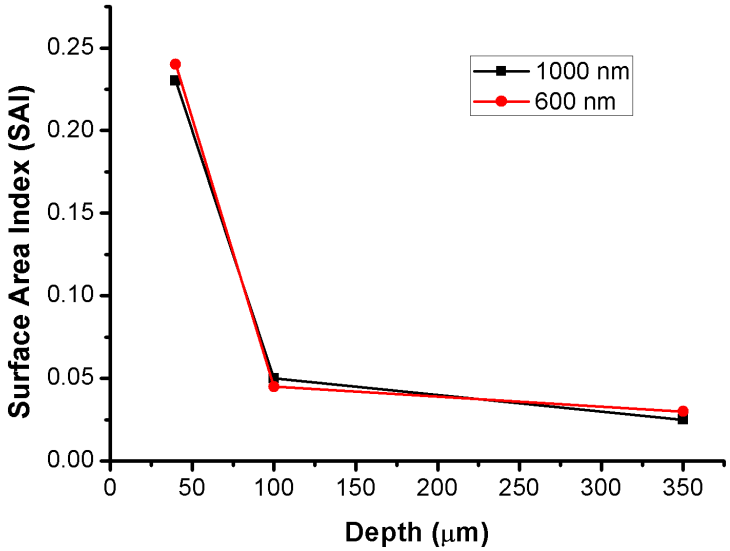

Figure 3.31. Calculation of surface area index for verification of nanocrater depth effect. Smaller than 100 nm in depth, SAI increased sharply regardless of diameter

3.4.4 Migration speed

From each image, identified cells were tracked and matched, and relative cell displacement (d_x and d_y) between the matched centers of nucleus of cells were measured for each time step. Migration trajectories was tracked (by connecting the positions of single cells in time sequence during migration) in order to provide the time history of cell migration. The initial position of each cell is assigned to a common origin. Experiments were repeated 3-5 times independently for different patterns. From the measured displacement and the applied time interval between successive two images used for calculation (Δt = 5 min), migration vectors (V_x and V_y) and migration speed ($S_{migration}$) are calculated for each time step, and average values are calculated for the entire migration periods [48]:

$$V_x = \frac{d_x}{\Delta t}$$

$$V_y = \frac{d_y}{\Delta t}$$

$$S_{migration} = \sqrt{{V_x}^2 + {V_y}^2}$$

The average cell migration angle ($\theta_{migration}$) is also calculated in similar way using the

$$\theta_{migration} = arctan\left(\frac{|d_y|}{|d_x|}\right)$$

The $\theta_{migration}$ takes values between 0° and 90°.

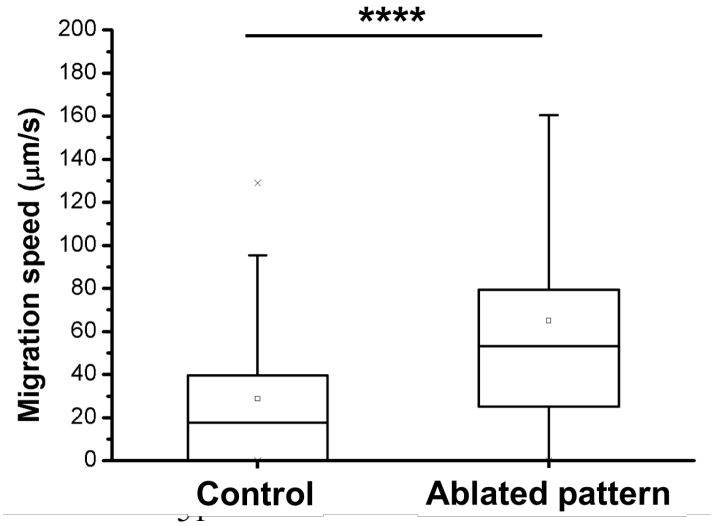

Figure 3.32. Migration speed on the ablated pattern of quartz

Regarding cell migration speed, cells on the spacing-gradient pattern showed significantly higher migration speed compared to those on the non-ablated surface ($p \leq 0.0001$).

On the anisometric pattern, the cell migration speed was measured on substrate with ablated pattern with different aspect ratio (AR=1-3-5-7). As a result, cells on the pattern with aspect ratio shows the highest migration speed. Based on this, we choose 5 as an aspect ratio for guiding pattern and in-between pattern for enhanced and hindered pattern.

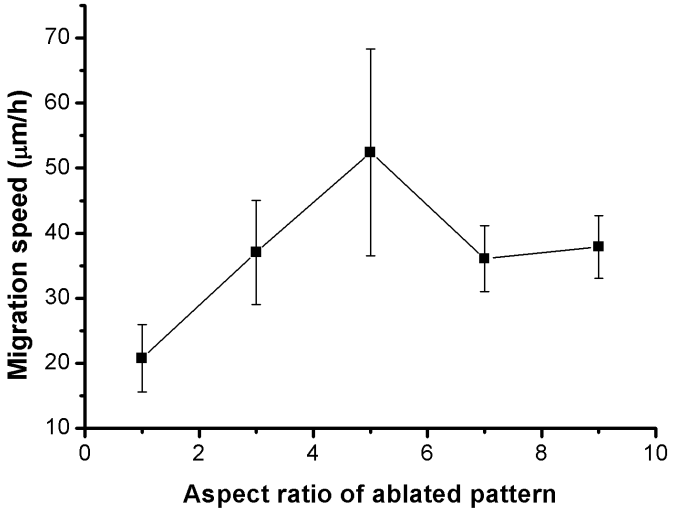

Figure 3.33. Migration speed on the different aspect ratio pattern

3.4.5 Persistent random walk model (Persistent time and distance)

Cell migration was examined by cell tracking and fitted using a persistence random walk model. From each image, specific cells were tracked and matched, and relative cell displacement (d_x and d_y) between the matched nuclei centers of the cells were measured for each time step. From the measured displacements, migration speeds were calculated (Section 3.4.4). For the persistence random walk modeling, mean square displacement, $\langle d^2 \rangle$, versus time increment was calculated by using the overlapping time interval sample method and averaging all the squared displacements [48]:

$$\langle d^2 \rangle = \frac{1}{N-i+1} \sum_{0}^{N-i+1} \left[\{x((i+k)\Delta t) - x(k\Delta t)\}^2 + \{y((i+k)\Delta t) - y(k\Delta t)\}^2 \right]$$

where x and y are the coordinates of each position, and N is the total number of time intervals over the entire cell migration track. Persistent time (P) and random migration coefficient (μ) were obtained by fitting the mean squared displacement data acquired from cell tracking experiments to the following theoretical equation[48, 50]:

$$\langle d^2(t) \rangle = 2n\mu \left\{ t - P\left(1 - e^{-\frac{t}{P}}\right) \right\}$$

where n represents the number of dimensions ($n = 2$ in this study). Persistent time (P) represents the average time length between drastic changes in the direction of the cell migration. The random motility coefficient (μ) is a quantitative measurement of random migration of the cell population.

$$\mu = \frac{{S_{migration}}^2 P}{n}$$

To reduce calculation error, the experimental data for time up to one third of the entire time period of the cell migration were used. Because, the true path of cell migration cannot be observed at longer time period.
For the calculation of persistence distances, it was defined by the migration length exceeding 10-μm before a cell changes direction significantly (over 70°). Furthermore, if the migration distance was shorter than 2 μm between two successive images, that data was neglected, and assumed as error.

Comparing the persistence time, cells on the non-ablated pattern shows longer persistence time than cells on the gradient-spacing pattern. In contrast to this, persistent distance wasn't significant for the conditions tested.

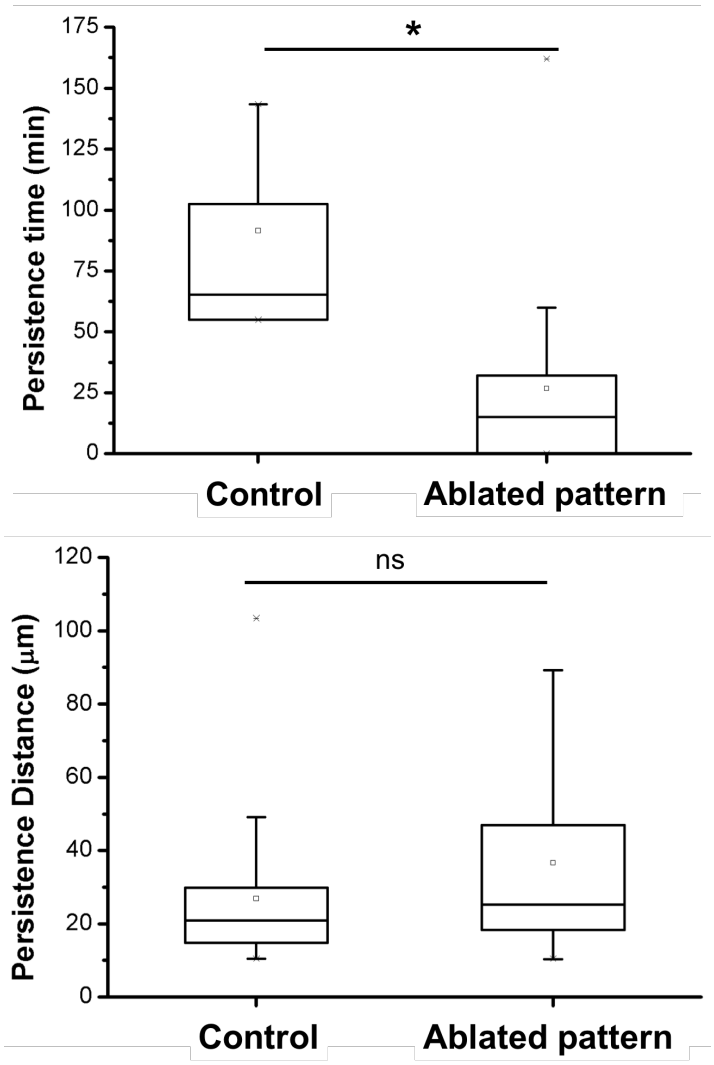

Figure 3.34. Persistent time and distance on the ablated pattern of quartz

Comparing the persistence time, cells on the anisotropic pattern with different aspect ratio doesn't show significant change for the condition tested. However, persistent distance, cells on the anisotropic pattern with aspect ratio as 5, it shows the significantly longest persistent distance than other pattern.

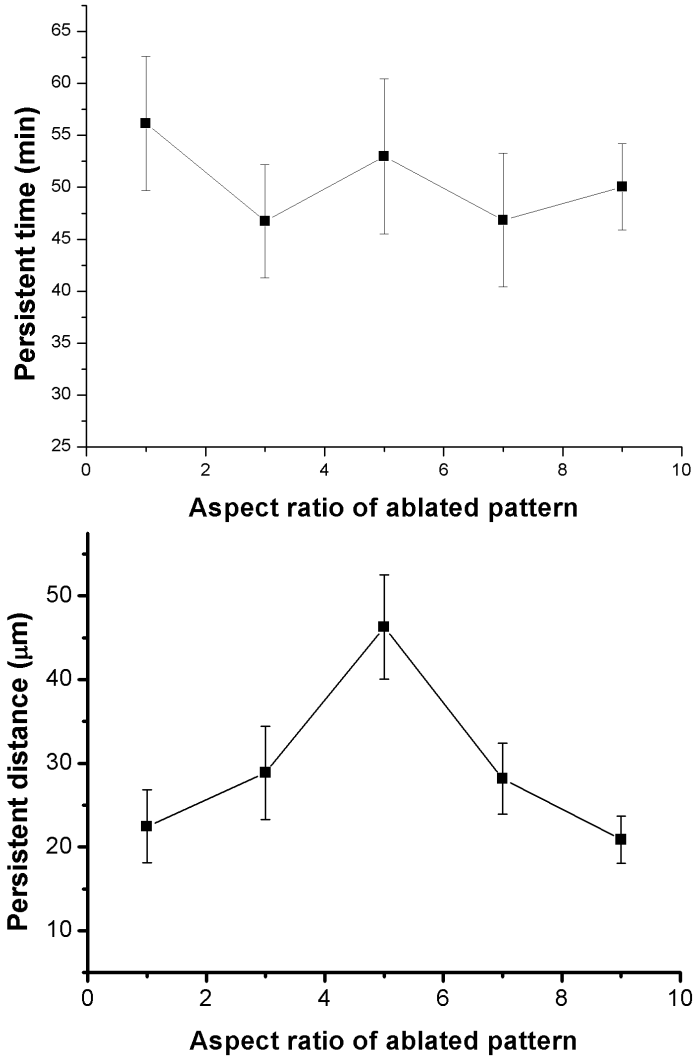

Figure 3.35. Persistent time and distance on the of the anisotropic pattern of quartz

However, enhanced and hindered patterns show significantly different persistent time and migration. Persistent distance of cells on the enhanced pattern is higher than that of hindered pattern. In contrast to this, persistence time of cells on the hinder pattern is higher than that of enhance pattern. Based on this, we could see the effects of in-between pattern type.

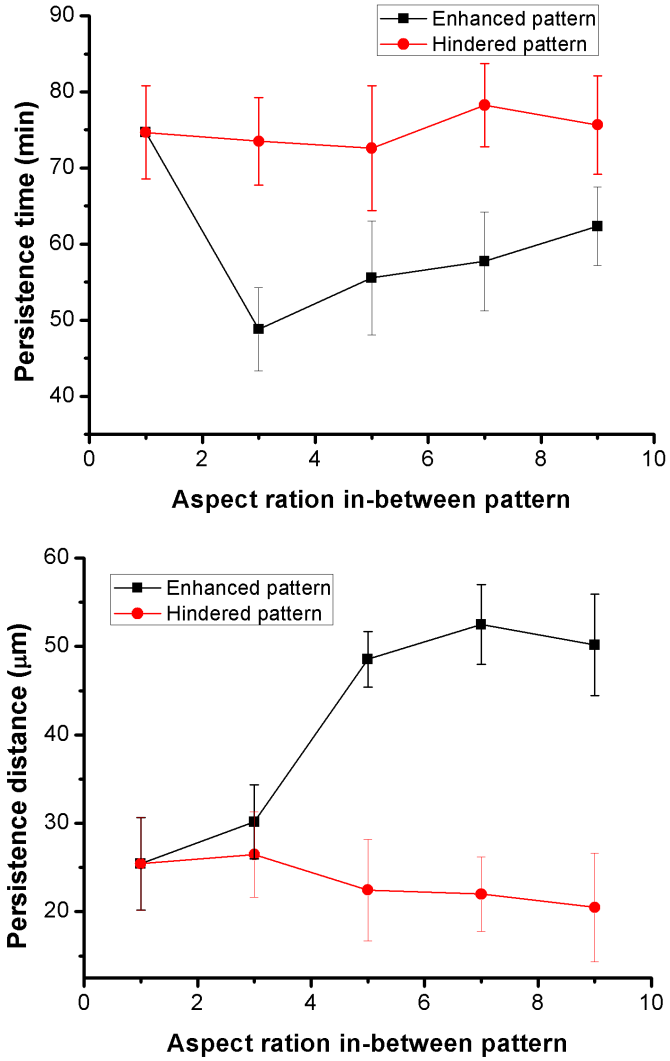

Figure 3.36. Persistent time and distance of the different aspect ratio in-between pattern for enhanced and hindered pattern

Hence, the anisotropic pattern shape (direction of in-between pattern) is also critical factor for persistent migration. If direction of in-between pattern is perpendicular to guide pattern, that reduce the persistent migration. In contrast, direction of in-between pattern is parallel to the guide pattern, it enhances the persistent migration. Comparing the persistent distance and time, it shows the higher persistent migration speed on the enhanced pattern that that of hindered pattern.

3.4.6 Directionality calculation

To calculate directionality of the cell migration, we took the symmetry of the patterns into account. On the ablated pattern, we defined the center featuring 1 μm spacing as the origin (0, 0) of a Cartesian coordinate system with X- and Y-axis through the symmetry axis of the pattern. Four quadrants are created featuring bilateral symmetry. In other words, if a cell moves from the center to the left-up in the 2nd quadrant, it has the same migration properties as a cell moving from the center to the right-up in the 1st quadrant, to left-down in the 3rd quadrant and right-down in 4th quadrant. Within each quadrant, there is an additional symmetry about the |y|=|x| axis. Hence, we can map the entire pattern on the region between the positive Y-axis and the y=x axis, and this defined as the unit region. To calculate and characterize the persistent migration (persistent time and distance) mapped on this unit region, two position mappings were necessary: First, we replaced the position data with their respective absolute values thereby flipping all quadrants onto the 1st quadrant. Second, we mirrored the resulting position data along the |y|=|x| axis. Considering the whole cell migration, this is composed of persistent and non-persistent migration segments. To calculate directionality of cell, we differentiated between persistent and non-persistent migration, and only considered the persistent motion. By assigning the starting point of the persistent migration segment to the origin (0, 0), we obtained directionality metrics such as the angle between X-axis and persistent migration distance. By normalizing the occurrence frequency of each angle with the total number of persistent segments, we then obtained the angular frequency. The angular graph for gradient ablated patterned interfaces shows a higher frequency of migration direction at 45◦ ± 15. However, the angular graph shows no preferential migration directionality on non-ablated regions [48].

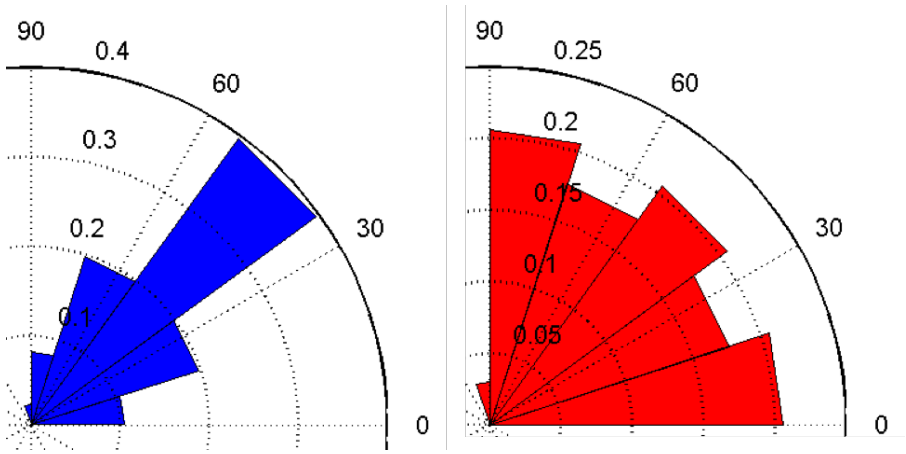

Figure 3.37. The angular graph for nanocrater-patterned interfaces shows a higher frequency of migration direction (a)gradient ablated region (b)unablated region

3.4.7 Characterization of cytoskeleton structure

3.4.7.1 Focal adhesion analysis

Vinculin is a focal adhesion protein recruited slightly after initiations of focal adhesion formation. To measure and calculate the focal adhesion size, we used the vinculin fluorescent image using ImageJ. First of all, background fluorescence was removed by subtracting background with a 4 pixel rolling ball radius. Only cells completely on patterns at the time of fixation were used for measurements. Kruskal-Wallis tests were performed for statistical analysis.

Over-expression of the first 405 amino acid sequence of the globular N- terminus of Talin-1 was accomplished using the Lonza Nucleofector 2B. GFP/Talin- 1(1-405) plasmids described by Bouaouina and others include the entire FERM domain and were shown to over-activate the 5 1 and 5 3 integrins in transfected cells. For each transfection, approximately 10 million cells were suspended in 100 of Nucleofector 2 Solution R with 8 of plasmid and transfected using program U-030. Immediately after transfection, 500 of Dulbecco's Modified Eagle Medium (ATCC) supplemented with 10% Fetal bovine serum (ATCC) was added to the cell solution. The sample was then incubated at 37 ° for 15 minutes. Cells were gently transferred into culture flasks and seeded at ~90% confluency in normal growth medium. After 24 hours, transfected cells were sorted using flow cytometry for GFP fluorescence. Cells were seeded on patterned samples 48 hours after transfection. Focal adhesions of the cells located on small pitch area or near the nanocraters look nascent, while elongated and mature focal adhesions were observed on non-ablated controls [48].

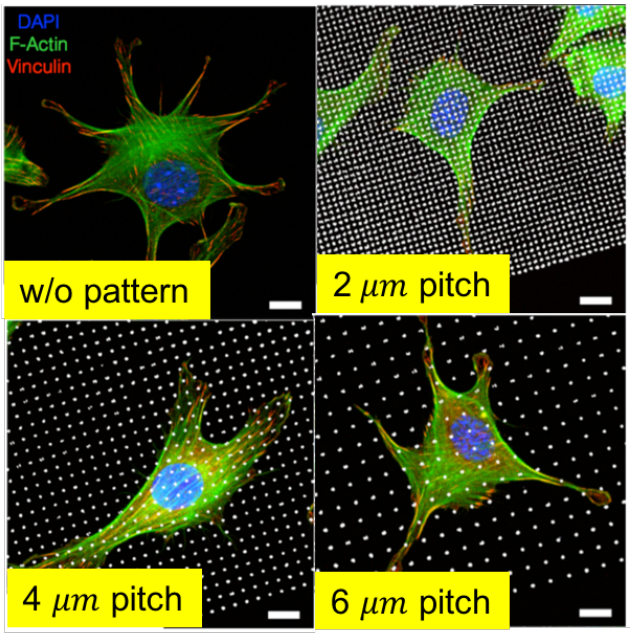

Figure 3.38. Immunofluorescence images of fibroblast cultured on patterned quartz surfaces with craters (1μm in diameter, 350 nm in depth) and un-patterned surface 2-4-6-μm isometric spacing with inverted DIC (scale bar : 10μm)

The nanocraters distort the focal adhesions formation. The cells were plated on the patterned surfaces in serum-containing medium for 1 hour. Depending on pattern pitch, cells reveal different morphology and focal adhesion distribution, where cells on surfaces with the lowest pitch have smaller and less pronounced focal adhesions that are primarily distributed at the leading and trailing edges of cells. Focal adhesions located on low pitch area or near nanocraters look nascent while larger and mature focal adhesions were located in on the planar "pitch" of the nanocraters. In contrast, focal adhesions of the cells on flat surfaces were scattered throughout the cell body [48].

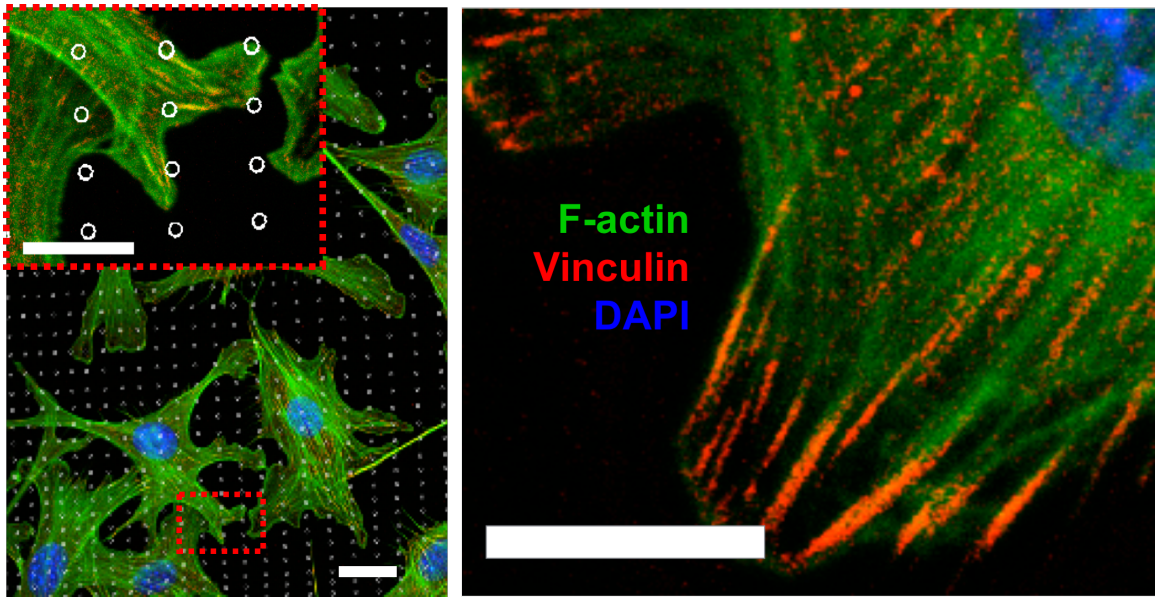

Figure 3.39. Focal-adhesion size distribution correlates with migration descriptors Immunofluorescence image of cells on a spacing-gradient pattern coated with fibronectin fixed 1 h after seeding. Blue inset showing small focal adhesions imaged through vinculin staining. On un-ablated control substrates, cells are able to form large focal adhesions. F-actin in green; vinculin in red; DAPI in blue (scale bar : 10μm)

We quantified focal adhesion maturity by the measurement of focal adhesion size, which moderately predicts cell speed and persistence. Cells were seeded on both gradient and isometric patterns with 2, 4, 6, and 8 μm spacing. After 1 hour of cell seeding, cells were able to form focal adhesions and spread on all patterns. In contrast, focal adhesion area of 2-μm ($p \leq 0.05$) and 4 μm ($p \leq 0.0001$) spacing patterns was significantly smaller. This is consistent of non-adhesion experiment of isometric pattern. As a result, formation of focal adhesion is important factor for cell migration. Mature focal adhesion formation of cells on non-ablated pattern doesn't induce the cell migration. In contrast, immature focal adhesion formation enhances the directional migration from ablated pattern toward non-ablated pattern [48].

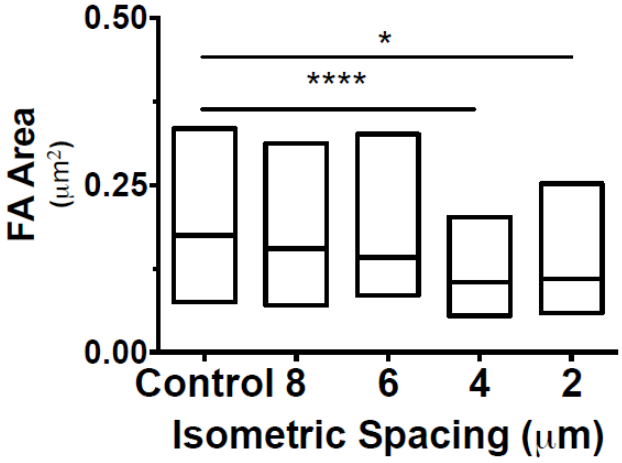

Figure 3.40. Focal-adhesion interquartile distributions on 4 μm and 2 μm isometrically spaced patterns were significantly different from the unablated control, but 8 μm and 6 μm patterns showed focal adhesion distributions similar to control samples. Cells were fixed after 1 h seeding. (NS: $p > 0.05$, * $p \leq 0.05$, ** $p \leq 0.01$, *** $p \leq 0.001$, **** $p \leq 0.0001$ (Kruskal–Wallis))

To investigate cell behavior on the patterned TCPS, we again used immunofluorescence staining of vinculin to characterize focal adhesion size on isometric patterns. Focal adhesions located on 2 μm pitch isometric pattern were distributed at the leading and trailing edges of cells, and appeared less mature compare to those on larger pitch patterns. These results are similar to quartz surfaces result, but the 2 μm pitch patterns on TCPS seem more mature, which we attribute to surface topography of a rim formed during laser ablation [48].

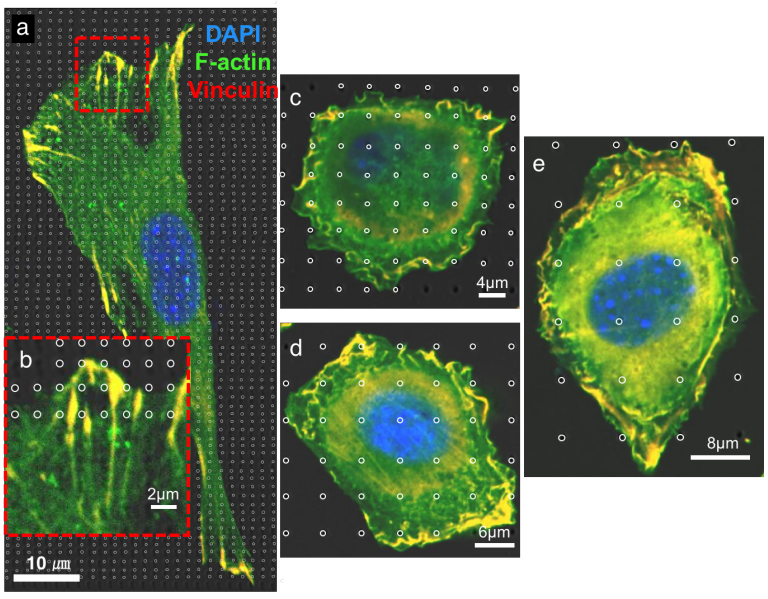

Figure 3.41. Immunofluorescence image of fibroblasts on ablated pattern of TCPS. (a) Immunofluorescence image of fibroblasts on isometric pitch (2 μm) patterns of TCPS. (b)Red inset from a showing focal adhesion distribution imaged through vinculin staining. (c-e) Immunofluorescence image of cells on different isometric pitch 4, 6 and 8 μm pitch pattern respectively. Distribution of focal adhesion on these patterns doesn't show significant directionality. F-actin in green; vinculin in red; DAPI in blue

Anisotropic patterns exhibit distinguishable focal adhesion formation, aligned parallel to the pattern. This focal adhesion distribution also effects on the cell migration and directionality. By reconfiguration of the cytoskeleton, the fibroblast cell nuclei also reoriented along the pattern direction. Quantification of nucleus direction in respect to pattern will be shown in the next section.

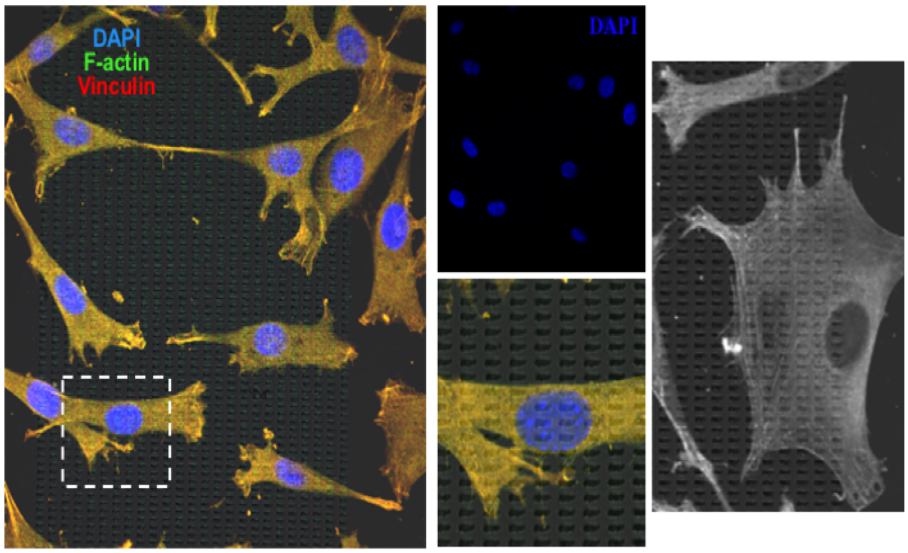

Figure 3.42. Immunofluorescence image of fibroblasts on ablated pattern of anisotropic pattern (AR=5). Cell aligned along the anisotropic pattern direction. Distribution of focal adhesion on these patterns show significant directionality. F- actin in green, Vinculin in red, DAPI in blue

3.4.7.2 Nucleus directional alignment analysis

To compare the alignment of cell on the isometric and anisometric patterns, we compare the nucleus alignment on each pattern. We set the axis of anisotropic pattern as reference axis (0°). For the calculation, we used the homemade MATLAB code for the image process. To obtain the outline of nucleus, we read the only blue data from immunofluorescence image. Using the fitted ellipsoidal shape, it is possible to determine the major axis and calculate the angle between the major axis of DAPI and the reference axis. According to this analysis, we can see that anisotropic pattern also enhance the focal

adhesion distribution, and also effect on the cell migration. We conclude that ablated pattern affect the focal adhesion distribution and direction, as well as the cell alignment along the axis of ablated pattern direction. Combining the results (persistence distance, time, immunostaining and nucleus directional alignment), indicates that cells on the 'Enhanced' pattern enhance the directional & persistent migration.

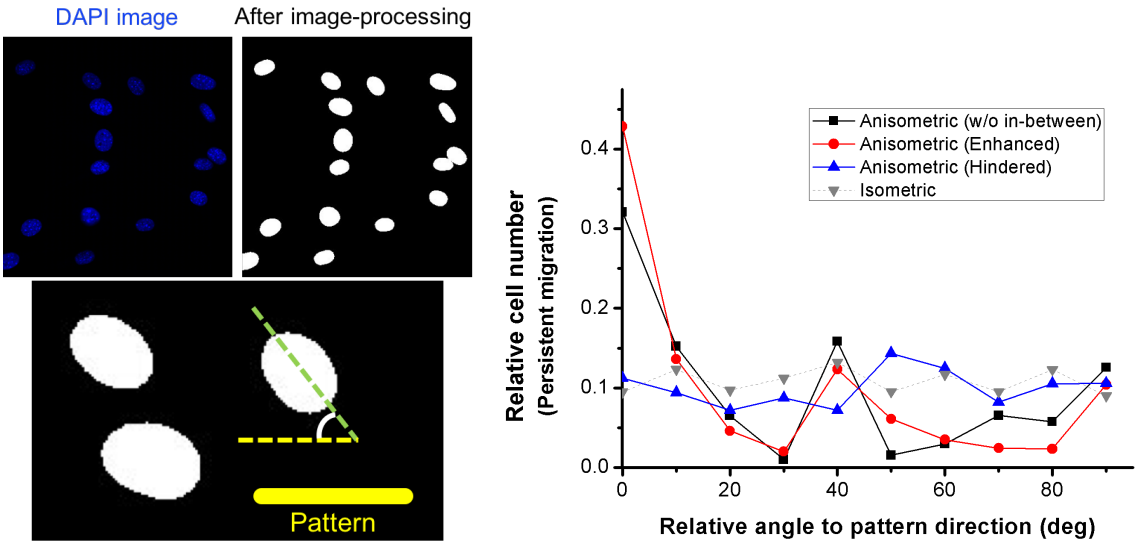

Figure 3.43. Calculation of nucleus direction with respect to major axis of anisometric pattern on the different type of anisometric pattern (w/o in-between, enhance and hinder pattern)

3.4.7.3 Talin overexpression (on the isometric pattern)

To test if integrin activation could re-stabilize focal adhesion formation disrupted by patterned nanocraters, cells were transfected with DNA plasmids encoded with Talin-1(405)/GFP. Talin is a focal adhesion protein that regulates integrin affinity for ligands in the ECM during cell adhesion, migration, and assembly. The first 405 N-terminal amino acids of Talin-1 are sufficient to activate both the $\alpha_5\beta_1$ and $\alpha_5\beta_3$ integrins. Cells overexpressing Talin-1(405) are capable of forming stable and mature focal adhesions with a smaller adhesive pad area compared to wild type cells through Talin's ability to increase integrin affinity for adhesion ligand. Cells transfected with Talin-1(405)/GFP overcame the 4-μm pattern disruption and exhibited focal adhesion size distributions similar to unpatterned control samples. Most important, the Talin-1(405) transfected cells on a spacing-gradient pattern do not show any directional migration, and have larger focal adhesion areas compared to their respective wild type controls, suggesting cell patterning is critically dependent on cell migration [48].

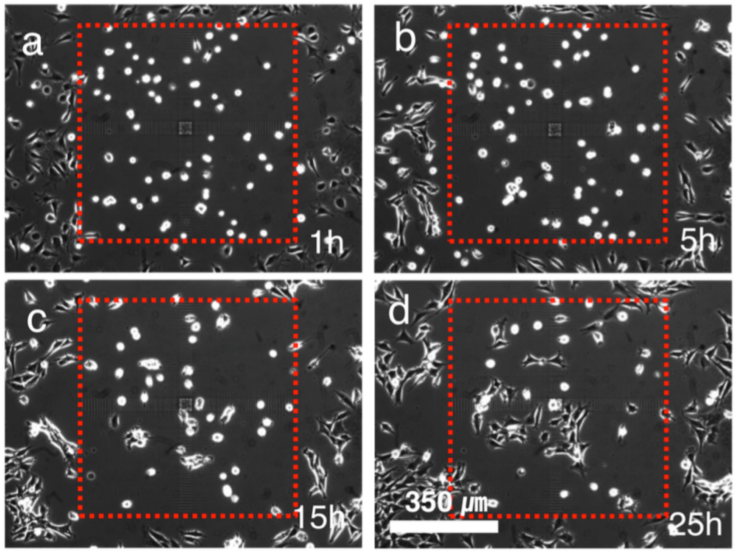

Figure 3.44. Time-lapse phase-contrast images of Talin-1(405) transfected NIH-3T3 cells cultured on the gradient pattern on the quartz with nanocraters (1 μm in diameter and 350 nm in depth)

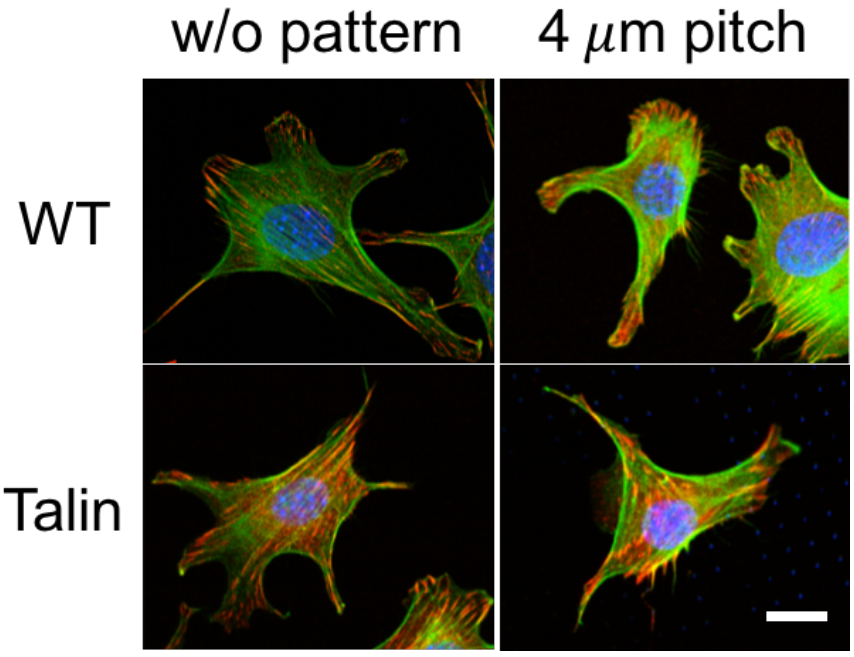

Figure 3.45. Talin-1(405) transfection enhance focal adhesion maturation. Immunofluorescence images of fibroblasts transfected with Talin-1(405) cultured on isometric patterned surfaces (quartz) with nanocraters of 1 μm in diameter and 350 nm in depth. (Scale bar : 10 μm)

Transfection with Talin-1(405) plasmids increased over focal adhesion formation throughout the cell body. Cells on patterns have focal adhesions concentrated in the leading and trailing edges that are much larger and mature in size than in wild type cells. Hence, focal adhesion formation (mature & immature) is critical factor for cell migration on nanocrater pattern [48].

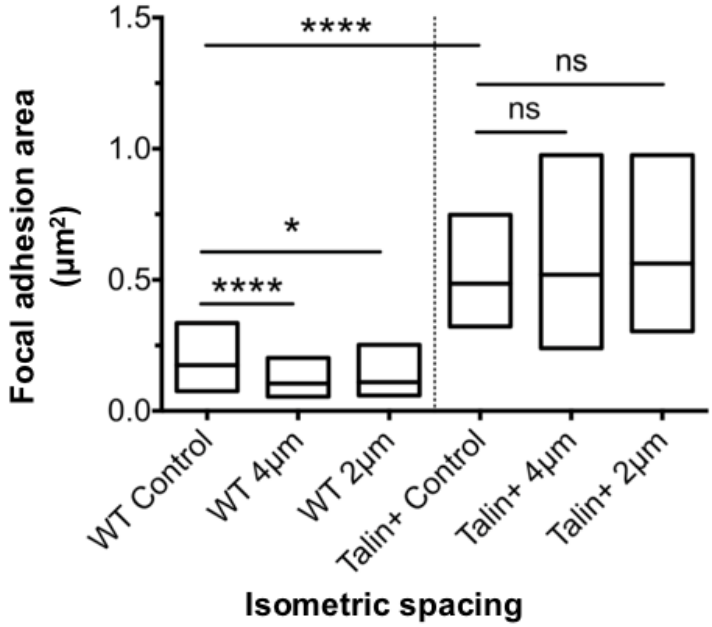

Figure 3.46. Talin-1(405) transfected cells showed significantly larger focal adhesion area compared to wild type cells. The cells were fixed 1 hour after seeding. Control surfaces were unpatterned (ns = p>0.05,*p≤ 0.05,**p≤ 0.01, ***p≤0.001, ****p≤0.0001 (Kruskal- Wallis)).

3.4.7.4 Blebbistatin

To explore the effect of cell migration on cell patterning in more detail, cells were treated with the small molecule inhibitor (blebbistatin), which has high affinity to myosin II and hinders binding of myosin II to actin. To prevent cell spreading while still allowing adhesion, we treated the cells with blebbistatin. This interference of binding results in inhibition of myosin II contractility and cell migration. In the blebbistatin treated sample, dendritic extensions appeared with deficient stress fibers and focal adhesions, resulting in lower cell motility, and directionality was not observed [48]. Cells seeded on the quartz patterns and treated with 50µM blebbistatin developed dendritic extensions with deficient stress fibers and focal adhesions but did not migrate. They adhered and remained at one position without significant movement (migration speed ≈ 0). Hence, distinct physical data such as migration speed, motility coefficient (≈ 0), persistent time (≈ infinite) and persistent distance (≈ 0) were non-existent. This finding confirms that the observed cell repellant effect is indeed due to migration and not to adhesion [48].

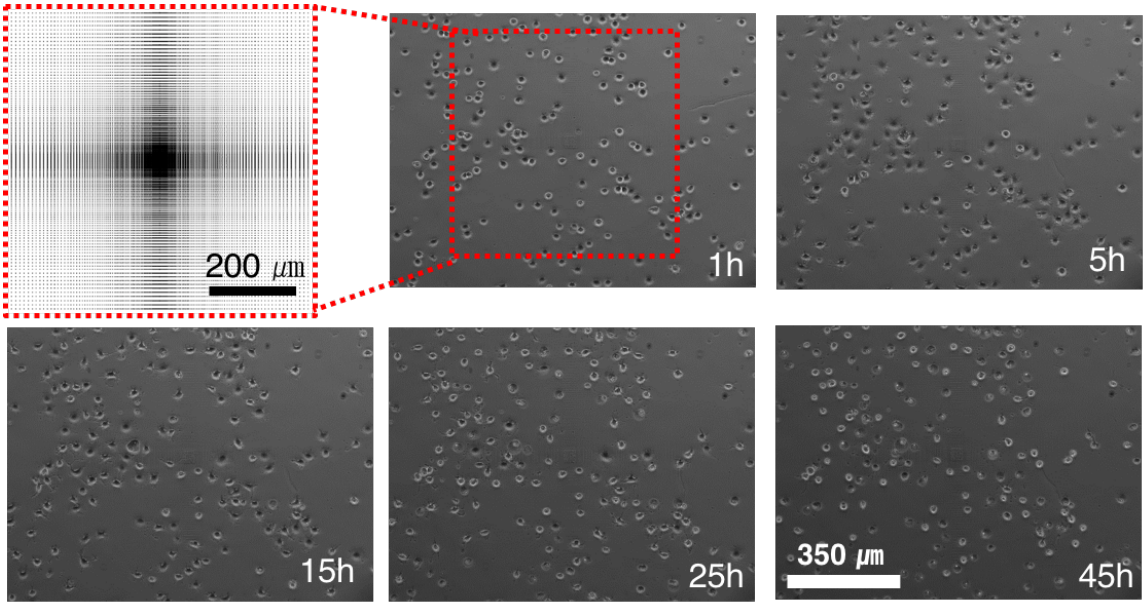

Figure 3.47. Time-lapse phase-contrast images of NIH-3T3 cells cultured on the gradient patterns (quartz) in medium containing 50 μM Blebbistatin. Directional migration was not observed (1,000 nm in diameter, 350 nm in depth nanocrater)

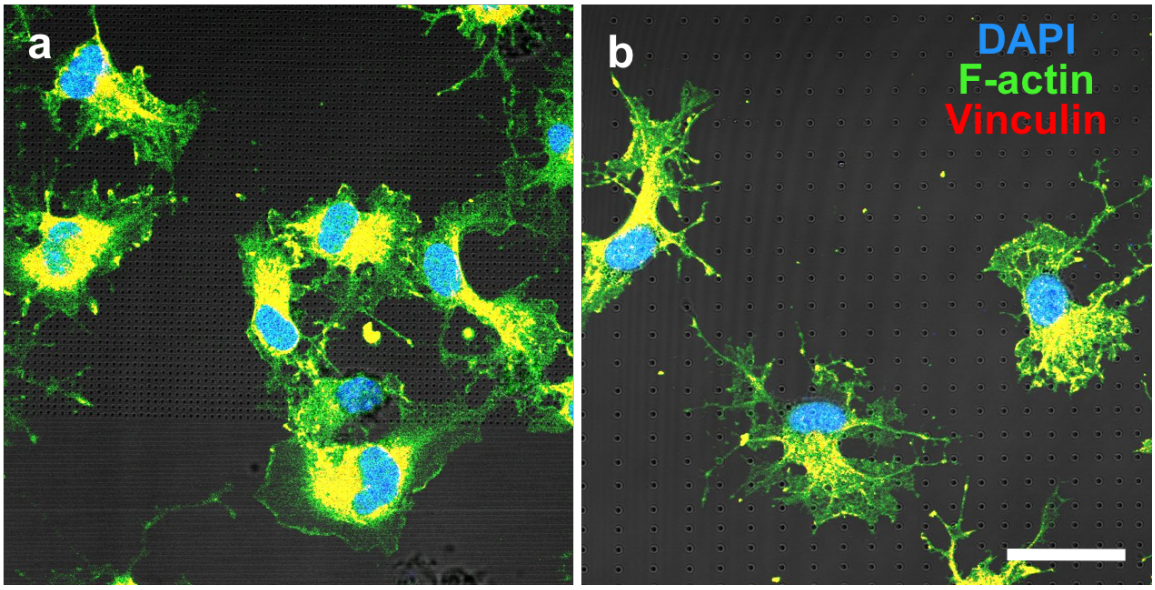

Figure 3.48. (a) Immunofluorescence image of fibroblasts on isometric pitch (2 μm) pattern of quartz in medium containing 50 μM Blebbistatin. (b) Immunofluorescence image of fibroblasts on spacing-gradient pattern of quartz in medium containing 50 μM Blebbistatin. The dendric extensions appeared with deficient stress cytoskeletal fibers and focal adhesions. F-actin in green, Vinculin in red, DAPI in blue (scale bar : 20 μm)

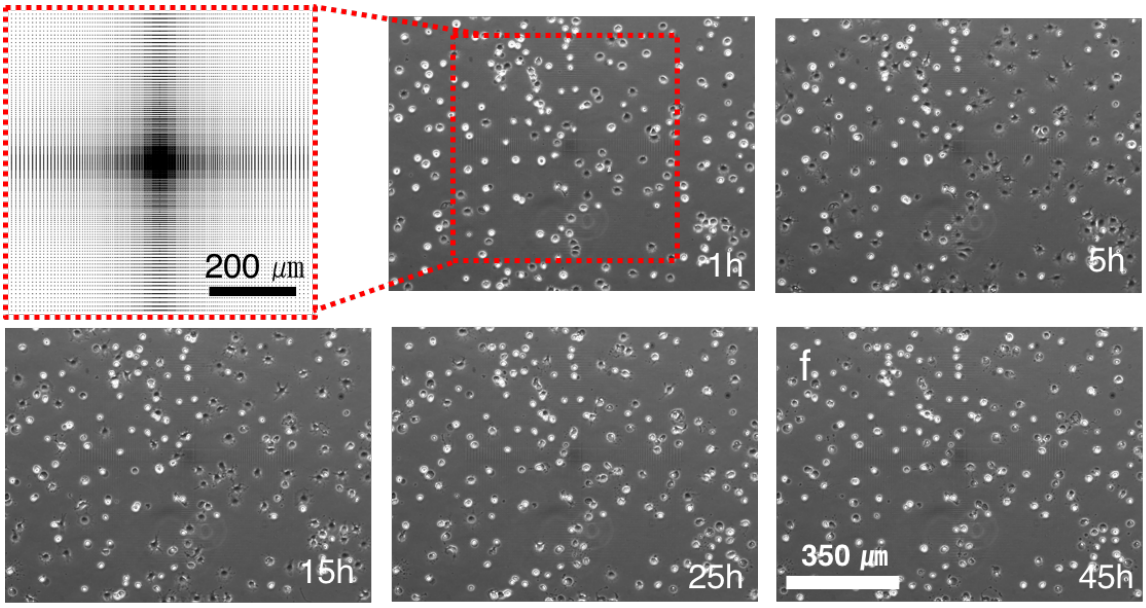

Figure 3.49. Time-lapse phase-contrast images of NIH-3T3 cells cultured on the gradient patterns (TCPS) in medium containing 50 μM Blebbistatin. Directional migration was not observed (1,000 nm in diameter, 350 nm in depth nanocrater)

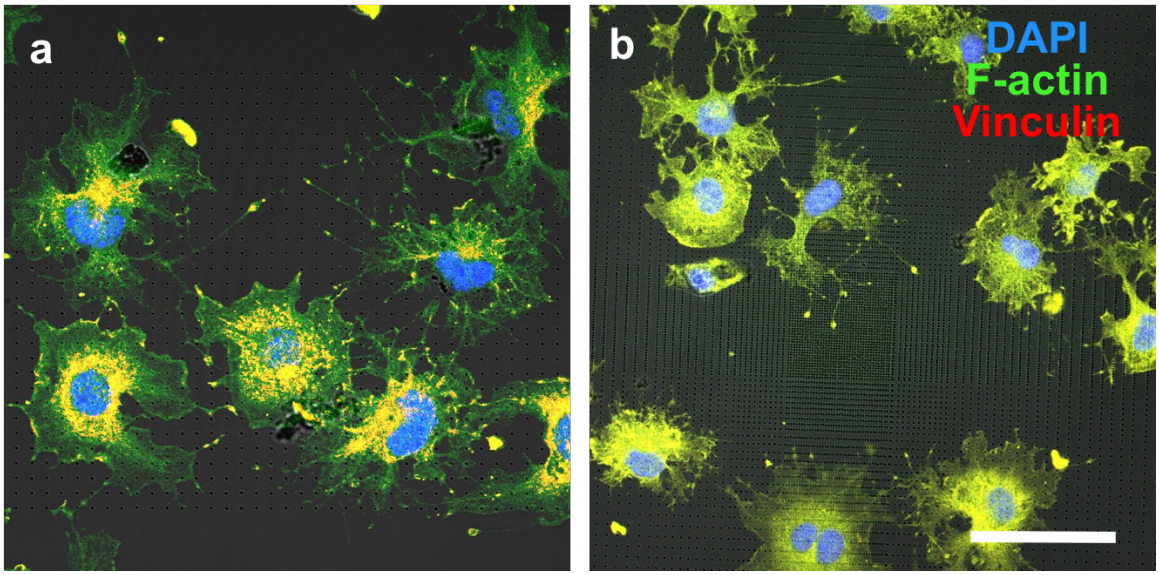

Figure 3.50. (a) Immunofluorescence image of fibroblasts on isometric pitch (2 μm) pattern of TCPS in medium containing 50 μM Blebbistatin. (b) Immunofluorescence image of fibroblasts on spacing-gradient pattern of quartz in medium containing 50 μM Blebbistatin. The dendric extensions appeared with deficient stress cytoskeletal fibers and focal adhesions. F-actin in green, Vinculin in red, DAPI in blue (scale bar : 20 μm)

3.4.8 Characterization of protein adsorption

To characterize the protein adsorption to quartz and TCPS surfaces, we performed quartz crystal microbalance with dissipation monitoring (QCM-D) experiments. The protein adsorption studies to quartz and TCPS surfaces (oxidized polystyrene) did not show significant differences in the absorption kinetics or total mass for protein (fibronectin) [48]. Protein adsorption at interfaces is influenced by the surface chemistry of the material. In order to further characterize the adsorption kinetics of fibronectin on both surfaces, we performed QCM-D measurements using SiO_2 and O_2 plasma-treated Polystyrene (oPS) sensors. Both surfaces yielded comparable results regarding frequency shifts after 50min incubation indicating a similar mass of fibronectin on both surfaces. The Δf values on the SiO_2 surfaces were 30 Hz, and adsorption to oPS resulted in a shift of 29.5 Hz [48].

3.4.9 Functionalization of surface on ablated pattern

To see the change of migration trend on the different chemical different concentration of environment, we applied the RGD peptide sequence concentration. Haptotaxis is the other example of directional migration controlled by surface density and distribution of ECM proteins[115-118]. When cells adhere to substrates, primary sites are focal adhesions that link the ECM to cytoskeletons via membrane-bound receptors. The focal adhesions are known to be capable of providing strong cell adhesion to the ECM and are regions of signal transduction regulating cell growth. The adhesion forces have a significant influence on motility. Initial cell-substratum attachment strength is a central variable governing cell migration speed and maximal speed can be obtained by cells moving on surfaces offering intermediate attachment strength. The gradient adhesion force due to the gradient of surface density of ECM proteins can regulate directional cell migration and specifically from the area of low-density to high-density of the ECM.

3.4.9.1 Migration speed

To figure the relationship between RGD peptide concentration (ligand density) and migration speed out, we made ablated pattern with same morphology (1μm in diameter and 350nm in depth), different spacing. After processing we coated the surface with different concentration of RGD-peptide sequence. For the consistence of experiment, we assumed the depth of nanocrater is enough deep that cell cannot sense the RGD peptide sequence at the bottom of crater.

Based on the result, cells migrate faster on the pattern with low ligand density (smaller pitch), and at higher RGD concentration they won't migrate with high speed. This result is consistent to that of on quartz and TCPS.

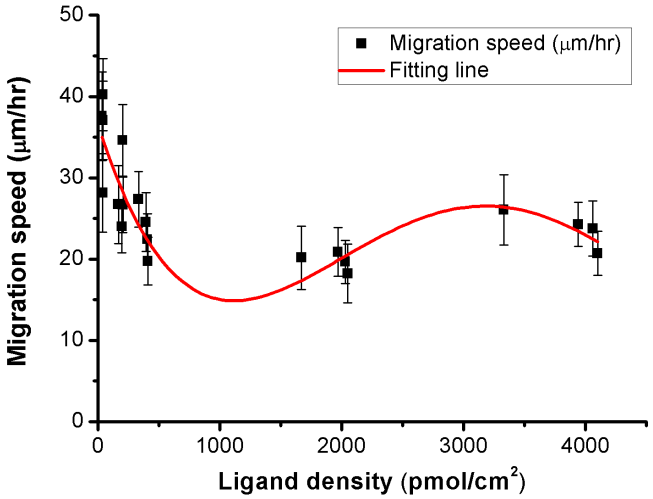

Figure 3.51. Migration speed on the substrate which coated different ligand density

3.4.9.2 Persistent random walk model (Persistent time and distance)

For calculation of persistence distance, it doesn't show significant differences by RGD-peptide concentration. However, persistence time of cells on ligand density with 1000 pmol/cm^2 show higher.

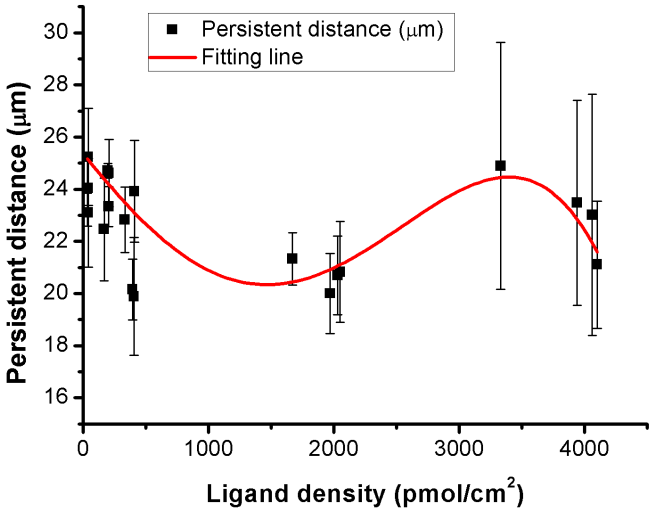

Figure 3.52. Persistent distance on the substrate which coated different ligand density

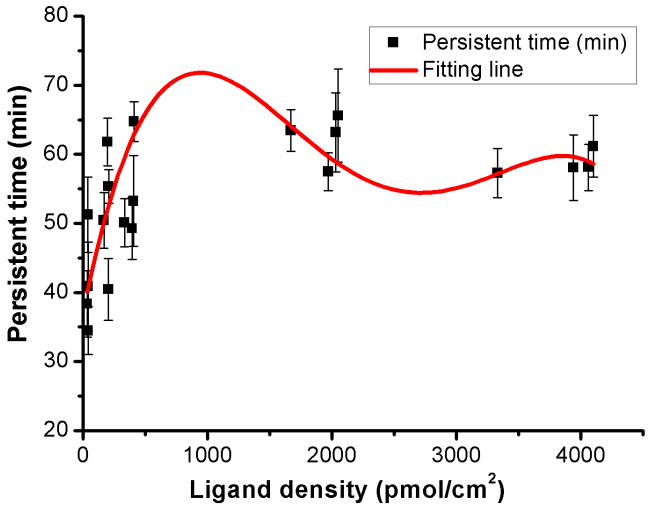

Figure 3.53. Persistent time on the substrate which coated different ligand density

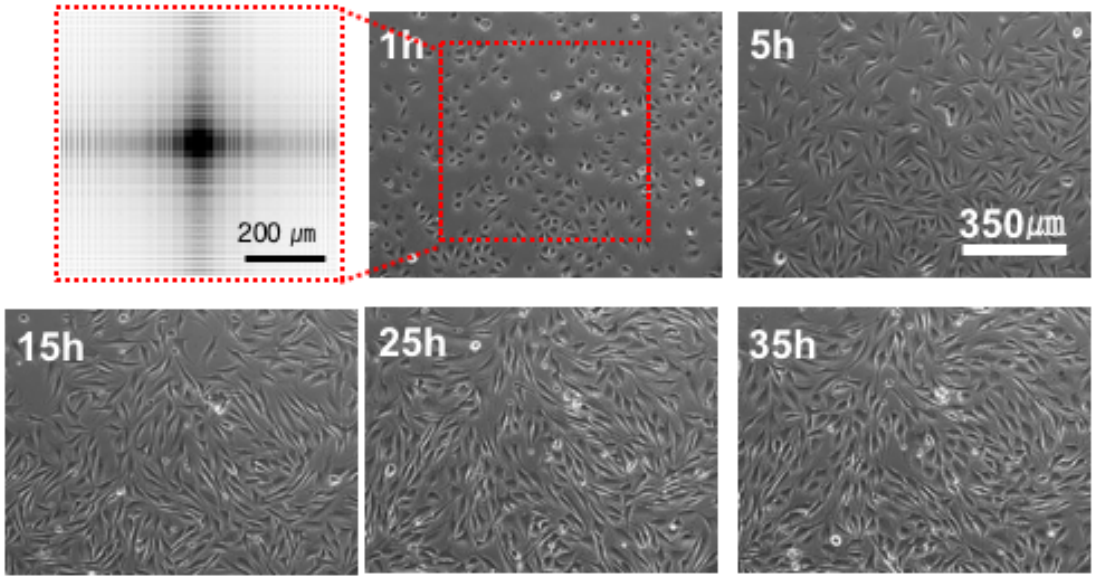

Figure 3.54. Time-lapse phase-contrast image of NIH-3T3 cells cultured on a patterned quartz coated 1000pmol/cm^2 with 1100 nm / 450 nm (diameter / depth).

However, it is hard to conclude that certain ligand density affects migration significantly. We expect that RGD-peptide sequences are filled into nanocrater with some thickness. In other words, there are not significant differences between the ablated and non-ablated patterns. For verification of RGD-peptide distribution on the pattern, we need additional tools such as very sensitive AFM with high resolution *etc*.

3.4.9.3 Directionality

On this result, we could not see the specific trend of migration on the different concentration of RGD peptide. Hence, comparing the effect of ablated pattern and ligand density, biophysical impact such as focal adhesion distribution is more effective for directional, and persistent migration.

3.4.9.4 Talin overexpression

Similar to the result of fibronectin-coated surface, it is hard to observe distinguishable migration of Talin transfected cells.

3.4.9.5 Blebbistatin

Similar to the result of fibronectin-coated surface, it is also hard to observe significant migration with blebbistatin treatment.

3.4.10 Enhancement of cell infiltration into electrospun fiber with ablated pattern

In order to better characterize the biological response to the microscale hole features, we demonstrated through our rat subcutaneous cell infiltration model that effective cell infiltration into electrospun scaffolds *in vivo* could be achieved and significantly enhanced by utilizing a femtosecond laser system to create desired ablations and increase scaffold porosity. We observed a noticeable increase in endothelial cell ingrowth of the ablated scaffolds. In a study aimed at elucidating the effects of pore size on tissue response to porous biomaterials[49]. Tightly controlled pore size promoted vascular ingrowth in which the degree of intra-matrix vascularization increased with decreasing pore size. However, as shown in $CD31^+$ staining indicated endothelial cell infiltration within the ablated holes after 1 week in vivo. In addition, the extent of endothelial cell ingrowth with respect to increased $CD31^+$ staining within the holes of the ablated scaffolds was more prominent after 2 weeks *in vivo*. This is suggestive of angiogenesis as endothelial cells were able to migrate into the holes and sprout new blood vessels. In contrast, regions without ablations, such as the spacing between adjacent holes as well as the control scaffold, showed no signs of endothelial cells within the scaffolds; instead, the distribution of $CD31^+$ staining was concentrated mainly in the surrounding tissue. These findings concur with previous studies that specifically engineered pore size is proangiogenic and can potentially induce more vascularization, although additional studies need to be conducted to investigate and better understand the process. Thus, because this approach can be extended not only to various polymers that may have different effects on inflammatory responses but also combined with other techniques such as the incorporation of sacrificial fibers in composite scaffolds, the appropriate selection of polymers or matrix proteins for fabricating electrospun scaffolds is important and

needs to be customized for various tissue-engineering and regenerative medicine applications.
Cell infiltration was significantly higher in the scaffold regions of ablated scaffolds compared to the control scaffold. We speculate that the ablations facilitated overall cell infiltration as the cells were able to better migrate through the ablated holes and infiltrate between layers of electrospun fibers into the scaffold from the post-ablation edges rather than from the relatively less porous surface.

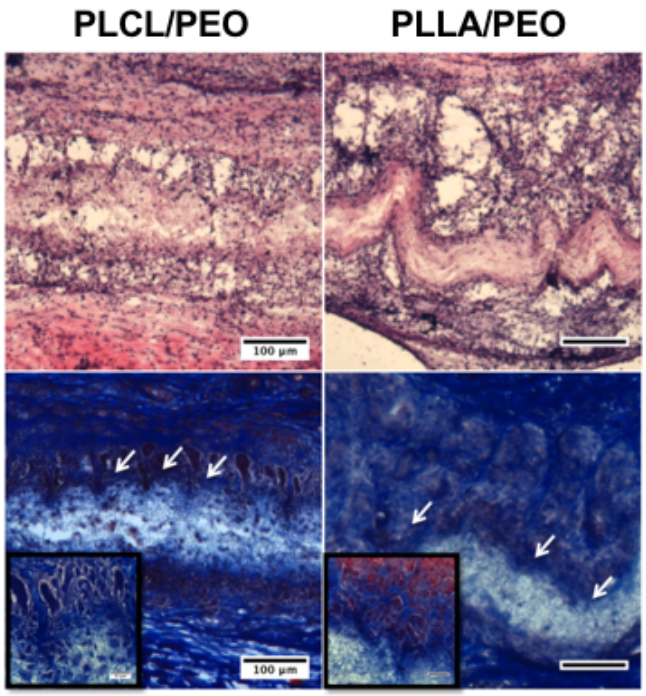

Figure 3.55. *in vivo* tissue response to channel at 2 weeks later after implantation

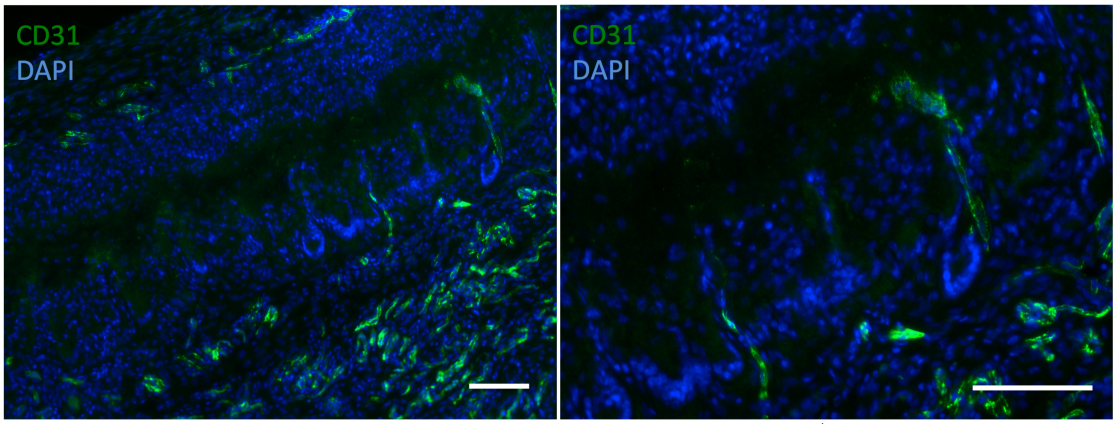

Figure 3.56. Enhancement of direct angiogenesis into scaffold. $CD31^{+}$ staining indicated endothelial cell ingrowth into the ablated channels (scalebar = 100 micron)

3.4.11 Resonance frequency change on microscale resonator

Femtosecond laser direct writing technique can be used for passive modification of micro-/nano-scale structure. For example, it can be used for frequency offset tuning in micromechanical resonators. Laser trimming is rather common in IC manufacturing, but micro- mechanical resonators are considerably more delicate and complicated than metal resistors. An advantage of laser trimming system is that it can be predictable and compatible with full automation. Here, we show that trimming locations can be selected using an FEM model to achieve a desired trim increment and that the Al top metallization can be removed via femtosecond laser without damaging the underlying AlN.

Width-Extensional mode piezoelectric AlN Resonators (WXR) were designed and fabricated. The resonator consists of a rectangular plate supported by two anchor beams attached at the sides. An array of interdigitated electrodes is used to excite two-dimensional plate acoustic waves within the thin piezoelectric layer.

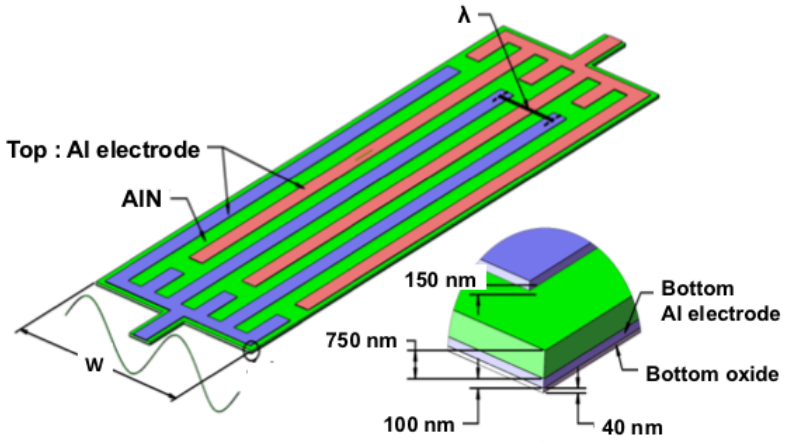

Figure 3.57. Schematic of WXR (Top Al (150 nm thickness) / AlN (750 nm thickness) / Bottom Al (100 nm thickness) / Bottom oxide (40 nm thickness)) and the direction in which acoustic wave travels

For this experiment, only Top Al layer should be ablated without damage of AlN layer. To optimize the laser condition, we did parametric study, found the optimal condition. To verify and characterize the ablated pattern, we took the SEM. This ablation process by femtosecond laser can eliminate interference by the ejecta, minimizing thermal effects occurring within the short pulse duration (~100fs), reducing the thermal stress and damage to the piezoelectric layer during the trimming process. Trimming was conducted using an automated system with computer control over stage motion and laser pulse firing. We applied 12.7nJ laser pulse energy with a long working-distance 50x objective

lens (Mitutoyo M Plan Apo, NA= 0.55) at the frequency double wavelength of 400nm, producing a 1.5μm diameter trim spot.

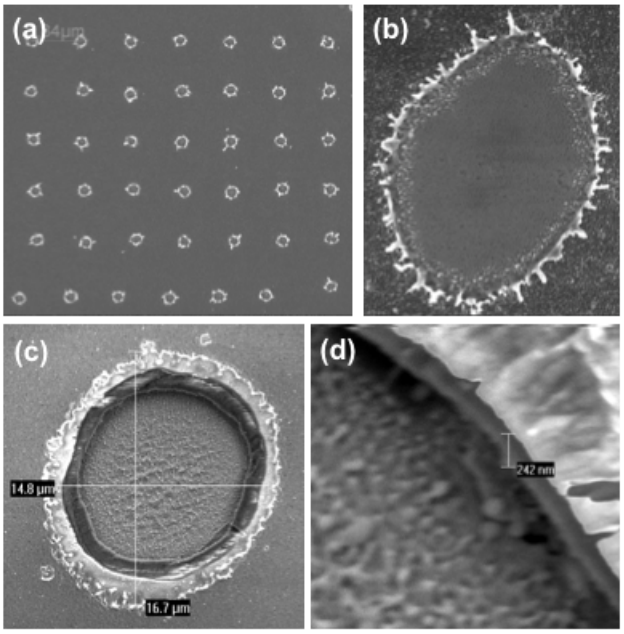

Figure 3.58. (a) Ablated pattern with same spacing (3.8 μm). (b) Ablation of top Al layer without damage of AlN layer. (c) AlN layer damaged pattern with high laser fluence. (d) Side view of damaged pattern (c)

Figure 3.61 shows the trimming pattern and the FEM model used to estimate the frequency shift. SEM images of a trimmed resonator, demonstrating removal of the Al layer without damage to the AlN. The FEM model predicts that both positive/negative frequency shifts can be achieved and the frequency shift varies sinusoidal depending on the ratio of the trimmed width to the electrode width (x/W_e). The origin of this effect is that the trimmed area changes both the local mass and stiffness. If the ratio x/W_e is less than 0.4, the mass reduction dominates over stiffness reduction and $\Delta f/f > 0$. In contrast to this, $x/W_e < 0$, the stiffness reduction dominates and $\Delta f/f < 0$. Frequency shift also highly depends on the mode shape and trimming has maximum effect where the displacement field is largest (electrodes edges).

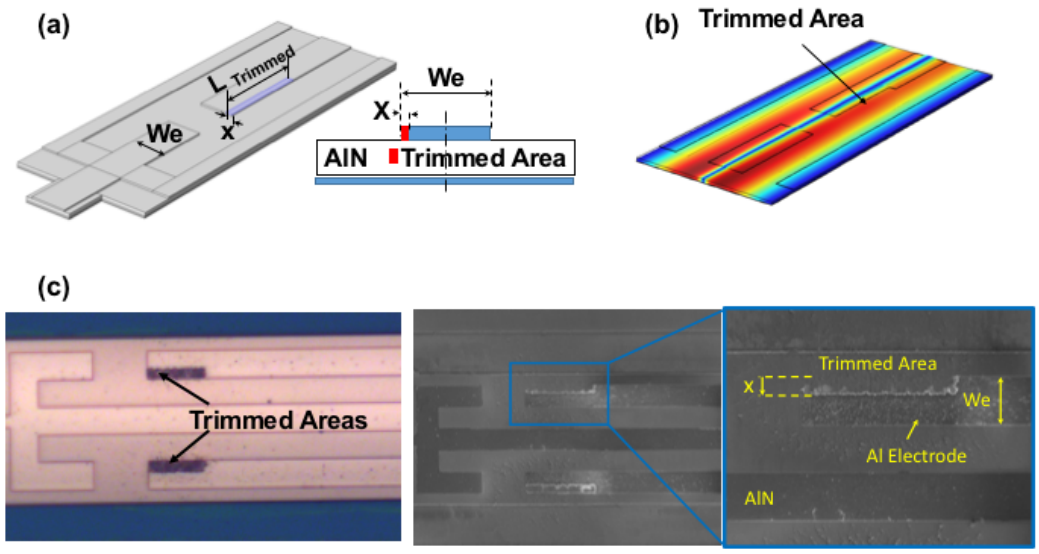

Figure 3.59. (a) WXR trimming pattern and cross-section of WXR which showing the trim pattern. (b) FEM model of WXR mode-shape showing the displacement field. (c) Optical microscope and SEM images of trimmed resonator

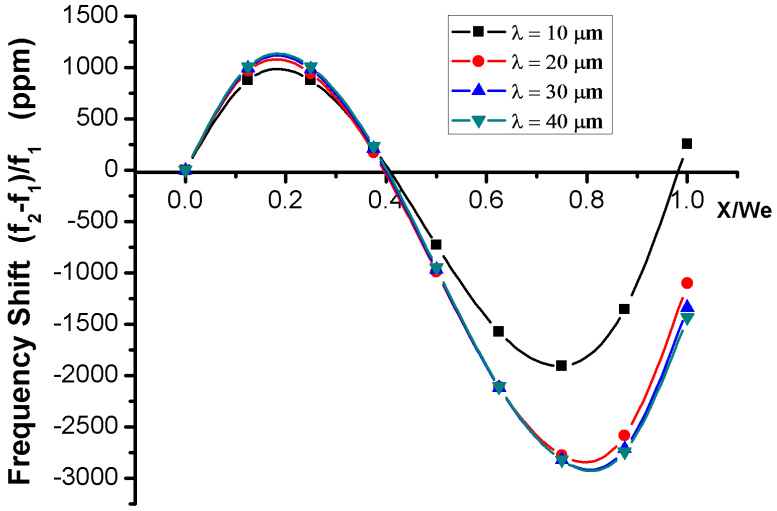

Figure 3.60. FEM prediction of frequency shift from trimming as the normalized trim length (X/We) is varied for WXR's with different acoustic wavelength (λ)

As a result, WXR resonance frequency peak shift occur after laser trimming (Figure 3.62). The measured frequency peak is 750 ppm.

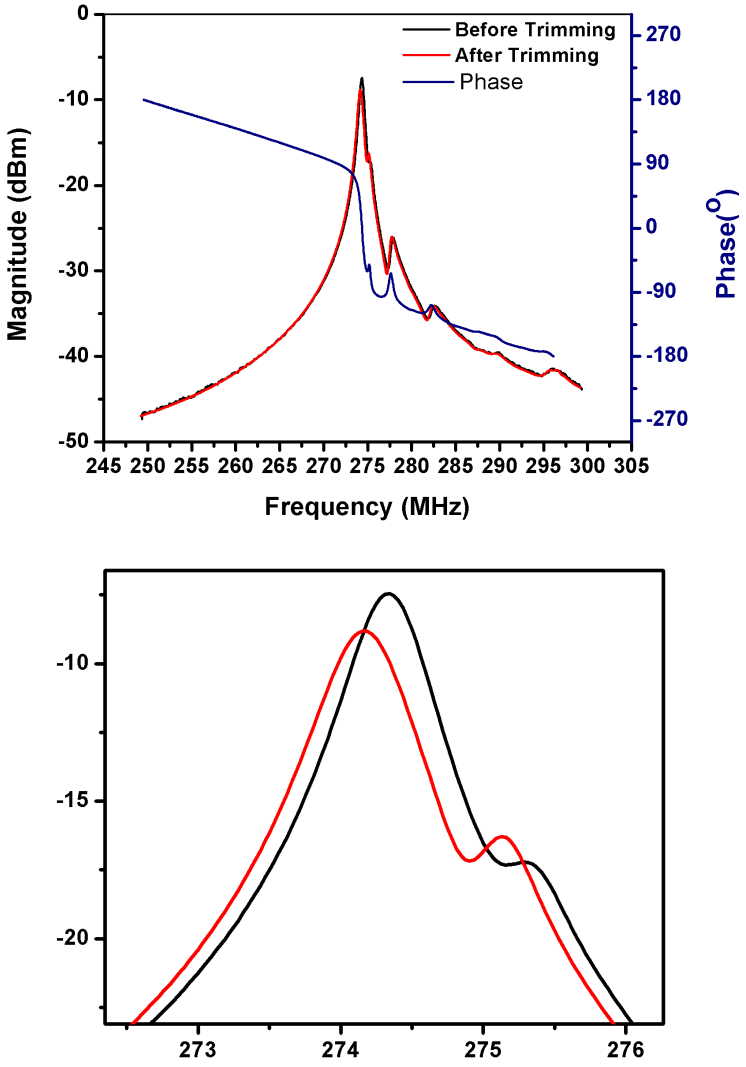

Figure 3.61. WXR frequency peak shift before and after laser trimming. The measured frequency shift is 750 ppm.

Figure 3.62 shows the measured frequency of a number of similar WXRs with same acoustic wavelength λ=22μm trimmed at two ratios: x/W_e= 0.2and 0.8. The experimental results are consistent with the FEM model. It is observed that when the trimming ratio (x/W_e) is fixed but the trimmed length is varied, the frequency shift is linearly related to the trim length.

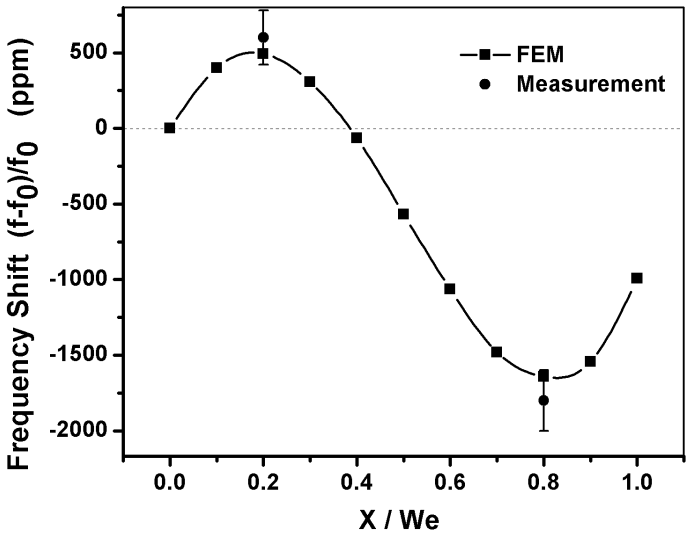

Figure 3.62. The measured frequencies of several WXRs (λ=22μm) trimmed at fixed x/W_e= 0.2 and 0.8.

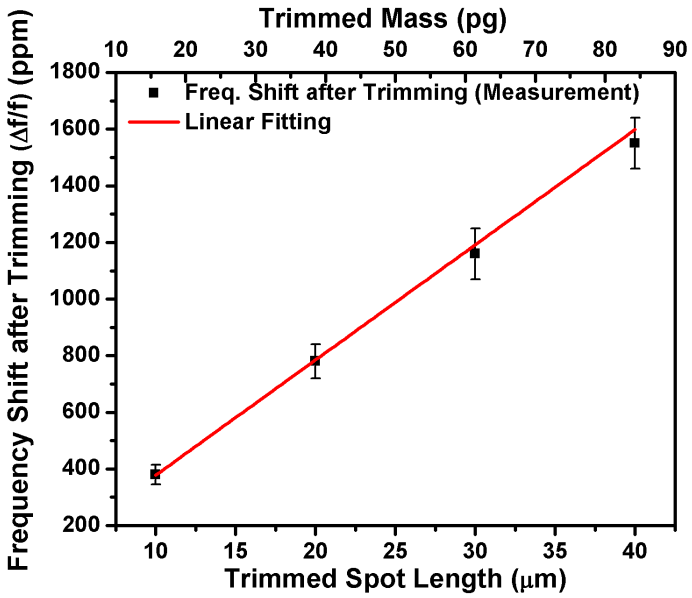

Figure 3.63. The frequency versus the trimmed mass at fixed trimming ratio (x/W_e= 0.8)

In conclusion, the results demonstrate laser trimming can remove Al metallization from the surface of AlN resonators to produce a predictable frequency trim increment.

3.5 Conclusion and outlook

Our results suggest that nanocrater patterns can be effectively designed and fabricated to generate cell repellant interfaces and induce guided cell migration into a desired shape (*i.e.* line or arc) or area. The ablated patterns with spacing gradient can provide stable and external stimuli to cells in order to control their adhesion and migration. And it can be easily fabricated compared to other gradient stimuli platforms for directional cell migration. We could exploit the induced migration phenomenon to demonstrate the formation of cell colonies of different shapes. The nanocrater patterning by FS-LDW (femtosecond laser ablation lithography technique)nanofabrication technique is of general applicability and amenable to fabrication on any biomaterial such as glass, ceramics, metals, and polymers, and even onto complex geometries under ambient processing conditions. Topographical nanocrater patterns are used to direct cell migration. Varying dimensions of nanocrater patterns were examined for effective cell migration and applied mechanical forces. The cells on the spacing gradient nanocrater array move towards area of lower ratio of texture versus plane (lower surface area of nanopits in a unit patterned surface). We conclude that the cell repellant effect is dependent on disrupting focal adhesion maturation, and this observation is robust and generic, but can be influenced by the surface topography surrounding the nanocraters. We anticipate our findings will be useful for surface patterning of biomaterials, controlling tissue formation with desired shapes or patterns, and understanding fundamental mechanisms of cell migration and sensing.

Guided cell migration also affected by chemically and topographically patterned surface in nanometer length scale was demonstrated. Ligand concentration is required chemicals for cell to adhere on the substrate. After ablated pattern fabrication, we coated the RGD peptide sequence to induce the chemical concentration gradient due to the topography of pattern. However, it is hard to observe the significant difference of cell migration on those pattern. To verify the effect of chemical gradient, additional experiment and characterization process be needed.

Moreover, porosity is a critical issue that must be addressed when utilizing electrospun fibrous structure as tissue-engineered nanofibrous scaffolds. Here, we demonstrate that FS lasers can be used to ablate electrospun scaffolds while preserving their overall structural integrity and effectively improving cell infiltration. Femtosecond lasers allow better control of laser power than nanosecond lasers and avoid fiber melting and consequently blockage of the porous structure. The diameter of the holes increases linearly with the laser energy, and the depth of the holes increases linearly with the number of laser pulses. In addition to their effects on cell morphology in vitro, electrospun PLLA/PEO scaffolds with femtosecond laser ablated holes of varying size and density exhibit significantly better endothelial cell ingrowth and macrophage infiltration compared to the control scaffold *in vivo*.

Ablation technique also can be applied to removal of structure on the MEMS structure. For the precise tuning of frequency of AlN resonator, only Al top electrode material is removed without removal of deformation of AlN piezoelectric layer beneath. Femtosecond laser direct writing is a good method for this purpose. Optimal conditions (i.e. pulse duration (~100fs), in 12.7 nJ per pulse), could be identified, minimizing

thermal effects. Frequency tuning of AlN piezoelectric resonators is demonstrated in steps as small as 400 ppm over a range of -3000 to 1500 ppm using a femtosecond laser trimming. An FEM model is used to identify the required locations for laser trimming to attain a desired shift in frequency, with the frequency increment proportional to the resonator's velocity at the trim location. On experiments, frequency change of up to 3000 ppm is measured for resonators with 275 MHz central frequency.

Chapter 4 Fast 3D High Aspect Ratio Structure Fabrication by Femtoseond Laser Direct Writing (Two-photon polymerization)

4.1 Introduction

Effective treatments for numerous cardiovascular diseases are in great demand. However, one biggest challenge is the lack of an established *in vitro* cardiac tissue model which would be useful for testing potential medical treatment. Although genetics play a critical role in cardiac disease, non-genetic issue such as stress, forces[119, 120] and paracrine factors normally experienced in the heart, or changes in those cues in the setting of drugs or disease also makes an important contribution to cardiac pathology. Therefore, developing a "patient-/disease-specific" 3D cardiac disease would be a significant advancement for understanding the cardiac disease mechanism with medical treatment or external stimulus *in vitro*. Native myocardial tissues [121-123] are organized and aligned into parallel cardiac muscle fibers with aligned intracellular contractile myofibrils. And gap junction complexes between contacting cardiomyocytes (CMs) are important for integrated electrical, chemical signal generation and mechanical properties of heart. Cells are surrounded by a 3D organization of supporting matrix[51, 124-126] in the natural tissue environment and neighboring cells with gradients of electrical, chemical and mechanical signals. Creating and forming a multi-cellular architecture with a highly controlled cellular environment, it makes it possible to fabricate or standardize *in vitro* models. Controlling the modulation of various parameters (*e.g.*, cellular composition, environmental factors) are amenable to drug screening (*i.e*. toxicity testing). *In vivo* CMs polarize their intracellular structure for contraction, and align with neighboring cells to facilitate the rapid spread of electrical activation. Hence, this alignment increases the contraction force. However, due to the difficulty of replicating such 3D aligned tissue microenvironments *in vitro*, cardiovascular pharmacology studies are particularly challenging. And this may result in false readouts. The limitations of existing 2D cell culture on the TCPS practices have therefore provided an impetus for the development of alternative cell-based *in vitro* models that better mimic the complex cardiac cellular architectures and functions of living hearts[126-128].

However, previous strategies for generating aligned 3D cardiac tissue relied on the implementation of mechanical loading by pairs of cantilever posts to stretch 3D matrices

with mixture between collagen I, fibrinogen[28, 126, 129] and CMs. By loading fibrin-based hydrogels mixed with CMs onto microfabricated polydimethylsiloxane (PDMS) cantilever post [130, 131], others have created a 3D cardiac tissue with aligned structure; however, these animal-derived ECM based-scaffolds suffer from vial-to-vial variability, inhomogeneous structure, inconsistent reproducibility and non-precise control over essential scaffold parameters. Electrospun 3D fibrous scaffolds with aligned nanofibers using synthetic polymers to structurally mimic the orientation of ECM in the myocardium[132-136], which helped CMs self-organize into an anisotropic structure. However, the electrospinning method results in small size (nanoscale) and uncontrollable porosity cannot allow immediate cell infiltration into the matrix to create a 3D cardiac cellular structure.

In order to systematically study stem cell behavior (*i.e*. hiPS) in a 3D environment, more advanced fabrication methods are needed to produce scaffolds with accurately defined mechanical/physical and micro-/nanoscale properties. Two-photon polymerization (2PP), which is a laser direct writing based on the multiphoton absorption, can be polymerize and cure the photo-curable material only near the laser focal volume, enabling arbitrary 3D structures fabrication with spatial resolution approximately 100 nm [67, 69, 137, 138]. We created a cardiac tissue model using precisely controlled 3D fibrous structure that allowed for self-assembly and dynamic remodeling of CMs. Using 2PP, we created different filamentous matrices by fabricating synthetic parallel fibers with different fiber thickness (*i.e*., 5 μm and 10 μm) [51] and spacing. Because of their elastic modulus, the thicker fibers (10 μm) have a higher mechanical resistance to cardiac tissue contraction than do the thinner fibers (5 μm). We grew wild-type hiPS-CMs (WT hiPS-CMs), transcription activator-like effector nuclease (TALEN)-engineered isogenic hiPS-CMs with Ca^{2+} reporter (GCaMP6f hiPS-CMs), and isogenic hiPS-CMs with loss-of-function cardiac isoform of myosin binding protein C (MYBPC3 hiPS-CMs) on the filamentous matrices to form anisotropic cardiac microtissues. Wildtype cardiac microtissues (WT hiPS-CMs) were able to adapt their contraction velocity, force and calcium ion flux to the alternations of mechanical resistance to the cardiac microtissues. MYBPC3 hiPS-CM microtissues exhibited significantly lower contraction forces compared to WT hiPS-CMs microtissues only when grown on the higher mechanical resistance matrices. Furthermore, low mechanical resistance microenvironment (*i.e.* thinner fibrous matrices) directed MYBPC3 cardiac microtissues to acquire a hypo-contractile phenotype that is an early sign of hypertrophic cardiomyopathy, whereas high mechanical resistance microenvironment directed MYBPC cardiac microtissues to manifest a cardiac failure phenotype with impaired cardiac output. This suggested that tissue's mechanical microenvironment facilitated the modeling of contraction deficits associated with MYBPC3 knockout (KO).

4.2 Laser-based polymerization technique for fiber fabrication

4.2.1 Nonlinear propagation

The system of Maxwell's equations constitutes the basis for the theory of electromagnetic fields and waves as well as their interactions with materials [66].

$$\nabla\times\vec{E} = -\mu\frac{\partial\vec{H}}{\partial t}$$

$$\nabla\times\vec{H} = J + \mu\frac{\partial\vec{D}}{\partial t}$$

$$\nabla\cdot\vec{D} = \rho$$

$$\nabla\cdot\vec{B} = 0$$

$$\vec{D} = \varepsilon_0\vec{E} + \vec{P}$$

$$\vec{H} = \frac{1}{\mu_0}\vec{B} - \vec{M}$$

where ε_0 is electric permittivity, $\vec{E}$ is electric dipole moment, μ is magnetic permeability, μ_0 is magnetic permeability in the vacuum, $\vec{H}$ is magnetic field, J is free current density vector, $\vec{D}$ is electrical displacement vector, ρ is charge density, $\vec{B}$ is magnetic induction field and $\vec{P}$ is polarization vector.
Recalling vector identity equations and operations, we can get a wave equation:

$$\nabla\times\nabla\times\vec{E} + \frac{1}{c^2}\frac{\partial^2\vec{E}}{\partial t^2} = -\frac{1}{\varepsilon_0 c^2}\frac{\partial^2\vec{P}}{\partial t^2}$$

In the linear regime when the electric field strength is small, the polarization is linearly related to the electric field by

$$\vec{P}(t) = \chi^{(1)}\varepsilon_0\vec{E}(t)$$

$\chi^{(1)}$ is the electric susceptibility and those equations can be simplified as

$$\nabla\times\nabla\times\vec{E}+\frac{{n_0}^2}{c^2}\frac{\partial^2\vec{E}}{\partial t^2}=0$$

where $n_0$is the index of refraction (linear), defined as

$$n_0=\sqrt{1+\chi^{(1)}}$$

However, at high field strength, the relations between $\vec{P}$ and $\vec{E}$ described above are no longer valid. The nonlinear dependence of the polarization on the applied electric field can be described as

$$\vec{P}=\varepsilon_0\left[\chi^{(1)}\vec{E}+\chi^{(2)}\vec{E}\vec{E}+\chi^{(3)}\vec{E}\vec{E}\vec{E}+\cdots\right]$$

The light absorption rate of a material is described by the susceptibility $\chi^{(n)}$. The greater the susceptibility, the greater is the ability of a material to polarize in an electric field and reduce the field inside the material by absorbing energy from it. The length of the material polarization $\vec{P}$ can be written as

$$P=\chi^{(1)}E+\chi^{(2)}E^2+\chi^{(3)}E^3+\chi^{(4)}E^4+\chi^{(5)}E^5+\cdots$$

where $\chi^{(1)}$ is linear susceptibility, and $\chi^{(2)}$ and $\chi^{(3)}$ is second and third order susceptibilities. Simultaneous absorption of two photons is a resonant process and in those processes the terms $\chi^{(2)}$, $\chi^{(4)}$, and higher order $\chi^{(n)}$ can be neglected

4.2.1.1 Nonlinear index refraction

When the high intensity laser pulses propagate through a material, the linear approximation of the polarization and the electric field is not valid, thus, resulting index of refraction (real part) can be derived as [66]

$$n=\sqrt{1+\chi^{(1)}+\frac{3}{4}\chi^{(3)}E^2}$$

where $\chi^{(1)}$ is the linear susceptibility and $\chi^{(3)}$ is the nonlinear susceptibility. This equation can be described as more convenient form,

$$n=n_0+n_2I$$

where n_0 is the linear refraction index, n_2 is the nonlinear refraction index and I is laser intensity. Laser intensity(I) can be defined

$$I = \frac{\varepsilon_0 c n_0 E^2}{2}$$

and n_2 is the nonlinear part of the refractive index defined as

$$n_2 = \frac{3\chi^{(3)}}{(4\varepsilon_0 c n_0)^2}$$

This nonlinear refractive index gives rise to nonlinear effects, such as self-focusing, when an intense femtosecond laser propagates through transparent materials.

4.2.1.2 Propagation of laser beam

The propagation of intense laser beam in wide bandgap material induces microscopic displacement of bound charges[66]. This displacement forms an oscillating of electric dipoles and the polarization at the frequency of the incident laser field. The refractive index of material accounting this nonlinear interaction ($n = n_0 + n_2 I$) can follow the previous section. Even though the values of n_2 is very low, intense laser pulses should be irradiated to enhance a nonlinear contribution ($n_2 I$) in refractive index of material. Hence, irradiation of a Gaussian beam can generate spatially varying refractive index in wide bandgap materials. In the Gaussian beam, the intensity along the center axis is higher than that of the periphery, the beam center experiences larger refractive index than in the periphery when the nonlinear refractive index is positive. As a result, the material acts as a focusing lens.

However, the electron density at the focus does not infinitely increase. When the nonlinear mechanisms that include multiphoton absorption and self-focusing effect generate electron-hole plasma at the focus, modification of the refractive index occurs. Adjusting to this change, the light diverges (plasma defocusing). The refractive index modification due to electron-hole plasma can be described as following equation:

$$n = n_0 - \frac{N}{2n_0 N_c}$$

where N_C is the characteristic plasma density when the plasma frequency is equal to the laser frequency:

$$N_c = \frac{\omega^2 \varepsilon_0 m_e}{e^2}$$

The balance between self-focusing and plasma defocusing creates self-trapping or filamentation of light in the material. Figure 4.1. depicts the self-trapping of light in a wide bandgap material. The exact balance between self-focusing and plasma defocusing elongates the depth of focus. Catastrophic collapse of the laser beam to a singularity is predicted when the peak intensity of the femtosecond laser pulse exceeds a critical power (P_{cr}) for self-focusing is

$$P_{cr} = \frac{3.77\lambda^2}{8\pi n_0 n_2}$$

where λ is the laser wavelength. The power of the irradiating laser pulse exceeds the critical power (P_{cr}), laser light can break up into several narrow filaments (*i.e.* the so-called filamentation). In real materials, other mechanisms such as defocusing due to nonlinear ionization halt the beam collapse by balancing with self-focusing.

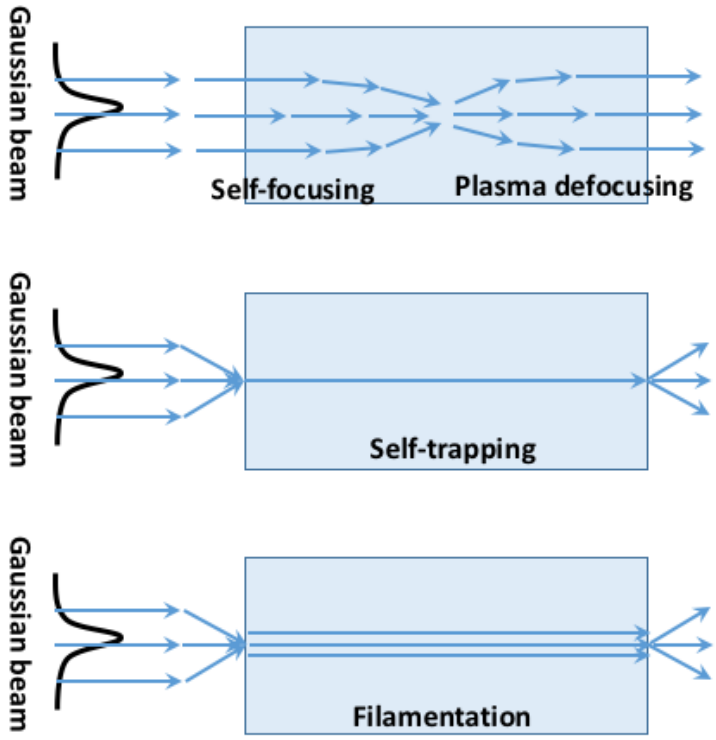

Figure 4.1. Self-action of light in wide bandgap materials. (a) Self-focusing and plasma defocusing, (b) Self-trapping, (c) Filamentation

4.2.2 Test panel fabrication drug screening for cardiac electrophysiology

The substrate stiffness contributed to the maturation of neonatal CMs and regulated sarcomere structure and calcium transient of adult CMs[139, 140]. Previous studies on

the disease mechanisms of Long QT syndrome 3 (LQT3) and drug screening for treatment were highly dependent on 2D culture[51, 141-143], which does not exactly represent the real cellular environment within the myocardium. The interplay between gene expression and environmental intricacies causes large functional variations of cells. For example, an "*in vivo*-like" microenvironment with aligned CMs has been shown to facilitate stem cell acquisition of cardiac-specific contractile cytoskeleton proteins, gap junction protein , transcription factors distribution, and electrophysiological properties[144, 145].
The CMs differentiated from LQT3 Induced pluripotent stem (iPS) cells were verified to faithfully recapitulate the electrophysiological abnormality (delayed repolarization and abnormal long QT signal). By seeding LQT3 iPS-CMs on such a highly controllable filamentous matrix, we generated a disease-specific 3D cardiac tissue and studied the contractility malfunctions associated with the electrophysiological consequences of LQT3 syndrome. By the comparison with general 2D cell culture model (*i.e.* on TCPS), we highlighted the different response of our 3D tissue model (*i.e.* on the fibrous structure by 2PP) to a panel of drugs associated with cardiotoxicity

4.2.2.1 Long QT syndrome

iPS cell technology allows the recapitulation of disease models *in vitro*. This can be used to both study "disease mechanisms" and "design and screening of personalized therapeutics" prior to large animal experiment or clinical trials. Patient-specific iPS cell-derived cardiomyocytes (iPS-CMs) have been shown to provide valuable models of congenital cardiomyopathies (LQT3) caused by mutations in genes coding for ion channels or ion channel-associated proteins. LQT3, with a mutation in the SCN5a gene, enhances late Na^+ channel currents (I_{Na+}) that fail to inactivate completely and conduct increased inward currents[51, 141-143]. This prolonged depolarization results in delayed repolarization, eventually prolonged QT interval and increases the risk of fatal arrhythmia.

4.2.2.2 Loss of function mutation of myosin binding protein C (MYBPC3)

The integration of complex *in vitro* cardiac tissue models with hiPS cells and genome editing tools (*i.e.* TALEN) has been shown to enhance the physiological phenotype, improve CMs maturity, and recapitulate the disease pathologies[146]. In this work, isogenic hiPS-CMs harboring loss-of-function (premature STOP codon) mutations was used which is mutation of the sarcomere associated protein, myosin binding protein C (MYBPC3). Cardiac microtissues derived from WT hiPS-CMs were able to adapt to the mechanical environment with increased contraction force and enhanced calcium ion flux. And this phenomena also depends on the stiffness of the fibrous structures [139, 147, 148]. In contrast, MYBPC3 cardiac microtissues exhibited impaired force development compared to WT tissues only when grown on matrices with higher fiber stiffness. This suggesting that biomechanical cues facilitated contractile deficits due to the MYBPC3 gene KO[139, 147-150]. By examining force and power generated from CMs, we discriminated hypo-contraction and impaired-contraction by variation of mechanical resistance to the MYBPC3 cardiac microtissues. Hence, choice of different tissue microenvironment will provoke different disease phenotype with the same genetic defect.

4.2.2.3 3D CM contraction force and mechanical environment

Contraction force is a key component of cardiac function. This is continuously regulated by the surrounding environments. The contraction force of CMs derived from hiPS-CMs has been deemed as one of the essential parameters for the evaluation of normal cardiac function, disease phenotypes, and response to pharmacological treatment[151-155]. Based on microfabricated cantilver posts, soft substratec which can be deformed by the contraction of CMs, traction force microscopy (TFM) has been widely used for single-cell force measurement at nano-Newton (nN) scale. Although 2D arrays provided substantially higher spatial resolution of the forces generated by individual CMs. However, the cells were forced into a 2D array is lacked 3D architecture, and cell-cell interactions occurring at the tissue level. Given the 3D nature of tissues and organs, 2D models are intrinsically limited for delivering physiological-relevant cell microenvironment and recapitulating the dynamics of the tissue-level responses.

To circumvent those problems with 2D cardiac celluar model, 3D engineered cardiac tissues that mimic native tissue structures have been developed using a variety of methodologies and materials. This share a common process of hiPS-CMs encapsulation into external hydrogels[28, 151]. To promote hiPS-CMs alignment and formation of physiologically relevant tissue structures, the 3D cardiac tissues were normally stabilized between two flexible cantilevers. And this structure also served as a force sensor to measure contraction force with tissue scale. However, this measurement was compromised by the mechanical properties of external hydrogel for CM trapping, which altered the tissue mechanical/physical properties (*i.e.* cellular contractile force). To solve the error by synthetic hydrogel encapsulation, self-assembled cardiac tissues relying on secretion of their own ECM are being explored to better assess measurement of contraction forces which allow for the consistent tissue remodeling. In parallel, the force sensors used to measure cardiac tissue contraction not only reported the contraction forces from hiPS-CMs, but also naturally became the external mechanical stimuli that regulated the cardiac tissue formation, remodeling and function[119, 151, 156, 157]. In TFM, variation of substrate stiffness altered the myofibril organization of hiPS-CMs, demonstrating physiological stiffness could improve the contractile activity of patterned hiPS-CMs. Flexible cantilevers used to anchor the cardiac tissue may also represent the rigidity of the external structure against the tissue contraction and consequently has been used to mimic *in vitro* cardiac tissue afterload[120, 130, 157-160]. Increase of the afterload to cardiac microtissues derived from patient-specific and genome-engineered hiPS cells has facilitated better modeling of dilated cardiomyopathy (DCM) associated with TITIN gene mutations[161-163]. In contrast, optimal mechanical load was critical for the 3D maintenance and maturation of hiPS-CMs with highly organized sarcomeres[164], as well as increased adherents and gap junction formation. Collectively, these studies indicate that 3D *in vitro* cardiac tissue models provide a high-controllable mechanical microenvironment that incorporates key niche elements to enable regulation of cardiac functions and disease phenotypes.

4.3 Experimental

4.3.1 Material preparation

4.3.1.1 Glass scaffold preparation

The UV-curable organic-inorganic hybrid polymer (ORMOCLEAR®, Micro resist technology) was spin-coated onto two glass plates (25 mm in length, 3 mm in width, and 1 mm in thickness) at 4000 rpm for 60 s, pre-baked on a hotplate at 80°C for 2 min, and cured under UV light lamp for 30 min. After completion of UV-curable material, those two glass plates were assembled with two 500μm-thick spacers at the ends and subsequently hard baked at 110°C for 1.5 h. Without this hard-baking process, glass scaffold tend to break during the development.

4.3.2 Experimental setup

The filamentous matrices were fabricated via the system based on a femtosecond laser beam irradiated vertically to the UV-curable organic-inorganic hybrid polymer (ORMOCLEAR®, Micro resist technology). The glass scaffold filled with UV-curable organic-inorganic hybrid polymer (ORMOCLEAR®) was mounted on the PC-controllable X-Y-Z motorized stages (Aerotech, ANT95-XY-MP for x-y direction and ANT95-50- L-Z-RH for z direction) with high precise positioning. Single fibers were fabricated along the laser beam path with a high-repetition rate femtosecond laser irradiation. The femtosecond laser (pulse duration: <400 fs, repetition frequency: 1 MHz, wavelength: 1045 nm, FCPA mJewel D-400, IMRA America, Inc.) was frequency-doubled to the wavelength of 522 nm by lithium triborate (LBO) second harmonic nonlinear crystal (Newlight photonics). And this femtosecond laser was focused onto the glass scaffold and ORMOCLEAR® interface with a 5x objective lens (Mitutoyo M Plan Apo, NA= 0.14). The different thickness of fibers could be fabricated by changing the laser power and exposure duration. Exposure duration was controlled by mechanical shutter which is connected to function generator. The laser power emitted downstream of the objective lens was measured by a power meter and controlled by a half-wave plate and a polarizing beam splitter (PBS). (Figure 4.2. (a))

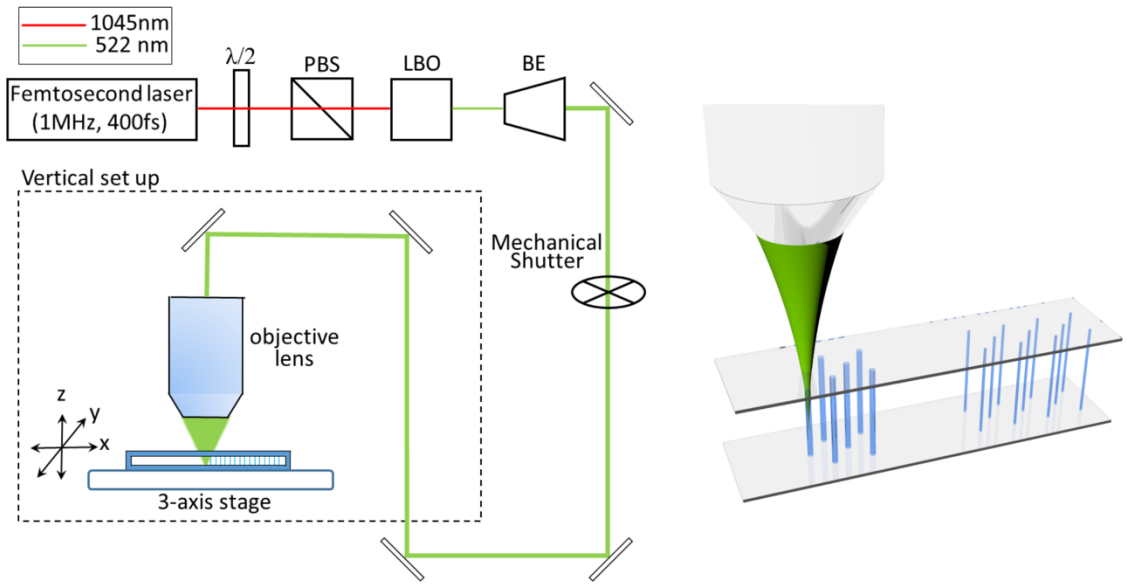

Figure 4.2. Schematic of fiber fabrication system for filamentous matrices by femtosecond laser

4.3.3 3D high aspect ratio structure fabrication with femtosecond laser pulse

4.3.3.1 Fiber structure fabrication

The filamentous matrices were fabricated by two-photon polymerization (2PP) of photo-curable organic-inorganic hybrid polymer (ORMOCLEAR® (Micro resist technology)). Individual fiber was fabricated after filling of by ORMOCLEAR® into glass scaffold the single laser radiation to the uncured ORMOCLEAR® through a high repetition rate femtosecond laser. Fiber diameter was determined by the laser power and exposure duration, which was controlled through mechanical shutter. 5 μm fibers were fabricated by 3.7 mW laser irradiation for 0.9 seconds, whereas 10 μm fibers were fabricated by 5.2 mW for 2 seconds. Fiber spacing was controllable by a 3D axis motorized stage with high precision of positioning (Aerotech, ANT95-XY-MP and ANT95-50-L-Z-RH). To fabricate several matrices within one set, we shut the laser irradiation during the movement from end point of previous fibrous matrix to the start point of next matrix. After fiber fabrication process, samples were hard-baked at 110°C for 30 mins, and developed for 1 hours with a mixture of 2-Isopropyl alcohol and 4-Methyl-2-pentanone with ratio 1:1. After developing process, samples were rinsed with 2-Isopropyl alcohol and distilled water several times subsequently, and dipped in 70% ethanol for sterilization.

4.3.3.2 High aspect ratio tube fabrication

The tubular structures with high aspect ratio were also fabricated by two-photon polymerization (2PP) of photo-curable organic-inorganic hybrid polymer (ORMOCLEAR® (Micro resist technology)). For the visualization for tube formation, we used the similar glass scaffold with 1-mm thickness spacer. Each tube structures were able to fabricated by the rotation with circular trajectory (x-y direction) with 1mm/s scanning speed. After one-layer fabrication, stage was moved to z-direction for next layer fabrication. At starting point, laser beam focused at the interface between glass coverslip and ORMOCLEAR® with 5x objective lens (Mitutoyo M Plan Apo, NA= 0.14). Spacing of high-aspect ratio tube was controllable by a 3D axis motorized stage with high precision of positioning (Aerotech, ANT95-XY-MP and ANT95-50-L-Z-RH). After tube fabrication process, samples were hard-baked at 110°C for 30 mins, and developed for 1 hours with a mixture of 2-Isopropyl alcohol and 4-Methyl-2-pentanone with ratio 1:1. After developing process, samples were rinsed with 2-Isopropyl alcohol and distilled water several times subsequently, and dipped in 70% ethanol for sterilization.

4.3.4 Cell culture and imaging

4.3.4.1 Cardiac differentiation from iPS cells

The CM cell types (WT, LQT3, hiPS, TALEN-engineered isogenic hiPS cells with Ca^{2+} reporter (GCaMP6f) and loss-of-function of cardiac isoform of myosin binding protein C (MYBPC3)) were obtained from Dr. Conklin's lab at the Gladstone Institute of Cardiovascular Research. A small molecule WNT-mediated protocol was used to derive iPS-CMs. Briefly, iPS cells were maintained on 6-well plates coated with Matrigel in mTeSR1 medium. On Day 3, cells were dissociated with Accutase (Invitrogen) for 5 min at 37°C and seeded onto Matrigel-coated cell culture plates at 25,000 cells/cm^2 in mTeSR1 containing 10 μM Y-27632. After 24 h later of cell seeding, the medium was changed to mTeSR1 without Y-27632. Cells were maintained in mTeSR1 for additional 2 days. On Day 0, cells were treated with 12 μM of a GSK3 inhibitor in RPMI 1640 medium containing B27 supplement without insulin for 24 h. The medium was changed on Day 1 to RPMI/B27-I and incubated for 48 hours, followed by a 48 hours treatment with 5 μM of an inhibitor of WNT production beginning on Day 3. On Day 5, the medium was changed to RPMI/B27-I for two days, and then changed to RPMI 1640 containing B27 complete supplement (RPMI/B27-C) on Day 7.

4.3.4.2 Isogenic heterozygous GCaMP5f hiPS-CMs

The isogenic heterozygous GCaMP6f knockin (KI) hiPS cell line was generated by inserting GCaMP6f open reading frame into AAVS1 locus under the control of CAG promoter and a puromycin resistance gene. The isogenic homozygous MYBPC3 knockout (KO) hiPS cell line was generated by inserting an artificial early stop codon into exon 1 of MYBPC3, which resulted in early transcript termination. Stable clones were selected using Puromycin (0.5 μg/ml) and screened via mCherry fluorescence. The

iPS cells were maintained on 6-well plates coated with growth factor reduced Matrigel in Essential 8 (E8) media (Life Technologies)[50, 51]

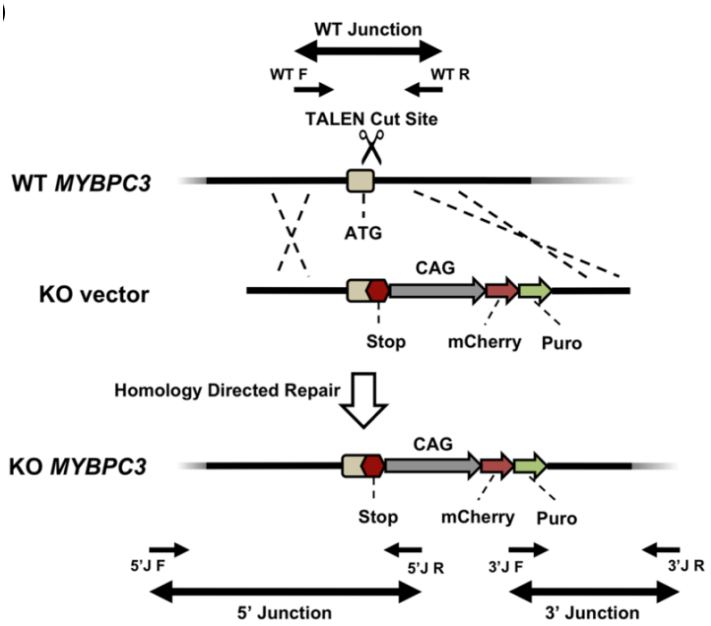

Figure 4.3. The schematics showed generation of MYBPC3 knockout hiPS cell line from WT through TALEN-mediated genome editing method

hiPS cells were plated at a density of 1.25-5×10^4 cells/cm^2 onto Matrigel coated 12-well plates in E8 with 10 μM Y-27632. hiPS cells were maintained in E8 for additional 2 days, and then started the differentiation "Day 0" with one treatment of 10 μM WNT agonist CHIR99021 (CHIR, Stemgent) in RPMI 1640 media containing B27 supplement without insulin (RPMI/B27-I). After 24 hour CHIR treatment, the cells were maintained in RPMI/B27-I media for one day, and then treated with 5 μM WNT inhibitor IWP-4 (Stemgent) in RPMI/B27-I media for two days. Subsequently, on Day 5, the media was exchanged to RPMI/B27-I for two days and replaced with RPMI 1640 media containing B27 complete supplement (RPMI/B27+C) on Day 7 for the continuous culturing.

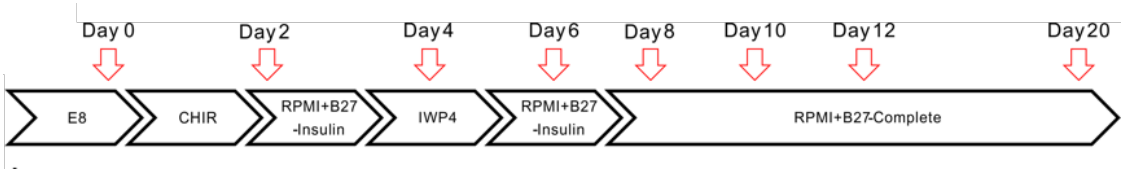

Figure 4.4. Characterization of hiPS-CMs differentiation. The cardiac differentiation was characterized at eight different stages from Day 0 to Day 20

4.3.4.3 Generation of 3D cardiac tissue

Each filamentous matrix was placed into one well of a 6-well plate. The matrices were rinsed with Dulbecco's phosphate buffered saline (DPBS) several times to remove the 70% ethanol which used for sterilization, and coated with 50 mg/mL fibronectin in DPBS for 1 h. The matrices were rinsed with DPBS several times before loading the cells.
Sheets of beating CMs were dissociated using a singularizing protocol. It included incubation with 1 mg/mL collagenase II with 40 Unit/mL DNase I in Hank's balanced salt solution (HBSS) for 1 h and followed by 0.25% trypsin/EDTA treatment for 5 min at 37°C. The cells were collected, pelleted and re-suspended in EB20 media (Knockout DMEM supplemented with 20% fetal bovine serum (FBS), 2 mM L-glutamine, 1 MEM non-essential amino acids (MEM-NEAA), 400 nM 2-mercaptoethanol and 10μM Y-27632). 500 μL cell suspension with a density of 1 million cells/mL was pipetted over each fibrous scaffold matrix. After 2 hours of cell seeding, another 4 mL EB20 media was added into each well to cover the whole matrix. The media was switched to RPMI/B27-C the next day to reduce the non-CMs overgrowth and changed every 2 days. Cryopreserved hiPS-CMs were thawed into EB20 media and plated onto Matrigel-coated 6-well plate with RPMI/B27+C media supplemented with 10 μM Y-27632. After 4 days recovery in RPMI/B27+C media, the cells were singularized by 0.25% trypsin/EDTA, quenched with EB20 media (over x2 quantity), and seeded into filamentous matrices with 1.5 million cells/scaffold in 500 μL RPMI/B27+C media supplemented with 10 μM Y-27632. After four hours, another 4 mL RPMI/B27+C media supplemented with 10 μM Y-27632 was added into each well to cover the whole set of filamentous matrices. The media was switched to RPMI/B27+C media on next day and changed every 2 days. To enrich hiPS-CMs upto 80% of total cell population, on day 15, sheet-beating hiPS-CMs were singularized by treatment of collagenase I in Hanks' balanced salt solution (HBSS) for 45 min and a following 0.25% trypsin treatment for 2 min, and quenched with EB20 media (Knockout DMEM media supplemented with 20% fetal bovine serum (FBS), 1X L-glutamine, 1X MEM non-essential amino acids (MEM-NEAA), 400 nM 2-mercaptoethanol, and 10 μM Y-27632), and re-plated onto Matrigel-coated 6-well plates in RPMI/B27+C media. After 2 days recovery in RPMI/B27+C media, cells were treated with glucose depleted DMEM media supplemented with 4 mM lactate for 2 days. Purified hiPS-CM were cryopreserved in mixture of 90% FBS containing 10% Dimethylsurfoxide (DMSO) and 10 μM Y-27632 with cell density of 2 million cells per mL.

4.3.5 Calcium flux recording

For calcium imaging, GCaMP6f hiPS-CMs were differentiated, purified, cryopreserved and seeded into the 2PP filamentous matrices for continuous calcium imaging for 20 days. The calcium flux images were recorded at 40 fps for 10 seconds using a Nikon Eclipse TS100F microscope and Hamamatsu ORCA-Flash4.0 V2 digital CMOS camera.

4.3.6 Fiber characterization

The fiber stiffness is represented as the effective elastic modulus (E_f) of the fiber, which can be measured by atomic force microscopy (AFM, XE-100, Park Systems) with tip-less AFM cantilevers (TL-CONT-SPL and TL-FM-SPL, Nanosensors). The shape of fiber is assumed to be a cylinder with circular cross-section, and the elastic modulus of the fiber can be calculated by :

$$E_f = \frac{64K_c d_c {l_f}^3}{3\pi {D_f}^4 (d_f - d_c)}$$

where l_f is the fiber length, D_f is the fiber diameter, d_c is the displacement of the tipless AFM cantilever, and d_f is the relative deflection of the fiber. The spring constants (K_c) of tip-less AFM cantilevers were determined using the thermal tune method and calculated using AFM software (XEI, Park system) to be as 0.0636 N/m using AFM software. Finally, Young's modulus of the fibers were calculated as 183.9 ± 11.7 MPa[165].

4.3.7 Finite element modeling

Finite element modeling for force-induced beam deflection was performed using COMSOL for both 5 μm and 10 μm-thickness fibers with length of 500 μm. Fibers were modeled with Young's modulus of 183.9 MPa based on the AFM measurement (Section 4.3.6), and discretized into hexahedral mesh elements. Two ends of fiber were assigned with fixed boundary condition, and the other area was assigned with free boundary condition. The distributed contraction forces (1 μN for 5 μm diameter and 10 μN for 10 μm diameter fibers) were applied perpendicularly to fiber axis with length of 200 μm to the center of the fibers. The maximal stresses were calculated based on maximal deflection of the fiber at the maximal contraction of the cardiac micro-tissues.

4.3.8 Quantitative analysis for contraction force on the fibrous structure

To calculate the contraction forces of the whole cardiac tissue, we made three assumptions:

Assumption 1 : Forces evenly distribute across the tissue cross-section (tissue width (W) multiplying tissue thickness (T))
Assumption 2 : All force vectors are parallel each other and perpendicular to the fiber axis
Assumption 3 : Cross-section of fiber is circular.

Based on those assumptions, we integrated the distributed forces (f_{dist}) along the fiber and consider a point force at the position of maximal fiber deflection, so that we could calculate the individual fiber point force (F_{point}) based on the beam deflection theory. Using the series of successive images recorded for cardiac tissue beating, we can measure the fiber deflection (δ_f), tissue thickness and its applied force position (a_f) between two consecutive images, so that we can calculate the point force (F_{point}) applying to the fibers based on the equation with Young's modulus (E_f), length (L_f) and diameter (D_f) of the fiber.

$$F_{point} = \frac{3\pi E_f {D_f}^4 \left(2a_f + L_f\right)^2}{128{a_f}^3 \left(L_f - a_f\right)^2} \delta_f$$

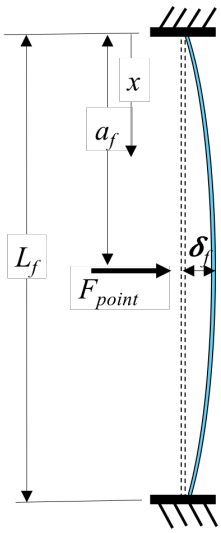

Figure 4.5. The schematics of the individual fiber point force calculation based on fiber deflection

Then, we can calculate the distributed force (f_{dist}) by dividing the point force (F_{point}) by the area of the force applying to the fiber (tissue width (W) multiplying tissue thickness (T)=W·T). Integrating the distributed force across entire tissue cross-section, we can calculate the total force generated by the cardiac microtissues (F_{tissue}). The static force was calculated based on the preload fiber defection (measured with the diastolic cardiac tissue in the resting state), and the contraction force was calculated based on the afterload

fiber defection that was measured with systolic cardiac tissue at maximal contraction (Figure 4.6).

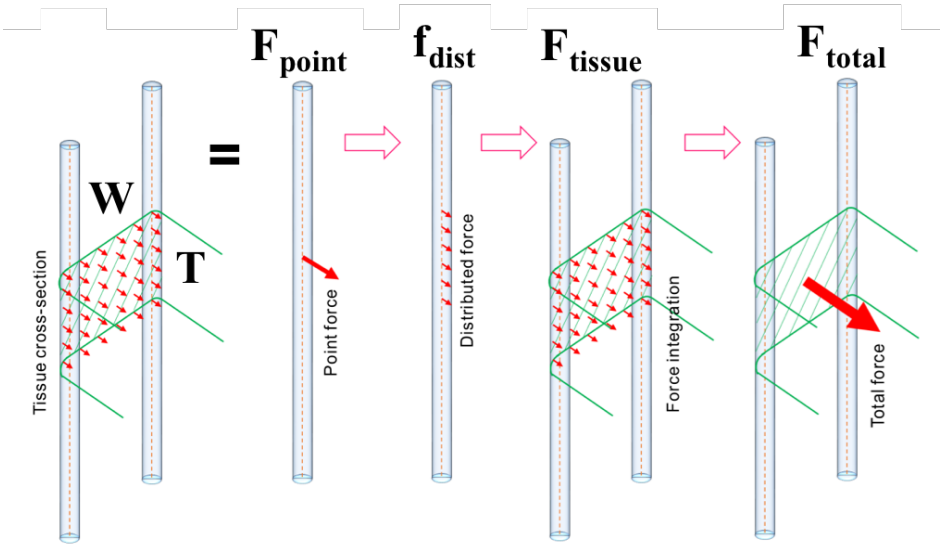

Figure 4.6. The schematics of the total force (F_{total}) calculation based on the assumption that force are evenly distributed throughout the tissue cross-section

4.3.9 Motion tracking analysis

We recorded the cardiac tissue beating at 100 fps for 10 seconds using a Nikon Eclipse TS100F microscope with temperature-controlled stage and Hamamatsu ORCA-Flash4.0 V2 digital CMOS camera. Videos of beating cardiac microtissues on both 2D culture dish and 3D filamentous matrices were exported as a series of single-frame image files and analyzed using in-house developed motion-tracking MATLAB software. The software can automatically output the motion heatmap and contraction waveform for calculation of beat rate and maximal contraction velocity[50, 51, 166, 167].

4.3.10 Immunostainning and microscopy

Cells were characterized using immunostaining and fluorescent microscopy. Samples were fixed with 4% (vol/vol) paraformaldehyde (PFA) for 15 min, permeabilized with 0.2% Triton-X-100 for 5 min, and blocked with 2% BSA, 4% goat serum and 0.1% Triton-X-100 for 30 min. The samples were then incubated with primary antibodies for 2

h and secondary antibodies for 1.5 h. DAPI was used to stain cell nuclei in monolayer cell culture and To-Pro-3 was used for filamentous matrices. Because fiber material was auto-fluorescent under UV excitation, to differentiate the nucleus and fiber, we used the different immunostaining material (To-Pro-3). For bright-field and epi-fluorescent microscopy, the images were taken using a Nikon Eclipse TS100F microscope with Hamamatsu ORCA-Flash4.0 V2 digital CMOS camera. For confocal microscopy, the images were taken with a Zeiss LSM710 laser-scanning microscope.

4.3.11 Flow cytometry analysis

The pluripotency of iPS cells and efficiency of cardiac differentiation was evaluated using flow cytometry. The iPS cells were dissociated with Accutase and stained using a human pluripotent stem cell multicolor flow cytometry kit against Oct4, SSEA4, and Sox2 (R&D system). hiPS-CMs were dissociated using the singularized with 0.25% trypsin/EDTA for 5 minutes and quenched with EB20 media. After washing with DPBS several times, fixed with PFA for 15 min, and incubated with primary antibody (mouse monoclonal cardiac Troponin T, Thermo Scientific) and secondary antibody (Alexa488, Life Technologies) for 30 min each in wash/permeabilizatin buffer. Flow cytometry analysis of cardiac troponin T (cTnT) showed the increase of cTnT+ cells starting from Day 6 to the final puritiy of CM ranging from 50% to 70%. The gene expression profiling confirmed the cell fate transiting from pluripotency, to mesodermal cells, to cardiac progenitors and finally to CMs. The monolayer sheet of hiPS-CMs vigorously beat in the tissue culture plates, and contraction motion could be monitored and analyzed by the motion-tracking software. The hiPS-CMs expressed cardiac specific sarcomere markers (α-actinin and myosin heavy chain) and junctional markers (connexin43 and N-cadherin). The labeled cells were analyzed by Guava easyCyte® Flow Cytometer (EMD Millipore).

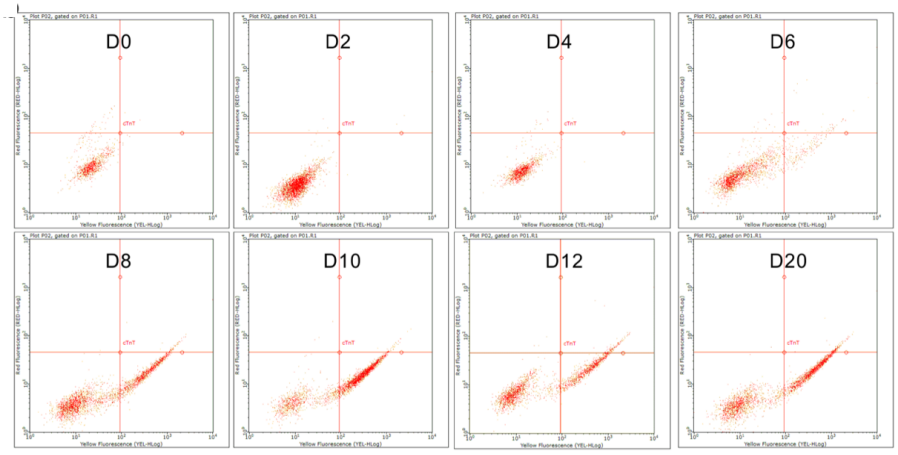

Figure 4.7. The flow cytometry analysis showed that cardiac differentiation started to produce cTnT+ cells from Day 6.

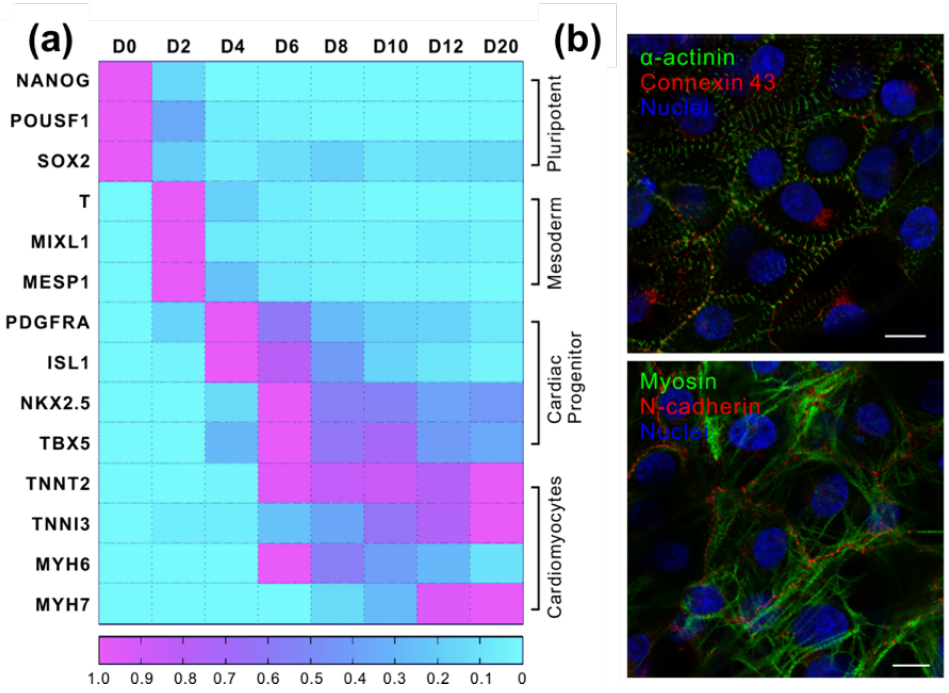

Figure 4.8. (a) The gene expression profiling showed cell fate transition from pluripotent stem cells to mesoderm, to cardiac progenitor, and finally to CMs (n = 4). (b) hiPS-CMs expressed cardiac specific sarcomere markers (α-actinin and myosin heavy chain) and junctional markers (connexin43 and N-cadherin). (Scale bar : 10 μm)

4.3.12 RT-qPCR analysis

The expression level of cardiac specific genes was analyzed using RT-qPCR at Day 12. Adherent cells were washed with DPBS and homogenized with 1 mL TRIzol LS reagent. Total RNA was collected and purified using RNeasy Mini Kit (Qiagen). The total RNA concentration was quantified using a Nanodrop and integrity was determined using the Agilent BioAnalyzer. Conversion of total RNA to cDNA was carried out using SuperScript III Reverse Transcriptase with random primers. qPCR was performed on the Applied Biosystems StepOnePlus instrument with customized target arrays in 96-well format, using 10 ng cDNA per reaction and SYBR Green ROX MasterMix (Qiagen). The data was analyzed using ΔC_t method relative to level of the housekeeping gene. The gene profiling was performed using RT-qPCR with customized target arrays for cardiac differentiation and commercial available TaqMan arrays for human NFAT & cardiac hypertrophy (ThermoFisher Scientific). To profile the transient gene expression during the cardiac differentiation, we normalized the expression of each gene at different days (Day 0-12) to the maximal expression of this gene during the differentiation process. To study the effect of mechanical environment on the gene expression for cardiac

hypertrophy between WT and MYBPC3 cardiac microtissues, we normalized the gene expression from the tissues growing on 10 μm fiber matrices to 5 μm fiber matrices.

4.3.13 hBNP production study

We used hBNP enzyme-linked immunosorbent assay (ELISA) kit (RayBiotech Inc.) to quantitatively measure hBNP level in the cell supernatants every 5 days for 20 days using a microplate reader SpectraMax i3 (Molecular Devices). The absorbance values of 10-20 days were normalized to the values of 5 days for both WT and MYBPC3 cardiac microtissues growing on 5 μm and 10 μm-thickness fiber matrices.

4.3.14 Quantification of sarcomere organization for iPS-CMs classification

A high-throughout, automated and quantitative analysis on sarcomere alignment was performed using an image-processing algorithm on 2D Fast Flourier transform (2D FFT). Well-aligned myofibrils in hiPS-CMs contain a spatially repeating pattern of sarcomere with a certain frequency. It can be extracted as a periodic signal by 2D FFT. Most of the energy in the frequency domain is present in the center of the image. The peak bands away from the center peak corresponding to the high-frequency data represented as the signal from aligned sarcomere. These high-frequency peak values can be extracted to calculate the 'Sarcomere Alignment Index', which is quantitative measurement of the level of sarcomere alignment.

4.3.14.1 Image processing for sarcomere alignment

Myofibrils in the iPS-CMs contain a spatially repeating pattern of sarcomeres having different orientations. Different classes of iPS-CMs have different spatial organization of sarcomere. For novel automated classification of iPS-CMs, the basic formulation (2D fast Fourier transform) for quantification of sarcomere alignment is used. Analysis based on the Fourier transform is an effective tool to analyze the repeating pattern of sarcomere organization. Fourier transform of a periodic signal results in peaky (impulse) functions centered at integer multiples of corresponding base frequency in the frequency domain. Similarly, 2D Fourier transform represents images, which is a linear sum of sinusoidal waveforms of different spatial frequencies and orientations. 2D discrete Fourier transform of a digital image $f(m,n)$ can be describe as

$$f(m,n) = \sum_{u=0}^{u=(M-1)} \sum_{v=0}^{v=(N-1)} F(u,v) e^{2\pi i\left(\frac{mu}{M}+\frac{nv}{N}\right)}$$

$$f(u,v) = \sum_{m=0}^{m=(M-1)} \sum_{n=0}^{n=(N-1)} F(m,n) e^{-2\pi i\left(\frac{mu}{M}+\frac{nv}{N}\right)}$$

represents the image as a sum of 2D spatial frequency components, where the Fourier transform component($F(u,v)$) indicates the strength of the 2D spatial frequency pattern (u, v) in the image. For calculation FFT2 function of MATLAB (2D Fast Fourier Transform) was used. The value at the origin corresponds to the cell image average. The other dominant frequencies along the radial direction correspond to the integer multiples of the spatial frequency signature of the periodic striations. This is equal to the inverse of the distance between two sarcomeres. Angular spread is determined by the directional variations of the sarcomeres pattern and the shape of the iPS-CM.

4.3.14.2 iPS-CM score for sarcomere organization quantification

All of radial profiles have a predominant radially decaying background component. The main difference is in the number of peaks and their strengths above the background decay. To extract and quantify those distinguishable features, the iPS-CM score was determined and calculated, following mathematical model for $y(r)$, the radial profile curve

$$y(r) = \left[a + \left(b \times e^{-r/R}\right)\right] + \sum_{i=1}^{M} w_i \times f(r - i \times p) + n(r)$$

where ($a, b, R, p, M\ and\ w_i$, $i = 1 \ldots M$) are the unknown model parameters. The first two terms in the equation shows the exponential decay for increasing radial frequency r (aperiodic component). The third term is a sum of unknown positive number (M), Gaussian-like functions $f(r - i \times p)$ whose centers/peaks are periodically spaced with p, unknown radial frequency spacing and with non-zero decreasing amplitudes (w_i , $i = 1\ to\ M$). The last term ($n(r)$) describes the residual model noise.

To quantify the parameters of this model, fitting the non-linear model to the data was used. However, there were too many parameters to obtain data fittings form the given data. To quantify the observed variation in the periodic pattern sarcomere organization and associate with their classification scale, identify the aforementioned peaks, corresponding to the periodic component of equation, and then to estimate the unknown number (M) and the amplitudes (w_i, $i = 1\ to\ M$) $of\ peaks$. For this, first of all, we need to estimate the aperiodic component of equation. After that we can subtract this to match up. Hence, we applied the Levenberg-Marquardt algorithm, which is one of the popular iterative and non-linear optimization algorithm, to estimate the unknown parameters (a, b, R) of the fist term (exponential decay). Upon convergence, the periodic component($\widetilde{y(r)}$) extracted as :

$$\widetilde{y(r)} = y(r) - \left[a + \left(b \times e^{-\frac{r}{R}}\right)\right] = \sum_{i=1}^{M} w_i \times f(r - i \times p) + n(r)$$

After this process, to identify the spatially separated local maxima and respective radial locations in periodic component, the local peak finding algorithm was applied, and excluding the high residuals around the frequency origin. As $w_i$values decrease for increasing i, the maximum peak value and location are set to w_2 and p respectively. Based on estimated p value and the other detected local peaks, M, the number of periods and their amplitudes w_i , $i = 2\ to\ M$ can be derived. Based on those results, the iPS-CM score is computed as

$$iPS - CM\ score = \sum_{i=1}^{M} w_i$$

along with the detected number of peaks (M) and angular spread at the peaks.

Angular spread is also computed at the peak radial locations as the median absolute difference (MAD) of the pixels on the corresponding circumferential contour. For fitting of cell shape, "regionprops" function in MATLAB was used which is based on the calculation of the major and minor axis of fitted ellipose shape.

4.3.15 Assessment of tissue formation

The formation of 3D cardiac tissue was assessed using fluorescent images from confocal microscopy. The cells penetrating the top layer and spreading on the middle layer (N_{CM})were counted by nuclei, and the total number of fibers (N_F) within the image was counted. Tissue formation was quantified as cells per fiber (N_{CM}/N_F).

4.3.16 Assessment of iPS-CM alignment

The CM alignments along the fiber direction was assessed with respect to the cell's elongation and orientation in fluorescent images from confocal microscopy. The cell nuclei were measured with transverse diameter (D_t) and conjugate diameter (D_c). The nuclei index representing the cell's elongation (ratio of D_c/D_t). The cell's orientation was measured with the acute angle between the fiber direction and nuclei transverse diameter as θ ($0° \leq \theta \leq 90°$). The alignment index relative to fiber long axis was calculated by $\cos\theta$.

4.3.17 Assessment of iPS-CM electrophysiology

The CM electrophysiology was assessed with an Multiple electrode array (MEA) system. The iPS-CMs on Day 15 were dissociated using the singularizing protocol described above and re-plated on an MEA chip with a density of 1 million cells/mL. The cells were cultured using RPMI/B27-C for 7 days before measurement start point. During the recording, the cells were maintained at 37°C in a sterile environment. The electrical waveform representing the field potential of CMs, and we can export the electrophysiological parameters such as beating frequency (BF), field potential duration (FPD) and field potential amplitude (FPA).

4.3.18 Assessment of iPS-CM contractility

The CM contractility was assessed based on the recorded video and motion tracking software. The video was taken at 30 fps and exported as image stacks for motion tracking analysis. The in-house developed motion tracking software (using MATLAB), based on block matching algorithms, was optimized for tracking CM beating events. This software can identify the contraction and relaxation events during the entire CM beating sequence and export the contractility parameters, including beating frequency (BF), maximal contraction velocity (MCV), maximal relaxation velocity (MRV), and beating duration (BD).

4.3.19 Statistical analysis

Data were presented as mean ± SD. For single comparisons, a two-sided student's t-test was used. For multiple comparisons, one-way analysis of variance was used with post-hoc Tukey tests. $p < 0.05$ was considered significant.

4.4 Results and discussion

4.4.1 Characterization of matrix fabrication

The filamentous matrices were fabricated using 2PP that produced scaffolds with accurately defined micro-/nanoscale features. Independent control of matrix parameters is essential for creating an enabling method capable of robust parametric analyses of the effect of each feature on CMs alignment and contractility. The design of filamentous matrices was divided into two classes as

Class 1 : Constant fiber spacing with varying fiber diameter (5 μm and 10 μm)
Class 2 : Constant fiber diameter with varying fiber spacing (25 μm, 50 μm and 75 μm)

Three layers of fibers were fabricated for each matrix to form a 3D structure. The filamentous matrices with different parameters were defined as "F/Diameter-Spacing". Based on previous studies, we concluded that the filamentous matrix with 500 μm fiber length in Y-direction, 50 μm fiber spacing in X-direction and 30 μm layer spacing in Z-direction generated 3D condensed cardiac microtissue (F/5-50) [51]. In this study, we fabricated multiple matrices units within one pair of glass scaffold by separating cohorts of fibers with matrix spacing (1 mm) in Y-axis. This design not only increased the throughput of result, but also made it easier to measure the fiber deflection by CM's contraction. Scanning electron microscopy (SEM) confirmed a matrix with parallel fibers, and the ability to control fiber diameter (*e.g.*, 5 μm and 10 μm) and spacing.

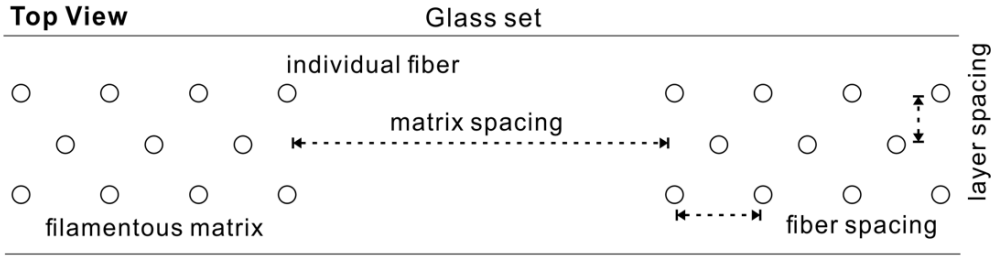

Figure 4.9. The schematic of one set of filamentous matrices with definitions of fiber spacing, layer spacing and matrix spacing

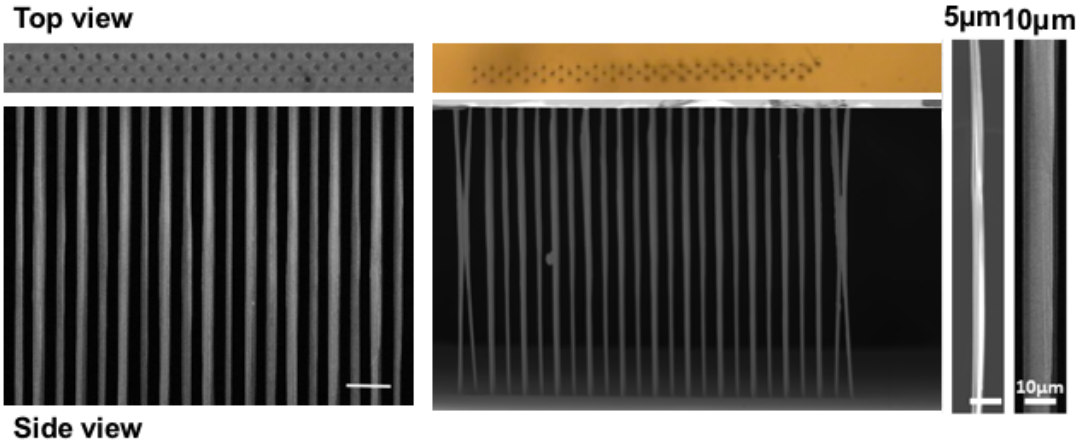

Figure 4.10. SEM images of a fabricated filamentous matrix and individual 5 μm and 10 μm fibers. (Scale bar : 50 μm (left) and 10 μm (right))

These synthetic fibers scaffolds serve as the backbone of the 3D cardiac tissue that mimic the perimysial collagen fibers of myocardium. Since their physical dimensions and mechanical properties of material correlate with CM alignment and contribute to myocardium nonlinear passive stiffness. Therefore, the fiber stiffness can mimic the tissue stiffness of the 3D cardiac tissue, and this serve as the passive mechanical stimulus to the CMs. Hence, mechanical properties such as stiffness has been considered as one of the critical and dominant factors in how the cellular microenvironment regulates cell's fate and function. It has been known that CMs were able to sense the local tissue stiffness through various cellular cytoskeleton system, and through mechanotransduction pathways alter their electrophysiology and contractility consequently by controlling the gene expression such as transcription and translation. By seeding and growing LQT3 iPS-CMs and WT iPS-CMs on F/5-50 and F/10-50 matrices, we found that beating iPS-CMs can easily bend the 5 μm fiber, but not the 10 μm fibers, and the iPS-CMs exhibited significantly more contractile motion on the F/5-50 matrices than that of on F/10-50 matrices. Interestingly, we observed that LQT3 iPS-CMs exhibited longer beat duration (BD) comparing to WT iPS-CMs only when they grow on the lower stiffness fibrous scaffold (5 μm-thickness fibrous structure), which suggested that variation of scaffold stiffness was required to facilitate monitoring of the genetic deficiency in LQT3 iPS-CMs. And it is also possible that scaffold stiffness itself plays a role in this etiology. Our work suggested that the 3D *in vivo*-like tissue structure (with physiological relevant stiffness) represented the significantly specific diseased phenotype and might be essential for generating an 3D *in vitro* model for understanding and studying the mechanism of cardiac diseases.

The differentiated sheet-beating CMs were dissociated and seeded directly onto the filamentous matrices. It took 3 days to form the 3D cardiac tissue on the fiber scaffold and restart the beating. The condensed and aligned cardiac tissue on the filamentous matrix was visualized with cytoskeletal staining for SM22. The CMs within the matrices were stained using an antibody against sarcomeric α-actinin specifically, imaged through

confocal microscopy. And Connexin 43 was found between CMs growing on the fibers. This ensure the electrical propagation though gap junction.

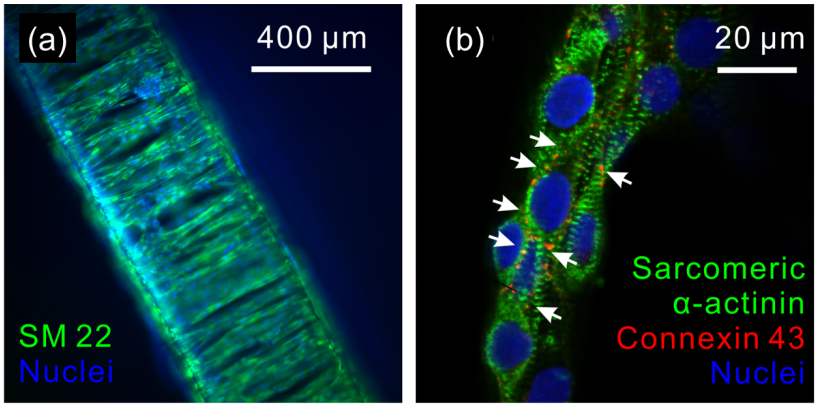

Figure. 4.11. Immunosfluoscence image of CMs on the fiber scaffold. (a) The entire 3D condensed cardiac tissue was visualized by staining SM22 (b) Confocal images of CMs aligned on one fiber showed the sarcomere structure stained by sarcomeric α-actinin and intercellular gap junctions stained by connexin 43, which ensured the electrical integration within the cardiac tissue (white arrow pointing to connexin 43 staining)

Confocal images of the middle layer of matrices were used to assess the 3D CM tissue formation and alignment on the different fiber diameters (5 μm and 10 μm) and spacing (25 μm, 50 μm and 75 μm). The tissue formation within matrices with 50 μm fiber spacing was significantly prominent than the other two types of matrices (25 μm and 75 μm). The smaller fiber spacing scaffold (25 μm) made it difficult for cells to penetrate from the top layer into inner layer to grow. Therefore, cells on these matrices spread as a 2D structure on the top fiber layer instead of 3D CM structure formation. In contrast, with the large fiber spacing scaffold (75 μm), the spacing was too large for cells to spread and connect to make bridge between adjacent CMs. As a result, the few cells grew inside the matrices and also failed to form condensed and connected tissue structure. Hence, the cells on F/5-50 and F/10-50 matrices were able to form highly connected tissue relative to the fiber backbone.

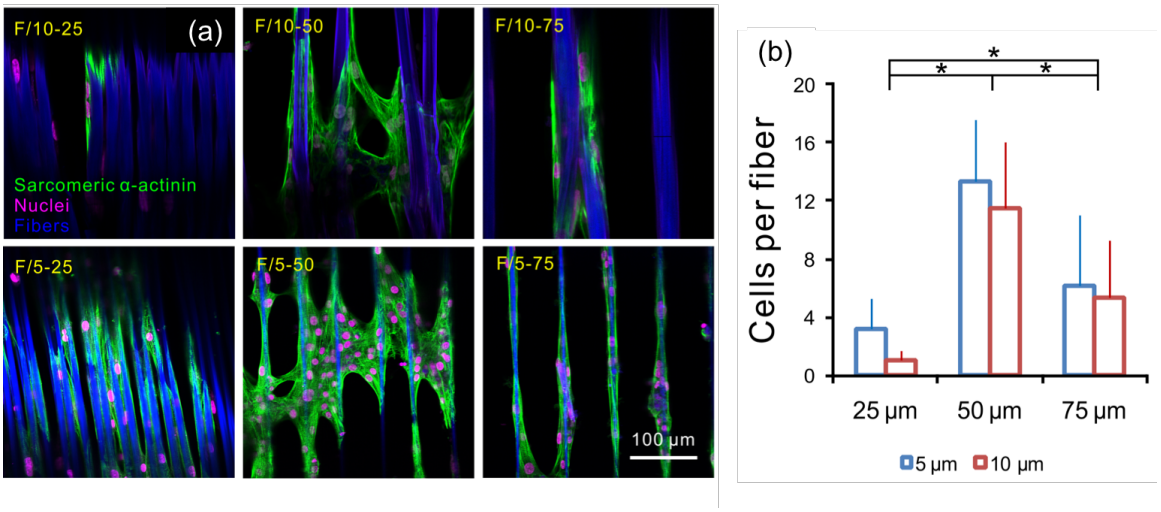

Figure 4.12. (a) The confocal images for LQT3 iPS-CMs growing on the middle layer of filamentous matrices and aligning along the fiber direction with different fiber diameters and spacing. The formation of 3D cardiac tissue was quantified by the cell number on the middle layer relative to the fiber number, and we found (b) matrices with 50 μm fiber spacing resulted in highest value of cell per fiber

3D tissue formation was quantified by cell per fiber, and CM alignment was measured as nuclei index and alignment index. CMs on the 75 μm spacing fibrous scaffold shows the largest nuclei index and alignment index. The nuclei index of CMs on the 50 μm spacing matrices was significantly larger than 25 μm spacing matrices. However, this was not true for alignment index. There was no significant difference between two fiber diameters with the same spacing.

On F/5-25 and F/10-25 matrices, due to the packing of CMs on the top layer, the alignment on the top layer was hampered. In constast, the cells that penetrated and grew on the middle layer were still able to align due to the parallel topographic feature of fibers. On the other hand, on F/5-75 and F/10-75 matrices, cells grew and elongated along single fibers, which resulted in the best cell alignment. Although F/5-75 and F/10-75 matrices had highest CM alignment, the wider spacing compromised 3D tissue formation.

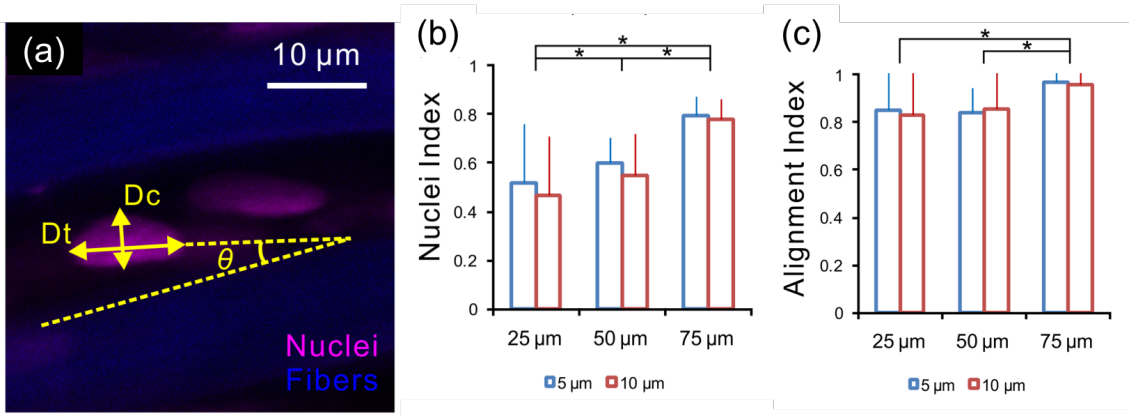

Figure 4.13. (a) Confocal images showed the cell nuclei within the filamentous matrix, and the parameters used for calculation of nuclei index and alignment index. The CM alignment was quantified by (b) nuclei index and (c) alignment index, and we found matrices with 75 μm fiber spacing resulted in highest value of CM alignment. (*p < 0.05)

According to all of those dates, 50 μm spacing matrices (F/5-50 and F/10-50) were used in the following experiments to determine the CM contractility and drug screening.

4.4.2 3D cardiac micro-tissue self-assembly and remodeling

We seeded hiPS-CMs (~1.5 million cells/scaffold) onto filamentous matrices without any external hydrogels. Generation of 3D cardiac microtissues required relatively purified hiPS-CM population and consistent cell handling procedures. As following the biochemical purification procedure, it can result in highly purified CM population (cTnT+ cells > 90%). However, previous studies on engineered cardiac microtissues suggested that it need for stromal cell population to enhance the connectivity of tissue and mechanical integrity. Instead of 4 days of treatment with purification media, we treated our cells for 2 days. This resulted in a mixed hiPS-CMs population (cTnT+ cells ~ 80%). After 6 days treatment of continual purification treatment, we could find that CM purity decreased. The hiPS-CMs growing on the filamentous matrices were able to self-assemble into 3D cardiac microtissues with approximately 60 μm-thickness, and maintained a stable beat rate after 5-days of culturing.

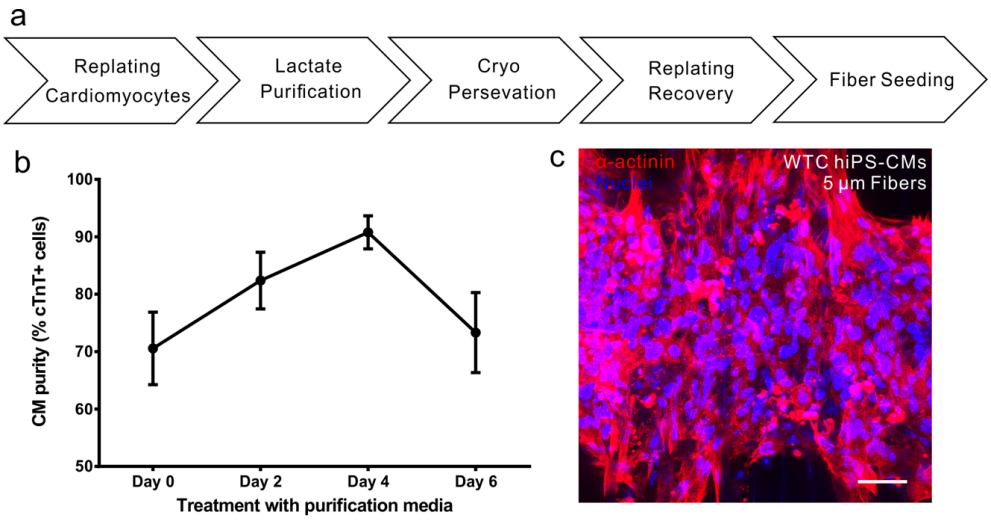

Figure 4.14. Generation of 3D cardiac microtissues on filamentous matrices. (a) The standard hiPS-CMs handling procedure to ensure defined cell population and consistent cell processing for generation of cardiac microtissues. (b) During the purification treatment, the CM purify (cTnT+ cells) increased from Day 0 to Day 4, but decreased at Day 6 (mean ± SD, $n = 4$). (c) The confocal fluorescent image showed a condensed cardiac tissue generated on a 5 μm-thickness fibrous matrix. (Scale bar : 50 μm)

4.4.3 Characterization of cardiac differentiation

The LQT3 and WT iPS cells were seeded as single cells and grown as a monolayer in defined mTeSR1 medium on Matrigel-coated 6-well plates. For the characterization of pluipotency, expression of Oct4, Sox2, and SSEA4 was confirmed by flow cytometry on both cell lines. The LQT3 iPS cells were further characterized by immunostaining with antibodies against Oct4, Nanog, and Sox2 one day after passage, which showed homogeneous expression of these pluripotent markers. Following the WNT-mediated differentiation protocol, the beating CMs were observed as early as Day 8 and developing CMs formed contracting sheets by Day 10.

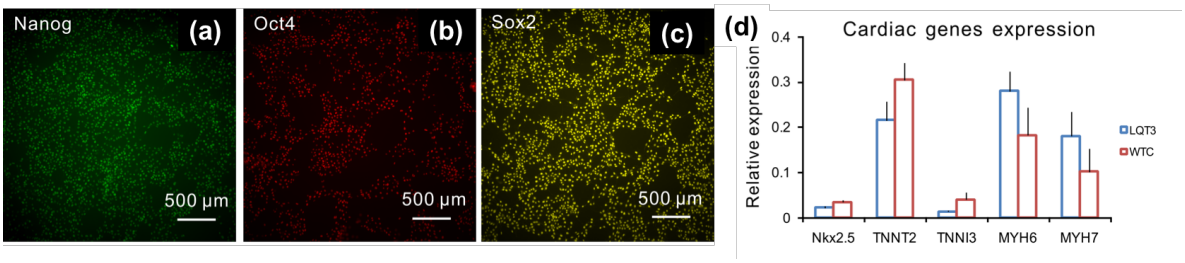

Figure 4.15. LQT3 iPS cells were characterized with immunostaining methods with antibodies against to (a) Nanog, (b) Oct4, (c) Sox2 and (d) Cardiac differentiation was characterized with RT-qPCR methods and showed upregulation of cardiac specific genes NKX2.5, TNNT2, TNNI3, MYH6, and MYH7 on both LQT3 and WT iPS-CMs at Day 12

According to RT-qPCR analysis at Day 12, it showed the upregulation of cardiac specific genes such as NKX2.5, TNNT2, TNNI3, MYH6, and MYH7 on both cell types (LQT3 and WT iPS-CMs). These sheet-beating CMs stained positive for sarcomeric α-actinin, cardiac Troponin T (cTnT), and β-myosin heavy chain (β-MHC).

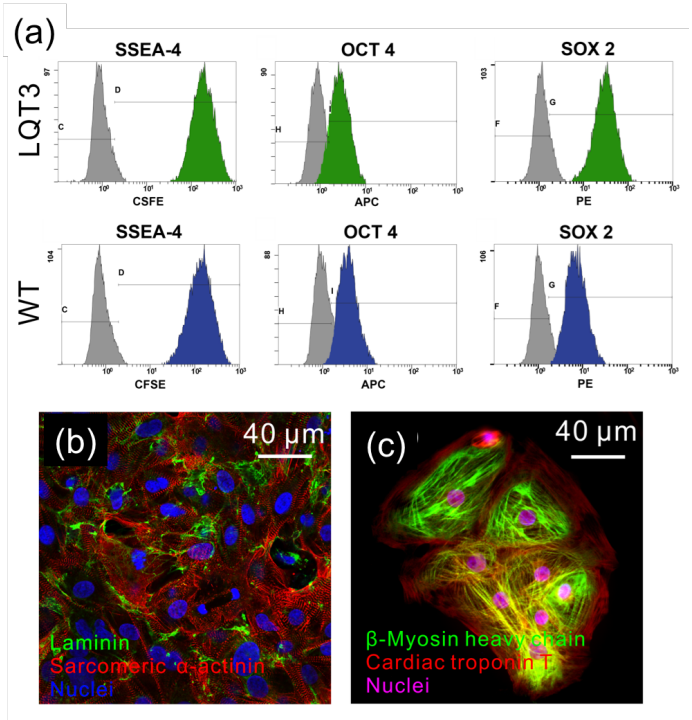

Figure 4.16. (a) Characterization of LQT3 and WT iPS cells with pluripotent markers SSEA4, Oct4 and Sox2 with flow cytometry method. The differentiated LQT3 iPS-CMs expressed cardiac specific markers: (b) sarcomeric α-actinin and (c) cardiac Troponin T (cTnT) and β-myosin heavy chain. The differentiation efficiency was characterized using flow cytometry method, and histogram

Flow cytometry with antibodies against cTnT demonstrated that the differentiation efficiency. Differentiation efficiency of LQT3 was about 90% and that of WTC was 75% CMs in the whole cell population.

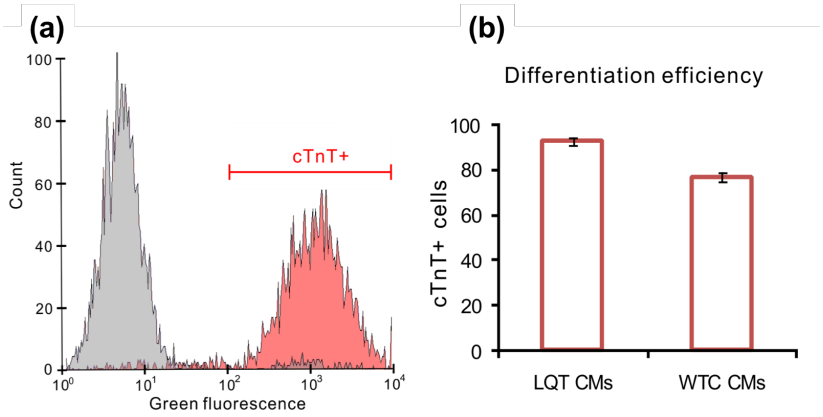

Figure 4.17. Differentiation efficiency (a) Selected cTnT+ population (red) represented the CMs relative to isotype control (gray), (b) We obtained about 90% purity for LQT3 iPS-CMs differentiation and 75% purity for WT iPS-CMs differentiation.

Using MEA analysis, LQT3 CMs exhibited prolongation of field potential duration compared to WT CMs, and this is equivalent to the longer QT interval in electrocardiography (ECG) measurement. Hence, LQT3 iPS-CMs can faithfully recapitulate the LQT3 electrophysiological abnormality *in vitro*.

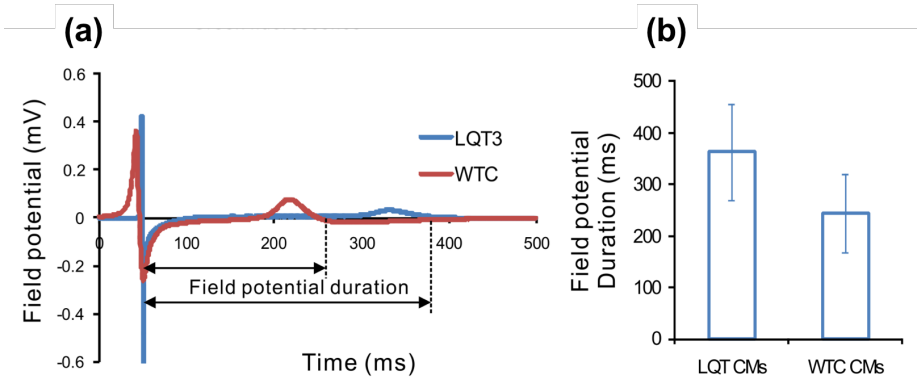

Figure 4.18. Field potential and field potential duration (a) The waveforms of field potentials measured using MEA system were plotted and showed elongated field potential duration (FPD) of LQT3 iPS-CMs comparing to WT iPS-CMs. (b) We found the average FPD for LQT3 iPS-CMs was 370 ms, whereas WT iPS-CMs was 250 ms

4.4.4 Effect of fiber stiffness on CM contractility

CM contractility of LQT3 iPS-CM on the F/5-50 matrix has been determined by simultaneously electrical measurement using the MEA system and motion-tracking analysis using bright-field microscopy image by video recording.
According to electrical waveform and the motion vectors, those were correlated to show that longer field potential duration (FPD) resulted in the longer entire contraction-relaxation duration. Heatmaps were plotted to visualize the spatial motion profile of CM beating on the filamentous matrix. The area with highest mean motion velocity was selected to plot the motion-tracking waveform.

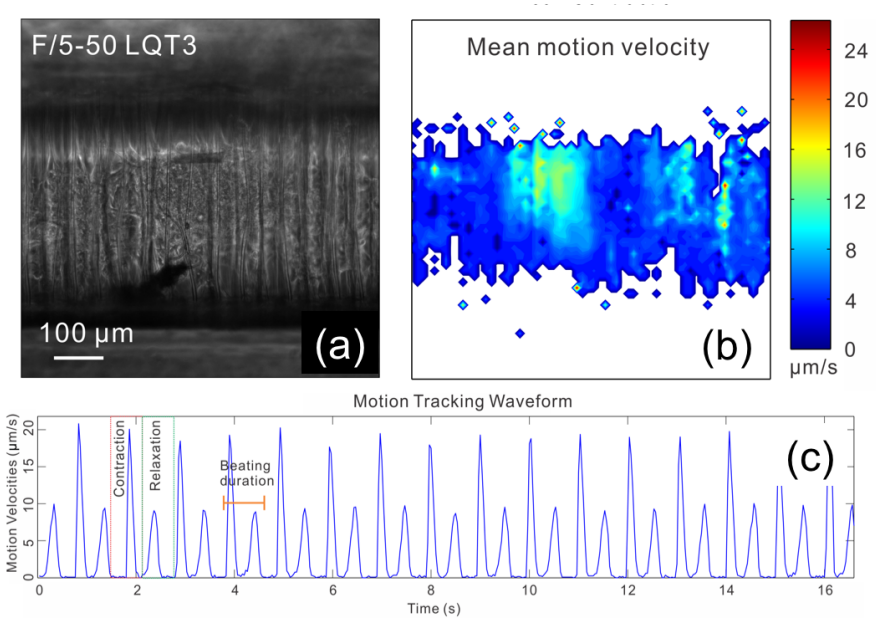

Figure 4.19. (a) LQT3 iPS-CMs grew as 3D condensed cardiac tissue on an F/5-50 filamentous matrix and were able to spontaneously beat, which was captured and analyzed by motion-tracking software. (b) The heatmap was plotted to show the area with highest mean motion velocity during the entire recorded video. (c) In the motion-tracking waveform, we can easily identify the contraction and relaxation during one CM beating and measure the beating duration

Using the waveform, we easily determined physiological properties such as the maximal contraction velocity (MCV), maximal relaxation velocity (MRV) and beating duration (BD). The features of CM contractility (MCV, MRV, and BD) of WT and LQT3 iPS-CMs were compared between two matrices with different fiber diameters (F/5-50 and F/10-50). Because of the different resistance of bending of the fibers with different thickness, the beating CMs were able to deform the fibers on F/5-50 matrices, but not on F/10-50 matrices. The MCV, MRV and BD of both cell types growing on F/5-50 matrices were larger than growing on F/10-50 matrices. LQT3 and WT iPS-CMs growing on F/10-50 showed no significant difference in contractility, but LQT3 iPS-CMs growing

on F/5-50 exhibited higher MCV and longer BD than that of WT iPS-CMs. Growing only on F/5-50 matrices, the LQT3 iPS-CMs exhibited contractility abnormality compared to WT iPS-CMs. Therefore, we used F/5-50 matrices in the following experiments to create tissue models from LQT3 iPS-CMs.

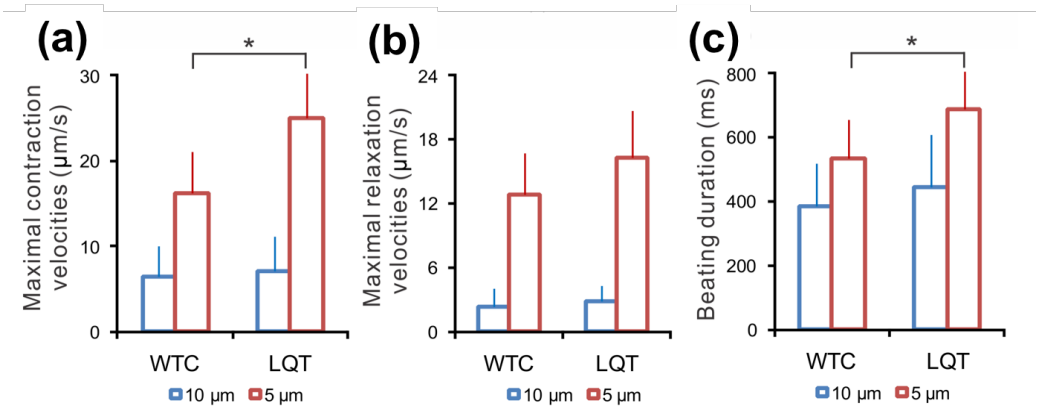

Figure 4.20. According to motion-tracking waveform, iPS-CMs on F/5-50 matrices had higher (D) MCV, (E) MRV, and (F) BD than the ones on F/10-50 matrices, and LQT3 iPS-CMs exhibited significant higher (D) MCV and (F) BD than WT iPS-CMs only on F/5-50 matrices. (*$p < 0.05$, N =10)

4.4.5 Tissue mechanical environment affected cardiac tissue functions

The cardiac microtissues continuously and progressively remodeled in the response to the passive mechanical resistance of the fibers, and active tissue contraction. To track the tissue remodeling associated with the change of functions, we measured physiological properties such as beat rate, contraction velocity, contraction force, and tissue width of the individual cardiac microtissues every 5 days. Since the individual fibers were fixed onto the glass slides at both ends, the contracting cardiac microtissues were only able to deflect the fibers in the X-direction (perpendicular to fibers), but not in Y-direction (parallel to fibers). Those mechanical constraints (fixed two ends and free surface of surfaces) resulted in the anisotropic contraction with higher contraction perpendicular to fiber axis (X-direction) than parallel to fiber axis (Y-direction), as defined by contraction heatmaps.

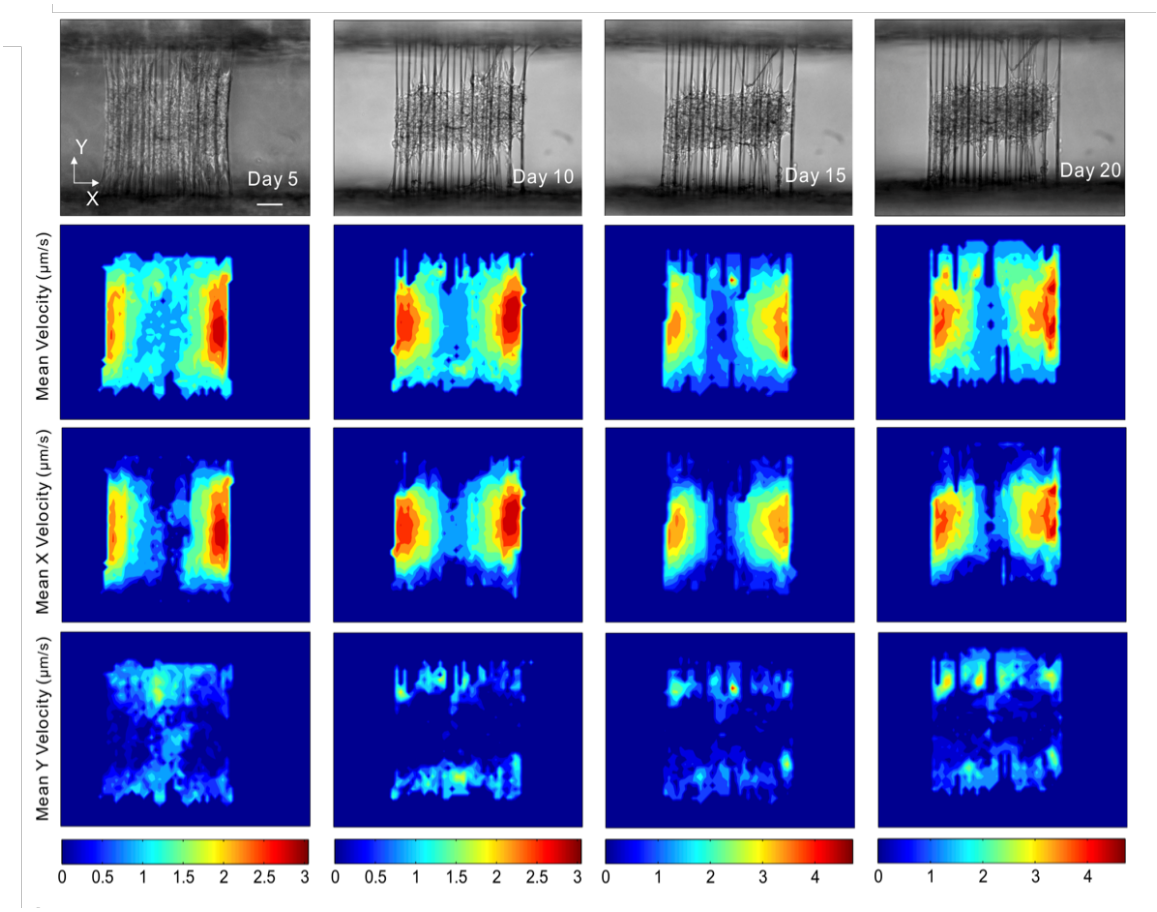

Figure 4.21. Cardiac microtissues remodeling on filamentous matrices. Cardiac microtissues growing on a 5 μm fiber matrix remodeled tissue shape Day 5-20. The contraction heatmaps showed anisotropic contraction with higher contraction in the X-direction comparing to the Y-direction (Scale bar : 100 μm)

We calculated the ratio of contraction velocity in the X and Y directions and found a significant increase from Day 5 to Day 20. And we also observed that the microtissues contracted along the Y-direction, but maintained the integrity along the X-direction. As a result, there was a significant decrease in the tissue cross-sections from Day 5 to Day 10-20. This suggested that the change in tissue shape occurred simultaneously with the re-orientation of the contraction directions. Hence, during the tissue remodeling, anisotropic contraction and tissue shape might mutually favor each other.

And we could change the fiber bending stiffness to modulate the mechanical resistance to the cardiac microtissues by changing the fiber thickness. Based on AFM calibration of our individual flexible fiber, we calculated the elastic modulus of the material as 183.9 ± 11.7 MPa, and this refers to the linear relation between required force for deformation of the fiber. Although the elastic modulus is the same for both fibers, the fiber mechanical bending resistance to the cardiac microtissue contraction, is proportional to the 4^{th} order of fiber diameter, thus 5 μm-thickness fibers are easier to be bent. We didn't observe a

significant difference in the beat rate of the cardiac microtissues on two different filamentous matrices (5 µm and 10 µm-thickness). However, beat rate slightly increased from Day 5-10 to Day 15-20. Since 5 µm-thickness fibers were easier to be bent, we found that higher maximal contraction velocity for cardiac microtissues growing on the 5 µm matrices compared to 10 µm matrices. As a results, those data suggested that modulating the mechanical/physical resistance of tissue microenvironment via changing fiber bending stiffness, it can alters the contractile function of cardiac microtissues.

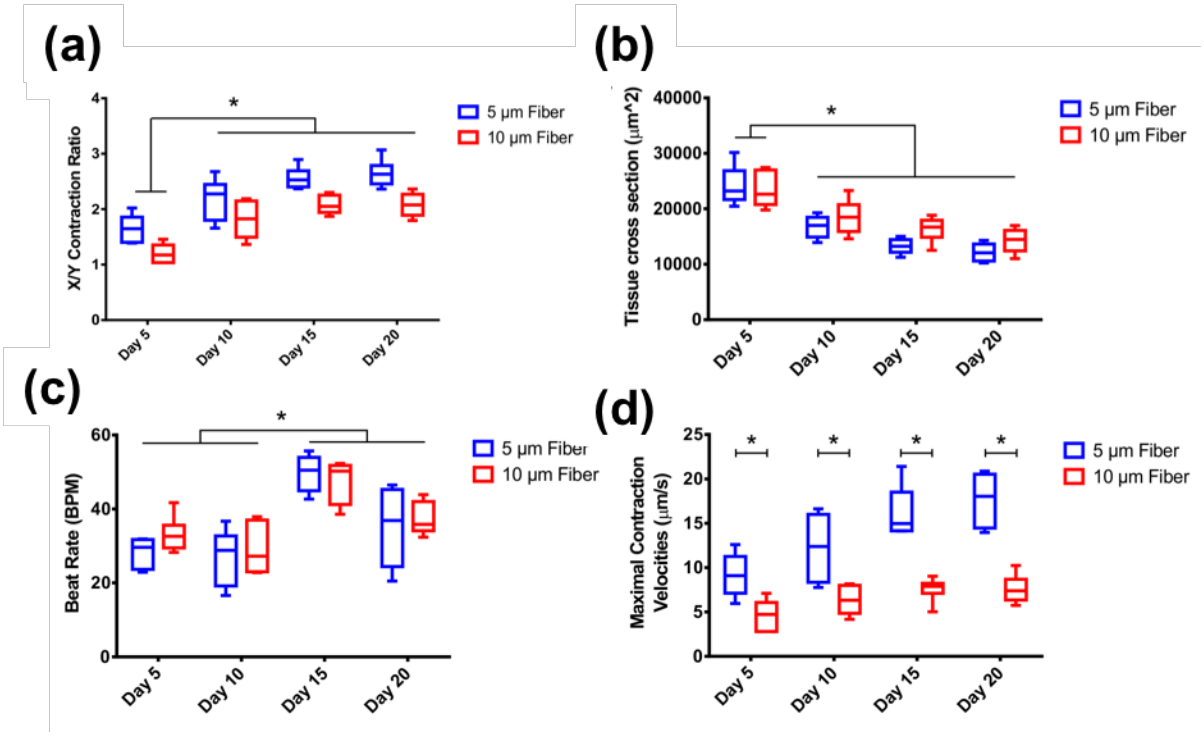

Figure 4.22. Cardiac microtissues remodeling on filamentous matrices. The progressive tissue remodeling manifested as (a) an increase of the ratio of mean contraction between X-axis and Y-axis and (b) a decrease of the tissue cross-section by comparing Day 5 to Day 10-20 (mean ± SD, n = 8). By investigating the effect of tissue mechanical environment on cardiac contractility, we found (c) no significant difference on beat rate (d), but much higher maximal contraction for the cardiac microtissues growing on 5 µm matrices than the ones on 10 µm matrices (mean ± SD, n = 8)

We used the deflection of individual fibers to calculate the contraction force of CMs. By assuming all the forces throughout the tissue cross-section were evenly distributed and parallel, we calculated the point force exerted on individual fiber based on the fiber deflection and force position (where the deflection locates) measured in a series of recorded images. Using this point force, we could also calculate the total force generated by the cardiac microtissues. Through contraction force calculations, we found that the cell's contraction force on 10 µm-thickness fiber scaffold was around 10-fold higher than that of 5 µm-thickness fiber. Therefore, artificially applying the forces at the center region of the fiber with 1 µN to a 5 µm fiber and 10 µN to a 10 µm fiber, we could

determine the stress generated on the fibers through COMSOL numerical simulation. High stress occurred at the center region of the fiber, where the force was applied to, and also occurred at the two ends of the fiber, where the fiber was fixed at the glass slides.

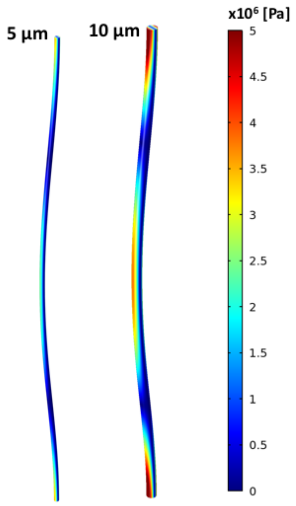

Figure 4.23. COMSOL simulation showed von Mises stress generated by applying 1 µN and 10 µN forces on individual 5 µm and 10 µm diameter fibers respectively

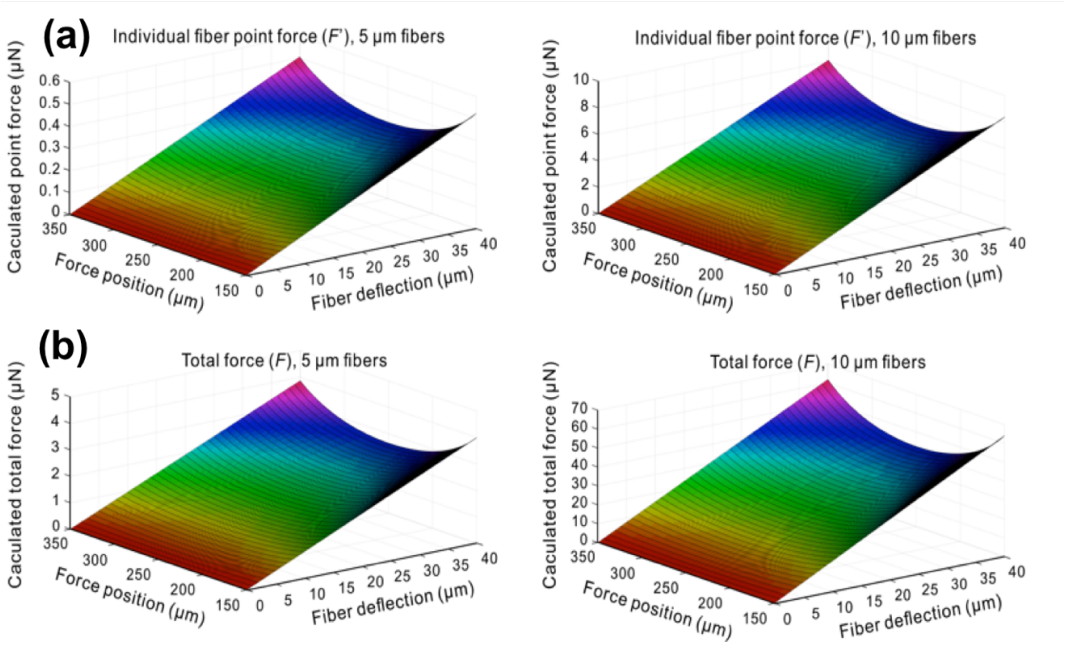

Figure 4.24. Theoretical analysis of force with position and deflection (a) Theoretical calculation of individual fiber force with different force positions and fiber deflections for individual 5 µm and 10 µm fibers. (b) Theoretical calculation of total force with different force positions and fiber deflections for 5 µm and 10 µm fiber matrices

When we took the cardiac microtissue image few days after cell seeding, it was possible to see the small deflection during the resting state. That is, we need to make sure the terms to characterize and analyze those phenomena.
Cardiac preload contraction is defined as end-diastolic myocardial wall tension. However, in this study, we refer to preload as the tension exerted by the fibers at two edges of the matrix to the diastolic cardiac microtissue in the resting state without any contraction force. And load opposing shortening of the ventricular muscles is termed cardiac afterload. However, in this study, the cardiac tissue afterload is defined as the fiber tension induced by the systolic cardiac microtissue at the maximal contraction. The afterload is considerably increased when the cardiac microtissues have to beat against stiffer fibers. Based on equation relation between the fiber deflections and force in the two-end fixed beam, we calculated the static forces (diastole) and contraction forces (systole) for the cardiac microtissues growing on both 5 µm and 10 µm-thickness filamentous matrices. The forces measured for the 10 µm-thickness filamentous structure showed a 10-fold increase in force compared to the forces measured for tissues on the 5 µm-thickness filamentous structures. This suggested that cardiac microtissues produced higher forces when growing on the matrices with high stiffness fibers (*i.e.* 10 µm-thickness filamentous matrices). We found that the static forces increased significantly from Day 5 to Day 20 for the cardiac microtissues growing on both 5 µm and 10 µm filamentous matrices, whereas the contraction forces increased significantly only when the tissues grew on the 10 µm matrices. Self-assembled WT hiPS-CMs on the 10 µm filamentous matrices were able to adapt to the high stiffness microenvironment and increase the contraction force through long-term mechanical conditioning

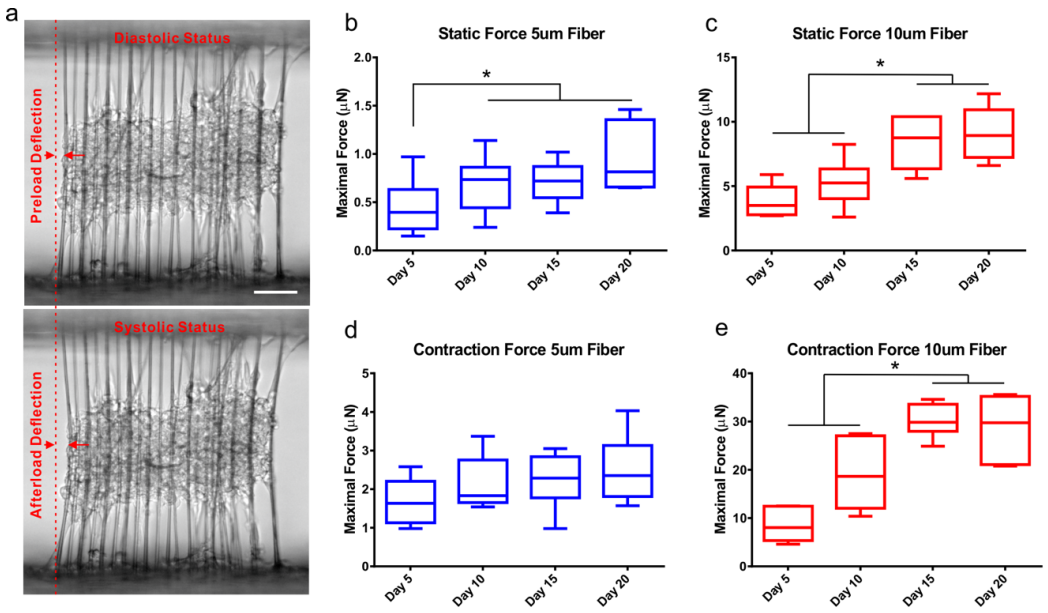

Figure 4.25. Force measurement based on fiber deflection. (a) The static force and contraction force were calculated based on preload deflection at diastolic status and afterload deflection at systolic status. The static forces increased during a long-term culturing for WT cardiac microtissues growing on both (b) 5 µm and (c) 10 µm matrices. (d) The contraction forces showed no significant increase for WT cardiac tissue on 5 µm fibers, (e) whereas the increase became significant for the tissue on 10-μm matrices (mean±SD, n=8)

4.4.6 Calcium flux of the cardiac microtissues

Current methodologies based on optical flow analysis do not directly allow for the quantitative assessment of electrophysiology. However, calcium flux during the beating is the key features of CM biology and physiology. traditional electrophysiological assessment such as sharp electrode invasion and usage of voltage sensitive dyes are not appropriate for long-term experiment and measurement due to their effect on the viability of the CMs. To consider this, we monitored spontaneous calcium flux in the cardiac microtissues formed by isogenic hiPS-CMs harboring the genetically-encoded Ca^{2+} reporter (GCaMP6f), which was inserted into the AAVS1 locus. High-speed imaging captured the fluorescent fluctuation of calcium flux from the GCaMP6f cardiac tissue growing on the filamentous matrices.

By tracking the contraction motion, fiber deflection, and GCaMP fluorescent signal and intensity from the same cardiac microtissue, we could characterize the temporal relationship among contraction velocity, force, and calcium flux simultaneously. According to the waveform of the calcium flux, we measured the calcium amplitude and full width half maximum (FWHM). Because, this is the important electrophysiological properties of the cardiac microtissues. We found that calcium amplitude significantly increased from Day 5 to Day 20, and this suggesting the cardiac microtissues could steadily increase (or enhance) the calcium flux level during a long period. This increase of calcium flux from the cardiac microtissues correlated with the increase of contraction force on stiffer fibrous structure with 10 μm-thickness. As a result, it is possible to conclude that excitation-contraction coupling was altered after the cardiac microtissues adapted to the mechanical/physical microenvironment. And we also observed that cardiac microtissues on 10 μm matrices showed higher calcium amplitude and longer calcium flux duration at the Day 15-20. These results suggested that the tissue mechanical environment not only directly affected the tissue mechanical outputs, such as contraction velocity and force, but also modulated the cardiac electrical properties through mechano-electrical feedback mechanisms.

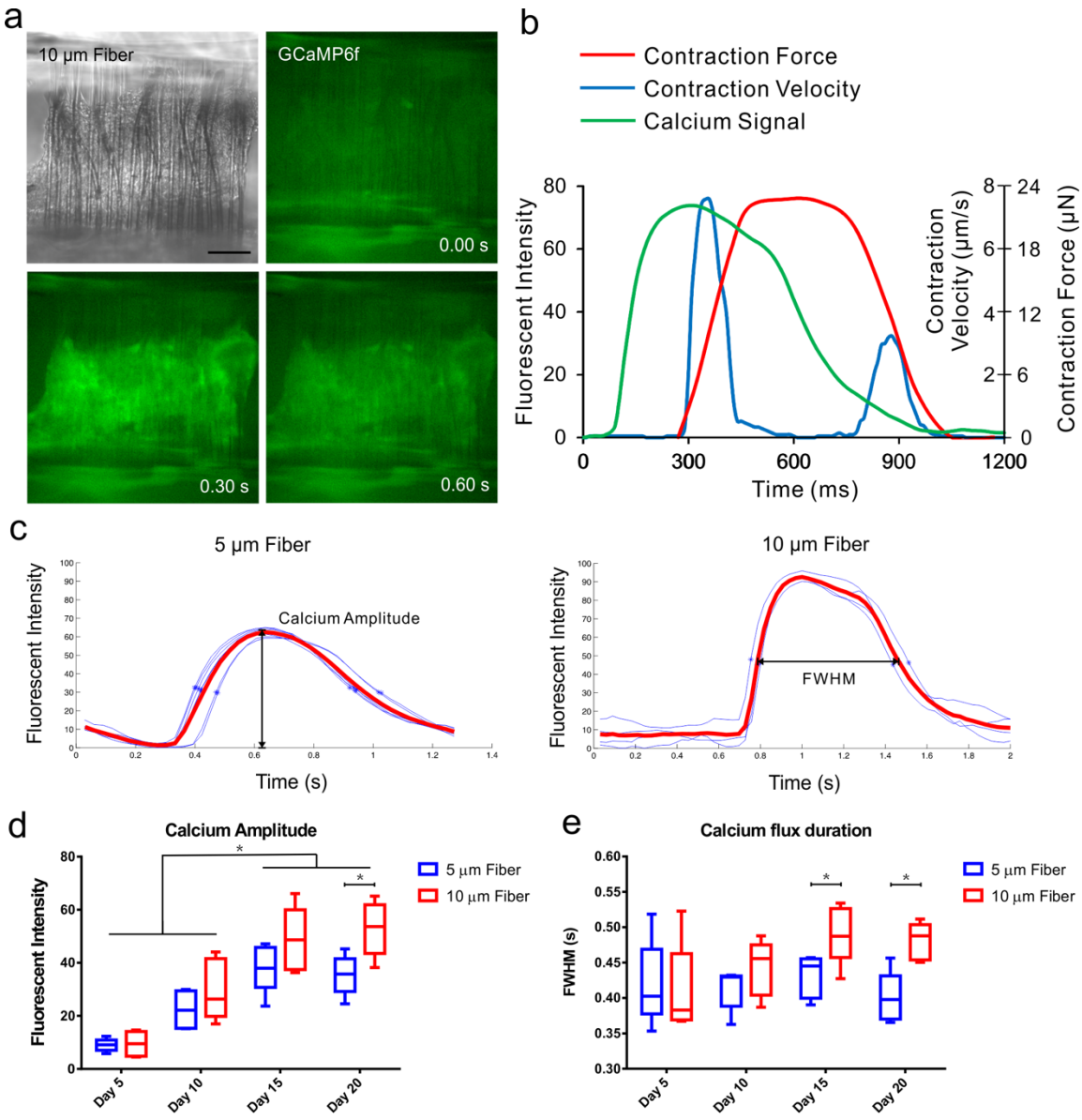

Figure 4.26. Calcium flux of the cardiac microtissues. (a) Growing GCaMP6f hiPS-CMs on 10 μm fiber matrices, we could record the fluorescence fluctuation of calcium flux with high-speed camera. (Scale bar :100 μm) (b) By tracking the contraction motion, fiber deflection and GCaMP fluorescent signal, we can characterize the temporal relationship among contraction velocity, force and calcium flux. (c) By plotting the calcium flux waveform, we could measure calcium amplitude and FWHM for the cardiac microtissues growing on 5 μm and 10 μm matrices. The cardiac microtissues on 10 μm matrices exhibited (d) higher calcium amplitude at Day 20 and (e) longer calcium flux duration at Day 15 & 20 than the ones on 5 μm matrices (mean ± SD, n = 8)

4.4.7 Tissue mechanical environment affected contractile deficits

To elucidate how mechanical load can affect the contraction deficits and pathological phenotypes, we harnessed recent advances in human iPS technology and gene-editing to create a human diseased cardiac tissue model with loss-of-function of the MYBPC3 gene. MYBPC3 is a thick filament associated protein, which play a principally structural role stabilization of the sarcomere sliding during contraction[139, 147-150]. This protein binds to myosin and actin, and regulate the probability of cross-bridge interactions. Eventually, this controls the rate of force development and relaxation in the cardiac muscles. Mutations in the MYBPC3 gene have been found to result in changes to not only the structure of the sarcomere, but also the structure of the heart that ultimately leads to hypertrophic cardiomyopathies (HCM). Our fiber-based cardiac tissue model can track the contractile functions of cardiac microtissues in a long-term culture, thus providing a unique platform to investigate the adverse effects of MYBPC3 gene knockout on the cardiac contraction at the tissue level.

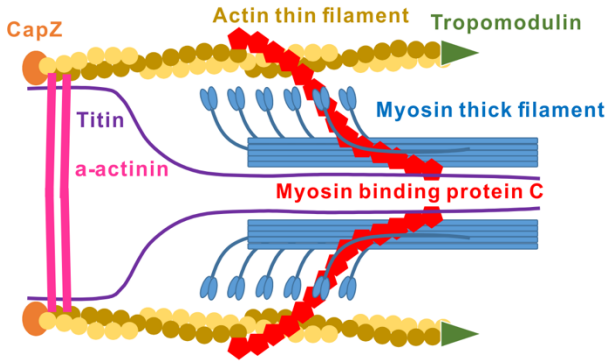

Figure 4.27. Generation of MYBPC3 cardiac microtissues. The schematics of MYBPC3 protein in one unit of myofibril showed this protein interacted with thin filament, thick filament and titin

The isogenic homozygous MYBPC3 knockout(KO) hiPS cell line was developed by TALEN (Transcription Activator Like Effector Nucleases)-mediated gene-editing method. MYBPC3 hiPS-CMs were differentiated and formed the 3D anisotropic cardiac microtissues on both 5 µm and 10 µm filamentous matrices. We compared the structural characteristics between WT and MYBPC3 cardiac microtissues on 5 µm and 10 µm diameter matrices. At Day 20, we found no significant differences on both tissue cross-section areas and sarcomere alignment indices from either two tissue types (WT and MYBPC3 hiPS-CM) or two matrix types (5 µm and 10 µm filamentous matrices). This suggest that MYBPC3 gene KO did not induce the tissue thickening and sarcomere disarray at the *in vitro* tissue level, which are common phenomena in hypertrophic cardiomyopathy at the whole real organ.

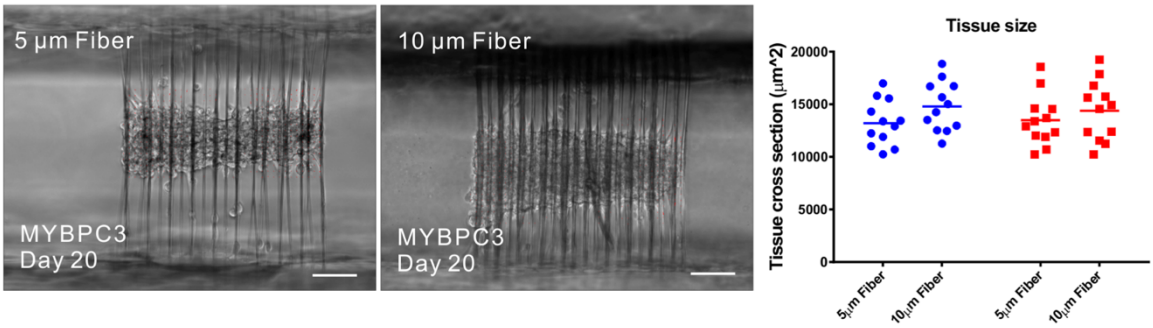

Figure 4.28. Bright-field microscopy showed no significant difference on tissue cross-section between WT and MYBPC3 tissues growing on 5 µm and 10 µm matrices at Day 20 (mean with all data, n = 12). (Scale bar : 100 µm)

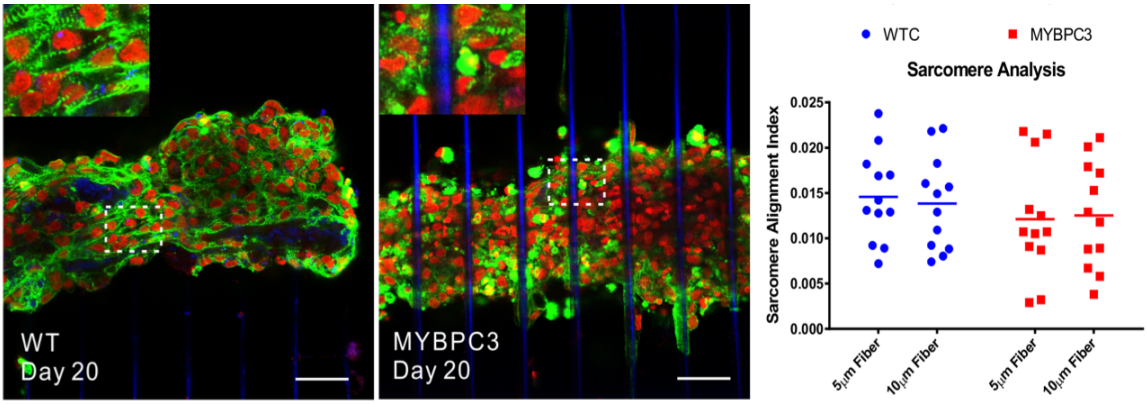

Figure 4.29. Confocal microscopy, and showed no significant difference on sarcomere alignment index between WT and MYBPC3 tissues growing on 5 µm and 10 µm matrices at Day 20 (mean with all data, n = 12) (Scale bar : 50 µm)

We also observed that there was no significant difference on static forces between WT and MYBPC3 cardiac microtissues on both matrix types (5 µm and 10 µm). Thus, we found that the cardiac preload due to tissue passive tension was not affected by the MYBPC3 gene knockout. However, the contraction forces of the MYBPC3 cardiac microtissues slightly increased only on 10 µm diameter matrices comparing Day 5 to Day 10-20.

Furthermore, the MYBPC3 cardiac microtissues exhibited significantly lower contraction forces comparing to WT microtissues only on 10 µm-thicknss matrices. We also found that the MYBPC3 cardiac microtissues showed higher contraction velocity compared to WT, and this velocity difference between two tissue types (WT and MYBPC3 cardiac microtissues) was exaggerated on 10 µm-thickness matrices.

As a results, modulating cardiac tissue mechanical environment facilitates disease modeling of contraction deficits due to MYBPC3 gene KO. We can expect that MYBPC3 protein might only serve as a contractility modulator susceptible to the external mechanical stress, instead of structurally affecting the sarcomere assembly and tissue formation.

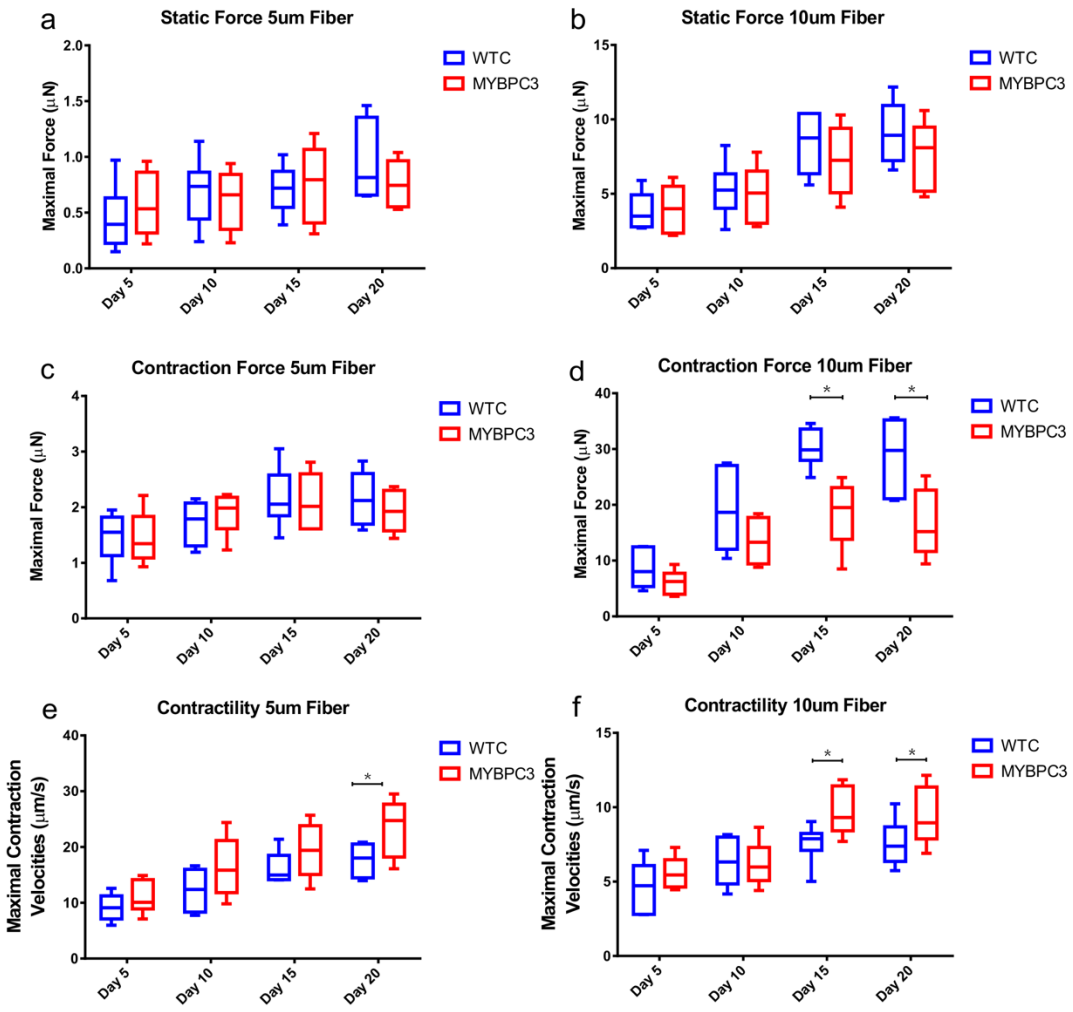

Figure 4.30. Tissue contraction deficits resulted from MYBPC3 KO. Comparing to WT cardiac microtissues, MYBPC3 KO had no effect on static forces for the cardiac microtissues on both (a) 5 μm and (b) 10 μm matrices, (c) no effect on contraction forces for the tissues on 5 μm matrices, (d) but induced lower contraction forces at Day 15 & 20 for the cardiac microtissues only growing on 10 μm matrices. MYBPC3 KO resulted in higher maximal contraction velocity for the cardiac microtissues growing on both (e) 5 μm matrices (Day 20) and (f) 10 μm matrices (Day 15 & 20) comparing to WT cardiac microtissues

Moreover, we plotted the force curves for WT and MYBPC3 cardiac microtissues on 5 μm and 10 μm matrices at Day 20 (after enough time for adaptation by mechanical microenvironment). By multiplying the force and velocity, we could plot the power curves and calculated the curve area as the total energy consumed by the cardiac microtissues for one contraction cycle. On both matrices, MYBPC3 cardiac microtissues developed the maximal contraction forces faster than WT microtissues. Since the force magnitude was similar between WT and MYBPC3 cardiac microtissues on 5 μm matrices, however, higher contraction velocity led to higher power output. As a result,

more energy was consumed by the MYBPC3 cardiac microtissues. This hypo-contractile phenomena has been widely accepted as an early sign of hypertrophic cardiomyopathies phenotype. On the other hand, MYPBC3 cardiac microtissues developed significantly lower contraction forces, less power output, but similar energy consumption comparing to the WT. Same energy consumption, low force generation from MYBPC3 cardiac microtissues indicated that MYBPC3 knockout CMs impaired the cardiac microtissues to contract in an energy-efficient manner. This impaired cardiac function possibly recapitulate the failing myocardium associated with external stress and genetic deficiency.

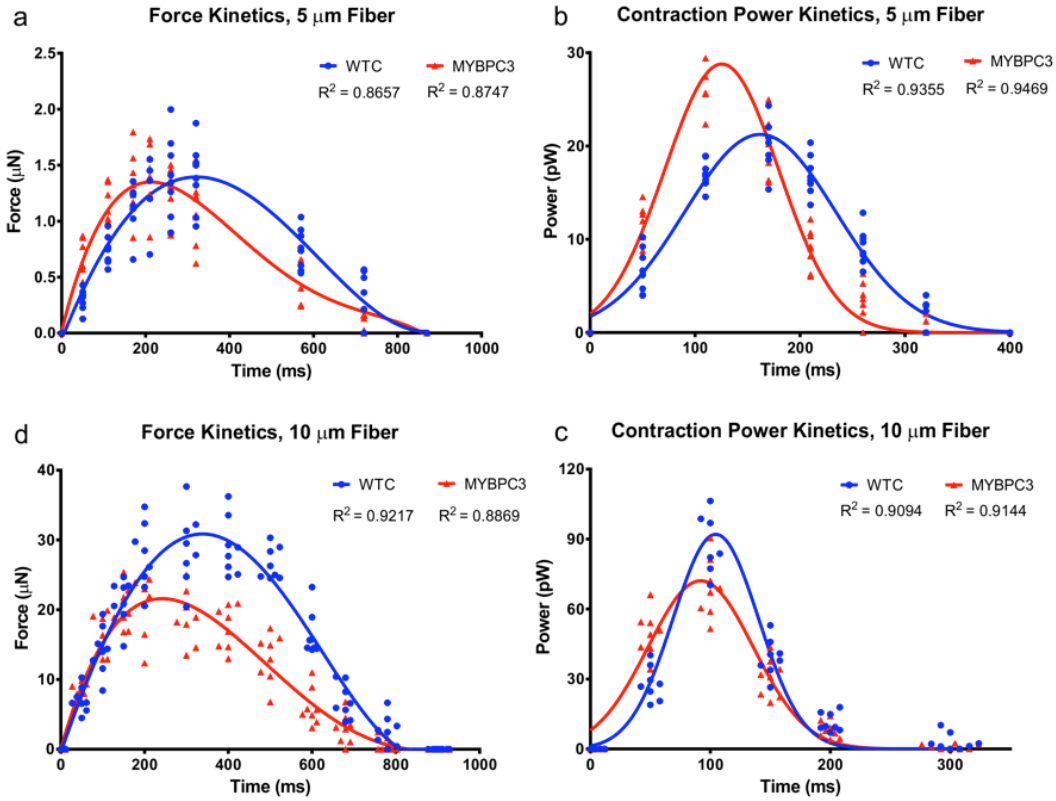

Figure 4.31. Mechanical environment altered contractile phenotype. (a) The force development of MYBPC3 cardiac microtissues on 5 μm matrices was faster than WT tissues, but no difference on the magnitude. (b) Higher power output of MYBPC3 cardiac microtissues comparing to WT suggested a hypo-contractile phenotype. (c) The force development of MYBPC3 cardiac microtissues on 10 μm matrices was faster but lower than WT tissues, (h) whereas the energy consumption of MYBPC3 tissues was similar to WT tissues (mean ± SD, n = 8)

4.4.8 Tissue mechanical environment affected on local cardiac contractile deficits

To further elucidate how the mechanical microenvironment affected the cardiac tissue contractility locally, we fabricated the hybrid matrices (by positioning the 5 μm and 10 μm-thickness fibers one next to each other) to create a mechanical mismatch region in the middle of each matrix. We seeded the MYBPC3 hiPS-CMs into the hybrid matrix to form 3D cardiac microtissues across the entire matrix. After enough time of adaptation (at Day 20), we found that the cardiac microtissues could synchronously contract with higher contraction velocity within the low stiffness region compared to the high stiffness region. In contrast, MYBPC3 cardiac microtissues growing on hybrid matrices showed higher contraction forces and larger tissue cross-section at high stiffness region than low stiffness region.

This results indicate that the entire cardiac microtissues had to balance the generated force between high and log stiffness microenvironment for synchronization of contraction. Such force equilibrium resulted in the tissue hypertrophy at the high stiffness region with high tissue cross-section. Furthermore, calculation of the local contraction velocity within the mismatch region (interface between high and low stiffness region), we found that the tissues had higher contraction along the X-direction within mismatch region of low stiffness (Region L). Contrast to this, higher contraction along the Y-direction within mismatch region of high stiffness (Region H). Hence, the mechanical mismatch induced the local uncoordinated contraction of cardiac tissue (Even though the sarcomere organization/orientation showed not significant differences across this mismatched region).

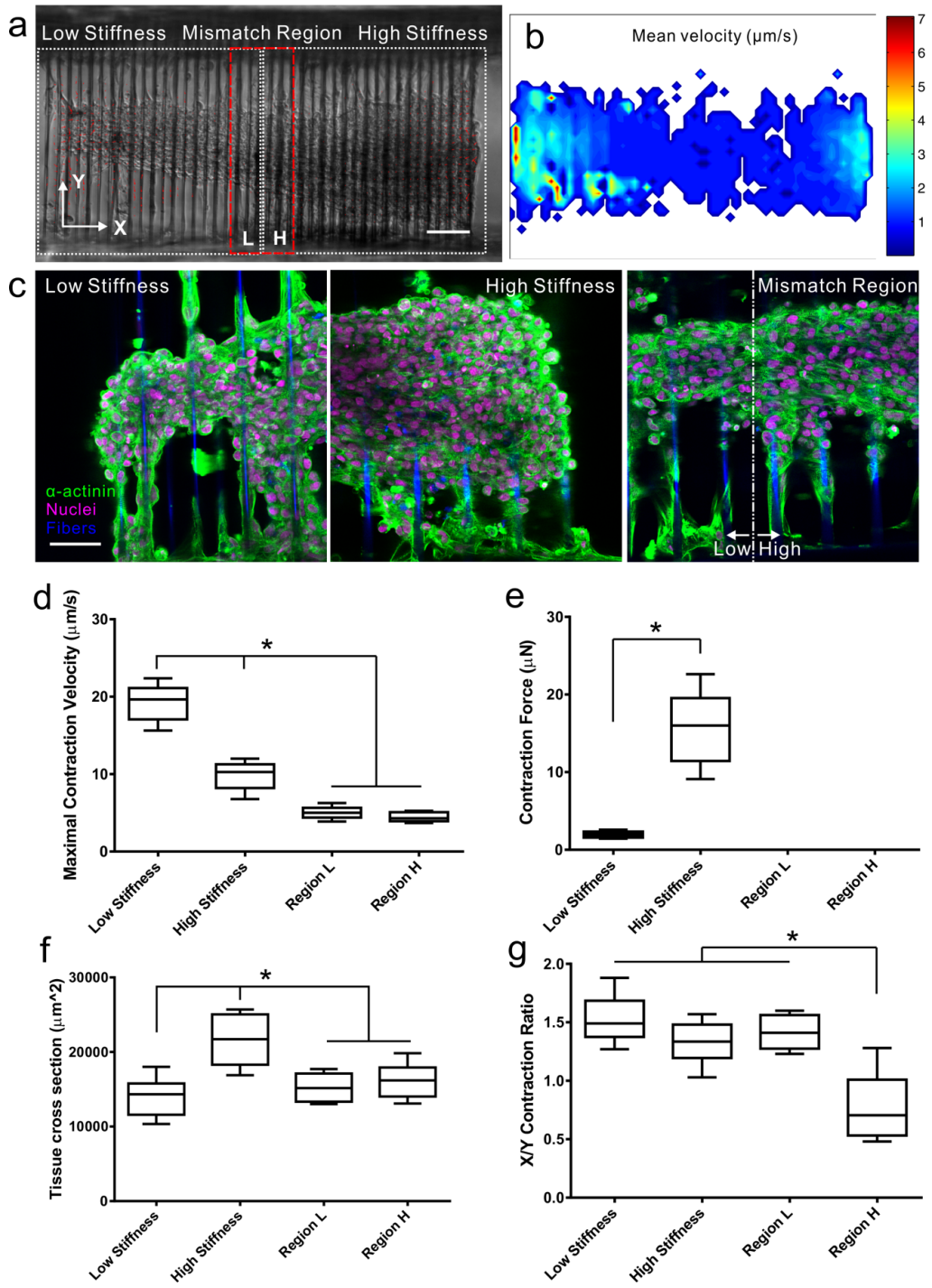

Figure 4.32. Mechanical mismatch induced contraction deficits. (a) The MYBPC3 cardiac tissue formed on a hybrid matrix fabricated with 5 μm fibers and 10 μm fibers one next to each other. Scale bar, 100 μm. (b) The contraction heatmap showed higher contraction velocity on the region within the low stiffness region. (c) The confocal microscopic images showed the sarcomere structure of MYBPC3 cardiac microtissues within the low stiffness region (left), high stiffness region (middle) and mismatch region (right). Scale bar, 50 μm. (d) Low stiffness region had

highest contraction velocity for the entire hybrid matrices (mean ± SD, n = 8). (e) Region H within mismatch region had lowest ratio of contraction velocity between X-direction and Y-direction, indicating higher contraction velocity along Y-direction (mean ± SD, n = 8). (f) High stiffness region had 10-fold higher contraction forces than low stiffness region, whereas no fiber deflection was detected within the mismatch region (mean ± SD, n = 8).

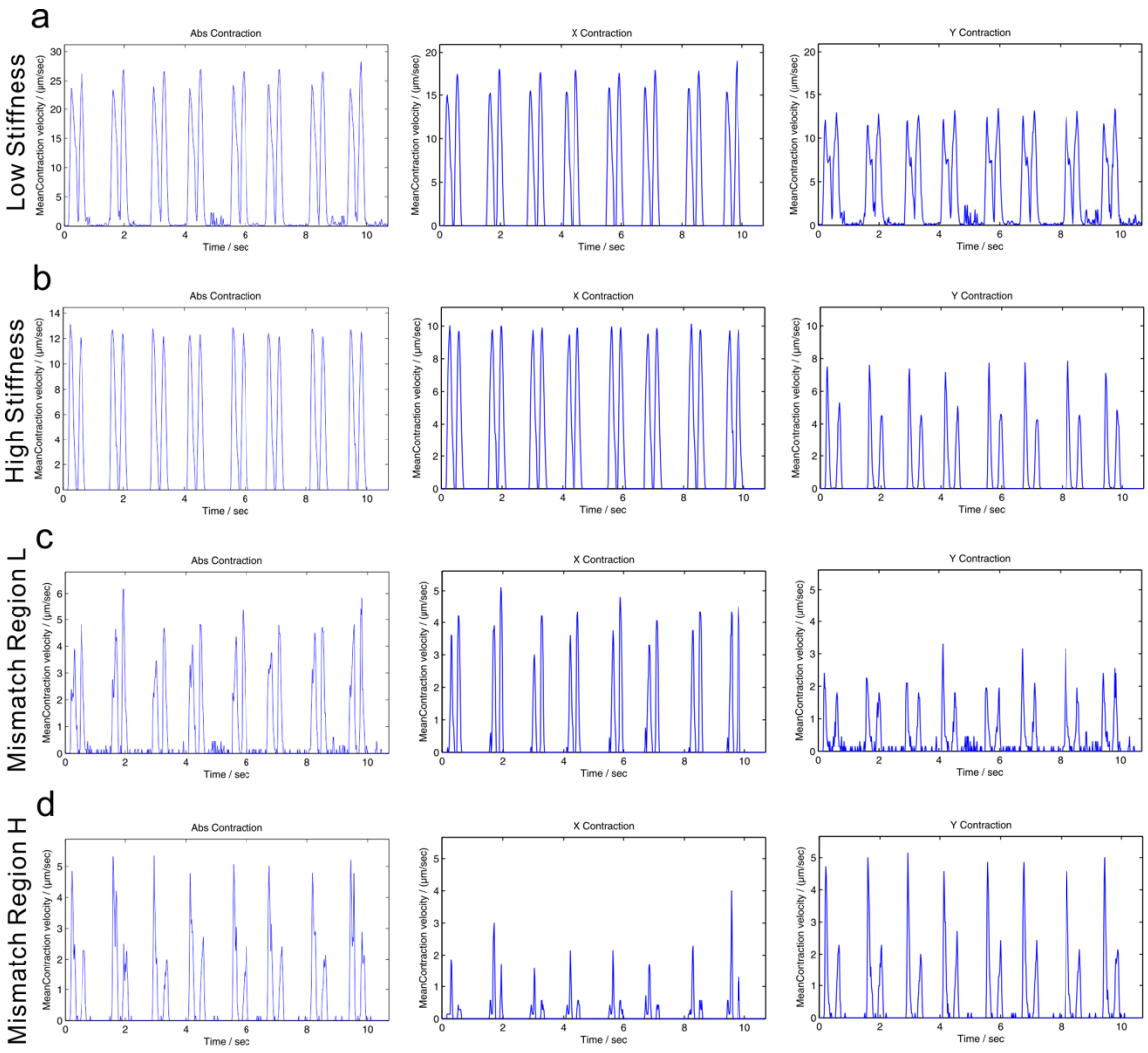

Figure 4.33. Contraction waveforms for the MYBPC3 cardiac tissue on a hybrid matrix. The contraction waveforms were listed as total contraction (left column), X-direction contraction (middle column) and Y-direction contraction (right column) for (a) low stiffness region, (b) high stiffness region, (c) mismatch region L and (d) mismatched region H.

4.4.9 Consideration of real model

MYBPC3 is a thick filament accessory protein of the striated muscle sarcomere A band. This protein determines the cardiac tissue contraction velocity and force, and ensures the generation of conservative power for efficient myocardial contraction at rest. And this also provides considerable contractile reserve for enhanced function during the contraction procedure. In a MYBPC3 heterozygous transgenic mouse model, the adult mice developed a mild hypertrophic cardiomyopathies phenotype with diastolic dysfunction, but no left ventricular hypertrophy or systolic dysfunction[139, 147-150]. *in vitro* engineered heart tissue system could unmask subtle abnormalities, and this were likely be concealed by the compensatory mechanisms. Considering the real *in vivo* model, there is some limitation on this research. Patients with hypertrophic cardiomyopathies were only found with heterozygous MYBPC3 gene mutations, however, we applied the cardiac microtissue with homozygous MYBPC3 gene KO with an emphasis on the mechanical role of MYBPC3 protein on cardiac contractile functions.

In this result, we applied that contractile deficits of human MYBPC3 KO cardiac microtissues under different mechanical environment by changing the mechanical properties of filamentous structure, and found that MYBPC3 tissues only exhibited reduced systolic contraction force growing on stiffer filamentous structure. This demonstrated that MYBPC3 KO impaired cardiac adaptation to increased mechanical load, induced contractile deficits, and activated hypertrophic signaling. The earliest signs of hypertrophic cardiomyopathies are also associated with hypo-contraction and impaired relaxation. By examining developed force and power of cardiac microtissue, we discriminated hypo-contraction as hypertrophic cardiomyopathies and impaired contraction as heart failure by variation of mechanical resistance to the MYBPC3 cardiac microtissues. By applying the different microenvironment of cardiac microtissue, that will provoke the different disease phenotype with same genetic defects. This different phenotype from hypo-contraction to impaired contraction also recapitulated the disease progress from moderate hypertrophic cardiomyopathies to severe heart failure by deteriorating the environmental stress.

In this research, we applied the advanced laser-based 3D fabrication (2PP), fabricated well-defined fibrous structure, and measure the fiber elastic properties using AFM. Based on this result, it is possible to compute the separate the cardiac microtissue relaxation and fiber elastic recoil. Hence, we can perform accurate measurement for the rate of diastolic relaxation for hypertrophic cardiomyopathies studies.

In the real cardiac tissue, cardiac hypertrophy has positive/negative sides. Normal postnatal development, continuous exercise, or pregnancy induce the reversible physiological hypertrophy that can strengthen the heart. In contrast, sustained hypertension, heart-valve regurgitation or aortic stenosis induce the irreversible pathological hypertrophy that can lead to irregular heart beat and heart beating failure [139, 147-150]. However, both physiological and pathological hypertrophy has common thing which characterized as the increase in CM size. However, only pathological hypertrophy is associated with increased apoptosis, interstitial fibrosis, and overall cardiac dysfunction.

In vitro cardiac hypertrophy models have been developed either passive (stretch of mimic CMs by increase the preload), or active (stiffening the flexible cantilevers to cardiac microtissues by increase the afterload) methods. In our 3D filamentous cardiac microtissue model, we mimicked the increase of afterload, and assessed the effects of mechanical stress on cardiac functions. However, WT and MYBPC2 iPS-CMs shows different phenomena. WT cardiac microtissues exhibited enhanced contractile functions in response to the increase of afterload, suggesting a phenotype of physiological hypertrophy. In contrast, MYBPC3 cardiac microtissues exhibited impaired contractile functions in response to the incrase of afterload, suggesting a phenotype of pathological hypertrophy.

We also found that the hypertrophic gene expression showed differential regulation of NFAT and AKT pathways for the WT and MYBPC3 cardiac microtissues in response to the increase of afterload. This result is consistent with the previous reports on the differences between physiological and pathological hypertrophy[149, 168-170]. Mutations in MYBPC3 accounts for 30% of all mutations linked to familial hypertrophic cardiomyopathies [139, 147-150]. We found that a decrease in brain natriuretic peptide (BNP) secretion from WT cardiac microtissues on both 5 μm and 10 μm matrices, suggesting a physiological hypertrophy. However, BNP secretion increase phenomena can be found from MYBPC3 cardiac microtissues only growing on 10 μm matrices, suggesting a pathological hypertrophy.

And we also performed a hypertrophic gene profiling for the WT and MYBPC3 cardiac microtissues on two different thickness filamentous structure with 5 μm and 10 μm – thickness matrices. We found that an increase in mechanical stiffness induced MYBPC3 cardiac microtissues to increase the expression of cardiac transcriptional factors such as MEF2C, GATA4, NKX2.5, and to activate the NFAT signaling pathway. Interesting thing is that increase of fiber stiffness led to the differential expression of the AKT signaling pathway. For the WT cardiac microtissue, this SKT signaling pathway was activated. In contrast, for the MYBPC3 cardiac microtissue, SKT signaling pathway was deactivated.

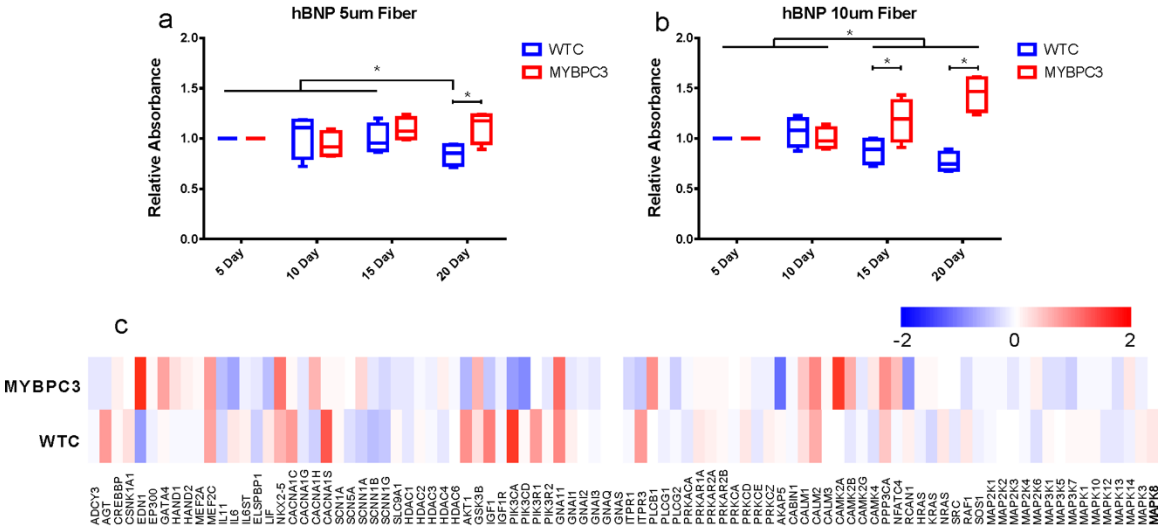

Figure 4.34. Effect of mechanical environment on expression of hypertrophic biomarkers. hBNP expression decreased for WT cardiac microtissues on both (a) 5 μm and (b) 10 μm matrices, but increased for MYBPC3 cardiac microtissues only on (b) 10 μm matrices (mean ± SD, $n = 4$). (c) Gene expression profiling of human NFAT & cardiac hypertrophy for WT and MYBPC3 showed differential gene expression for WT and MYBPC3 cardiac microtissues with variation of tissue mechanical environment by normalizing the gene expression of the tissues on 10 μm matrices over 5 μm matrices ($n = 4$)

4.4.10 Drug testing on cardiac model

Once we optimized the 3D cardiac tissue for LQT3 iPS- CMs formation such as alignment, and abnormality contractility, we validated this model by testing the response of LQT3 iPS-CMs to different chemicals treatment which had well-known their effects on cardiac tissue. After growing LQT3 iPS-CMs on F/5-50 matrices for 7 days, they were treated with two different doses of each chemicals, and response of cardiac tissue had evaluated using real-time video recording system and motion-tracking MATLAB sofrware to measure the contractility malfunctions [167].
For example, caffeine is well-known to increase heart rate and enhance the internal Ca^{2+} release from the sarcoplasmic reticulum (SR), and this effects on the CM contractility. Applying this caffeine to 3D LQT3 iPS-CMs tissue model, it caused the increase of beating frequency (BF) and maximal contraction velocity (MCV). Nifedipine is well-known as L-type Ca^{2+} channel blocker, it decreased the BF and MCV, and increased the beating duration (BD) by decreasing CM Ca^{2+} influx.
Heat beating was also effected by amount of dosage. Higher doses of caffeine (500 nM) and nifedipine (300 nM) both caused LQT3 iPS-CMs to cease beating without any uncoordinated beating resulting from arrhythmias. E4031 (a hERG K^{+} channel blocker) and propranolol (a beta-adrenergic antagonist) showed similar effects on LQT3 iPS-CMs, decreasing BF and MCV and increasing the BD in a dose-dependent manner. E4031 caused a small level of irregular beating patterns shown in the baseline of the motion-tracking waveform. However, propranolol induced significant uncoordinated irregular beating patterns, suggestive of cardiac arrhythmias[51].

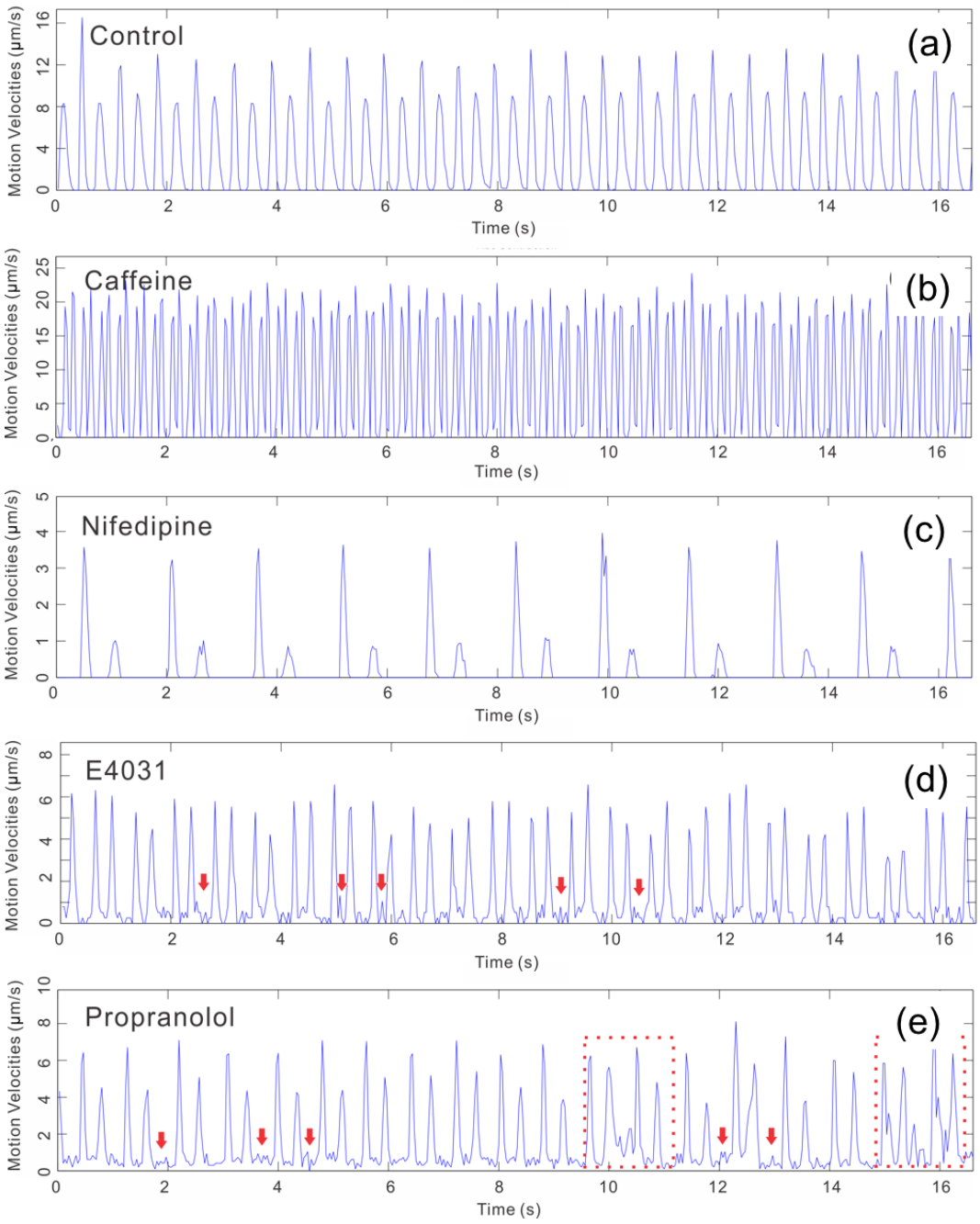

Figure 4.35. The motion-tracking waveforms were recorded for LQT3 iPS-CMs on F/5–50 matrices with drug testing: (a) control without treatment, (b) treatment with 100 nM caffeine, (c) treatment with 200 nM nifedipine, (d) treatment with 200 nM E4031, (e) treatment with 30μM propranolol. LQT3 iPS-CMs treated with E4031 and propranolol experienced with irregular baseline contraction (pointed by red arrows) and uncoordinated beating (framed by red boxes)

To compare the drug response of LQT3 iPS-CMs between 3D cardiac filamentous tissue model and traditional 2D cell culture platform (*i.e.* TCPS), we grew LQT3 iPS-CMs on general tissue culture plate (for 2D) and F/5-50 and F/10-50 matrices (for 3D). To verity the response of LQT3 iPS-CMs on the different platform, we applied 30 μM propranolol to those two different type of culture platform, and quantify the physiological properties such as BF, MCV and BD. The change in CM contractility on F/5-50 matrices was significantly larger than that of F/10-50 matrices and 2D surfaces. LQT3 iPS-CMs were more sensitive to the chemicals (or medicine) if they grew as a 3D tissue structure with lower stiffness microenvironment. The change in MCV on F/10-50 matrices was larger than 2D surfaces, but no significant difference of BF and BD between these two substrates.
And we also quantified the percentage of uncoordinated beating within one motion-tracking waveform with different doses of propranolol (10, 30 and 60 μM). As increase the propranolol dosage for all substrate, it shows the increase of percentage of uncoordinated beating. However, the difference was not significant among these substrates until the concentration was increased to 30 μM, at which time LQT3 iPS- CMs experienced more arrhythmias growing on F/5-50 matrices than F/10-50 matrices and 2D surfaces. At a higher dosage of 60 μM propranolol, it shows about 70% irregular and uncoordinated beating of LQT3 iPS-CMs on F/5-50. The percentage of uncoordinated beating on F/5-50 was still the largest, and the that of on F/10-50 also became significantly larger compared to the 2D surfaces.
As a result, LQT3 iPS-CMs became more susceptible to cardiotoxicity caused by pharmacological interference when grown as a 3D cardiac tissue with lower stiffness.

Although characterized by the same syndrome(Long QT), patients with LQT1 (KCNQ1) and LQT2 (hERG) experience cardiac arrest due to exercise and emotional stress[171], in contrast, LQT3 patients experience it with a slower heart rate during sleep and rest. According to the clinical evidence clearly indicates that only certain environmental conditions can amplify the electrophysiological disorder into the sudden heart dysfunction. Therefore, drug testing for LQT3 iPS-CMs in different cellular microenvironments may result in different pharmaceutical responses. Our findings indicated that LQT3 iPS-CMs were more susceptible to drug-induced cardiac toxicity growing on 3D fibrous structure with lower stiffness (F/5-50 matrices) compared to stiffer condition (F/10-50 matrices) and standard 2D surface. LQT3 iPS-CMs on F/5-50 matrices experienced higher risk of uncoordinated and irregular beating compared to 2D surfaces with 60μM propranolol treatment. The high frequency of contractility malfunction observed in LQT3 iPS-CM on F/5-50 suggests that there might be false-negative readouts during toxicity testing on 2D culture platform which is usually used for drug or toxicity testing.

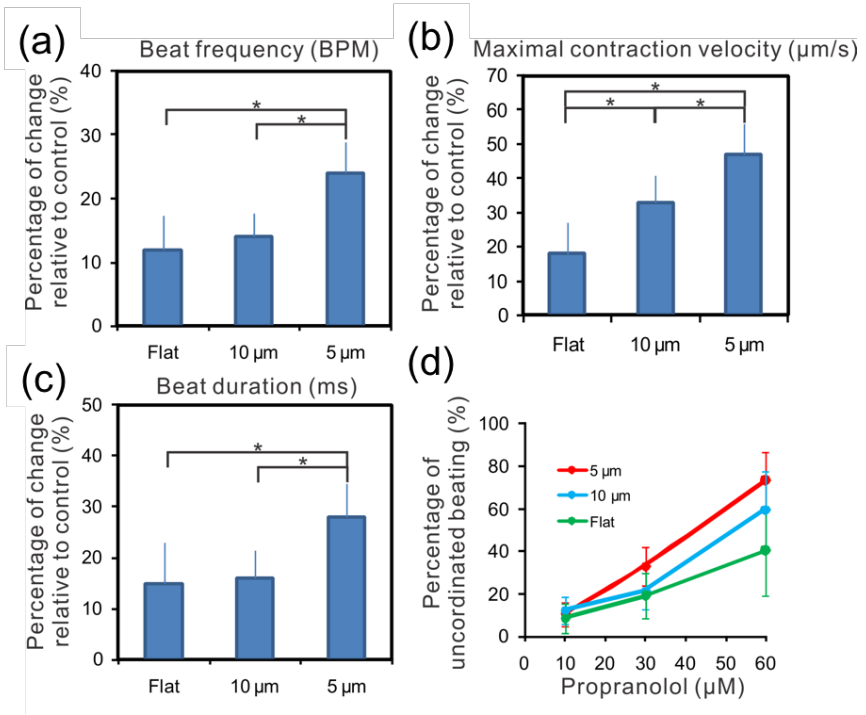

Figure 4.36. The LQT3 iPS-CMs response to 30 μM propranolol was tested on three different substrates: general culture plate (2D) and F/10-50 and F/5-50 matrices (3D_. The change of (a) BF, (b) MCV and (c) BD resulted from drug treatment was calculated relative to control groups, and LQT3 iPS-CMs experienced higher changes on F/5-50 matrices than 2D surfaces and F/10-50 matrices. (d) The uncoordinated beating also measured within individual trace of motion-tracking waveform for different substrates and dose of propranolol (10, 30 and 60 μM)

Further drug testing on LQT3 iPS-CMs with other chemicals showed that increased beating frequency by caffeine did not result in uncoordinated beating. This was consistent with clinical records of LQT3 patients who had cardiac arrest with slow heart rate. The nifedipine (L-type Ca^{2+} channel blocker) has been reported to shorten the CM action potential duration. Conversely, its effect on LQT3 iPS-CMs on F/5-50 matrices was found to elongate the beating duration. This is the consequence of slow Ca^{2+} influx, which results in a longer release time of the internal Ca^{2+} stored in the sarcoplasmic reticulum (SR) necessary to complete the contraction. This result suggests that contractility of CMs might not fully represent the electrophysiology, especially with drug interference. The E4031 (hERG K^{+} channel blocker) has been known as the drug inducing severe arrhythmias. In this research, this chemical used for testing the cardiotoxicity tolerance and contractility malfunction of LQT3 iPS-CMs growing on F/5e-50 matrices. According to our result, E4031 decreased the contractility, elongated the beating duration, and induced irregular contractions of LQT3 iPS-CMs. This irregular beating between contraction and relaxation within one beating cycle were most likely the result of early after depolarizations (EADs). And irregulat beating between two beats

most likely the result of delayed after depolarizations (DADs)[142, 152]. In this study, we found this drug-induced uncoordinated beating was consistent with clinical cases.

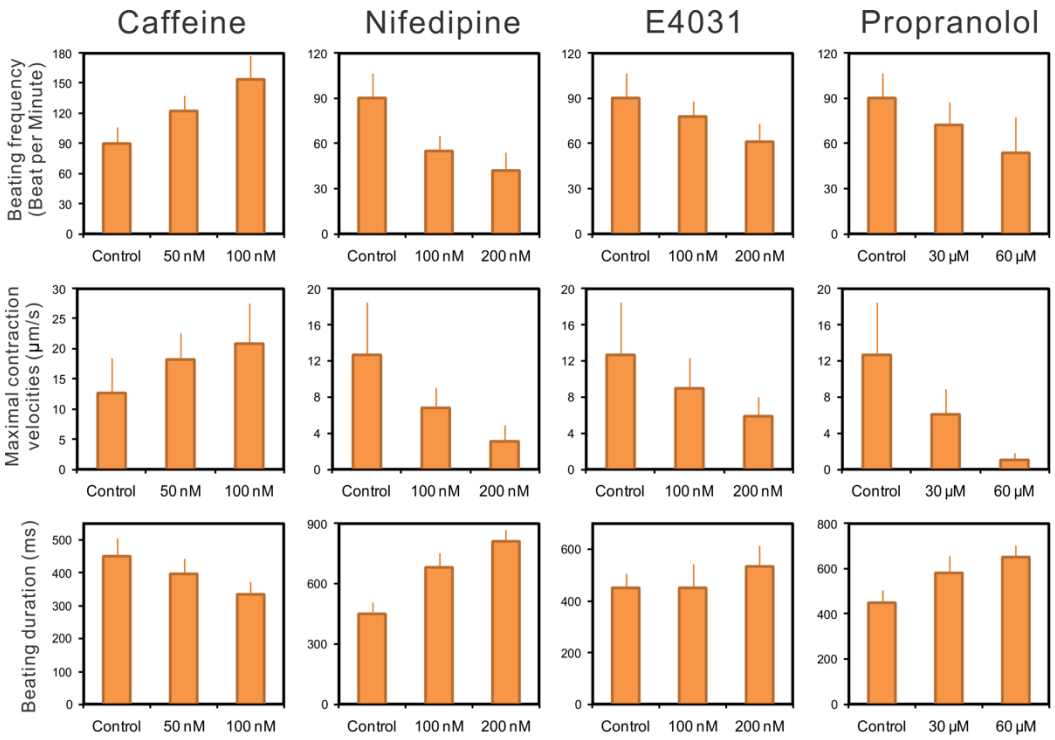

Figure 4.37. The LQT3 iPS-CMs on F/5-50 matrices were tested the contractility changes (BF, MCV, and BD) to four different chemicals (caffeine, nifedipine (L-type Ca^{2+} channel blocker), E4031 (hERG K^{+} channel blocker) and propranolol (β-adrenergic antagonist))

4.4.11 3D structure fabrication for multiple functionalization

Comparing to other general MEMS technique, it is possible to fabrication complex three dimensional structure using two photon polymerization. On the MEA system, it is possible to measure the electrical signal from the diverse tissue. Casting the cell into the biomaterials (hydrogel) is another good method for tissue formation and it can measure the electrical signal from tissue. To differentiate the contraction force and electrical signal from cardiomyocyte, it is need to fabricate 3D structure for hydrogel trapping. Generally, the multiple steps and masks are needed for complicate 3D structure. And another application is platform for single cell contraction force measurement. Moreover, for exact measurement of electrical signal on MEA, that structure should be fabricated in very affinity to substrate with high resolution. However, conventional 3D printing could not guarantee the high resolution compare to two-photon polymerization.

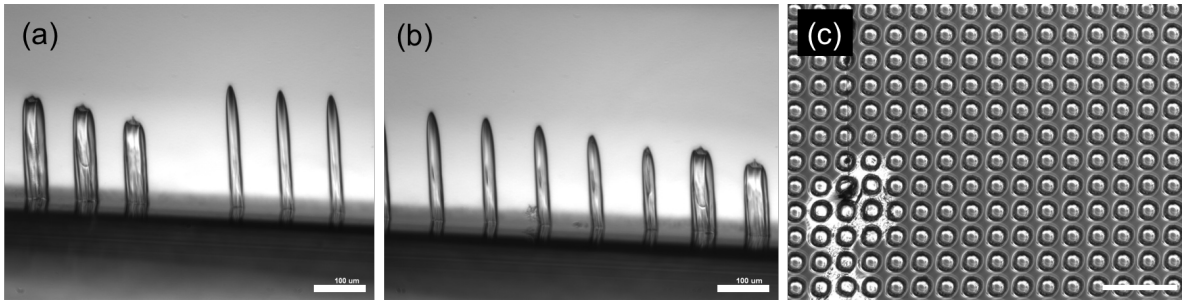

Figure 4. 38. High aspect ratio tube structure fabrication (a &b) side view of tube structure and (c) top view of tube array for cell trapping (scale bar : 100 μm)

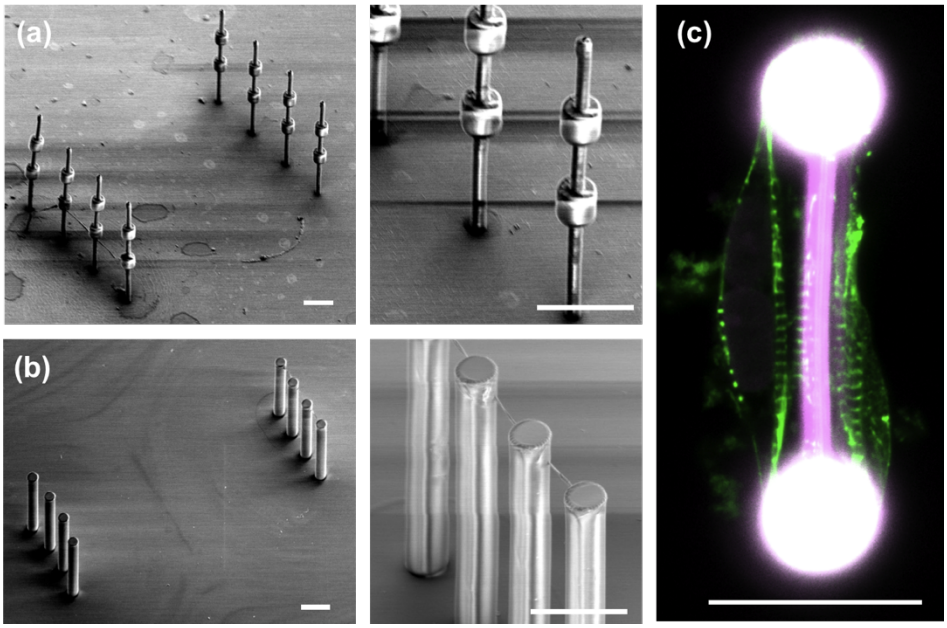

Figure 4.39. Application for high-aspect ratio structure (a) 3D structure on MEA for collagen trapping, (b) Fiber on the rod structure for single cell traction force measurement and (c) Single hiPS-CM on the fiber (scale bar : 100 μm)

4.5 Conclusions and outlooks

Two-photon polymerization(2PP) technique by femtosecond laser used to fabricate precisely defined 3D filamentous matrices of artificial tissue scaffolds and to study cell and 3D material interaction. Despite excellent initial progress in understanding cell

behavior in 2D, there still remain many limitations in current materials and fabrication technologies, which cannot mimic the nature 3D filamentous matrices and ultimately real tissues. For the deeper understand how cells were reacted and response by stimulation and environment, advance 3D structure fabrication technique is required precisely mimic the physical and chemical properties of real *in vivo* system. Furthermore, advancement of human *in vitro* cardiac tissue model make it possible to understand, study and develop the new strategies for treating cardiac arrhythmias and related cardiovascular diseases. In this research, we developed an 3D *in vitro* model of human cardiac microtissue by populating synthetic filamentous matrices with cardiomyocytes derived from wildtype (WT) and patient-specific LQT3 induced pluripotent stem cells (iPS-CMs) to mimic the connected and aligned human ventricular myocardium. For the efficient 3D iPS-CM microtissue scaffold formation which aligned along the fiber direction, we determined the optimized properties of fibrous scaffold such as spacing (50 μm). We observed that LQT3 iPS-CMs exhibited more contractility abnormality than WT iPS-CMs, and were more susceptible to cardiotoxicity when grown on the lower stiffness filamentous structure scaffold. This highly defined human 3D cardiac model will help us to better understand the cardiovascular disease mechanism and formulate better therapeutic strategies such as medicine treatment. This model is also a pioneering testbed for assessing drug efficacy for patients with rare genetic disorders, moving drug discovery and development into the era of personalized medicine. We studied the contractility malfunctions associated with the electrophysiological consequences of LQT3-CMs and their response to chemical treatment. Due to the different stiffness of filamentous matrices, LQT3 iPS-CMs exhibited different level of contractility abnormality and susceptibility to drug-induced cardiotoxicity.

However, the limitations of this 3D cardiac tissue model need to be stated. The CMs generated from iPS cells were immature embryonic or neonatal-like CMs, which morphologically cannot compare with large and stiff ventricular CMs in the adult human heart. That is, cardiac tissue constructed by iPS-CMs had significantly lower field potentials and contraction forces than adult ventricular tissue. Hence, it is not possible to be considered as exactly same to *in vitro* model of mature myocardium. Electrical stimulation would be one of alternative to help CM maturation, and a long-term stimulation system is under development, which can adjust the magnitude and frequency of the electrical field.

However, compared to microstructured 2D substrates, 3D fibrous matrices showed much stronger similarity to the topographic complexity *in vivo*, where fiber structures constituted the dominant structural elements. In particular, our matrices could be fabricated over a wide range of dimensions, and bending stiffness also can be easily and accurately tuned. Since fibers were deflected by the contraction of cardiac microtissue, we could calculte the CM's contraction forces on those platforms with different thickness. The combination of well-defined filamentous matrices by 2PP and computational finite element analysis approaches presented a biomechanical model of cardiac tissue to map the relationship among external stress, cardiac contractility, and force generation. Through this 3D *in vitro* model, we demonstrated that how mechanical/physical environment effects on the generation of physiological and pathological response in a 3D human iPS-based cardiac tissue. Our studies highlighted the possibility of exploiting the mechanical load to the cardiac tissue, which will hopefully lead to deeper and

comprehensive understanding of the role of mechanical/physical environment into homeostasis and pathogenesis of cardiac tissue.

A majority of chronic cardiac diseases with complex phenotypes was effected by genetic networks and genetic-environment interactions. Currently, human induced pluripotent stem (hiPS) cell technology has provided previously unanticipated possibilities to model human heart disease in cell culture as "disease-in-a-dish"[172]. However, genetic background variations between patient-derived iPS cells and their wildtype pose considerable risks for interpreting a supposedly diseased phenotype attributed to a single gene mutation, external environmental perturbations, or genetic background noise. To understand pathogenesis from specific gene mutation and its interaction with environmental exposure requires precise control on both genetics background and environmental conditions. Exciting advances in genome-editing technologies by endonuclease (TALEN) or palindromic repeat (CRISPR) are being introduced to engineer cardiac disease-associated gene mutations into hiPS cell lines with the same genetic background[173]. Engineered tissue models aim to accurately mimic the dynamic, complex, and 3D *in vivo* biological contents, as well as reconstitute the pathological environmental stresses to reveal the etiology of cardiac diseases. Combination of hiPS cell technology, genome editing technique and engineered tissue models leads to the next-generation of hiPS-based cardiac disease modeling. And it recapitulates the synergism of genetic deficiencies and environmental stresses that are required to induce the life-threatening cardiac diseases, especially chronic cardiomyopathies.

Table 4.1 Primary Antibodies used in this study

Antibodies	**Animal**	**Vendor**	**Cat. No.**
Sarcomeric α-actinin	Mouse	Sigma Aldrich	A7811
Cardiac troponin T (Flow Cytometry)	Mouse	Thermo Scientific	MS295P
β-myosin heavy chain	Mouse	Abcam	ab97715
Connexin 43	Rabbit	Sigma Aldrich	C6219
N-cadherin	Rabbit	Abcam	ab12221
Nuclei (DAPI)	-	Life Technologies	R37606
Nuclei (Topro3)	-	Life Technologies	T3605

Table 4.2. PCR Primers in the customized target array for cardiac differentiation profiling

Cardiac Differentiation Profiling					
NANOG	POUSF1	SOX2	T	MIXL1	MESP1
NM_024865	NM_002701	NM_003106	NM_003181	NM_031944	NM_018670
PDGFRA	ISL1	NKX2.5	TBX5	TNNT2	TNNI3
NM_001202	NM_002202	NM_004387	NM_000192	NM_000364	NM_000363
MYH6	MYH7	GAPDH	HSP90AB1		
NM_002471	NM_000257	NM_002046	NM_007355		

Table 4.3. Primary Antibodies

Antibody Target	Animal	Vendor	Cat. No.
Nanog	Rabbit	Abcam	ab21624
Oct4	Rabbit	Abcam	ab19857
Sox2	Rabbit	Abcam	ab92494
Sarcomeric α-actinin	Mouse	Sigma Aldrich	A7811
Laminin	Rabbit	Abcam	ab14055
Cardiac troponin T (FC)	Mouse	Thermo Scientific	MS295P
Cardiac troponin T (ICC)	Rabbit	Abcam	ab45932
β-myosin heavy chain	Mouse	Abcam	ab97715
Connexin 43	Rabbit	Sigma Aldrich	C6219
Nuclei (DAPI)	-	Invitrogen	R37606
Nuclei (Topro3)	-	Invitrogen	T3605

Table 4.4. PCR Primers

Gene	Accession #	Primer
Nkx2.5	NM_004387	F: GCGATTATGCAGCGTGCAATGAGT R: AACATAAATACGGGTGGGTGCGTG
TNNT2	NM_000364	F: TTCACCAAAGATCTGCTCCTCGCT R: TTATTACTGGTGTGGAGTGGGTGTGG
TNNI3	NM_000363	F: CTGCAGATTGCAAAGCAAGA R: CCTCCTTCTTCACCTGCTTG
MYH6	NM_002471	F: GATAGAGAGACTCCTGCGGC R: CCGTCTTCCCATTCTCGGTT
MYH7	NM_000257	F: TGTCCAAGTTCCGCAAGGT R: TCGGCTTCAAGGAAAATTGC
GAPDH	NM_002046	F: CCCCTTCATTGACCTCAACTACA R: TTGCTGATGATCTTGAGGCTGT
HSP90AB1	NM_007355	F: GGAAGTGCACCATGGAGAGG R: GTTCCTGAGGGTTGGGGATG

Table 4.5 Drug-screening compounds

Name	Vendor	Cat. No.
Caffeine	Sigma Aldrich	C7731
Nifedipine	Sigma Aldrich	N7634
E4031	Abcam Biochemicals	Ab120158
Propranolol	TCI	P0995

Chapter 5 Induction and Enhancement of Nanomaterial Self-assembly in Ultraprecise 3D structure fabricated by Femtosecond Laser Direct Writing (Two-photon polymerization)

5.1 Introduction

Research of nanomaterials is promising for development of diverse technological applications including optics, energy devices and bioengineering tools *etc*. In recent years, rapid expansion has occurred for nanofabrication towards tailoring artificial materials with desired nanostructures. However, current nanofabrication methods are subject to limitations regarding application of nanomaterials into mass manufacturing. Step-by-step separate processes are needed to functionalize the nanomaterials. Bottom-up approaches are feasible to produce two-dimensional structures, however, they cannot still accommodate the increasing demand of structural complexity. To solve this issue, top-down process broaden the usage of manufacturing with complex and functionally advanced platforms if appropriate processing is developed.

Self-assembly of materials is broadly considered an attractive means of generating nanoscale structures and patterns over large areas. We can take advantage of the self-assembly characteristics of block copolymers (BCP) that are intrinsically scalable and amenable to large area processing[174-178]. Spontaneous formation of equilibrium nanostructures in response to temperature and concentration changes.

For the backbone for the self-assembly of block copolymer, femtosecond laser direct writing (two-photon polymerization) is a good alternative for nanoscale 3D structure fabrication with nanoscale precision[138, 179, 180]. Integration of two-photon polymerization (2PP) and block copolymer directed self-assembly (DSA) would open new possibilities. The central motivation of this work is to develop a new paradigm for design and manufacturing that offers scalability and flexibility. Eventually, this technique makes it possible to fabricate and manufacture mesoscale (~100 nm & ~5 nm) 3D structures with nanoscale functionality. Consequently, new approach is needed to enable precision layout and assembly of heterogeneous components into functional device architectures such as 3D sensor with high sensitivity and renewable energy system with high efficiency.

For energy conversion engineering, photovoltaic energy conversion is promising option for supplying renewable, environmentally friendly energy[47, 181] . However, substantial reduction of costs should consider for wide usage. The high surface-to-volume ratio makes these inorganic materials with complex 3D confined structures suitable for photovoltaic cell electrodes. The size of these inorganic structures is similar to or less than the wavelength of visible light.

Structures with very small size but sophisticated 3D architecture can be used for photonic crystals and metamaterials. Introducing functional inorganic nanoparticles, such as metal, semiconductor, or oxide nanoparticles, magnetic nanoparticles, into 3D confined polymeric materials has created a new class of organic–inorganic composite materials that have various functions. Noble metal nanoparticles assembled into nanostructures formed by 3D confined polymeric materials can be used as a template for plasmonic materials, due to plasmon coupling between noble metal nanoparticles. Semiconductor nanoparticles in 3D confined polymeric materials. BCPs that naturally self-assemble into periodic ordered nanostructures can be utilized for controlling morphologies, directional alignment of domains, and combinations of these factors. Additional advantages include lower weight, mechanical flexibility, and tuning ability of optoelectronic functions by utilization of BCP[176, 181].

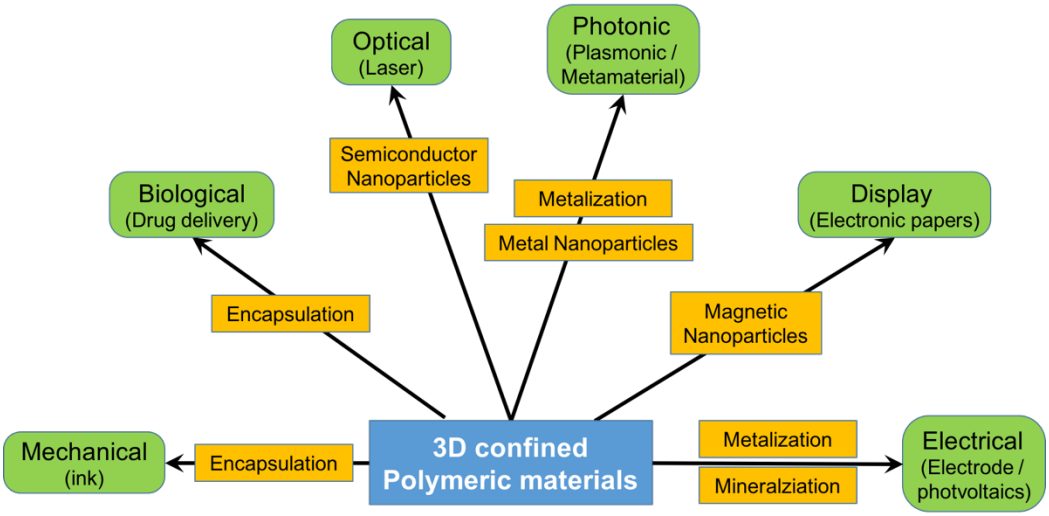

Figure 5.1. Diverse possible applications of 3D confined polymeric materials (BCP)

5.1.1 Advanced 3D structure fabrication technique

5.1.1.1 3D printing

3D printing technology has been received increasing attention and applied to diverse fields, including large-scale industrial prototyping, the tissue scaffolds fabrication, biomimetic microvascular system fabrication, the manufacture of electronic and pneumatic devices. 3D printing begins with a 3D model of the object, which is then digitized and sliced into model layers. The 3D printing system then prints 2D layers into 3D by adding each new layer on top of the prior layer. Thin layers of a material that can be cured with ultraviolet (UV) light are sequentially printed to form a solid 3D structure. However, general 3D printing technique has limitation such as low resolution. Minimal size of 3D printing structure depends on the material and nozzle size. Material jetting and

curing by UV light is repeated, it does not guarantee higher resolution. Due to the poor penetrating ability, the UV light is absorbed by the photoresist within the first few micrometers[182-184].

5.1.1.2 Ultraprecise 3D structure fabrication using femtosecond laser direct writing (Two-photon polymerization)

Unlike other 3D printing technologies, two-photon polymerization (2PP) induced by a near-infrared femtosecond laser beam, and can fabricate arbitrary and ultraprecise 3D microstructures with high resolution not only on the microscopic scale but also on the nanoscale[138, 180]. This innovative method for 3D structuring of structural and functional materials has distinct benefits. First of all, the achievable feature resolution of about 100 nm is about one order of magnitude better than general μ-stereolithography. Furthermore, due to the optically non-linear process it is possible to directly write inside a given volume, since the polymerization only takes place inside the tightly focus of the laser beam. Therefore, complex 3D structures can be inscribed into a suitable resin material that can be selectively cured. These advantages perfectly fulfill the demands for various future applications such as different mechanical, electronic and optical devices, polymer based optical waveguides on integrated circuit boards, photovoltaic platform and bio-inspired architectures, which requiring three dimensional structures with resolutions in the sub-μm range.

5.1.2 Block copolymer

Block copolymers are unique polymers that can self-assemble into ordered microdomains with sizes from 3 nm to about 50 nm. Block copolymers form appealing mesoscale structures. In thin films, self-assembled block copolymer microdomains with long-range lateral order can serve as ideal templates or scaffolds for patterning nanoscale functional materials and synthesizing nanostructured materials with size scales that below the minimum size of photolithography. The ordering processes during phase transitions and the resulting phase-separated structures of polymer blends.

5.1.2.1 Self-assembly of block copolymer

The block copolymers consist of two chemically distinct polymers that are covalently linked at one end. Non-favorable segmental interactions, coupled with the inherent entropic loss due to the long-chain nature of the block copolymer. This causes separation of the blocks into domains with the microdomain size. This is determined by the molecular weight of the block copolymer and the shape of the domain. Block copolymers attain shapes such as spherical, cylindrical, gyroid or lamellar, is determined by the volume fraction of the components. Since the polymer chains are covalently bonded together at one end, the size scale of the domains must be commensurate with the size of the polymer chain, typically on the tens of nanometer length scale or less[47, 181, 185-

188]. The theory of block copolymers self-assembly is well developed and successfully predicts the phase diagram of the equilibrium morphology of block copolymers bulk melts, as shown in Figure 5.2 by the Flory-Huggins segmental interaction parameter (χ), total number of repeating units (N) signifying the degree of polymerization, and the volume fraction (f) of one block. Predicted block copolymer domain spacings are in good agreement with experimental results. Block copolymers with large χ usually have marked differences in the surface energies between two blocks, making it difficult to orient the microdomains normal to the film surface. Usually, balanced interfacial interactions and surface energies are required to achieve this orientation. Different methods have been reported to balance the surface energy mismatch in high χ BCPs. Here, χ is proportional to the unfavorable interactions between different blocks. Block copolymer phase behaviors are described by [187]

Strong segregation limit (SSL): $\chi N > 100$, $L_0 \sim \chi^{1/6} N^{2/3}$
Intermediate regime: $10 < \chi N < 100$
Weak segregation limit (WSL): $\chi N < 10$, $L_0 \sim N^{1/2}$

where L_0 is the domain spacing. This can be used for description of block copolymer chain conformation and chain stretching. According to mean field theory, diblock copolymer phase behavior in the melt can be described by χN and f as shown in Figure 5.2. Diffusion coefficient of block chains in the microphase-separated domain is much slower (up to 4-order magnitudes) than that of homopolymer with similar molecular weight. The linear diblock copolymers with large χN typically take enormous time to self-assemble, which gives the upper limits for the domain spacing self-assembled by block copolymers. In contrast, manipulating the structure of diblock copolymer (use of long side chain brush copolymer instead of linear block copolymer) enables faster self-assembly of block copolymer to form micrometer size scale structure.
Symmetric diblock copolymers form lamellar microdomains, and asymmetric diblock copolymers form cylindrical microdomains or spherical microdomains with decrease the volume fraction of the minor block.
The phase behavior of BCPs is also strongly affected by the temperature. For most block copolymers, χ is inversely proportional to temperature as:

$$\chi = A + \frac{B}{T}$$

where A and B are both constants (B usually has positive values). As the temperature increases, χ decreases, and at a sufficient low χN value, the block copolymer no longer maintains phase separation and undergoes an order-to-disorder transition (ODT). On the other hand, upon cooling of the heated and phase mixed BCP sample, the BCP undergoes a disorder-to-order transition (DOT) to form microphase-separated microdomains, due to the increased χ.

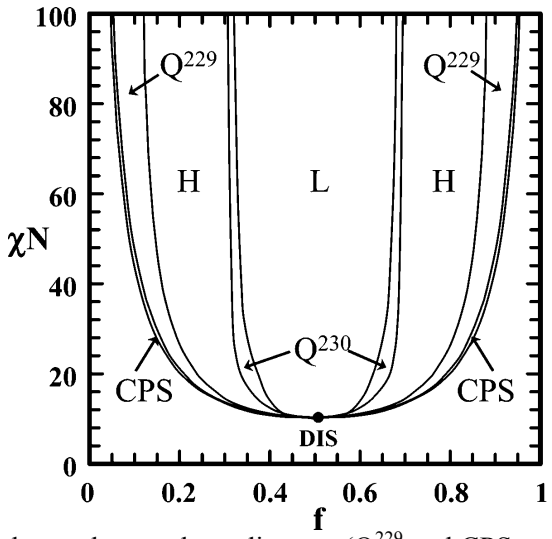

Figure 5.2. Revised diblock copolymer phase diagram (Q^{229} and CPS : spherical phases, Q^{230} : gyroid, H : cylindrical and L : lamella) [187]

5.1.2.2 1D / 2D / 3D confinement effect on block copolymer self-assembly [189]

Surfaces separating the space where copolymers phase-separate from the outside environment also play an important role. Surface properties can be altered by chemical or physical means for phase-separation. For example, surface chemistry can be used to change the affinity of one of the blocks in a block copolymer. Hence, tuning the wettability is effective way to control the confined phase. Chemical modification of surfaces is carried out by adding or modifying substrate functional groups, or by immobilizing polymers as polymer brushes. Asperities can be applied to the surfaces, such as roughening surfaces by chemical treatment or by pressing templates into the surface to create specific surface patterns.

Dimensionality is another crucial parameter for describing confinement. One-dimensional confinement is a thin film in which the substrate surface can be chemically modified to induce wetting of one of the phase-separated domains inside the film (chemical asymmetry).

Examples of two-dimensional (2D) confinement include the inside of electrospun fibrous structure, internal anodic aluminum oxide (AAO), trench structure and nanoimprinted trenches. Similar to the 1D confinement, the confinement surface can be either chemically or physically modified.

Three-dimensional (3D) confinement can be formed by several processes, such as self-organized precipitation (SORP), emulsion and 3D porous template. In this research, we approached the 3D fabrication with femtosecond laser direct writing (2PP), which can fabricate submicron scale with precision.

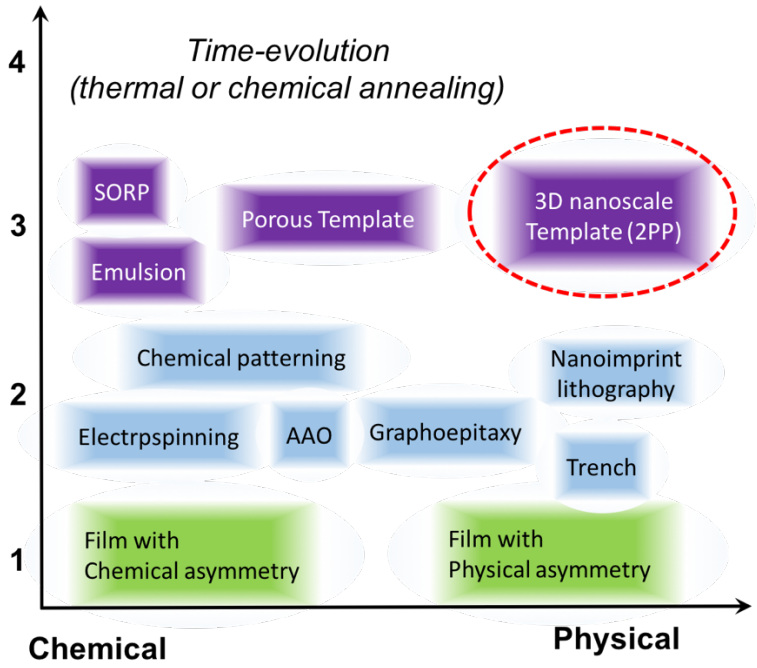

Figure 5.3. Types of confinement with different dimensionality and modification by chemical and physical method [189]

5.1.2.3 Towards functional materials and devices

Block copolymers provide a versatile and potentially low-cost means of engineering nanotechnology-relevant material systems and devices. Block copolymer lithography has been a very strong method in the development of directed self-assembly in thin films. Direct pattern transfer requires appropriate etching contrast between the block copolymer domains. The required etch resistance can be provided by the presence of a suitable, inorganic, etch-resistant species in one block. Pattern transfer can also be performed indirectly by generating a nanoporous film and carrying out a subsequent etch or deposition step. A wide variety of substrates have been patterned in this manner using etched PMMA domains[174, 190]. Finally, templated nanomaterial synthesis in block copolymers has advanced using a variety of materials. P4VP and P2VP[191] are commonly used as they are effective in binding and sequestering a broad range of ions that serve as precursors for synthesis of various elemental metals and oxides. The simplicity of the method has encouraged its broad adoption. In some cases, block copolymer templated synthesis of low-dimensional nanomaterials can now be used as a reliable tool to further other research, rather than being the object of study itself.

5.1.2.4 Block copolymer annealing

Block copolymers are a unique class of polymers that can self-assemble into ordered microdomains with ~10 nm to ~100 nm sizes, appealing mesoscale material. Further treatments of as spun film are used to enhance the ordering of the block copolymer

microdomains, either by thermal or solvent vapor annealing, introducing the mobility to the polymer chain to facilitate microphase separation and annihilation of defects.

5.1.2.4.1 Solvent vapor annealing (SVA)

Among many annealing methods, solvent vapor annealing (SVA) is a low-cost, highly efficient way to annihilate defects in block copolymer[177, 191, 192]. It also facilitates the formation of highly ordered microdomains within short time. Directing the self-assembly of block copolymers leads to the formation of domains with near perfect lateral ordering. Solvent vapor annealing provides means to anneal block copolymers that are sensitive to thermal degradation. Furthermore, the solvent vapor annelaing is generally a more effective method to anneal defects compared to thermal annealing of block copolymers with the same molecular weight. Solvent vapor mediates the polymer/air surface energy and acts as neutral layer to both blocks. By using selective solvent to anneal block copolymer film are exposed to solvent vapor that permeates, asymmetric swelling of block copolymers changes relative volume ratio between block copolymer blocks, thus changing the morphology of the block copolymer film until solvent is totally removed. Order is achieved through the increased mobility of the polymer chains by a plasticization effect (effectively reducing glass transient temperature (T_g)) and reduction of the interaction parameter (χ) through dilution of the polymer chains.
However, a limitation for solvent vapor annealing is that high-temperature and long annealing times are undesirable. More facile and reliable routes to prepare ultrahigh density lamellar block copolymer perpendicular to substrate are needed. And other factors affecting the morphology of a block copolymer film after removal of solvent vapor are selectivity of the solvent, amount of swelling given to block copolymer film, solvent removal rates, film thickness, humidity, and temperature *etc*.

5.1.2.4.2 Thermal annealing (TA)

Compared to the solvent annealing method, thermal annealing can produce well-ordered, low-defect films by temperature gradient and topography features[189, 193]. The fast solvent evaporation (from solvent vapor annealing) traps the block copolymer chain into non-equilibrium, disorganized and poorly ordered states. Thermal annealing is widely used to remove defects in block copolymer thin film. For this process, block copolymers are heated above its glass transition temperature (T_g) of the respective blocks of the copolymer and then held at elevated temperature for a long time until block copolymers were self-assembled with thermodynamically stable state. After this, samples are cooled down to room temperature. The morphology of block copolymer samples depends on the solvent and coating methods. A solvent with low boiling temperature evaporates much faster than a high boiling-point solvent, and the polymer chains have less time to respond to any variation in the solvent concentration; thus, the resultant morphology is kinetically trapped. In contrast, thermal annealing reduces the side effect due to solvent by long time self-assembly with thermodynamically stable state.
Advanced the other type of thermal annealing is zone annealing, which is a fast way to anneal out the defect in the block copolymer thin films. In this method, the samples are annealed by passing them over heating and cooling zone to create a sharp temperature gradient.

5.1.2.5 Etching of block copolymer

To take full advantage of the nanostructures offered by the direct self-assembly of block copolymers, selective pattern transfer techniques with high fidelity are required[176, 189, 194, 195]. Typically, a two-step etching process is needed to transfer the self-assembled block copolymer pattern to other functional materials. In the first step, one block of the block copolymer is selectively removed to make an etch mask. The etch mask is further pattern-transferred to other functional materials in the second step. Selective removal of block A from diblock copolymer (A-b-B) is not a simple task. Most block copolymers are made of organic materials, where etching contrast between different blocks is lacking. Simple oxygen reactive ion etching (RIE) removes both organic polymer blocks at a similar rate, leaving a flat film that is unsuitable for further pattern transfer. Thus, different methods, depending on the chemical structure of block copolymer, have been introduced to selectively remove a minor block but not the other. For inorganic containing block copolymer, the mask fabrication from block copolymers is much easier. The inorganic containing block is resisting to oxygen RIE. A simple oxygen RIE treatment removes organic block, and converts the inorganic block into the inorganic oxides. Among etching techniques, dry etch is typically used as a directional etch process since the etchant gas is ionized by a high radio frequency field and ions are accelerated towards the sample surface by an electrical field. The highly energetic ions can chemically react with the etch mask and substrate, and can also transfer their kinetic energy to physically remove material via a sputtering mechanism. The mask itself determines the lateral resolution of the transferred pattern. However, the achievable depth of etching profile is limited by the thickness of the mask material, the selectivity of the etching recipe, and the etch quality. An undercut below the mask material is one of the main challenges limiting achievement of high aspect ratio etching profiles. Also a limited mask thickness and poor selectivity make pattern transfer difficult. Oxygen gas RIE is commonly employed to oxidize and remove organic polymer materials. A higher radio frequency power increases ion density and thus increases etch rate. Ion milling is basically similar to the RIE etching, but it is a purely directional physical sputtering process. Argon ions are typically used for the ion milling process. Dry etching is the preferred method for pattern transfer, as it is generally more controllable and generates less waste. Furthermore, dry etching avoids capillary induced pattern collapse of small polymer features and shifting of features that can occur with wet processing.

5.2 Ultraprecise 3D structure fabrication using two-photon polymerization (2PP)

Direct laser writing by multiphoton polymerization is laser-based 3D printing technology which allows the construction of readily assembled structures with sub-100nm resolution. Femtosecond laser direct writing has been recently recognized as a promising candidate

of precise fabrication. It is based on the nonlinear photon absorption by photopolymers; the beam of an ultrafast laser is tightly focused inside the volume of a transparent material, causing it to absorb two or more photons and polymerize locally[138, 180]. Compared to general fabrication technique, femtosecond laser direct writing offers superior resolution and does not require additional process such as recoating or layer-by-layer fabrication. However, it is much slower process and requires expensive and specialized equipment. To three-dimensional structure fabrication, scanning a tightly focused laser beam according to designed patterns from the bottom slice to the upside slice. Photons are absorbed in a nonlinear manner (two- or multi-photon absorption) in a volume much smaller than the cubic wavelength. The high spatial resolution of femtosecond laser direct writing is much beyond the optical diffraction limit. The laser light deeply penetrates into a bulk without absorptive power loss, making it possible to tailor materials from inside.

5.2.1 Mechanism of Two-photon polymerization

The principle of 2PP is based on the transparency of the photoresist at near infrared wavelengths [196]. This process can be expressed as multiphoton excitation-induced photochemical reactions:

$$\Delta W_{1PA} = h\nu_1 = 2 \cdot h\nu_2 = 3 \cdot h\nu_3$$

$$h\nu_1 = 2 \cdot h\nu_2 = 3 \cdot h\nu_3$$

$$\lambda_1 = \frac{\lambda_2}{2} = \frac{\lambda_3}{2}$$

For one-photon absorption (1PA) brings the photon energy directly from the ground state to the excited state. In cotrast, simultaneous multiple absorption (*i.e.* two-photon absorption (2PA) and three-photon absorption (3PA)) requires the virtual state(s).

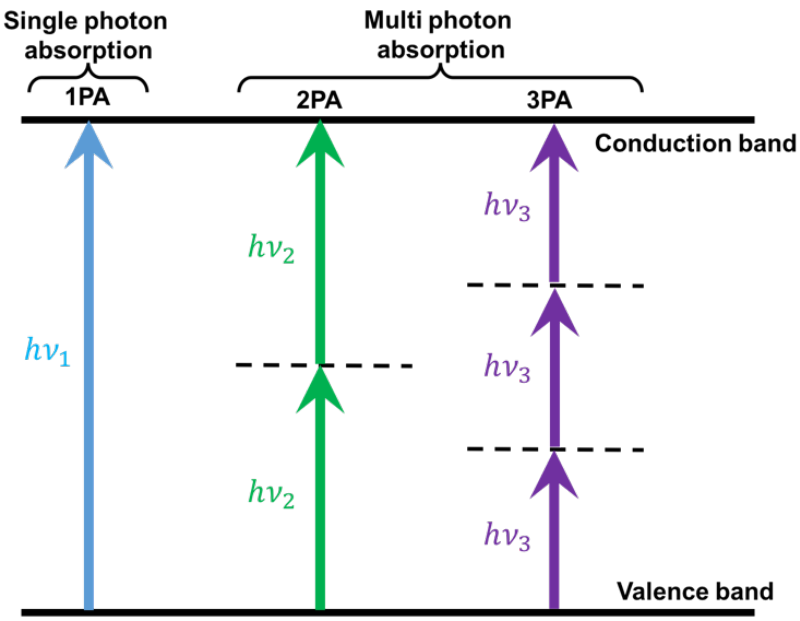

Figure 5.4. Energy diagram of one-, two-, and three-photon absorption (1PA, 2PA and 3PA) (Solid lines : real energy quantum state / Dashed lines : virtual energy quantum state)

In simultaneous 2PA, there is no real intermediate state, but a virtual intermediate state is created by the interaction of the absorbing species with the first photon. The second photon arrives in a very short time (order of femtosecond(10^{-15} sec)) interval so that both photons are absorbed in the same quantum event. In this case, two photons that both carry half the energy of the gap between the two energy levels induce the electron transition. Thus, it is apparent that higher intensities are required for the simultaneous 2PA, which usually requires femtosecond lasers. The probability of n-photon absorption is proportional to the n^{th} power of the photon flux density. Thus, high photon flux densities are required in order to observe this phenomenon.

Femtosecond laser pulse is focused into the volume of a photo-curable material and initiates two-photon polymerization via a two photon absorption (2PA) process. Using this technology, it is possible to fabricate 3D structures with nanoscale precision that are difficult to obtain using conventional miniaturization technologies.

The difference between single-photon and two-photon polymerization lies in the manner the energy is provided. In single-photon polymerization, there is a linear response of the material to the light intensity. However, if the material response is proportional to the square of the photon density, the integrated material response is greatly enhanced at the focal point (Figure 5.5). Even though two-photon transition rate is extremely low, very high spatial resolution can be obtained.

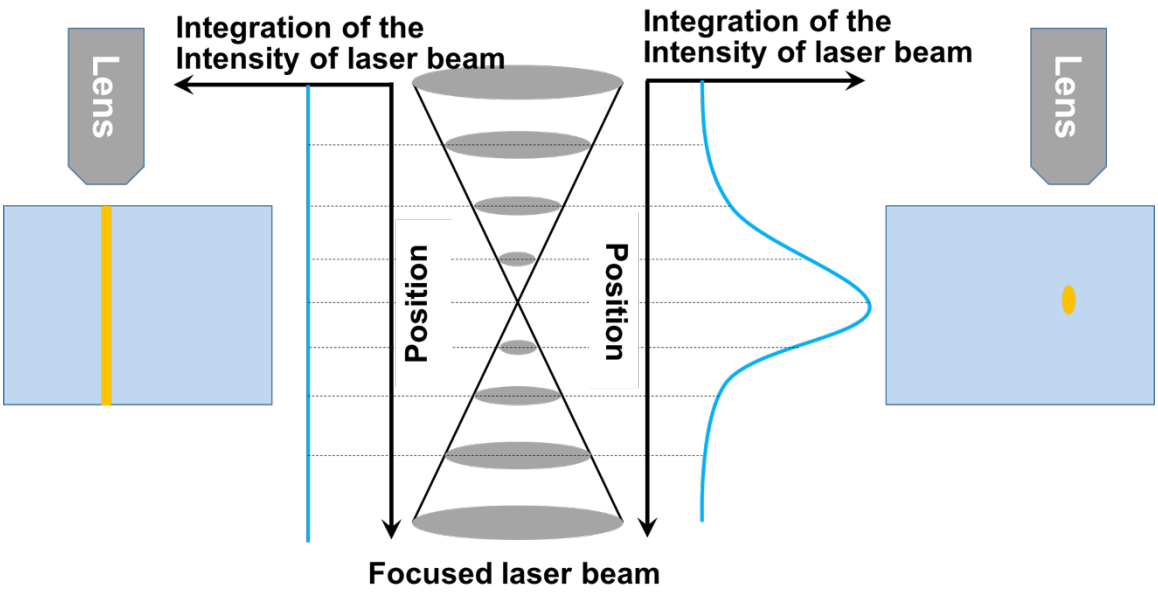

Figure 5.5. Comparison of single-photon and two-photon absorption and integration of the intensity by focused laser beam

The intensity profile of the Gaussian laser beam is

$$I(r_0) = I_0 \exp\left(\frac{{r_0}^2}{{\omega_0}^2}\right)$$

where I_0 is the laser beam intensity at the central axis in the focus plane, r_0 is the radius of laser beam and ω_0 is the radius of the focused beam spot. When a laser beam (with near-IR) of high intensity is focused into the volume of a transparent photo-curable material, two-photon activation has enhanced by the photoinitiator. Excitation by the simultaneous absorption of two-photons, the free radical generated (Initiation step).

Initiation step: $PI \xrightarrow{2h\upsilon'} PI^* \rightarrow\rightarrow\rightarrow R\cdot$

Those radicals formed react with monomers(M), producing monomer radicals that participate in a chain reaction (Propagation step).

Propagation step: $R\cdot + M \rightarrow RM\cdot + nM \rightarrow RM_{n+1}\cdot$

This propagation step will continue until the all monomer consumed or two radical reacted (Termination step).

Termination step: $RM_n\cdot + RM_m\cdot \rightarrow RM_{n+m}R$ or $RM_n\cdot + RM_m\cdot \rightarrow RM_n + RM_m$

Where $2h\nu$ denotes photon frequency in the two-photon excitation, PI is the photoinitiator and PI^* is the excited photoinitiator after absorbing the photon energy, $R\cdot$ is the free radical and M is the monomer. The density of radicals (ρ_R) produced by femtosecond laser pulse, and this varied with square of intensity (I) as

$$\frac{\partial \rho_R}{\partial t} = (\rho_{R0} - \rho_R)\delta_R I^2$$

where δ_R is the effective two-photon cross-section for radical generation.

5.2.2 Resolution enhancement of two-photon polymerization structure

5.2.2.1 Resolution, Threshold and line-width of two-photon polymerization

There are several definitions of the optical diffraction limit or resolution. The Ernst Abbe definition is

$$a_{xy} = \frac{\lambda}{2n \sin \alpha_{diff}}$$

In the above, a_{xy} is the lateral resolution with wavelength (λ), refractive index (n) between the lens and sample, and α_{diff} the half angle of the light cone. The numerical aperture (NA) of an objective lens as a measurement of resolving power

$$NA = n \times \sin \alpha_{diff}$$

Hence, Ernst Abbe definition is rewritten:

$$a_{xy} = \frac{\lambda}{2{\times}NA}$$

For the fine structure fabrication by 2PP, the lateral and axial resolution should be considered. Abbe's definition can be extended to yield the minimum axial resolution:

$$a_z = \frac{\lambda}{n(1 - \cos \alpha)} = \frac{\lambda}{n - \sqrt{n^2 - (NA)^2}}$$

For the ideal case ($\alpha = 90°$), the axial size is 2 times bigger than that of lateral voxel

$$a_z \xrightarrow{\alpha=90^\circ} \frac{\lambda}{n} = \frac{\lambda}{NA} = 2 \cdot a_{xy}$$

To apply this for our setup (wavelength(λ) = 780 nm, numerical aperture (NA) =1.4 and refractive index (n) = 1.518), it is possible to calculate the lateral and axial resolution as

Lateral resolution: $a_{xy} = \frac{1}{2}\frac{\lambda}{NA} = 279\ nm$

Axial resolution: $a_z = \frac{\lambda}{n-\sqrt{n^2-NA^2}} = 838\ nm$

However, Abbe criterion also has limitation since it does not reflect the 2PA. Assuming the Gaussian beam profile, the normalized intensity in radial direction described as

$$I(r_1) = I_0 exp\left(-\left(\frac{r_1}{R}\right)^2\right)$$

where I_0 is the maximum intensity (at the center), R is the intensity spot size defined as the radius where the intensity is $\frac{1}{\mathrm{e}}\mathrm{I}_0$. For the 2PA, this equation change as

$$I^2(r_2) = {I_0}^2 \times e^{-2\left(\frac{r_2}{R}\right)^2} = {I_0}' \times e^{-2\left(\frac{r_2}{R}\right)^2}$$

where ${I_0}'$ is the maximum of the squared intensity. When I_0 and ${I_0}^2$ are both normalized the new width of the profile is smaller by a factor of $\sqrt{2}$.

$$r_{2PP} = \frac{r_{1PP}}{\sqrt{2}}$$

For the 3PA, achievable resolution can be smaller by a factor of $\sqrt{3}$., and intensity and width of the profile would change as

$$I_{3PP} = {I_0}^3$$

$$r_{3PP} = \frac{r_{1PP}}{\sqrt{3}}$$

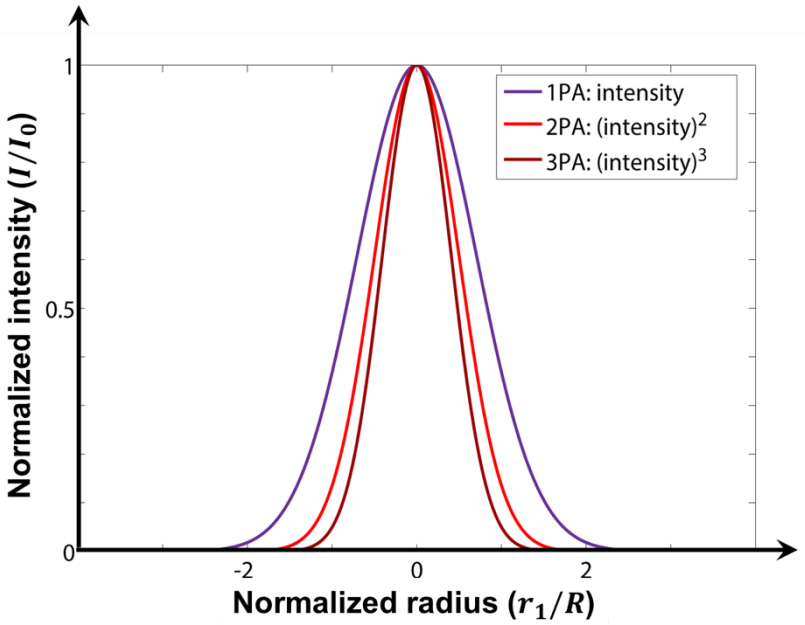

Figure 5.6. Normalized Gaussian intensity profile for 1PA, 2PA and 3PA

The lateral and axial resolution of 2PA can then be given by:

$$a_{xy,2PA} = \frac{1}{2\sqrt{2}} \times \frac{\lambda_{2PA}}{NA} \approx 0.35 \frac{\lambda_{2PA}}{NA}$$

$$a_{z,2PA} = \frac{1}{\sqrt{2}} \times \frac{\lambda_{2PA}}{n - \sqrt{n^2 - NA^2}} \approx 0.71 \frac{\lambda_{2PA}}{n - \sqrt{n^2 - NA^2}}$$

And for 3PA

$$a_{xy,3PA} = \frac{1}{2\sqrt{3}} \times \frac{\lambda_{3PA}}{NA} \approx 0.29 \frac{\lambda_{3PA}}{NA}$$

$$a_{z,3PA} = \frac{1}{\sqrt{3}} \times \frac{\lambda_{3PA}}{n - \sqrt{n^2 - NA^2}} \approx 0.58 \frac{\lambda_{3PA}}{n - \sqrt{n^2 - NA^2}}$$

Energy change can be described as

$$\frac{dW}{dt} = \langle \vec{E} \cdot \vec{P} \rangle = \frac{8\pi^2 \omega_2}{c^2 n^2} I^2 \times Im\left[\chi^{(3)}\right]$$

where ω_2 is angular frequency of an incoming photon, c is the speed of light, n is the refractive index of photocurable material and I is an intensity. The absorption rate therefore depends on intensity as:

$$\frac{dW}{dt}_{2PA} \propto I^2$$

The resolution of feature depends on the size of the focal spot and is limited by diffraction. The minimum feature size cannot be smaller than half the wavelength of the laser. However, 2PA is nonlinear and, resolution beyond the diffraction limit can be achieved. Achievable feature size can be down to 100 nm, which is almost one-order smaller than the wavelength of laser. The basic structure unit volume of focused region (volume pixel, called voxel) has ellipsoidal shape.
The intensity threshold for polymerization is defined as the minimum intensity required for the initiation of the polymerization process leads to irreversible change in the material and the size of the single voxel depends on the irradiation dosage. Using the intensity near the polymerization threshold, we can fabricate high-resolution structures such as multiple scan technique.

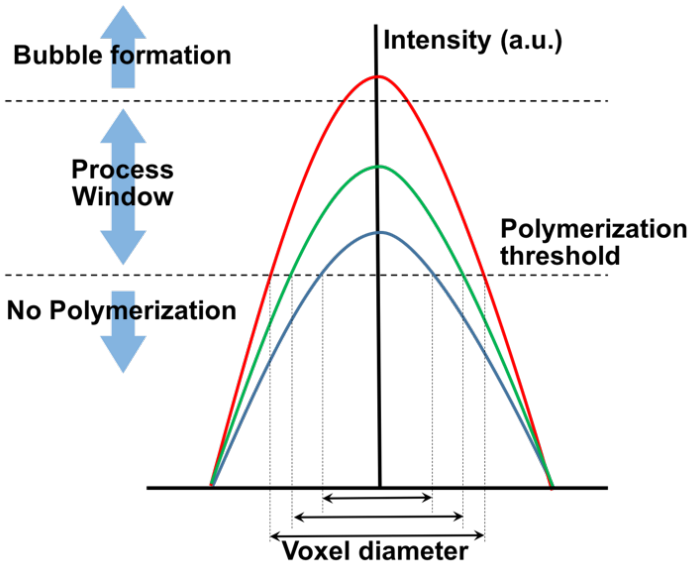

Figure 5.7. Relation between intensity and voxel sizes (Red : 1PA, Green : 2PA and Blue : 3PA)

The threshold sharpness is dependent on the chemical composition of the photo-curable material and directly influences the surface roughness of the developed structure.

$$w_{1PA} \approx \frac{\lambda_0}{\pi NA} = 177\ nm$$

The full width at half maximum is

$$FWHM_{1PA} = \frac{\sqrt{ln(2)}}{\sqrt{2}} \times w_{1PA} = 104\, nm$$

If we correct for the sharper profile for two-photon absorption (2PA) we get

$$FWHM_{2PA} = \frac{1}{\sqrt{2}} FWHM_{1PA} = 74\, n\mathrm{m}$$

Complicated structures are built from voxels that can overlap with each other in the case of femtosecond laser direct writing. The higher precision was technically guaranteed by the following factors: (i) high reproducibility of the shape and size of voxel. The laser pulse energy instability that leads to fluctuation of the voxel size. (ii) high positioning accuracy of voxels due to the usage of piezo moving stage with motion accuracy. (iii) surface quality, particularly for optical components. (iv) another consideration is the development process. Surface Gibbs free energy is expected to be smaller than that at the voxel tip end. The un-polymerized trapped resin is thus difficult to remove in the rinsing process. Furthermore, the locally rugged surface tends to be straightened due to surface tension when the surface starts to be expose to air. The local surface reforming due to the surface tension, also called self-smoothing effect, can significantly improve the surface quality. Femtosecond laser direct writing technology with a particular emphasis placed on a systematic analysis why fabrication resolution far beyond the optical diffraction limit has been achieved. Optical nonlinearity STED (stimulated-emission-depletion): the narrowed spatial distribution of equivalent light intensity), chemical nonlinearity (Quencher: thresholding effect induced photo-polymerization rate out of proportion to the concentratios of radicals), and material nonlinearity (materials shrinkage due to removal of small molecules escape from polymer network in solvents) are another critical factor for high resolution.

5.2.2.2 Resolution enhancement via Quencher diffusion-assisted direct laser writing

There has been a lot of research about improvement of resolution of direct laser writing (DLW) technology. The method which most successfully has increased the resolution not only of single lines but also of 3D structures inspired by stimulated-emission-depletion (STED) fluorescence microscopy. In STED-DLW[41, 197], two laser beams are used; one is used to generate the radicals, and second beam is used to deactivate them. Structures with very high resolution and very small structure with intra layer distances have been fabricated using this approach. However, the installation and maintenance of STED-DLW is complicated, requiring very fine beam control and specialized photoinitiators which not only have high two-photon cross-section, but also high fluorescence quantum efficiency.

However, it is also possible to increase the writing resolution of multiphoton polymerization by employing quencher diffusion-assisted direct laser writing[41]. This is based on the combination of a mobile quenching molecule with a slow laser scanning speed, allowing the diffusion of the quencher in the scanned area, the depletion of the

generated radicals, and the regeneration of the consumed quencher. The material used as quencher is 2-(dimethylamino) ethyl methacrylate (DMAEMA), an organic monomer which is also part of the polymerized structure.
This material has amine moieties, this is the same monomer employed as a metal ligand, to enable the selective metallization. Metallic nanostructures are very interesting due to their potential electromagnetic functionalities. Metallic periodic nanostructures can significantly modify the properties of light with wavelength close to their periodicity, resulting in potential optical applications. To fabricate 3D dielectric nanostructures containing the metal binding material DMAEMA and subsequently selectively metallize them with silver using electroless plating. Electroless plating is a fairly simple process that does not require any specialized equipment.
Addition of this quencher has caused major improvement in the spatial resolution of the written lattices, having not only changed the level of the polymerization threshold, but also affected the polymerization due to diffusion. Depletion by free-diffusing quencher molecules can be an alternative to STED-DLW. The quencher molecules should be small enough and not bonded to the photocurable material so the assumption of free diffusion can be made. When a quencher molecule reacts with a radical it will terminate the chain reaction and be built into the polymer. This can have a significant impact on the properties of the structure. The quenching scales with the quencher concentration and the squared intensity of the irradiation. Diffusion timescale can be estimated by

$$t_{diff} \sim \frac{l^2}{D}$$

where l is the length scale and D is the diffusion coefficient.
To understand the effect of the quencher diffusion during the scan process, basic photo-polymerization model was considered. The evolution of the spatial distributions of the number densities of the quencher molecules (q), free radicals (R_f) and free monomer molecules (M) can be modeled by the following equation set:

$$\frac{\partial R_f}{\partial t} = S(\vec{r}, t) - k_{tQ} q R_f$$

$$\frac{\partial q}{\partial t} = D_Q \, \Delta \, Q - k_{tQ} q R_f$$

where k_{tQ} is reaction rate and S is source, diffusion coefficient of the quencher is D_Q, Δ is the Laplacian. Polymerization rate can be described as:

$$-\frac{\partial M}{\partial t} = k_p R_f M$$

Free radicals are generated as a result of the laser light absorption by the photoinitiator. For 2PA, the source term is proportional to the square of the local field intensity (I), pulse duration (τ) and pulse repetition rate (R_p) as

$$S \propto I^2(\vec{r}, t)\tau R_p$$

As a result of the quenching reaction, both the quencher and the radical are consumed with the reaction rate(k_{tQ}). The polymerization rate (p) is proportional to the monomer number density (M), the radical number density and the propagation constant (k_p).

$$p = \frac{M_0 - M}{M_0}$$

where M_0 is the initial number of monomer. This polymerization rate equation indicates the degree of polymerization.
Having the faster diffusion by orders of magnitude shows that the quencher diffusion can have a significant impact. Depending on the spot size and initial quencher concentration the quencher might be depleted at the center of focus since the diffusing quencher could be consumed on the way into the focus. For this graph, quencher concentration assumed that it is fully depleted at the center of laser focus (Figure 5.8).

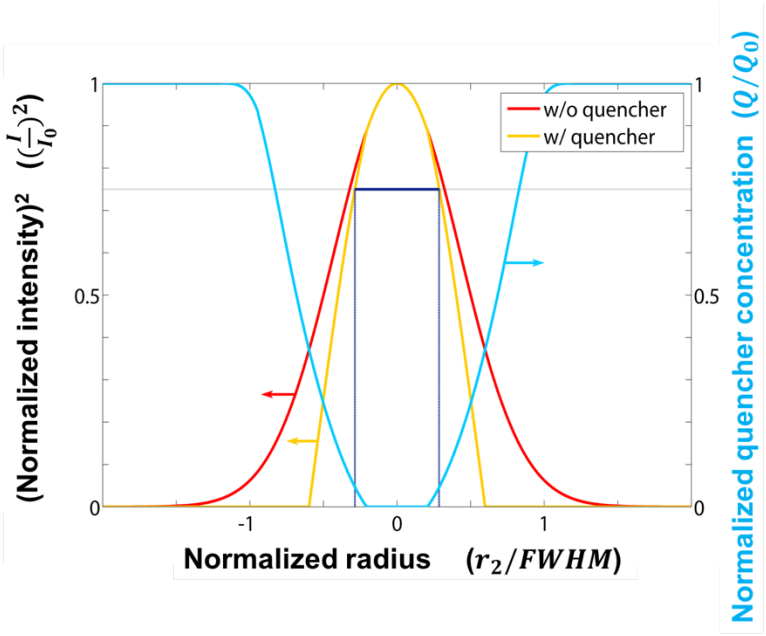

Figure 5.8. Quencher effect and diffusivity. Normalized intensity profile in the material without quencher (Red) and with quencher (Yellow) and quantitative normalized quencher concentration profile (Blue).

If we assume the laser beam with spherically symmetric Gaussian, and radius of the quencher-free domain(r_1) can have calculated as

$$r_1 = L\sqrt{2ln\left(\frac{I_0 L^2}{Q_0 D_Q}\right)}$$

where Q_0 is initial quencher number density. It can be seen that the radius can be made arbitrarily small by tuning the laser beam intensity, since the radical source magnitude is $S \propto I^2(\vec{r}, t)\tau R_p$. For fabrication of high precision structure with small spacing, the polymerization degree is important for achieving high spatial resolution and mechanical stability. The irradiation time does not affect the quencher-free domain size but increases the polymerization degree within the quencher-free domain. Without quencher diffusion, the maximal polymerization degree of a nanoscale feature can be increased by applying higher irradiation dose either by increasing beam intensity or irradiation time (Figure 5.9). In contrast, increase the intensity also increase the polymerized feature size. By employing the diffusion of the quencher, one can handle both the size and the maximal polymerization degree of the polymer feature separately.

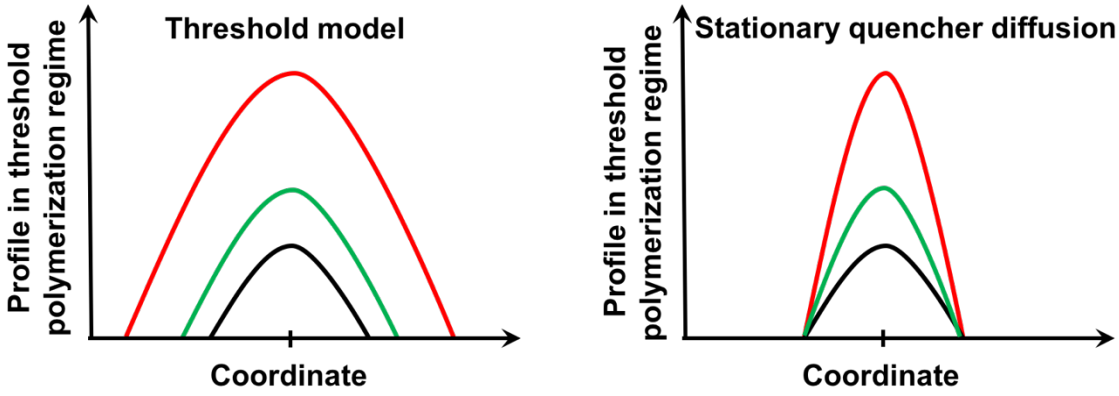

Figure 5.9. Profiles in threshold polymerization regime for different intensity (left) and profiles in model of stationary quencher diffusion (right) for different irradiation times and fixed irradiation intensity

5.2.3 Hybrid sol-gel material

The sol is produced from inorganic or organic precursors, and molecular precursors of the organic moiety blended with photosensitive molecules can give photocurable resins. These photosensitive sol-gel materials are effective for the fabrication of 3D structures by multi-photon absorption. Obvious advantage of inorganic-organic hybrids is that they can favorably combine dissimilar properties of the organic and inorganic components in one material. Sol-gel process is one of the modern methods employed for preparing novel inorganic-organic materials from molecular precursors. This process involves two main

reactions as hydrolysis and condensation. Characteristics and properties of a particular sol-gel inorganic network are affect by the rate of hydrolysis and condensation reactions.

5.2.3.1 Hydrolysis

The reaction is called hydrolysis, because a hydroxyl ion becomes attached to the metal atom as in the following reaction:

$$Si(OR)_4 + H_2O \rightarrow HO - Si(OR)_3 + ROH$$

where R represents an alkyl group and ROH is an alcohol. For coordinately saturated metals in the absence of catalyst, hydrolysis and condensation, both occur by nucleophilic substitution mechanisms. Depending on the amount of water and catalyst present, hydrolysis may go to completion so that all of the OR groups are replaced by OH, or stop when the metal is only partially hydrolyzed.

5.2.3.2 Condensation

Two partially hydrolyzed molecules are linked together, in a process called condensation reaction. By definition, condensation liberates a small molecule, such as water or alcohol:

$$(OR)_3Si - OH + HO - Si(OR)_3 \rightarrow (OR)_3Si - O - Si(OR)_3 + H_2O$$

or

$$(OR)_3Si - OR + HO - Si(OR)_3 \rightarrow (OR)_3Si - O - Si(OR)_3 + ROH$$

This type of reaction can continue to build larger and larger metal containing molecules. As the number of metal bonds increases, the individual molecules are bridged and jointly aggregate in a sol. When the sol particles aggregate, or inter-knit into a network, a gel is formed. Upon drying, trapped volatiles, such as water, alcohol *etc*, are driven off and the network shrinks as further condensation can occur.

5.3 Experimental

5.3.1 Material preparation

5.3.1.1 Zirconium-based photo-curable material (SZ2080) preparation

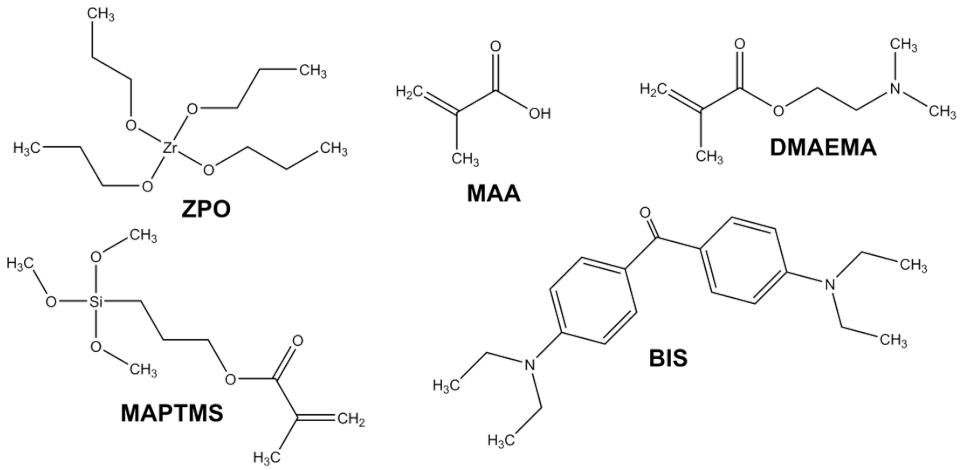

Figure 5.10. Materials for SZ2080 preparation

First, Zirconium propoxide (ZPO) was added to Methacrylic acid (MAA) at a molar ratio of 1:1 and stirred for 30 min. Special care has to be taken that the ZPO transfer from the bottle into the MAA is fast since ZPO deformation such as oxidation. One of the four propyl legs of the ZPO is complexed with the MAA, it changed into (Methacryloyloxy)tripropoxy-zirconium (MAZPO)

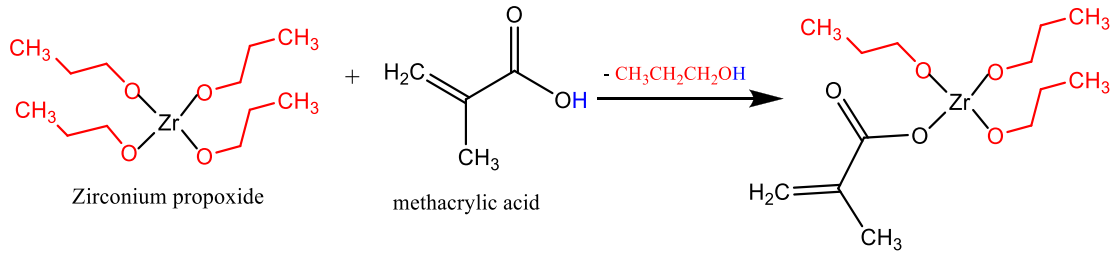

Figure 5.11. Reaction of Zirconium propoxide with Methacrylic acid into MAZPO

While the MAZPO is stirring 3-[(methacryloyloxy)propyl]trimethoxysilane(MAPTMS) is hydrolyzed in a separate vial using a 0.1M HCl solution. The molecular ratio of

MAPTMS : H_2O is 1 : 3. The solution is stirred using a vortex mixer until it becomes clear indicating that the MAPTMS is fully hydrolyzed, shown in Figure 5.12.

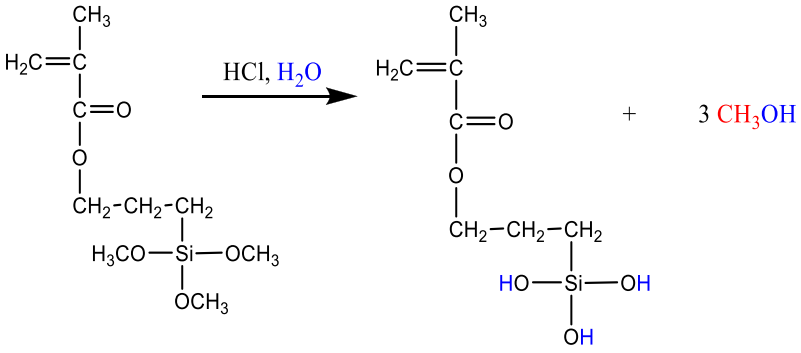

Figure 5.12. Hydrolysis reaction of MAPTMS

Then MAZPO is added to the hydrolyzed MAPTMS at a molar ratio of MAPTMS : ZPO = 4 : 1 and stirred for 30 min. Then water is added at a molar ratio of MAPTMS : H_2O = 1 : 2 and the solution is stirred for another 10 min. Figure 5.13. shows a condensation reaction with one MAZPO and one hydrolyzed MAPTMS. Ratio of MAPTMS : ZPO = 4:1 should enhance the mechanical stability as well as preserve good resolution and development conditions. Please note that the inorganic network of Si-O-Zr is defined by the Si : Zr = 4 : 1 ratio, the way the organic parts form on the other hand is not that simple. In the figure all of the before produced methanol molecules were built into the organic network. Also there would be isopropylalcohol available in excess form previous steps and from the solution of ZPO which might link to the organic network.

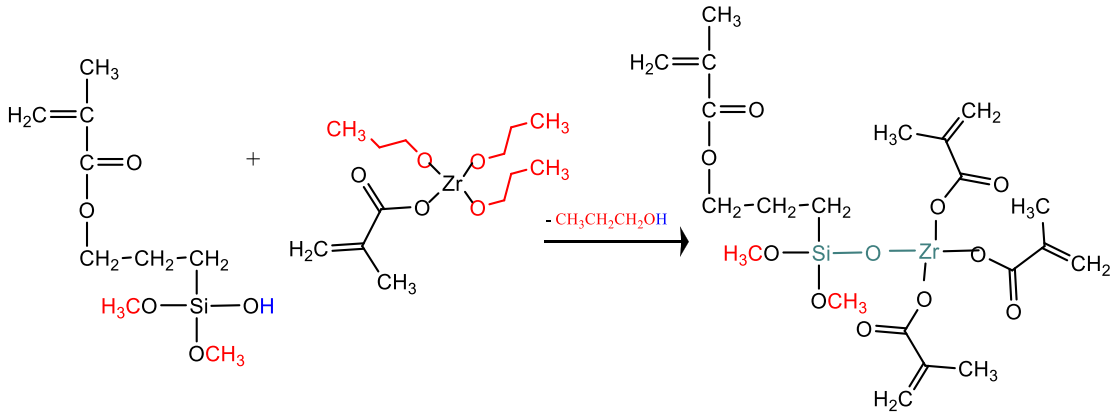

Figure 5.13. Condensation reaction and formation of the inorganic network

To improve the absorption properties of the materialm, photoinitiator 4,4'-bis(diethylamino) benzophenone (BIS) and the quencher molecule 2-(dimethylamino)ethyl methacrylate (DMAEMA), are added, followed by another 15 min of stirring and filtering using a standard Polyvinylidene Fluoride syringe filter (PVDF) with a pore size of 0.22 μm to remove the unsolved (remained) photoinitiator and other dust to hinder polymerization.

5.3.1.2 Glass substrate preparation

For the cleaning of glass substrate, glass substrate sonicated in the acetone for 1 hr. After sonication processing, it is cleaned with 2-propanol for 30 min and deionized water multiple times. To enhance the adhesion between fabricated 3D structure and substrate, additional processing is needed after cleaning process. Sonication of samples in the solution of MAPTMS in the Dichloromethane by the 1 : 80 for 4 hours. After this modified surface cleaned with ethanol over two times

5.3.1.3 Sample preparation

The SZ2080 material was drop-casted or spin-coated onto cleaned and surface-modified glass cover slips and resultant films were dried under vacuum at ambient temperature for three days before 2PP process. The drying process resulted in the evaporation of the solvents and the condensation of the hydroxy-mineral moieties leading to the formation of the inorganic network.

5.3.1.4 Block copolymer sample preparation

For preparation of block-co-polymer solution, block-co-polymer was solved in the Toluene and Tetrahydrofuran (THF) mixture. Quantity of block copolymer is very small, we used the small-diameter glass vial with magnetic stirring bar for efficient mixing. This vial cap should be sealed with Teflon wrapping tape to prevent the solvent evaporation during the stirring. About 12 hours vigorous mixing, BCP solution filtering using a standard Polyvinylidene Fluoride syringe filter (PVDF) with a pore size of 0.22 μm. After filtering, each sample vial cap should be sealed with tefron tape to prevent evaporation solvent for constat solution concentration.

5.3.2 Experimental setup

The laser source was a femtosecond pulsed erbium-doped fiber laser (Toptica, Femtofiber pro NIR, 80MHz, <100fs). It operates mode-locked at 1560 nm primary wavelength and includes a second harmonic generator for a second output at 780 nm. The beam is almost perfectly Gaussian (TEM00) and linearly polarized (> 95%). The laser beam is reflected at a first mirror which is used to correct for a possible beam shift and then passes the first

iris. Setting the two iris, it was able to align the laser beam without distortion. Beam control was achieved by using a fast mechanical shutter (LS6Z2, Uniblitz). Beam intensity controlled by mechanical attenuator (Altechna) is placed which is one piece including a motorized half-wave plate and two Brewster-type thin film polarizers, combination of neutral density(ND) filters. Beam expander (BE-5, Thorlabs) are needed to align the beam concentric with the lens aperture and perpendicular at the same time. A 100x oil immersion lens (Zeiss Plan Apochromat, NA=1.4) was used to focus the laser beam into the volume of the SZ2080. SZ2080 was mounted on the sample holder, and sample holder is mounted on the high accuracy piezo stage (P-611.3 NanoCube® XYZ Piezo Stage, Physik Intrumente) which is then fixed on the long range mechanical stage (M-112.1DG Compact Micro-Translation Stage, Physik Intrumente). Large scale movement was achieved using a mechanical stage. And for small distance during the fabrication, high accuracy piezo stage was used. All system was controlled by the home-made LABVIEW program. The monitoring of the photopolymerization was achieved with a CCD camera, mounted behind a dichroic mirror. As the refractive index of the material changes during polymerization, the green LED light illuminated into underneath of sample, it becomes visible during the fabrication process.

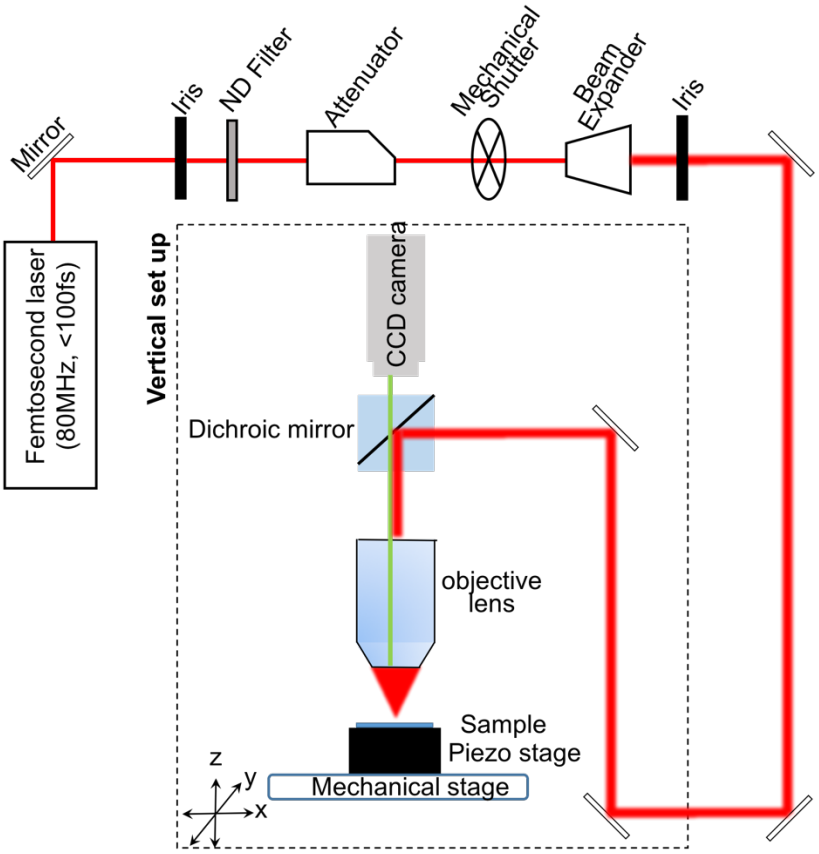

Figure 5.14. Schematic of the experimental setup for two-photon polymerization

5.3.3 Nanoscale 3D structure fabrication

We fabricated 3D template multi-layered woodpile structures consisting of multiple unit blocks. Each unit block has repeated four layers and each layer was composed by one-dimensional rods with stacking sequence. The distance between for adjacent layer is a_z, and within each layer, the parallel rods were separated by distance a. The adjacent layers were rotated by 90° (Figure 5.15).

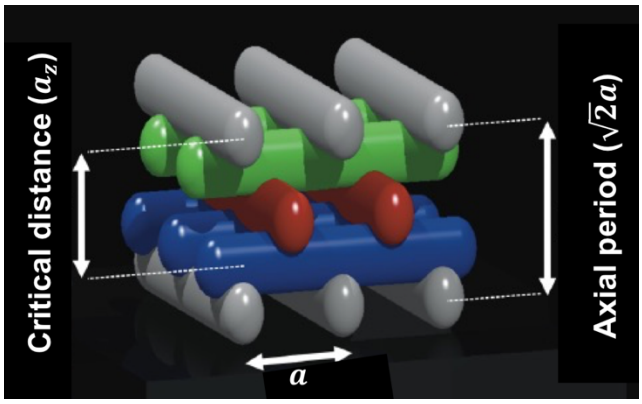

Figure 5.15. Schematic of unit woodpile structure of single unit block

5.3.4 Developing

The last parameter for achieving high resolution structures is development. Most of the solvents do not manage to penetrate inside the complex 3D structures. However, if one manages to fabricate high resolution structures with high integrity, there is no point if it cannot be separated from the unpolymerized material. The unpolymerized material was removed by developing the samples sequentially in 4-methyl-2-pentanone, 2-propanol and dimethyl sulfoxide (DMSO). After the development process, the samples were immersed in a sodium sulfide solution in water. The samples remained immersed for 6 hours in the solution, to form pale yellow nanocomposites. Finally, they were rinsed several times with deionized water and dried at room temperature.

5.3.5 Block copolymer loading on to 3D structure

5.3.5.1 Drop-casting method

The overall objective of this project is to develop 3D architectures over large areas by using the woodpile structures with the directed self-assembly of block copolymers. Filling of block copolymers into the woodpile structures is important and critical process to induce 3D block copolymers morphologies. To obtain well-defined nanopatterns consisting of block copolymers microdomains, including poly(styrene-block-methyl methacrylate) (PS-b-PMMA) and poly(styrene-block-dimethylsiloxane) (PS-b-PDMS) were performed the solvent vapor or thermal annealing.

We devised a method to infuse block copolymer into a woodpile structure. First, a single droplet of block copolymer solution from a syringe is dropped onto the arrays of the woodpile structures. Then, block copolymer solution is covered the entire area of the woodpile structures but the solution moves across the woodpile structures soon with evaporation. Meanwhile, block copolymer is filled into these 3D woodpile structures by capillary force. we have used the tissue (Kimwipes, KIMTECH SCIENCE) for absorbing block copolymer solution after dropping, which increases in velocity of solution movement.

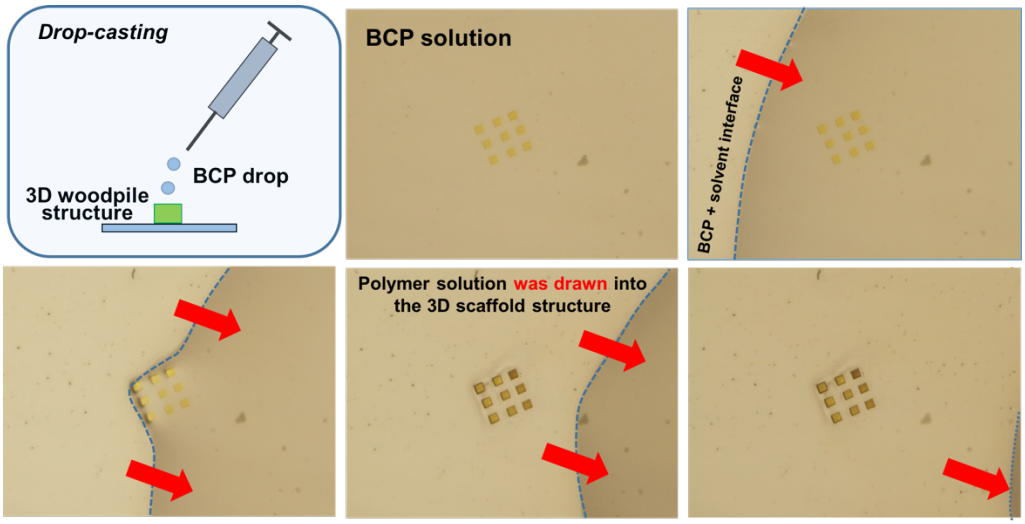

Figure 5.16. Drop casting method for block copolymer loading into 3D woodpile structure

5.3.5.2 Spin coating method

Spin coating is generally used employed to coat the block copolymer thin film on silicon substrate with high uniformity across large areas. This rather simple coating process, however, creates a problem: the fast solvent evaporation traps the block copolymer chain into nonequilibrium, disorganized and poorly ordered states. Further treatments of as spun film are used to enhance the ordering of the block copolymer microdomains, either by thermal or solvent vapor annealing, which introduces the mobility to the polymer

chain to facilitate microphase separation and annihilation of defects. On this experiment, we used the 4000 rpm spin coating speed for 30 sec to reduce the solvent evaporation effect.

5.3.6 Annealing process

5.3.6.1 Solvent vapor annealing (SVA)

After infiltration of block copolymer into the woodpile structure, block copolymer films were placed in a custom-designed solvent vapor-annealing chamber. Tetrahydrofuran (THF) vapor was introduced into the chamber using nitrogen (N_2) as the carrier gas. Two gas streams, a pure N_2 gas and a THF-rich N_2, were mixed before flowing into the annealing chamber, so that the vapor pressure could be controlled. The fraction of solvent vapor in the experimental cell, *i.e.* the partial pressure and vapor pressure of THF, could be varied by adjusting the relative flow rates of the pure and THF-rich N_2. This design also enabled the removal of solvent vapor inside the chamber by closing the THF-saturated vapor inlet and purging the chamber with pure N_2. The rate of solvent removal from the chamber was controlled by varying the flow-rate of pure N_2 into the chamber. Flow rates varied from 5 standard cubical center meter per minute (sccm) to 50 sccm for slow to rapid removal of the solvent, respectively.

5.3.6.2 Thermal annealing (TA)

After infiltration of block copolymer into the woodpile structure, BCP films were placed in a custom-designed solvent vapor-annealing chamber. For the thermal annealing, we used the annealing chamber and maintain the temperature 150ºC for 5days. After 5 days, chamber was purged with pure N_2. The rate of solvent removal from the chamber was controlled by varying the flow rate of pure N_2 into the chamber. Flow rates varied from 5 standard cubical center meter per minute (sccm) to 50 sccm for slow to rapid removal of the solvent, respectively.

5.3.7 Post-annealing process for cross-sectional morphology imaging

One of our approaches to examine the inside morphologies is to break the block copolymer filled woodpile structures. After freezing samples in liquid nitrogen, we used a hand scriber to cleave the samples. For the cross-sectional imaging, O_2 /Ar RIE was performed at 75 W for 5s to 30s in Oxford instrument Plasmalab 80 plus. Flow rate of O_2 and Ar were 20 sccm and 2 sccm respectively, the chamber pressure was 10 mTorr. The

SF_6 and O_2 cryo-ICP etching was performed at 5 W for etching chamber and 1000 W for plasma generator chamber for 5s to 20s in Oxford instrument Plasmalab 150. Flow rate of SF_6 was 34 sccm and O_2 was 16 sccm, chamber pressure was 30 mTorr

5.4 Results and discussion

5.4.1 Ultraprecise 3D structure fabrication (via 2PP)

For imaging of fabricated ultraprecise 3D structure, scanning electron microscopy (SEM) was used. The fabricated structures were coated with 10 nm gold (Au) film using the sputtering system.

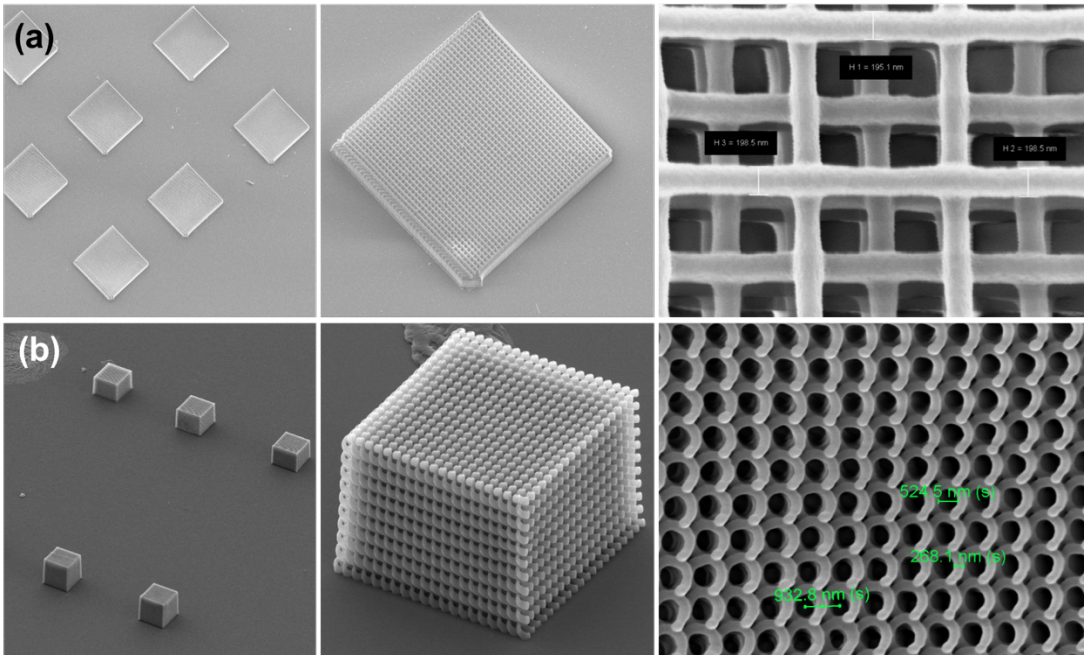

Figure 5.17. SEM images of 3D structure by two-photon polymerization (a) woodpile (b) spiral structure.

5.4.2 Quencher diffusion-assisted direct laser writing

To fabricate smaller and higher resolution structures, quencher diffusion-assisted two-photon polymerization technique used. Different quantity of quencher (DMAEMA) was

mixed, and different fabrication (laser power and scanning speed) was used to find the optimal fabrication conditions. As increase of DMAEMA quantity, thinner structure with higher precision can be structure fabricated due to quencher diffusion effect. However, the obstacle of fabricated structure with higher DMAEMA concentration, its stiffness is too low to maintain their shape due to the higher organic bond percentage. With 10μm/s in scanning speed, and 1.25mW in laser power, we could see the top part deformation with 30% DMAEMA (Figure 5.18 (e)). However, this deformation issue had been solved by increase the laser power into 1.5mW before objective lens (Figure 5.18 (f)). According to the SEM image, fabricated fiber thickness was about 120 nm.

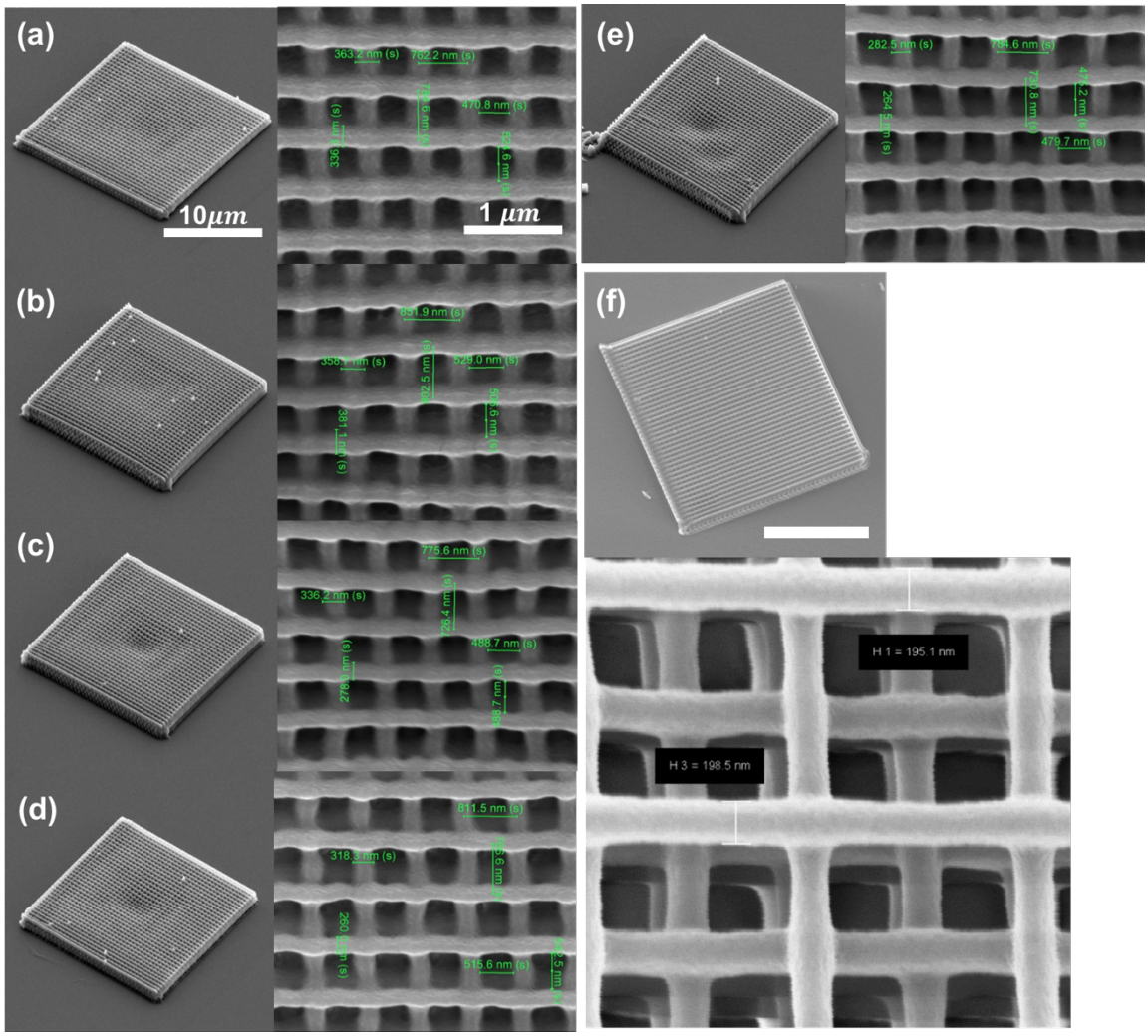

Figure 5.18. SEM image for verification of quencher quantity for 3D 2PP structure fabrication (a) 10%, (b) 15%, (c) 20%, (d) 25%, (e) 30% DMAEMA (10μm/s in scanning speed and 1.25mW in laser power) and (f) 3D woodpile structure with optimal condition (SZ2080 with 30% DMAEMA. 10μm/s in scanning speed and 1.5mW in laser power)

5.4.3 Characterization of block copolymer loading method

Applying the block copolymer into 3D structure need another technique for stable loading. We apply the block copolymer into 3D woodpile structure, and make remained block copolymer soak to the kimwipes to remove the over-dosage block copolymers. However, it was really hard to get the uniform results due to the non-uniform block copolymer loading, and optimal etching condition also changed according to different coating thickness. Top layer thickness of block copolymer is closely related with oxygen etching condition.

When we change the loading method from drop casting to spin coating method, we could get the uniform result (top layer thickness) of block copolymer (Figure 5.20). This process should be quickly completed to obtain well-filled block copolymer by avoiding generation of thick block copolymer film not only on the top surface, but also around the woodpile structure. Generally, the slow movement of block copolymer solution results in a polymer hill around 3D woodpile structure (Figure 5.19 (a)) so that we cannot take full advantage of the woodpile structure as a 3D template directing for block copolymer self-assembly. If evaporation rate of solvent is fast, we can get the clean structure without remained material around the 3D woodpile structure (Figure 5.19 (b)). Otherwise, slow evaporation speed of solvent can make the material remained outside of woodpile structure (Figure 5.19 (a)).

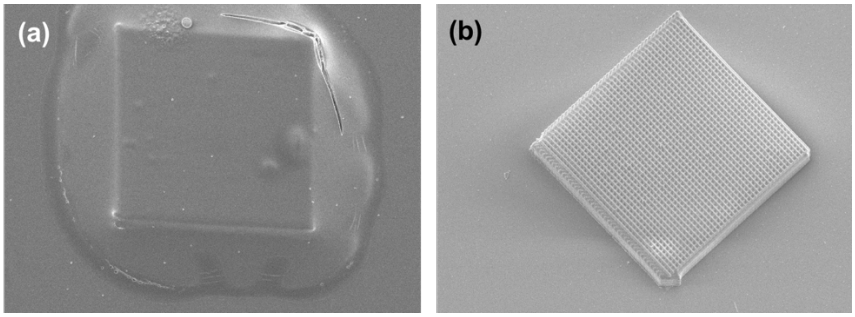

Figure 5.19. Block copolymer loading property with drop casting method with (a) low speed solvent evaporation and (b) high speed solvent evaporation

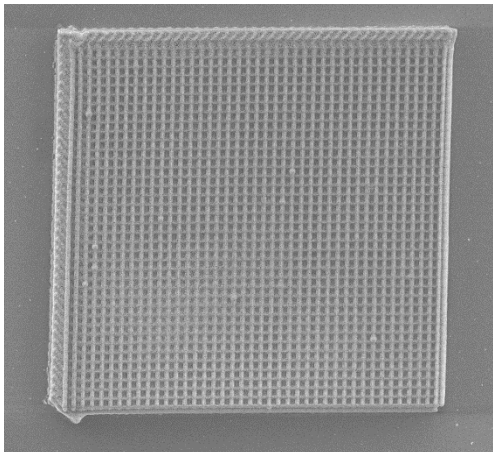

Figure 5.20. Result of block copolymer loading into 3D woodpile structure using spin coating (4000 rpm, 30 sec) method

Hydrophobicity and wettability is important factor for efficient block copolymer loading. To see the hydrophobicity effect by quencher amount of SZ2080, we measure the hydrophobicity on the coated surface. However, there was not distinguishable difference between of them (Figure 5.21).

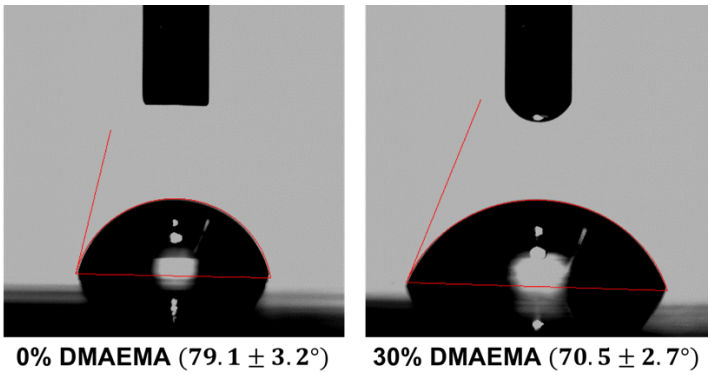

Figure 5.21. Hydrophobicity measurement of SZ2080 coated surface with 0% and 30% DMAEMA

5.4.4 Self-alignment of block copolymer in the 3D nanoscale structure

To obtain well-ordered block copolymer thin films, typically, block copolymer solution is spin-coated on a solid substrate, followed by either solvent vapor or thermal annealing to introduce microphase separation between the two immiscible blocks of the copolymer.

Solvent vapor annealing provides a rapid means to achieve microdomains with a high degree of lateral order, whereas thermal annealing is a rather slow process yielding thermodynamically stable, well-ordered block copolymer morphology without additional re-ordering by solvent evaporation.

5.4.4.1 Block copolymer self-assembly in lower height 3D nanoscale structure

For the reference experiment, we did the same experiment on the lower height of 3D nanoscale structure (with 1-2-3-4 layers) to see the interaction between block copolymer and 3D confinement structure. However, we could not see any distinguishable morphology change of block copolymer (Figure 5.22). With small number of layer (lower height), it is not enough confinement to change the morphology due to 3D confinement. Hence, it shows the similar morphology on the 2D substrate.

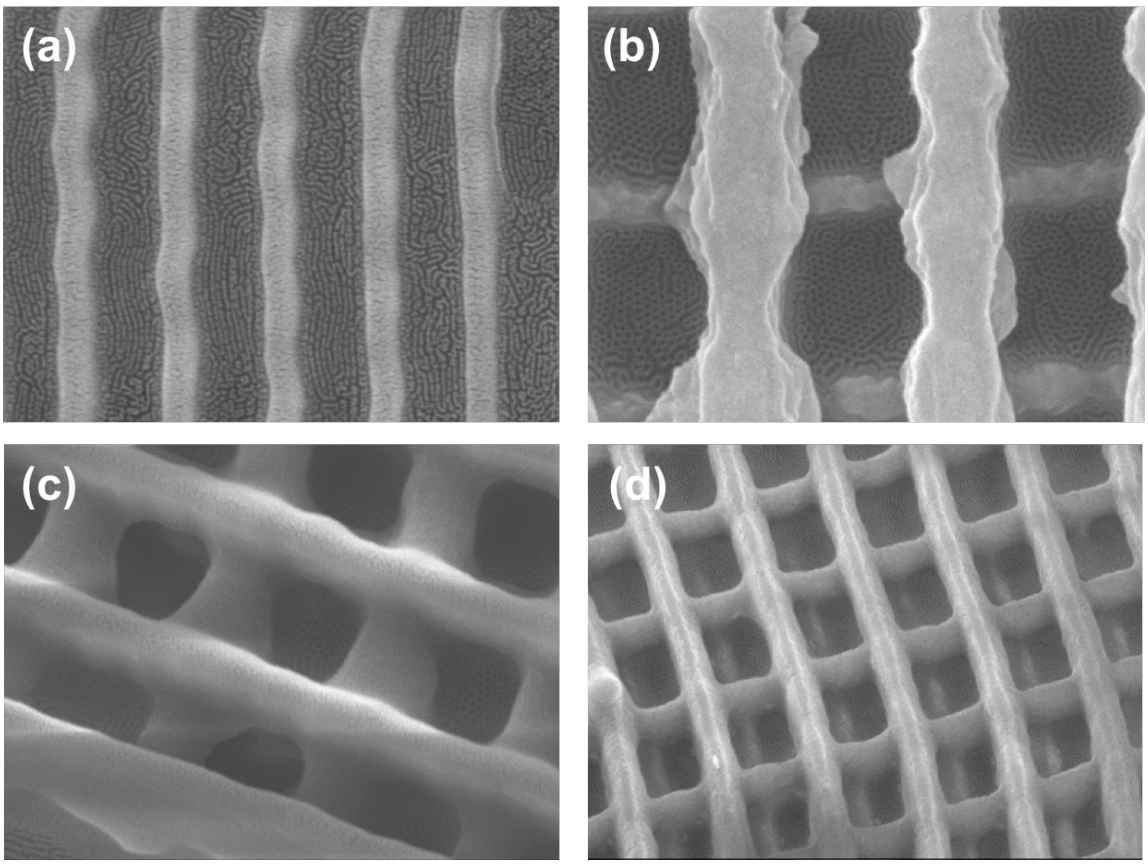

Figure 5.22. BCP self-assembly of the thin structure with 1-2-3-4 layers of WPS

5.4.4.2 Block copolymer self-assembly in higher height 3D nanoscale structure

5.4.4.2.1 Different self-assembled morphology with different solvent

To characterize self-assembly in the higher height 3D nanoscale structure, we applied the Poly(styrene-block-dimethylsiloxane) (PS-b-PDMS (31k-b-14.5k)) into 8 cells (4 layers/cell × 8 cells = 28 layers) structure. Polydimethylsiloxane (PDMS) has a much lower surface energy compared to polystyrene (PS), thus a wetting PDMS layer segregates to the air/polymer interface after solvent vapor annealing. Top coats, which aimed to balance the surface energies for PS and PDMS, were used the cross solvent. A polymer containing maleic anhydride moiety was designed, which, upon annealing, switched its polarity to create a neutral surface for silicon-containing block copolymer, thus allowing the lamellae PS-b-PDMS (31k-b-14.5k) microdomains to be oriented normal to substrate.

And to characterization of solvent effect, we used the different type of solvent (dioxane and acetone) for direct self-assembly experiment in 3D nanoscale structure for PS-b-PDMS (31k-b-14.5k) mixing. As a result, it shows the different type of morphology with different solvent. As a result, it shows the upright cylindrical morphology with dioxane (Figure 5.23), and lamellar morphology with acetone (Figure 5.24). Hence, selection of solvent should be considered for different type of morphology during the solvent vapor annealing.

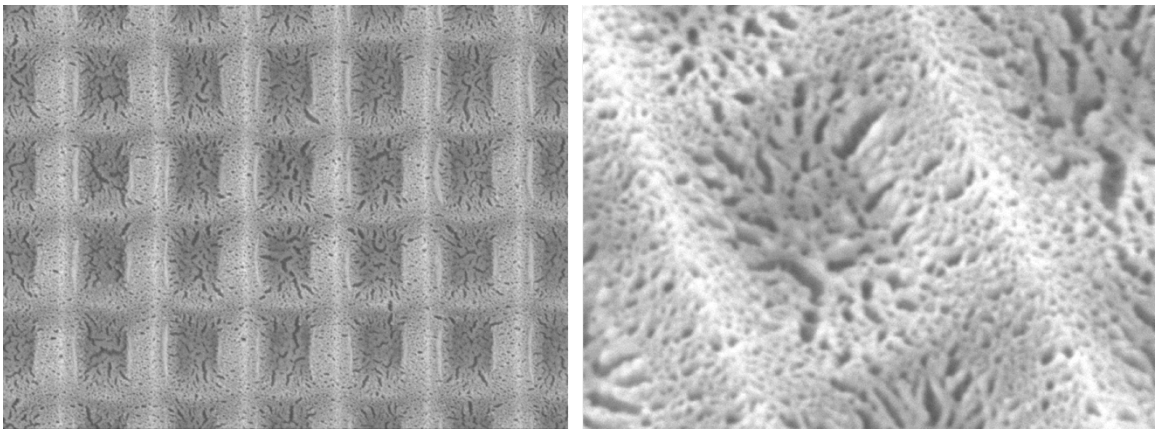

Figure 5.23. SEM images of block copolymer (PS-b-PDMS (31k-b-14.5k) in dioxane) microdomains in the higher 3D structure after solvent vapor annealing followed by CF_4 and O_2 plasma etching

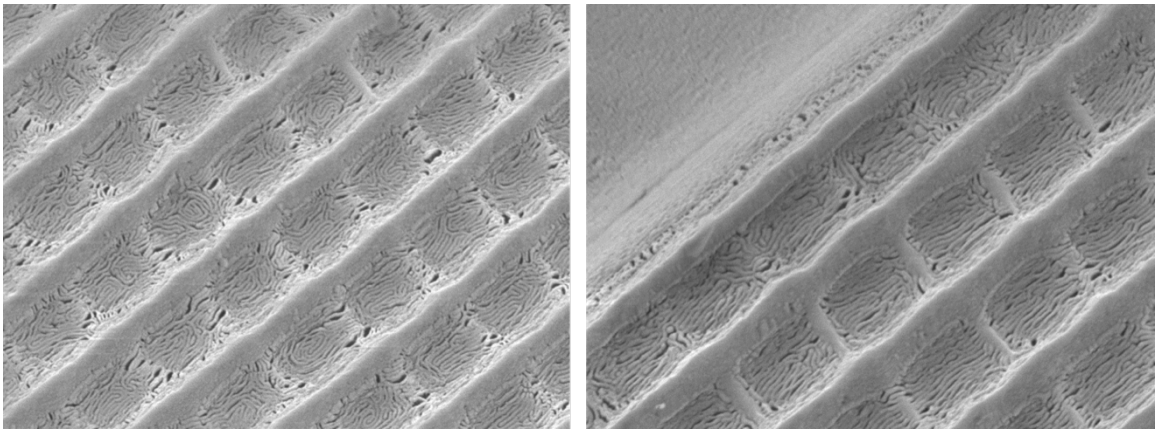

Figure 5.24. SEM images of block copolymer (PS-b-PDMS (31k-b-14.5k) in acetone) microdomains in the higher 3D structure after solvent vapor annealing followed by CF_4 and O_2 plasma etching

5.4.4.2.2 Visualization of cross-section inside of 3D nanoscale structure

After the directed self-assembly of block copolymers in the woodpile structures, the removal of one blocks of block copolymer is generally required to investigate microdomains. In this study, we used oxygen reactive ion etching (RIE) to remove the PMMA block from PS-b-PMMA(38k-b-36.8k) and PDMS block from PS-b-PDMS (31k-b-14.5k) and reconstruct the morphology to enhance contrast.

To visualize the block copolymer morphology inside of woodpile structure, we cleaved the sample after liquid nitrogen dipping. After cleavage of the structure, all direction oxygen RIE process applied to see the morphology. We obtained cylindrical microdomains with parallel orientation on the top surface (Figure 5.25) using PS-b-PDMS (31k-b-14.5k). These microdomains were also observed at the side surfaces, showing stacked hexagonal arrays and line patterns in the vertical direction of the woodpile structure. As a result, it was also possible to know the infiltration of block copolymer into whole 3D woodpile structure.

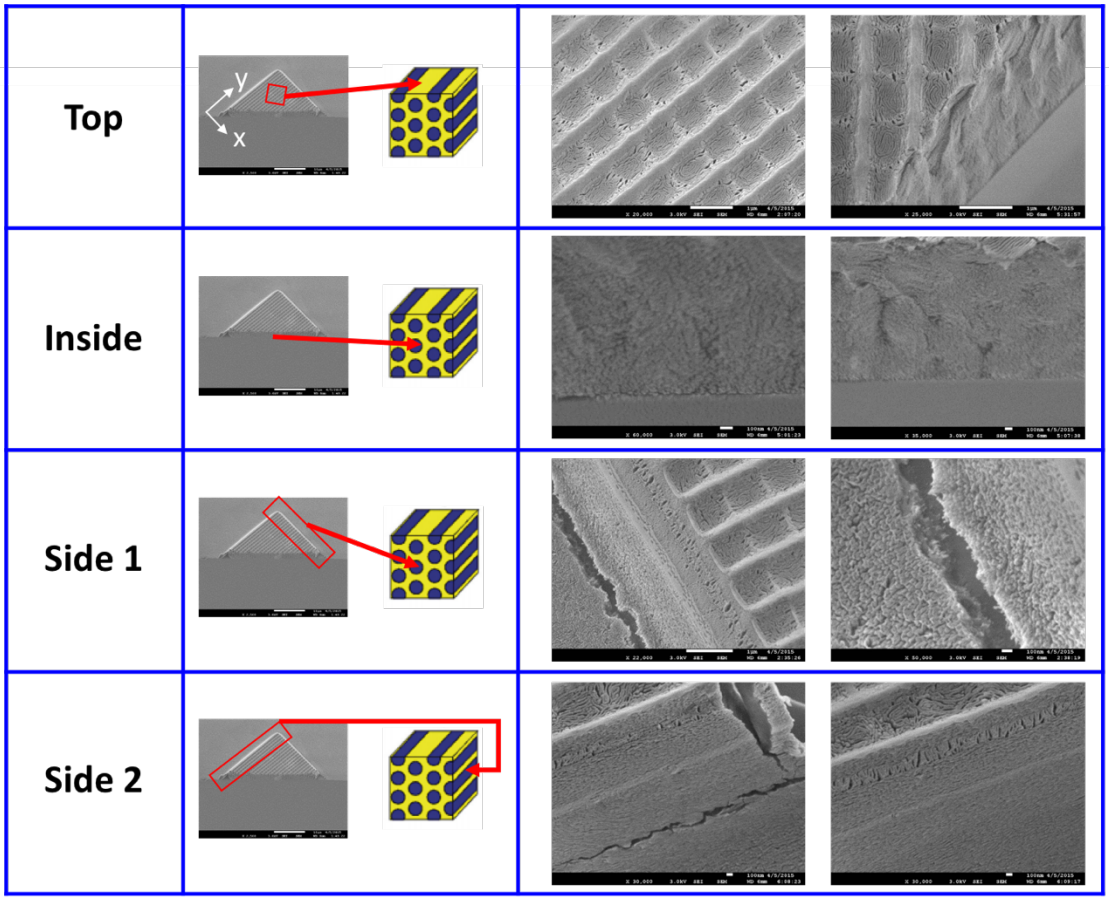

Figure 5.25. SEM images of cleaved 3D structures with PS-b-PDMS (31k-b-14.5k) microdomains in all direction (Top, inside and sides) after acetone vapor annealing followed by CF_4 and O_2 plasma etching

5.4.4.2.3 Preference of one block of block copolymer

We also used the poly(styrene-b-methylmethacrylate) (PS-b-PMMA (38k-b-36.8k)) for direct self-assembly. This block copolymer has distinguishable properties. Poly(methyl methacrylate) (PMMA) cylinder or lamellae in PS-b-PMMA(38k-b-36.8k) block copolymers prefers a parallel orientation to the surface of a silicon wafer due to the preferential interactions of PMMA with the Si-OH at the substrate surface. PMMA block preferentially interact with the 2PP structure with oxide functional group compare to PS block. When we varied the annealing time and the dimension of the woodpile structure, we could obtain in-plain cylindrical microdomains with ring structures (Figure 5.27), well-aligned line patterns along the fibers of the woodpile structure (Figure 5.26), and hexagonal arrays of cylindrical microdomains with perpendicular orientation. We also observed cylindrical microdomain with parallel orientation produced by thermal annealing of PS-b-PMMA(38k-b-36.8k).

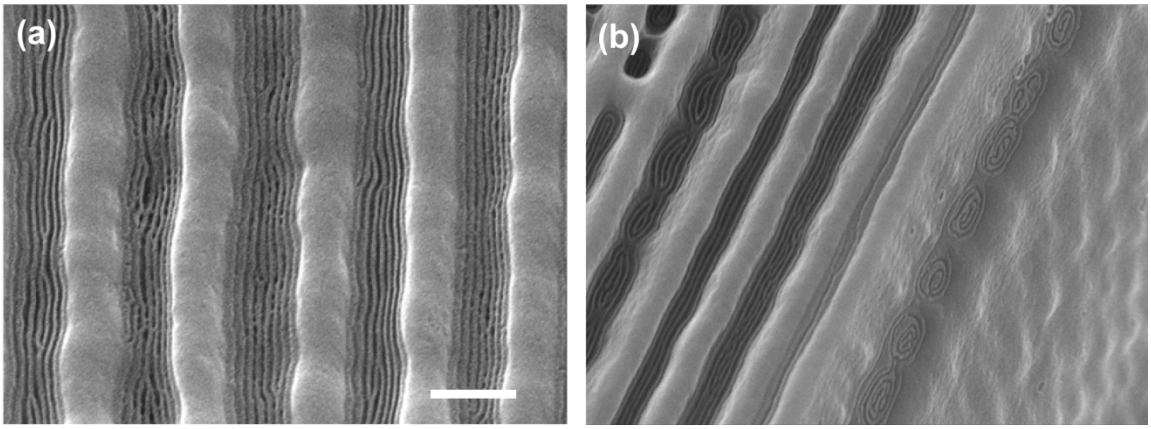

Figure 5.26. SEM images of self-assembly of block copolymer (PS-b-PMMA(38k-b-36.8k)) within the confined line shape pattern. (a) on the line pattern, and (b) edge of woodpile structure (scale bar : 500nm)

Self-assembled PS-b-PMMA (38k-b-36.8k) morphology in 3D woodpile structure with different pitch shows different morphology. In the smaller pitch structure (650-nm pitch), it shows the co-centric circular morphology. By contrast, co-centric rectangular morphology had detected on the wider pitch structure (1000-nm pitch).
However, to figure the 3D confinement effect, visualization of inside cross-section should be conducted.

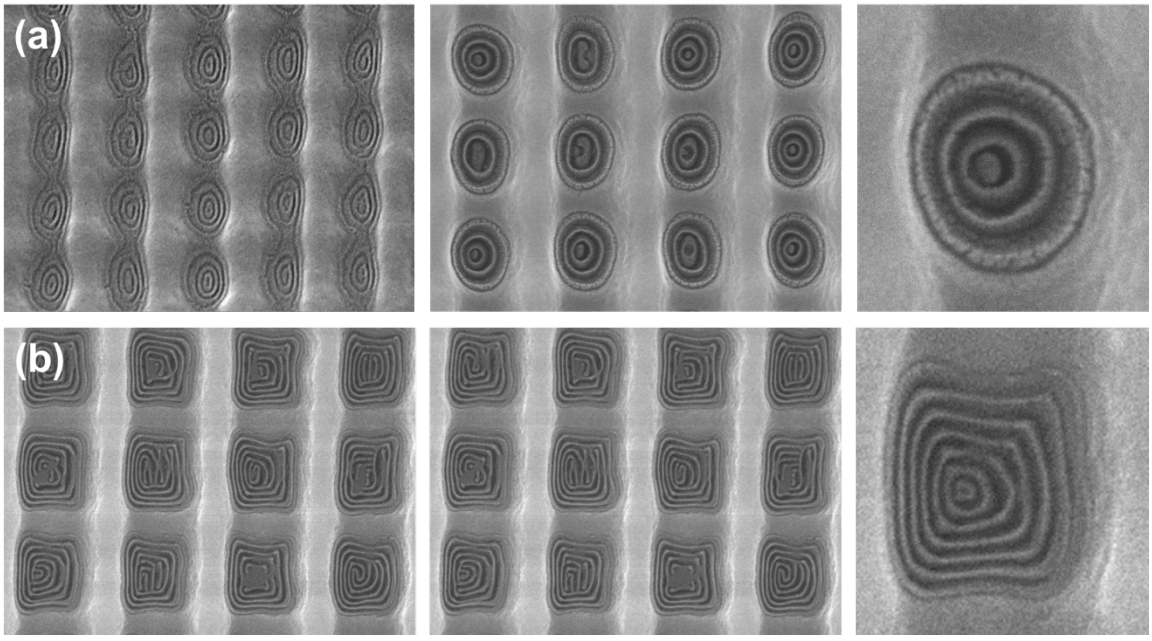

Figure 5.27. SEM images of self-assembled block copolymer (PS-b-PMMA (38k-b-36.8k)) with specific shape with confined structure (a)in-plane ring structure in 3D structure with 650-nm pitch and, (b) in-plane rectangular structure in 3D structure with 1000-nm pitch

5.5 Conclusion and outlooks

The low-cost, high throughput, large area block copolymer lithography has great potential in energy and data storage applications. Further shrinkage of the feature size using photolithography is restricted by both the wavelength of the light source and photoresists. Hence this self-assembly of block copolymer can be a good advanced lithography candidate. While lasers enable multiscale maskless processing over a broad range of resolution. Devices requiring smaller and denser features can be augmented by the directed self-assembly of block copolymers, and it allowed the intrinsic nanoscale arrangement of domains within the mesoscale structure. These 3D structures are ideal scaffolds where, by capillary forces, molten BCPs can be rapidly drawn into the 3D 2PP structure and the preferential interactions of the blocks with the scaffolding directs the assembly of the BCPs, extending the characteristic length scale to the tens or sub-10 nanometer length scale. The periodic microdomain morphology of the BCPs (spherical, cylindrical or lamellar) was directed by the scaffolding, mirroring the construct to nanoscale level. In this work, it was possible to get the self-assembled block copolymer in the 3D fabricated structure by two-photon polymerization. By thermal annealing at temperatures above the glass transition temperatures of the blocks, nanoscale morphologies, biased by the interactions of the blocks with the constructs had been produced by direct self-assembly, amplifying the characteristic length scale of the 2PP construct producing well-defined, nanoscopic morphologies consisting of microdomains of two chemically distinct polymers.

The chemical dissimilarity between the blocks will enable the selective removal on one component to generate a nanoporous, 3D networks that serve as scaffolds and templates for subsequent device fabrication. Alternatively, nanoparticles (NPs) can be preferentially introduced within one of the microdomains, enabling exquisite precision in the 3D spatial arrangement of the NPs. This approach gives rise to unique avenues to generate bi-continuous, two-phase systems or even chiral systems, though neither component is chiral.

Poly(styrene-b-(2-vinylpyridine)) (PS-b-P2VP) is next target material for diverse applications. PS-b-P2VP has much larger, non-favorable segmental interactions enabling access to microdomains that are less than 10 nm in dimension. P2VP is strongly hydrophilic and, will interact preferentially with the oxide framework, enabling a very simple, yet strongly directed self-assembly. Moreover, P2VP can easily be complexed with metal salts and acids, so as to preferentially dope the P2VP microdomains with a range of metals and nanoparticles. Eventually, P2VP can fabricate conductive nanoscale structure which can used for metamaterial to control the light.

To identify the 3D confinement effect on block copolymer self-assembly, we need additional steps to see the inside of woodpile structure. If we use the e-beam lithography to cut the 3D structure with higher height, it usually takes long time for cutting whole structure. Hence, we will use ultrafast pulsed laser ablation to see the cross-sectional morphology.

Chapter 6 Environmentally friendly conductive patterning with laser induced electron transfer for direct reduction and sintering (L-ETRS)

6.1 Introduction

Biocompatible high-resolution direct laser writing method (L-ETRS) has been demonstrated efficient reduction and sintering process for the high conductive silver electrode. This laser based patterning technique could rapidly generate free electrons to reduce the silver ions to nanoparticles, and these reduced nanoparticles were sintered to silver patterns at same time. The main components of precursor solution were silver (I) ions contained in gelatin hydrogel, which can stabilize the silver (I) ions in the solution and easily deposit on the substrate as thin film. To increase the reduction rate of silver (I) ions, redox-active tyrosine was added to the gelatin solution. Moreover, this tyrosine added gelatin-based hydrogel could efficiently transport free electrons to silver, and help to control the particle size of silver nanoparticles when the UV laser irradiates to the precursor solution. In addition, our unique environmental-friendly direct laser writing method can possible to fabricate high conductive silver patterns on both of solid (SiO_2) and flexible (Polyimide) substrates. This environmental friendly solution based direct laser writing method would be applicable in several applications such as flexible display, sensors, solar cells and several other electronic devices.

Laser techniques increase the ability to precisely fabricate functional materials due to the controllability of thermal penetration at low-temperatures. Furthermore, laser processing can directly fabricate functional patterns in local areas on a substrate without any masks, chemical waste, or additional annealing processes. Hence, high-resolution direct laser writing (DLW) methods were developed to fabricate delicate micro/nano sized architectures. Because various functional micro/nano materials can be easily designed and modified into 2D and 3D structures on diverse substrates. Recently, DLW method was shown to be an excellent candidate for fabricating delicate or well-defined micro/nano sized electrode patterns[198]. In previous works, micro or nano metallic electrodes could be patterned on several substrates by using continuous wave (CW) laser. Due to the surface plasmon resonance (SPR) properties of nanomaterials, metallic nanoparticles or nanowires were photothermally sintered for the electrode patterns[199]. The SPR frequency of nanomaterials can enhance the laser beam absorption and eventually increase the local temperature for sintering of nanomaterials. During this process, uniform sized metal nanoparticles or nanowires are essential for the fine metallic patterns. Non-uniformity of nanoparticles or nanowires distribution decreased the electrical conductivity due to the formation of several grain boundaries during the sintering process. Therefore, several polymeric scaffolds or surfactants were applied for fine patterns for efficient sintering process. However, removal of polymeric scaffolds or

surfactants is a critical issue for increasing electrical properties. The polymers are attached to the surface of metallic nano materials and affected the final electrical conductivity. Therefore, several solution-based metal ionic inks have been utilized for the high conductive patters. However, it still remains a challenge to increase the metal reduction rate and final electrical conductivity of those metallic patterns. In biological systems, various functional groups of amino acid in peptides, such as cysteine, histidine, tryptophan and tyrosine can work cooperatively with metal ions to afford efficient catalytic properties[200-205]. Wherein, the free-electrons are easily and effectively generated and transferred by those functional groups of peptide chains to facilitate important redox reactions or bio-mineralization. For example, several inorganic structures or layers are bio-mineralized by functional peptides to protect important organs. In the photosynthesis II system (PS II), especially, tyrosine residues are generated free-electrons, and adjacent histidine and tryptophan residues support the tyrosyl radicals to facilitate long-range electron transportation via a proton-coupled electron transport[204, 206]. Borrowing these ideas from nature, several biological materials have recently been utilized as mild reducing agents in bio-inspired fabrication of metal nanoparticles. Herein, we introduce the innovative fabrication method for high conductive silver (Ag) patterns inspired by biological system of free electron generation and transport. We directly reduced Ag (I) ions with biologically redox-active tyrosine amino acid in gelatin solution (Ag & Tyr / Gel'n) to fabricate fine Ag patterns by using ultraviolet (UV) nanosecond laser. Large amounts of small Ag nanoparticles (NPs) were rapidly generated in Ag (I) ions and tyrosine contained gelatin solution (Ag & Tyr / Gel'n). These reduced Ag NPs were directly sintered into ultrafine Ag conductive patterns by photonic energy from UV laser. Moreover, these fine Ag conductive patterns could be fabricated on different substrates (*i.e.* Polyimide as flexible substrate) with high conductivity.

6.2 Nature-inspired metal reduction using amino acid and peptide

6.2.1 Electron transfer system in the nature

Photosynthetic energy conversion in biological systems is based on charge separation. The electron-transfer reactions involved in the charge separation often occur as a proton-coupled or proton-assisted electron transfer. On the leaf, photosystem II (PS II) [204, 206]of oxygen-evolving organisms a tyrosine group donates an electron to the primary electron donor (P680) and release its phenolic proton to a nearby base when being oxidized. pKa value of tyrosine changes from 10 to -2 upon oxidation, and it cannot hold its phenolic proton in the water solution. Thus, the electron transfer coupled deprotonation and may occur either as consecutive electron transfer/deprotonation reactions or as a single, concerted, reaction step. In PSII the tyrosine group is crucial for stabilization of the primary charge separation.

In aromatic amino acids, tryptophan (Trp) and tyrosine (Tyr) have been the subject of study because of their importance in UV photochemistry of protein[205, 207, 208]. The crucial role of free and protein-bound tryptophan (TrpH) and tyrosine (TyrOH) in the light sensitivity of biological systems has received considerable attention, either following the direct absorption of light with ultraviolet wavelength, and promoted by compoundes acting as photosensitizers. Trp and Tyr are susceptible to UV light and an oxidant, and represent important sites of photo-oxidative damage in proteins. The tryptophan indolyl radical and tyrosine phenoxyl radical often appear in damaged proteins. For example, electron transfer can occur between Trp/O· and Tyr residue in apoenzyme of DNA photolyase[209]. During this process, successive electron transfer between excited FADH· and Trp is important procedure for apoenzyme of DNA photolyase. Therefore, knowledge of the electron transferring properties of tyrosine is therefore of great interest. In this research, photophysical and photochemical behavior of Trp and Tyr under wavelength UV light were used for metal nanoparticle generation from metal ion. Generated free electron during tyrosyl radical formation can be transferred to adjacent metal ion, generating the metal nanoparticle with intense UV light source (i.e. Laser).

6.2.2 Sintering

6.2.2.1 Introduction to sintering

Thermal analysis of laser processes can be used to predict thermal stresses of microstructures. Thermal analysis is also the basis for feedback control of laser processing parameters in manufacturing. Selective laser sintering/melting (SLS/SLM) has become a promising manufacturing route[198, 210, 211]. Because SLS/SLM, a layer manufacturing technique, allows structures to be fabricated without any part-specific tools being required, and it shortens the design and production cycle. This is promising to revolutionize traditional manufacturing processes by significant time and cost savings. Each layer created by scanning a laser spot over the required cross-sectional area by melting, sintering and bonding particles together in a thin lamina. By deposition of further layer on top of the previously processed layer and repeating laser scanning process, subsequent layers are created and simultaneously bonded to already existing layers, 3D geometry can be fabricated. Functionalize the graded materials is promising areas for the application of selective laser sintering.

6.2.2.2 Heat transfer model

Since temperature distribution in laser sintering is important to predict thermal stresses and deformation of fabricated structures [10]. The laser scans on the top layer following a prescribed scan pattern. The heat transfer process consists of thermal radiation, convection, heat conduction between substrate and precursor materials such as particles. The latent heat of fusion is large in selective laser sintering. The complexity brought about by phase change and the corresponding variation of the thermal properties during

selective laser sintering. The most common formulation considers selective laser sintering thermal evolution as a heat transfer process utilizing Fourier heat conduction theory

$$k\left(\frac{\partial^2 T}{\partial x^2}+\frac{\partial^2 T}{\partial y^2}+\frac{\partial^2 T}{\partial z^2}\right)+q=\rho c_{heat}\frac{\partial T}{\partial t}$$

For the initial condition

$$T(x,y,z,0)=T_0$$

Surface convection and radiation:

$$-k\frac{\partial T}{\partial z}=\varepsilon_\theta\sigma\left(T^4-{T_e}^4\right)+h(T-T_{ab})$$

If we assume that no heat loss at the bottom

$$-k\left.\frac{\partial T}{\partial z}\right|_{z=0}=0$$

where T is the temperature, k is the thermal conductivity coefficient, ρ is the density, c_{heat} is the heat capacity coefficient, q is the internal heat, T_0 is the initial temperature of substrate, T_{ab} is ambient temperature, ε_θ is the thermal radiation coefficient, σ is the Stefan-Boltzamnn constant and h is the convection heat transfer coefficient.
In order to better understanding of the SLM process, the simplest laser beam has been assumed to be a point source that is not in conjunction with reality. Assumption that laser beam as the Gaussian beam distribution as

$$I(r)=I_0 e^{-\frac{d^2}{{d_1}^2}}$$

where d_1 is the beam diameter corresponds to the point where the irradiance (I_0) diminishes by a factor of $1/e^2$, and d is the radial distance of a point from the center, similarly, the thermal heat flux ($q(r)$) is modeled

$$q(r)=\frac{2P_L}{\pi{r_0}^2}e^{-\frac{2r^2}{{r_0}^2}}$$

where P_L is the laser power, the spot radius and r the radial distance. The average heat flux (q_m) on the laser spot is,

$$q_m=\frac{1}{\pi{r_0}^2}\int_0^{r_0}q(2\pi r)\,dr=\frac{0.865\alpha P_L}{\pi{r_0}^2}$$

where α is the absorption rate.
The laser beam distribution has been assumed to be either surface or volumetric in nature. To avoid the complexity, the particle has been considered to be a homogenously absorbing and scattering continuum with effective radiation transfer properties equivalent to all surface area. In ray tracing model has been formulated in which the geometry and structure of the particle have been taken into account. The laser beam is taken as the ray which penetrates into the particles, which is reflected and absorbed by those particles. This model allows for calculation of the ratio of the total absorption with respect to the material absorption, laser beam penetration, and more. Volumetric line heat source has been considered with the energy characteristics shown as

$$E_L = \frac{P_L}{v_s}$$

$$E_F = \frac{P_L}{h_s v_s}$$

where E_L is the line energy, E_F is the area energy, P_L is the laser power, v_s is the scan speed, and h_s is the hatch spacing.
Understanding of the interaction between the substrate and laser beam is key to the laser penetration and substrate absorption. The laser energy absorption of a material is known to depend on a number of factors such as the nature of the surface, level of oxidation, the wavelength of the incident laser beam, surface temperature and thermal properties (*e.g.,* density, thermal conductivity, heat capacity and enthalpy). In selective laser sintering, the effective thermal conductivity has been used. Because, thermal conductivity is temperature dependent. The effective thermal conductivity is a function of solid and gas thermal conductivity. The thermal conductivity of the material (k_e) has been expressed as

$$k_e = \frac{\mu k_s}{1 + \Phi \frac{k_s}{k_g}}$$

where k_s is the conductivity of the solid material, k_g is the conductivity of air, μ is the solid fraction ($= \rho/\rho_s$) and Φ is an empirical coefficient.
Rosenthal solutions for a point and line heat source have been proved to be extremely useful in laser-based manufacturing. The three dimensional (3D) Rosenthal's point solution for temperature distribution using a steady state point heat source moving on the surface of a semi-infinite plate along the x axis is given by

$$\bar{T} = \frac{e^{-\left(\widetilde{x_0} + \sqrt{\widetilde{x_0} + \widetilde{y_0} + \widetilde{z_0}}\right)}}{2\sqrt{\widetilde{x_0} + \widetilde{y_0} + \widetilde{z_0}}}$$

where

$$\bar{T} = \frac{T - T_0}{\left(\frac{\alpha P_L}{\pi k}\right)\left(\frac{\rho c_{heat}\, v_s}{2k}\right)}, \qquad \widetilde{x_0} = \frac{x_0 \rho c_{heat}\, v_s}{2k}, \widetilde{y_0} = \frac{y_0 \rho c_{heat}\, v_s}{2k}, \widetilde{z_0} = \frac{z_0 \rho c_{heat}\, v_s}{2k}$$

The 2D Rosenthal's line solution for the temperature distribution using a steady state line heat source moving on the surface of a semi-infinite plate along the x axis is given by

$$T = T_0 + \frac{P_L}{k} f(x',\, y')$$

where

$$f(x',\, y') = \frac{1}{2\pi} exp(x') K_0 \sqrt{x'^2 + y'^2}, \qquad x' = \frac{v_s x}{2k}, \qquad y' = \frac{v_s y}{2k}$$

and α is the absorption rate, P_L is the laser power, v_s is the scan velocity, ρ is the density, c_{heat} is the heat capacity, k is the thermal conductivity and K_0 is the modified Bessel function of the second kind and order zero. The Rosenthal's solution plays an important role in the study of selective laser sintering temperature distribution.

6.3 Experimental

6.3.1 Material preparation

6.3.1.1 Precursor material preparation

The 30 μM L-tyrosine (Sigma) was added to 200 mg gelatin (Sigma Aldrich) contained aqueous solution. The additive amount of 50 ml dimethyl sulfoxide (DMSO; Sigma Aldrich) was added to dissolve the tyrosine in the solution. The 4.7 mmol silver (I) nitrate (Sigma Aldrich) was fully dissolved on 200 ml deionized water. This 200ml silver (I) nitrate solution was added to the tyrosine contained gelatin (Tyr & Gel'n) aqueous solution, and then stirred for 10min in room temperature.

6.3.1.2 Substrate preparation (SiO_2 and PI)

We cleaned the diced silicon oxide wafer using acetone, isopropyl alcohol and deionized water multiple times for the cleaning of silicon substrate. For polyimide film cleaning, we cleaned with isopropyl alcohol in an ultrasonic bath for 30 min and then dried in a vacuum oven at 80°C.

6.3.1.3 Precursor material coating

Before dropping the precursor material (Ag & Tyr/Gel'n), substrates were applied the oxygen plasma for enhancement of wettability. We could get precursor thin film with the uniform thickness after spin coating with 4000 rpm for 60 sec.

6.3.2 Experimental setup

The spin coated precursor film was mounted on the X-Y-Z motorized stage (Aerotech, ANT95-XY-MP and ANT95-50-L-Z-RH) with high precise positioning (Figure 6.1). Patterns were fabricated along the laser beam path with high-repetition rate nanosecond DPSS laser (Pulse duration : ~20ns, repetition frequency : 20 kHz, wavelength : 355 nm, Navigator 1064, Spectra-physics). Laser beam was focused by near UV x100 objective lens (M Plan Apo NUV, NA=0.5, Mitutoyo). The pattern with different width could be fabricated by changing the laser power and scanning speed. The power of laser beam emitted downstream of the objective lens measured by a power meter (Coherent, co.ltd.) and controlled by a half-wave plate ($\lambda/2$) and polarizing beam splitter (PBS). Scanning speed was controlled by the program and computer. Laser processing could change the structural and electronic characteristics of the precursor thin film, the degree of change was tunable by varying the laser parameters such as laser power and scanning speed.

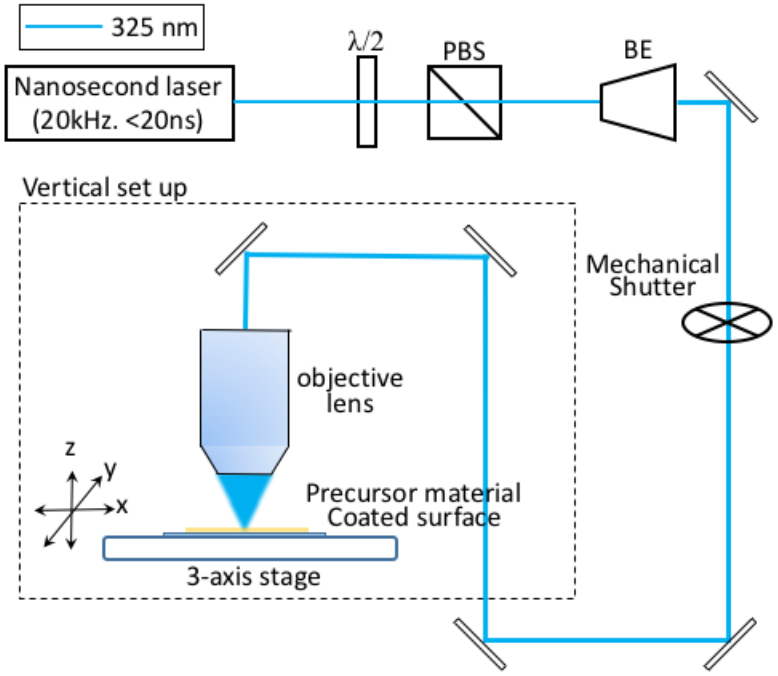

Figure 6.1. Schematic of experimental setup

6.3.3 Post-processing of patterning

To remove the unpatterned part, we used the characteristic of precursor material. We used the gelatin as backbone material, and this gelatin works as control of generated nanoparticle sizes. Addition to this, thin layer of gelatin can be dissolved in the water by swelling. Using this characteristics, we put the substrate after fabrication to remove the unpatterned surface. For the efficient removal of precursor material (gelatin and silver solution), we heated the deionized water about 60°C, and put the sample for 1min.

6.3.4 Characterization of silver nanoparticle formation

Aliquot (20 μl) of the Ag NPs containing gelatin solution was deposited on a carbon-coated copper grid (200 mesh) and air-dried for 12 hr. The prepared transmission electron microscopy (TEM) grids were kept in a desiccator before TEM imaging to ensure the removal of moisture. Then, the microscopic images were observed at 80 kV using a JEOL JEM-1010 transmission electron microscope.

6.3.5 Characterization of pattern

To verify the reduced/sintered silver pattern, we used the scanning electron microcopy (SEM; FEI XL30, Phillips Co.) with energy-dispersive X-ray spectroscopy (EDX; Hitachi 2460 with KEVEX) analysis was carried out at Biomolecular Nanotechnology Center of University of California at Berkeley.

6.3.6 Conductivity measurement of conductive pattern

The resistance was measured using a two-probe technique with a semiconductor parameter analyzer (HP4155A) at room temperature. To reduce the contact resistance between the sintered patterns and probe tips, silver paste was applied at each end of sintered line.

6.3.7 Conductive patterning on the flexible substrate

For checking the bending effect, we fabricate the pattern on the polyimide substrate. To reduce the deformation of substrate, we selected the flexible substrate material as polyimde and patterned on this polyimide. For the efficient patterning,

6.4 Results and discussion

6.4.1 Verification of particle generation by photochemical process

With optimal concentration condition, we could get the large amount of homogeneous Ag NPs (size is approximately 10 nm to 20nm) can be generated in our tyrosine contained gelatin precursor (Ag & Tyr/Gel'n) solution (Figure 6.2). However, non-uniform size nanoparticle was generated in the solution without gelatin.

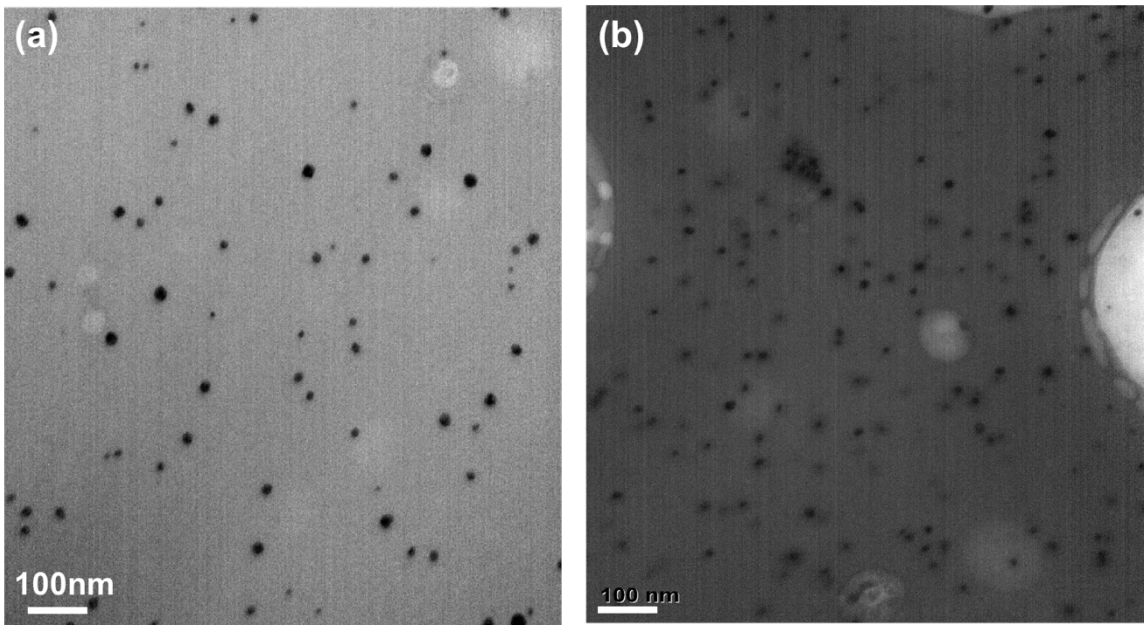

Figure 6.2. TEM images : Silver nanoparticle generation (a) without gelatin and (b) with gelatin

Gelatin works as the enhancing material for electron transfer, and stabilizing material for metal ion by cheating mechanism. Homogeneous nanoparticle distribution is a critical factor for conductive patterning. Without gelatin, we could not fabricate the highly

conductive pattern due to the non-uniform nanoparticle size. In contrast, with gelatin, we could fabricate the conductive pattern which is fully connected and sintered.

6.4.2 Conductive pattern fabrication

For the simultaneous direct Ag (I) ion reduction and sintering, we applied 20 ns pulse nanosecond laser with ultraviolet UV wavelength (355nm) to fabricate fine Ag patterns. This process is based on both photochemical and photothermal reactions. When UV laser beam is irradiated into Ag thin precursor film, Ag (I) ions were photochemically reduced into Ag NPs rapidly, and these reduced Ag NPs were photothermally sintered to massive Ag aggregates at the region of laser beam focused. Therefore, we can easily fabricate or modify the Ag patterns shape without additional mask modification process.
For the efficient pattering process, the conversion rate of Ag NPs from Ag (I) ion is critical for ultrafine sintered Ag pattern. To increase the reduction rate of Ag (I) ions into Ag nanoparticles, we applied gelatin as a scaffold. Gelatin is a representative soluble biological protein, which can reduce and stabilize the metal nanoparticles (Figure 6.2). Because, gelatin is an ideal biomaterial for bio-templating metal NPs due to the functional side groups including amine (- NH_2), hydroxyl (-OH), thiol (-SH) and carboxyl (-COOH) in polypeptide chains. These functional groups can effectively donate and transport the electrons to metal ions. Sintering process is critically depending on the nanoparticle sizes (R_{NP})[212-214] as

$$\Delta T_{max} \propto R_{NP}^2$$

The required temperature for nanoparticle melting (ΔT_{max}) depends on the nanoparticle sizes (R_{NP}). As increase the size of nanoparticle, higher temperature is required for melting and sintering. Hence, non-homogeneous size of nanoparticle induces the non-uniform pattern due to the different melting temperature. Therefore, controlling the nanoparticle size is significant in nanoparticle-based thermal sintering process.

6.4.3 Characterization of pattern

6.4.3.1 Micro-scale silver patterning using electron transfer of amino acid

To characterize the sintered Ag patterns, we conduct scanning electron microscopy (SEM) and energy-dispersive X-ray spectroscopy (EDX). With amino acid (tyrosine or tryptophan), well-connected pattern can be fabricated with intense UV light source, and optimal conditions such as concentration of silver ion, amino acid (tyrosine and tryptophan), scanning speed and laser power. For the stable fabrication, those parameters were considered, and verify through SEM and conductivity measurement. With optimized chemical condition (4.7M Ag(I) ion and 44μM tyrosine), 5μW of laser power

and 20μm/s of scnning speed, we could get the well-connected silver sintered pattern (Figure 6.3). To verify the material composition after sintering process, we took the EDX (Figure 6.3 (c)).

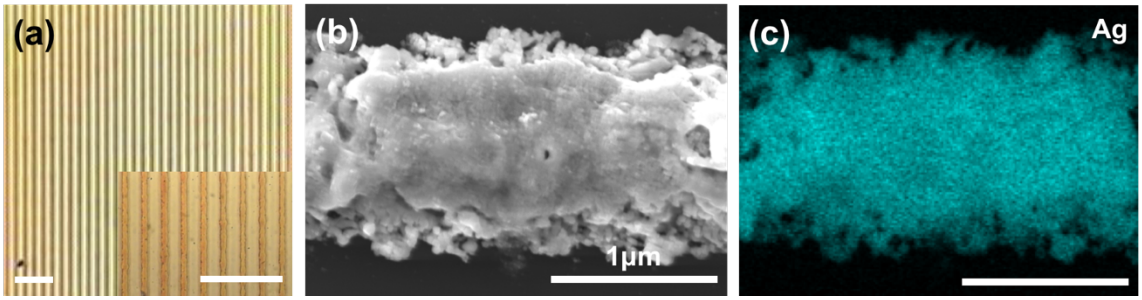

Figure 6.3. Sintered silver (Ag) pattern images. (a) objective microscope (scale bar : 20μm), (b) SEM and (c) EDX (scale bar : 1μm)

6.4.3.2 Micro-scale copper patterning using electron transfer of peptide

Using only amino acid, reduction efficiency is relatively lower than that of peptide (YYCACYY). Peptide has cysteine-alanine-cysteine sequence for efficient electron transfer. For comparison of efficiency of reduction, we used the 1/4 quantity of peptide to match the same quantity of silver patterning. As a result, it was not possible to fabricate copper pattern with only tyrosine. However, when we used the peptide for copper patterning, copper pattern can be fabricated (Figure 6.4). Hence, we found that electron transfer efficiency of peptide is higher than that of amino acid.

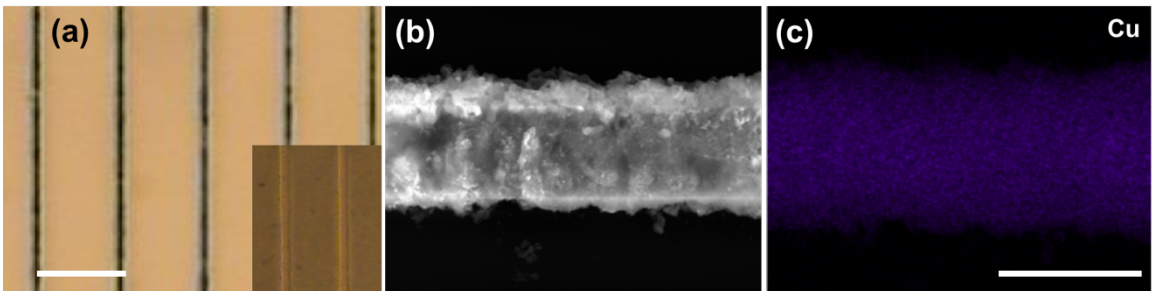

Figure 6.4. Sintered copper (Cu) pattern images. (a) objective microscope (scale bar : 5μm), (b) SEM and (c) EDX (scale bar : 1μm)

6.4.4 Optimization of parameters for stable patterning

6.4.4.1 Laser fabrication condition (Laser power and scanning speed)

Controlling the scan speed and laser power is critical for fine metallic patterns fabrication in our L-ETRS pattering process. Without enough photonic energy, Ag NPs cannot be generated from ion state precursor, and sintering process cannot occur effectively. In contrast, excessive irradiated laser power can be induced the deformation of patterns and substrates, and get the bimodal structure. Therefore, we control the laser power density and scanning speed to find optimal conditions of L-ETRS pattering process to avoid thermal damage of Ag patterns. Reduced Ag NPs were not effectively sintered with scanning speed over than 50 μm/s. With scanning speed of 20μm/s, we could fabricate fully connected fine Ag patterns (Figure 6.3 (a)). As decrease the scanning speed from 20μm/s to 0 μm/s, bi-nodal structure has been noticed due to movement of center material to nearby (Figure 6.3 (b)-(d)). Finally, we optimized the condition of our L-ETRS pattering method for fine Ag patterns (laser power: 5 μW, scanning speed: 10 μm/s with 2times scanning).

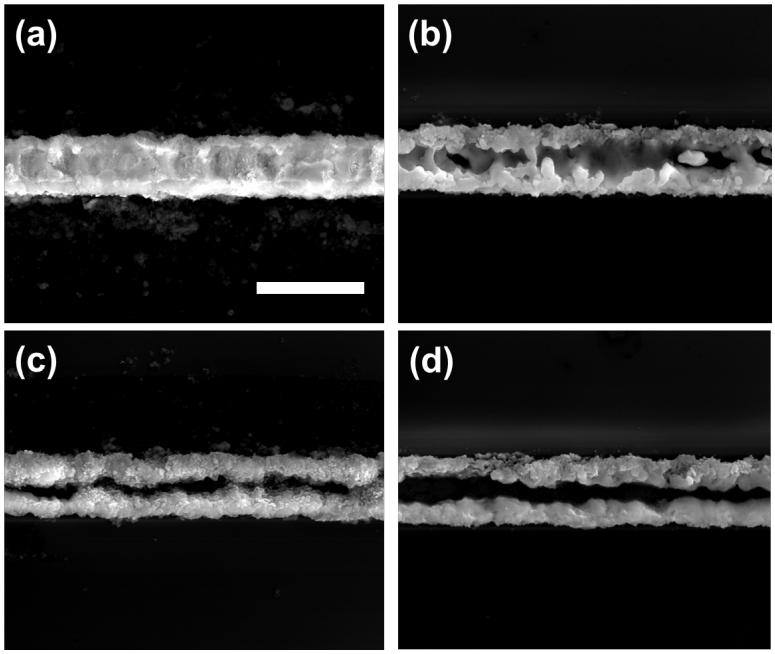

Figure 6.5. Bi-nodal sintered silver pattern with 5μW laser power and different scanning speed (a) 20μm/s, (b) 10μm/s, (c) 5μm/s and (d) 1μm/s (scale bar : 2μm)

6.4.4.2 Precursor material compositon

6.4.4.2.1 Gelatin

For the backbone material, gelatin was used. Gelatin also has tyrosil group, and this also enhance the chelating the metal ion. This also can be transfer the electron efficiently

through tyrosyl functional group. Due to those effect, gelatin help to generate the homogeneous size of nanoparticle stably and efficiently. Without gelatin mixture, well-connected pattern doesn't generate due to the non-homogeneous size nanoparticle generation. Hence, for the stable reduction and sintering, concentration ratio between gelatin and silver ion/tyrosine should be considered.

6.4.4.2.2 Silver ion and tyrosine / tryptophan concentration

On L-ETRS process, we found Ag (I) ion, tyrosine and gelatin concentration is critical for the fine Ag patterns. For metal ion reduction and sintering process, concentration of tyrosine/tryptophan is critical for well-connected sintered pattern. First of all, without tyrosine/tryptophan, only Ag (I) ion and gelatin mixture solution (Ag / Gel'n), the reduction rate of Ag NPs was very slow to fabricate large amount of Ag NPs, and sintered Ag patterns were not fully connected. To increase the reduction rate of Ag NPs, small amount of UV-active tyrosine was added to Ag (I) ion / Gelatin solution as a photochemical reducing agent. As a result, the sintered Ag patterns were fully connected as fine patterns by adding tyrosine. These fine Ag pattern was capable to use as high conductive electrode.

In particular, the concentration of Ag (I) ion is most significant for the fabrication process of fine Ag patterns. For verification of relationship between Ag (I) ion concentration and pattering process, we change the concentration of Ag (I) ions from 0 M to 4.7 M with constant tyrosine concentration (44 μM) with optimized patterning condition. With low concentration of Ag(I) ion, it was not able to fabricate the full-connected Ag patterns. Thus, the conductivities were sharply decreased in Ag (I) ion concentration below 4.7 M. We also change the concentration of tyrosine and gelatin in the precursor solution. We changed the tyrosine concentration from 0 μM to 44 μM in the precursor solution to find the optimized concentration of tyrosine in enough Ag concentration (4.7 M). We found the rate of Ag NPs generation varied depending on the concentration of tyrosine and gelatin. In addition, we found that at least 30 μM of tyrosine was required for the fine Ag patterns with high electrical conductivity. Lower than this concentration, Ag patterns were not fully connected and the conductivities were exponentially decreased.

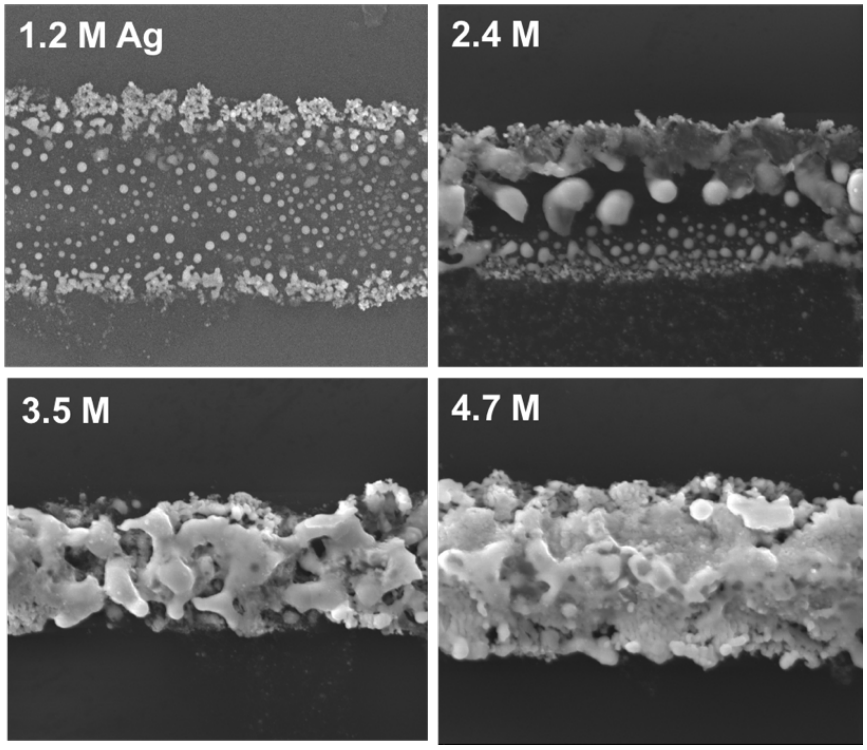

Figure 6.6. SEM imaged of sintered silver pattern with different concentration of silver ion (with 44 μM of tyrosine, 5 μW in laser power and 20 μm/s in scanning speed)

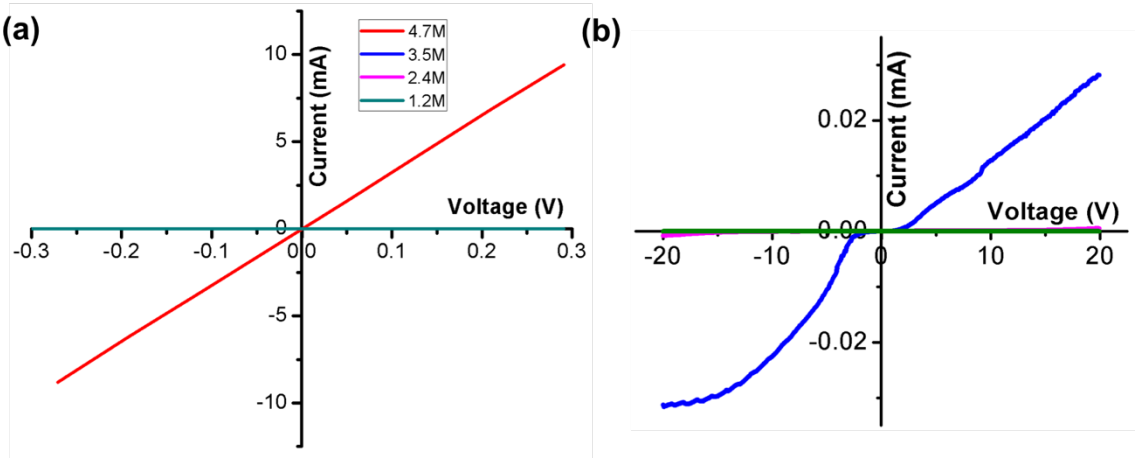

Figure 6.7. Conductivity of sintered silver pattern with concentration of silver ion (with 44 μM of tyrosine, 5 μW in laser power and 20 μm/s in scanning speed). (a) conductivity from 1.2 to 4.7 M of Ag(I) ion, (b) conductivity from 1.2 to 3.5 M of Ag(I) ion.

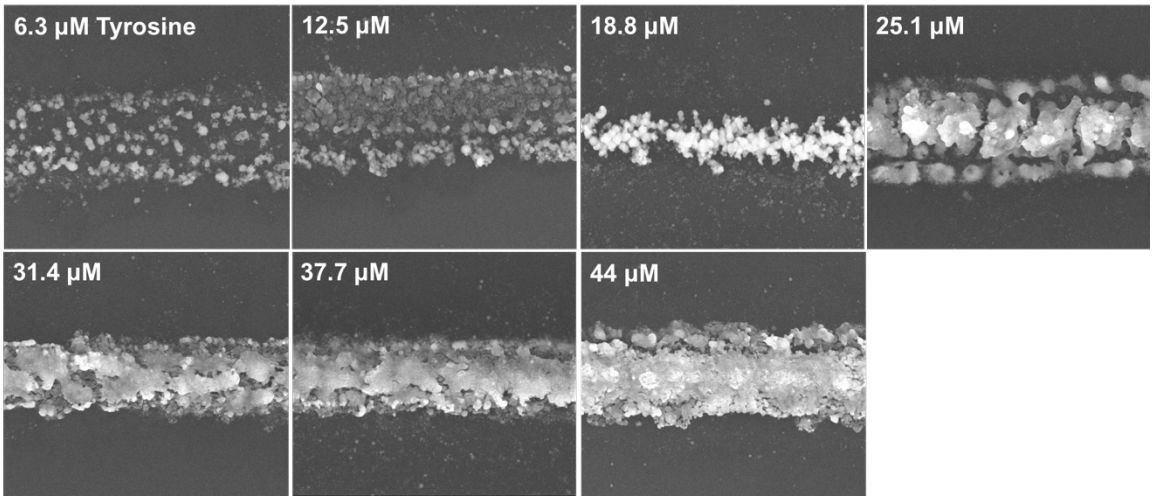

Figure 6.8. SEM imaged of sintered silver pattern with different concentration of tyrosine (with 4.7 M silver(I) ion, 5 µW in laser power and 20 µm/s in scanning speed)

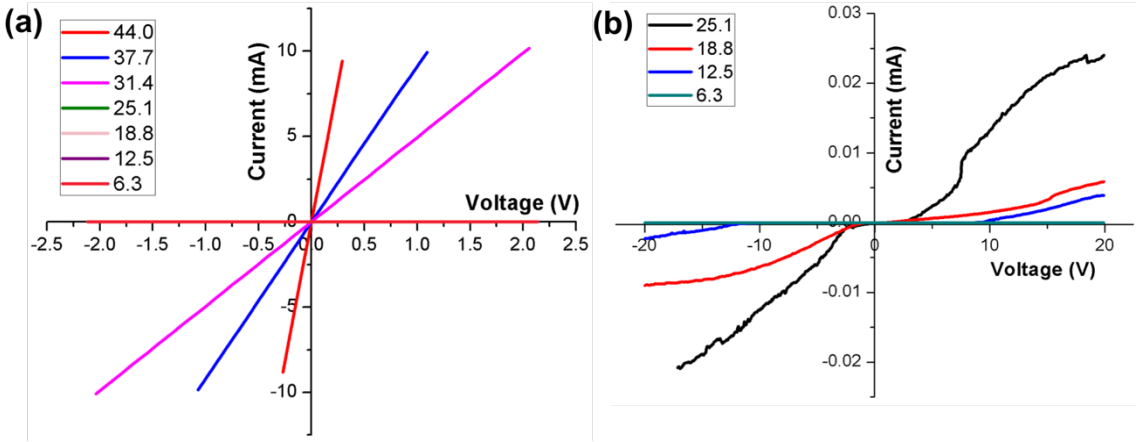

Figure 6.9. Conductivity of sintered silver pattern with concentration of tyrosine (with 4.7 M silver(I) ion, 5 µW in laser power and 20 µm/s in scanning speed). (a) conductivity from 6.3 to 44 µM of tyrosine, (b) conductivity from 6.3 to 25.1 µM of tyrosine.

6.4.5 Removal of un-patterned region

Generally, un-patterned region need to be removed by using some organic solvents after pattering process. In our L-ETRS process, the precursor solution is composed by the biocompatible and water-soluble gelatin and tyrosine. Therefore, we could found that un-patterned regions were clearly removed by dipping into the 60°C deionized water for 1

min (Figure 6.10). As a result, we could only remain the ultrafine and conductive Ag patterns on the substrates.

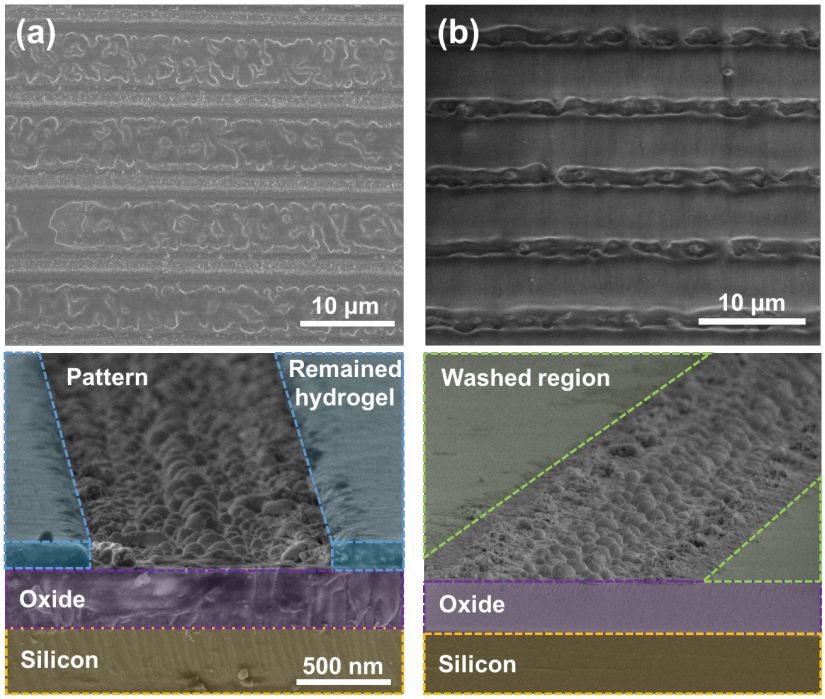

Figure 6.10. Cleaning of un-patterned region with deionized water : before washing(a) and after washing(b)

6.4.6 Conductive pattern fabrication on flexible substrate

Flexible devices have become attractive formats for several applications such as display, sensors, solar cell and wearable devices. Therefore, there is a strong need for the development of high-resolution conductive patterns. Generally, most of polymer substrates are limited in thermal sintering process due to their low glass transition temperature (T_g) values. Therefore, it was difficult to apply several polymer substrates in thermal sintering process. Our L-ETRS method was promising for fabrication of electrode on flexible substrates due to minimize the thermal deformation of polymer substrate by laser beam. We applied our L-ETRS method for fabricating the Ag pattern on the flexible polymer substrate to verify the applicable fabrication on the flexible substrate. Polyimide (PI) films retained their physical properties over a high temperature range. Hence, PI film was used as a substrate for the L-ETRS patterning process. Before the patterning process, we attached the silicon wafer underneath of the film to reduce the loss of phonic energy. To increase the coating properties of precursor on PI film, we treated the oxygen plasma before spin coating process. To verify the possibility for

application of flexible display, we configure the electrical circuit with battery and LED lamp on the breadboard. As shown in Figure 6.11, we could observe the LED light turned ON and OFF when we open and close the circuit respectively. And fabricated Ag electrode can be maintained their stable connectivity with substrate bending (Figure 6.11).

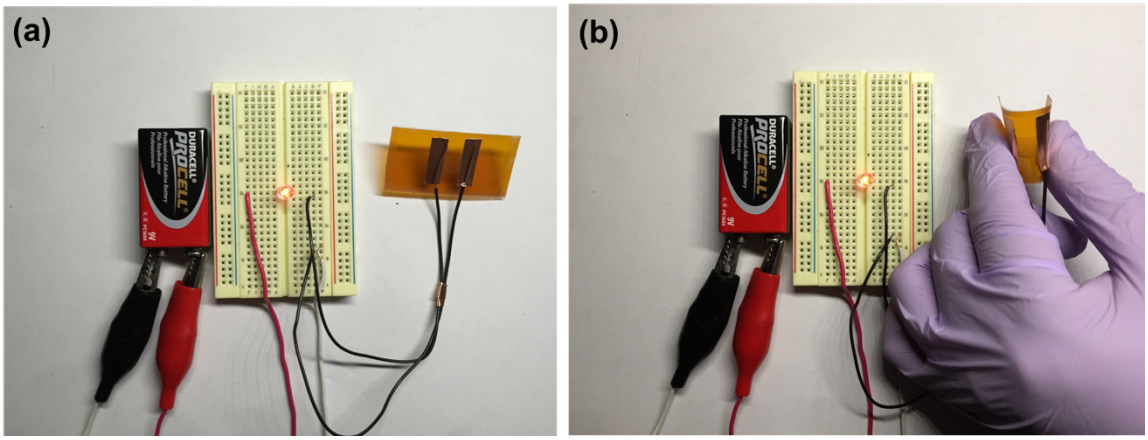

Figure 6.11. Conductive pattern on flexible substrate and bending test. (a)before bending and (b) after bending

6.5 Conclusions and outlook

We demonstrated ultrafine and high conductive Ag patterns by simple and biocompatible laser based pattering process (L-ETRS). In the pattering process, Ag (I) ions were rapidly reduced to Ag NPs and directly sintered to fine Ag patterns. For the efficient photochemical reduction of Ag (I) ions, redox-active tyrosine was added to the gelatin based precursor solution. When the UV laser beam applied to the thin film of our precursor solution, tyrosine and gelatin can efficiently generate and transport free electrons to generate large amount of Ag NPs. In addition, this pattering process was promising for environmentally friendly conductive patterning due to easily remove the non-patterned region by using water without any other toxic organic solvents. Our unique L-ETRS could open the way to a new generation of bio-patches, flexible displays, sensors, solar cells and several other electronic devices.
For the future work, incorporation of direct laser writing and L-ETRS, it is possible to fabricate the conductive pattern on the biomaterial such as hydrogel. On previous research, we could get the highly stretchable hydrogel with conductive (sintered) pattern. Due to the advantage of direct laser writing, it is possible to make pattern without other masks. This can be applied to stretchable and biocompatible patch with conductive pattern.

Chapter 7 Conclusion

In conventional photolithographic procedures, issues of concern are residue after the development process, and the limited spatial resolution due to the diffraction of light. In contrast, femtosecond laser direct writing (FS-LDW) enables high-resolution fabrication without requiring photomasks. From this point of view, FS-LDW is regarded as promising technique micro- and nanoscale fabrication of various materials given the rapid advance in their performance including their stability, output power and reliability. The simplest way that materials respond to light excitation involves the first order linear optical effect. Under multiphoton absorption, the response is practically restricted to two and high orders. The square light intensity distribution is spatially narrower than that of linear one, suggesting that the light-material interaction volume would be reduced. Hence, it is possible to fabricate higher resolution.

High-quality internal fabrication and modification of transparent materials (e.g., fused silica, glass, or crystalline materials) are possible by multiphoton absorption using femtosecond lasers. Refractive index modification inside transparent materials is an important application. These techniques enable integration of optical microcomponents (waveguides, couplers, splitters, volume Bragg gratings and diffractive lenses) in a single glass chip. Moreover, beam shaping techniques are of great use for controlling the cross-sectional shapes of optical components, leading to the fabrication of higher performance.

Microscale patterns are powerful cues to control cell behavior. However, they have limitation to independently control the size and the distribution of the cell adhesive domains and the ligand density. We fabricated nanoscale pit patterned surfaces with spatial gradient by multiphoton laser ablation to demonstrate the gradient force generated. We applied FS-LDW (via ablation) with various objective lenses on fused quartz in order to optimized the process and fabricate the desired design. Nanoscale topographical patterns can generate spatial gradients of the nanoscale pit array that can realize force gradients generated by the nanoscale features. Higher density of the nanoscale-pits repels cells and the gradient density of the nanoscale-pits can direct cell migration. Hence, it is possible to realize new experimental platforms for the study of regenerative medicine. Because, these surfaces will functionalize or control a stem cell differentiation and proliferation. By expanding nanopatterning technique to the biocompatible soft biomaterials, it could be used in dental and medical implants, in order to control cell behavior at the biomaterial interface.

Cells exhibit a number of behaviors and fates such as self-renewal and differentiation, that are interconnected, orchestrated and integrated throughout development and into adulthood within multicellular organisms. However, these behaviors and fate decisions are controlled by the 3D niches surrounding cells, which are structurally complex material microenvironments presenting cells with numerous chemical and physical cues

in the form of soluble growth factors, ECM, and surrounding cells. We used the 2PP process to create a cohort of 3D filamentous matrices that regulate the structural organization of cells and their functions. This approach offers a number of significant advances beyond current practice including : unprecedented control of matrix fiber architecture and dimensions, and a 3D filamentous matrix with independently tunable elastic modulus and biological content.

Progress in nanotechnology relies on the ability to control the spatial organization of structures precisely with length scales from ~100 nm down to molecular dimensions. The required long-range order can be generated using "top-down" or "bottom-up" methods. In the "top-down" approach, nanoscale features are commonly produced using lithographic techniques which include methods such as conventional photolithography, EBL, FIB etching, contact printing, micro-/nano-imprint lithography *etc*. In many cases, top-down approaches are constrained by low throughput due to the sequential nature of the pattern formation. And it also constrained by low resolution due to the optical physics regarding the diffraction-based limits for features produced by photolithography. Hence, limitations include lower speed and efficiency as well as feature non-uniformity. In contrast, "bottom-up" approaches take advantage of self-organization or assembly of atomic, molecular building blocks to provide access to nanostructures with a corresponding range of characteristic length scales. While the range of symmetries or structures is somewhat limited, the promise of high throughput low-cost processing and hierarchical structure formation over large areas. Based on this processing methods, self-assembly will have vital roles to play in the development of advanced nanotechnology.

Ultrashort pulse lasers have proven to be efficient tools for precise fabrication applications due to advantages such as reduced heat and shock affected zones, as well as sharp and significantly lower material modification. In particular, the nonlinear absorption of the short pulses into dielectric materials offers a unique advantage in the fabrication of 2D and 3D structures. This thesis demonstrates micro/nanoscale and 2D/3D structures fabricated by femtosecond laser induced two-photon polymerization (2PP) and multi-photon ablation lithography methods and their applications for functionalize the structures. The 2D patterned surfaces (via ablation) and fibrous matrices (via 2PP) demonstrated in this thesis can also be used for further regulation of cell fate (*e.g.*, stem cell differentiation into specific lineage).

References

[1] Maruo S, Saeki T. Femtosecond laser direct writing of metallic microstructures by photoreduction of silver nitrate in a polymer matrix. Opt Express. 2008;16:1174-9.
[2] Shi X, Li X, Jiang L, Qu L, Zhao Y, Ran P, et al. Femtosecond laser rapid fabrication of large-area rose-like micropatterns on freestanding flexible graphene films. Sci Rep. 2015;5:17557.
[3] Tanaka T, Ishikawa A, Kawata S. Two-photon-induced reduction of metal ions for fabricating three-dimensional electrically conductive metallic microstructure. Appl Phys Lett. 2006;88.
[4] Wang A, Jiang L, Li X, Liu Y, Dong X, Qu L, et al. Mask-Free Patterning of High-Conductivity Metal Nanowires in Open Air by Spatially Modulated Femtosecond Laser Pulses. Adv Mater. 2015;27:6238-43.
[5] Xiong W, Zhou YS, Hou WJ, Jiang LJ, Gao Y, Fan LS, et al. Direct writing of graphene patterns on insulating substrates under ambient conditions. Sci Rep. 2014;4:4892.
[6] Lin J, Xu Y, Fang Z, Wang M, Song J, Wang N, et al. Fabrication of high-Q lithium niobate microresonators using femtosecond laser micromachining. Sci Rep. 2015;5:8072.
[7] Leo G, Altucci C, Bourgoin-Voillard S, Gravagnuolo AM, Esposito R, Marino G, et al. Ultraviolet laser-induced cross-linking in peptides. Rapid Commun Mass Spectrom. 2013;27:1660-8.
[8] Heisterkamp A, Grigoropoulos CP, Jeon H, Hidai H, Hwang DJ, Neev J, et al. Femtosecond laser patterning of biological materials. 2011;7925:792506--9.
[9] Jeon H, Schmidt R, Barton JE, Hwang DJ, Gamble LJ, Castner DG, et al. Chemical patterning of ultrathin polymer films by direct-write multiphoton lithography. J Am Chem Soc. 2011;133:6138-41.
[10] Bäuerle D. Laser Processing and Chemistry. Springer. 2011.
[11] Sugioka K, Meunier M,´ AP. Laser Precision Microfabrication. 2010.
[12] Zhang W, Chen S. Femtosecond laser nanofabrication of hydrogel biomaterial. Mrs Bull. 2011;36:1028-33.
[13] Kim J, Staunton JR, Tanner K. Independent Control of Topography for 3D Patterning of the ECM Microenvironment. Adv Mater. 2016;28:132-7.
[14] Di Cio S, Gautrot JE. Cell sensing of physical properties at the nanoscale: Mechanisms and control of cell adhesion and phenotype. Acta Biomater. 2016;30:26-48.
[15] Broderick AH, Azarin SM, Buck ME, Palecek SP, Lynn DM. Fabrication and Selective Functionalization of Amine-Reactive Polymer Multi layers on Topographically Patterned Microwell Cell Culture Arrays. Biomacromolecules. 2011;12:1998-2007.
[16] Mobasseri A, Faroni A, Minogue BM, Downes S, Terenghi G, Reid AJ. Polymer scaffolds with preferential parallel grooves enhance nerve regeneration. Tissue Eng Part A. 2015;21:1152-62.
[17] Pilipchuk SP, Monje A, Jiao Y, Hao J, Kruger L, Flanagan CL, et al. Integration of 3D Printed and Micropatterned Polycaprolactone Scaffolds for Guidance of Oriented Collagenous Tissue Formation In Vivo. Adv Healthc Mater. 2016.

[18] Nakayama KH, Surya VN, Gole M, Walker TW, Yang W, Lai ES, et al. Nanoscale Patterning of Extracellular Matrix Alters Endothelial Function under Shear Stress. Nano Lett. 2016;16:410-9.
[19] Liu Z, Liu Y, Chang Y, Seyf HR, Henry A, Mattheyses AL, et al. Nanoscale optomechanical actuators for controlling mechanotransduction in living cells. Nat Methods. 2016;13:143-6.
[20] Serbo JV, Kuo S, Lewis S, Lehmann M, Li J, Gracias DH, et al. Patterning of Fibroblast and Matrix Anisotropy within 3D Confinement is Driven by the Cytoskeleton. Adv Healthc Mater. 2016;5:146-58.
[21] Ferlin KM, Prendergast ME, Miller ML, Kaplan DS, Fisher JP. Influence of 3D printed porous architecture on mesenchymal stem cell enrichment and differentiation. Acta Biomater. 2016.
[22] McGann CL, Akins RE, Kiick KL. Resilin-PEG Hybrid Hydrogels Yield Degradable Elastomeric Scaffolds with Heterogeneous Microstructure. Biomacromolecules. 2016;17:128-40.
[23] Kim MH, Kumar SK, Shirahama H, Seo J, Lee JH, Cho NJ. Phenotypic regulation of liver cells in a biofunctionalized three-dimensional hydrogel platform. Integr Biol (Camb). 2016.
[24] Bornes TD, Jomha NM, Mulet-Sierra A, Adesida AB. Optimal Seeding Densities for In Vitro Chondrogenesis of Two- and Three-Dimensional-Isolated and -Expanded Bone Marrow-Derived Mesenchymal Stromal Stem Cells Within a Porous Collagen Scaffold. Tissue Eng Part C Methods. 2016.
[25] Rodenhizer D, Gaude E, Cojocari D, Mahadevan R, Frezza C, Wouters BG, et al. A three-dimensional engineered tumour for spatial snapshot analysis of cell metabolism and phenotype in hypoxic gradients. Nat Mater. 2016;15:227-34.
[26] Li S, Huang J. Cellulose-Rich Nanofiber-Based Functional Nanoarchitectures. Adv Mater. 2016;28:1143-58.
[27] Lee S, Yun S, Park KI, Jang JH. Sliding Fibers: Slidable, Injectable, and Gel-like Electrospun Nanofibers as Versatile Cell Carriers. ACS nano. 2016.
[28] Joanne P, Kitsara M, Boitard SE, Naemetalla H, Vanneaux V, Pernot M, et al. Nanofibrous clinical-grade collagen scaffolds seeded with human cardiomyocytes induces cardiac remodeling in dilated cardiomyopathy. Biomaterials. 2016;80:157-68.
[29] Hughes LA, Gaston J, McAlindon K, Woodhouse KA, Thibeault SL. Electrospun fiber constructs for vocal fold tissue engineering: effects of alignment and elastomeric polypeptide coating. Acta Biomater. 2015;13:111-20.
[30] Pu J, Yuan F, Li S, Komvopoulos K. Electrospun bilayer fibrous scaffolds for enhanced cell infiltration and vascularization in vivo. Acta Biomater. 2015;13:131-41.
[31] Park SM, Kim DS. Electrolyte-assisted electrospinning for a self-assembled, free-standing nanofiber membrane on a curved surface. Adv Mater. 2015;27:1682-7.
[32] Zhu B, Li W, Lewis RV, Segre CU, Wang R. E-spun composite fibers of collagen and dragline silk protein: fiber mechanics, biocompatibility, and application in stem cell differentiation. Biomacromolecules. 2015;16:202-13.
[33] He X, Cheng L, Zhang X, Xiao Q, Zhang W, Lu C. Tissue engineering scaffolds electrospun from cotton cellulose. Carbohydr Polym. 2015;115:485-93.

[34] Xu BB, Zhang YL, Xia H, Dong WF, Ding H, Sun HB. Fabrication and multifunction integration of microfluidic chips by femtosecond laser direct writing. Lab Chip. 2013;13:1677-90.
[35] Obata K, El-Tamer A, Koch L, Hinze U, Chichkov BN. High-aspect 3D two-photon polymerization structuring with widened objective working range (WOW-2PP). Light: Science & Applications. 2013;2:e116.
[36] Andrews DL, Matsuoka T, Galvez EJ, Nishi M, Sakakura M, Glückstad J, et al. Functionalized 2PP structures for the BioPhotonics Workstation. 2011;7950:79500Q.
[37] Ovsianikov A, Schlie S, Ngezahayo A, Haverich A, Chichkov BN. Two-photon polymerization technique for microfabrication of CAD-designed 3D scaffolds from commercially available photosensitive materials. J Tissue Eng Regen Med. 2007;1:443-9.
[38] Vasilantonakis N, Terzaki K, Sakellari I, Purlys V, Gray D, Soukoulis CM, et al. Three-dimensional metallic photonic crystals with optical bandgaps. Adv Mater. 2012;24:1101-5.
[39] Cabrini S, Sakellari I, Kabouraki E, Gray D, Fotakis C, Pikulin A, et al. High-resolution 3D woodpile structures by direct fs laser writing. 2012;8456:84560E.
[40] Mills B, Kundys D, Farsari M, Mailis S, Eason RW. Single-pulse multiphoton fabrication of high aspect ratio structures with sub-micron features using vortex beams. Applied Physics A. 2012;108:651-5.
[41] Bickauskaite G, Manousidaki M, Terzaki K, Kambouraki E, Sakellari I, Vasilantonakis N, et al. 3D Photonic Nanostructures via Diffusion-Assisted Direct fs Laser Writing. Advances in OptoElectronics. 2012;2012:1-6.
[42] Malinauskas M, Žukauskas A, Purlys V, Belazaras K, Momot A, Paipulas D, et al. Femtosecond laser polymerization of hybrid/integrated micro-optical elements and their characterization. J Optics-Uk. 2010;12:124010.
[43] Noginov MA, Sakellari I, Gaidukeviciute A, Giakoumaki A, Gray D, Fotakis C, et al. Direct laser writing of photonic nanostructures. 2009;7392:73920Y-Y-9.
[44] Jin HM, Lee SH, Kim JY, Son SW, Kim BH, Lee HK, et al. Laser Writing Block Copolymer Self-Assembly on Graphene Light-Absorbing Layer. ACS nano. 2016.
[45] Cummins C, Ghoshal T, Holmes JD, Morris MA. Strategies for Inorganic Incorporation using Neat Block Copolymer Thin Films for Etch Mask Function and Nanotechnological Application. Adv Mater. 2016.
[46] He C, Stoykovich MP. Photopatterning of cross-linkable epoxide-functionalized block copolymers and dual-tone nanostructure development for fabrication across the nano- and microscales. Small. 2015;11:2407-16.
[47] Darling SB. Block copolymers for photovoltaics. Energ Environ Sci. 2009;2:1266.
[48] Jeon H, Koo S, Reese WM, Loskill P, Grigoropoulos CP, Healy KE. Directing cell migration and organization via nanocrater-patterned cell-repellent interfaces. Nat Mater. 2015;14:918-23.
[49] Lee BL, Jeon H, Wang A, Yan Z, Yu J, Grigoropoulos C, et al. Femtosecond laser ablation enhances cell infiltration into three-dimensional electrospun scaffolds. Acta Biomater. 2012;8:2648-58.
[50] Ma Z, Wang J, Loskill P, Huebsch N, Koo S, Svedlund FL, et al. Self-organizing human cardiac microchambers mediated by geometric confinement. Nat Commun. 2015;6:7413.

[51] Ma Z, Koo S, Finnegan MA, Loskill P, Huebsch N, Marks NC, et al. Three-dimensional filamentous human diseased cardiac tissue model. Biomaterials. 2014;35:1367-77.
[52] Tong J, Li XY. Electron transfer between tryptophan and tyrosine - ab initio study on redox reactivity and electronic transition energy. Acta Chim Sinica. 2002;60:1029-34.
[53] Lu CY, Liu YY. Electron transfer oxidation of tryptophan and tyrosine by triplet states and oxidized radicals of flavin sensitizers: a laser flash photolysis study. Bba-Gen Subjects. 2002;1571:71-6.
[54] Hardy JG, Hernandez DS, Cummings DM, Edwards FA, Shear JB, Schmidt CE. Multiphoton microfabrication of conducting polymer-based biomaterials. J Mater Chem B. 2015;3:5001-4.
[55] Quick AS, Rothfuss H, Welle A, Richter B, Fischer J, Wegener M, et al. Fabrication and Spatially Resolved Functionalization of 3D Microstructures via Multiphoton-Induced Diels-Alder Chemistry. Advanced Functional Materials. 2014;24:3571-80.
[56] Mueller P, Thiel M, Wegener M. 3D direct laser writing using a 405 nm diode laser. Opt Lett. 2014;39:6847-50.
[57] Lu WE, Zhang YL, Zheng ML, Jia YP, Liu J, Dong XZ, et al. Femtosecond direct laser writing of gold nanostructures by ionic liquid assisted multiphoton photoreduction. Opt Mater Express. 2013;3:1660-73.
[58] Sugioka K, Cheng Y. Ultrafast lasers—reliable tools for advanced materials processing. Light: Science & Applications. 2014;3:e149.
[59] Jun I, Chung YW, Heo YH, Han HS, Park J, Jeong H, et al. Creating Hierarchical Topographies on Fibrous Platforms Using Femtosecond Laser Ablation for Directing Myoblasts Behavior. ACS Appl Mater Interfaces. 2016;8:3407-17.
[60] Mortensen LJ, Alt C, Turcotte R, Masek M, Liu TM, Cote DC, et al. Femtosecond laser bone ablation with a high repetition rate fiber laser source. Biomed Opt Express. 2015;6:32-42.
[61] Wu D, Niu LG, Wu SZ, Xu J, Midorikawa K, Sugioka K. Ship-in-a-bottle femtosecond laser integration of optofluidic microlens arrays with center-pass units enabling coupling-free parallel cell counting with a 100% success rate. Lab Chip. 2015;15:1515-23.
[62] Kapyla E, Sedlacik T, Aydogan DB, Viitanen J, Rypacek F, Kellomaki M. Direct laser writing of synthetic poly(amino acid) hydrogels and poly(ethylene glycol) diacrylates by two-photon polymerization. Mater Sci Eng C Mater Biol Appl. 2014;43:280-9.
[63] Jiang LJ, Zhou YS, Xiong W, Gao Y, Huang X, Jiang L, et al. Two-photon polymerization: investigation of chemical and mechanical properties of resins using Raman microspectroscopy. Opt Lett. 2014;39:3034-7.
[64] Cao HZ, Zheng ML, Dong XZ, Jin F, Zhao ZS, Duan XM. Two-photon nanolithography of positive photoresist thin film with ultrafast laser direct writing. Appl Phys Lett. 2013;102.
[65] von Freymann G, Ushiba S, Shoji S, Kuray P, Masui K, Kono J, et al. Two photon polymerization lithography for 3D microfabrication of single wall carbon nanotube/polymer composites. 2013;8613:86130Y.
[66] Grigoropoulos CP. Transport in Laser Microfabrication: Fundamentals and Applications. CAMBRIDGE UNIVERSITY PRESS. 2009.

[67] S D, De L, G. Otuka AJ, Tribuzi V, R C. Two-Photon Polymerization Fabrication of Doped Microstructures. 2012.
[68] Sun ZB, Dong XZ, Chen WQ, Shoji S, Duan XM, Kawata S. Two- and three-dimensional micro/nanostructure patterning of CdS-polymer nanocomposites with a laser interference technique and in situ synthesis. Nanotechnology. 2008;19:035611.
[69] Kawata S, Formanek F, Takeyasu N, Tanaka T, Chiyoda K, Ishikawa A, et al. Three-dimensional fabrication of metallic micro/nanostructures by two-photon polymerization for metamaterials. 2006;6324:63240T-T-6.
[70] Lau UY, Saxer SS, Lee J, Bat E, Maynard HD. Direct Write Protein Patterns for Multiplexed Cytokine Detection from Live Cells Using Electron Beam Lithography. ACS nano. 2016;10:723-9.
[71] Lin E, Sikand A, Wickware J, Hao Y, Derda R. Peptide microarray patterning for controlling and monitoring cell growth. Acta Biomater. 2016.
[72] Tanaka N, Ota H, Fukumori K, Miyake J, Yamato M, Okano T. Micro-patterned cell-sheets fabricated with stamping-force-controlled micro-contact printing. Biomaterials. 2014;35:9802-10.
[73] Fisher JS, Kottke PA, Kim S, Fedorov AG. Rapid Electron Beam Writing of Topologically Complex 3D Nanostructures Using Liquid Phase Precursor. Nano Lett. 2015;15:8385-91.
[74] Ahn H, Ju YM, Takahashi H, Williams DF, Yoo JJ, Lee SJ, et al. Engineered small diameter vascular grafts by combining cell sheet engineering and electrospinning technology. Acta Biomater. 2015;16:14-22.
[75] Ma L, Yang G, Wang N, Zhang P, Guo F, Meng J, et al. Trap Effect of Three-Dimensional Fibers Network for High Efficient Cancer-Cell Capture. Adv Healthc Mater. 2015;4:838-43.
[76] Kaplan J, Grinstaff M. Fabricating Superhydrophobic Polymeric Materials for Biomedical Applications. J Vis Exp. 2015:e53117.
[77] Jeffries EM, Allen RA, Gao J, Pesce M, Wang Y. Highly elastic and suturable electrospun poly(glycerol sebacate) fibrous scaffolds. Acta Biomater. 2015;18:30-9.
[78] Chen F, Hochleitner G, Woodfield T, Groll J, Dalton PD, Amsden BG. Additive Manufacturing of a Photo-Cross-Linkable Polymer via Direct Melt Electrospinning Writing for Producing High Strength Structures. Biomacromolecules. 2016;17:208-14.
[79] Wang K, Zheng W, Pan Y, Ma S, Guan Y, Liu R, et al. Three-Layered PCL Grafts Promoted Vascular Regeneration in a Rabbit Carotid Artery Model. Macromol Biosci. 2016.
[80] Lin CC, Fu SJ. Osteogenesis of human adipose-derived stem cells on poly(dopamine)-coated electrospun poly(lactic acid) fiber mats. Mater Sci Eng C Mater Biol Appl. 2016;58:254-63.
[81] Shao W, He J, Sang F, Ding B, Chen L, Cui S, et al. Coaxial electrospun aligned tussah silk fibroin nanostructured fiber scaffolds embedded with hydroxyapatite-tussah silk fibroin nanoparticles for bone tissue engineering. Mater Sci Eng C Mater Biol Appl. 2016;58:342-51.
[82] Kobayashi M, Lei NY, Wang Q, Wu BM, Dunn JC. Orthogonally oriented scaffolds with aligned fibers for engineering intestinal smooth muscle. Biomaterials. 2015;61:75-84.

[83] Estrada MF, Rebelo SP, Davies EJ, Pinto MT, Pereira H, Santo VE, et al. Modelling the tumour microenvironment in long-term microencapsulated 3D co-cultures recapitulates phenotypic features of disease progression. Biomaterials. 2016;78:50-61.
[84] Srinivasan A, Tahilramani M, Bentley JT, Gore RK, Millard DC, Mukhatyar VJ, et al. Microchannel-based regenerative scaffold for chronic peripheral nerve interfacing in amputees. Biomaterials. 2015;41:151-65.
[85] Lang NR, Skodzek K, Hurst S, Mainka A, Steinwachs J, Schneider J, et al. Biphasic response of cell invasion to matrix stiffness in three-dimensional biopolymer networks. Acta Biomater. 2015;13:61-7.
[86] Kojima T, Moraes C, Cavnar SP, Luker GD, Takayama S. Surface-templated hydrogel patterns prompt matrix-dependent migration of breast cancer cells towards chemokine-secreting cells. Acta Biomater. 2015;13:68-77.
[87] Kivelio A, Ochsenbein-Koelble N, Zimmermann R, Ehrbar M. Engineered cell instructive matrices for fetal membrane healing. Acta Biomater. 2015;15:1-10.
[88] Li Y, Wang S, Huang R, Huang Z, Hu B, Zheng W, et al. Evaluation of the effect of the structure of bacterial cellulose on full thickness skin wound repair on a microfluidic chip. Biomacromolecules. 2015;16:780-9.
[89] Wong SY, Ulrich TA, Deleyrolle LP, MacKay JL, Lin JM, Martuscello RT, et al. Constitutive activation of myosin-dependent contractility sensitizes glioma tumor-initiating cells to mechanical inputs and reduces tissue invasion. Cancer Res. 2015;75:1113-22.
[90] Abagnale G, Steger M, Nguyen VH, Hersch N, Sechi A, Joussen S, et al. Surface topography enhances differentiation of mesenchymal stem cells towards osteogenic and adipogenic lineages. Biomaterials. 2015;61:316-26.
[91] Grabias BM, Konstantopoulos K. Notch4-dependent antagonism of canonical TGF-beta 1 signaling defines unique temporal fluctuations of SMAD3 activity in sheared proximal tubular epithelial cells. Am J Physiol-Renal. 2013;305:F123-F33.
[92] Ghosh G, Lian XJ, Kron SJ, Palecek SP. Properties of resistant cells generated from lung cancer cell lines treated with EGFR inhibitors. Bmc Cancer. 2012;12.
[93] Grabias BM, Konstantopoulos K. Epithelial-mesenchymal transition and fibrosis are mutually exclusive reponses in shear-activated proximal tubular epithelial cells. Faseb J. 2012;26:4131-41.
[94] Yang HS, Lee B, Tsui JH, Macadangdang J, Jang SY, Im SG, et al. Electroconductive Nanopatterned Substrates for Enhanced Myogenic Differentiation and Maturation. Adv Healthc Mater. 2016;5:137-45.
[95] Tan KK, Tann JY, Sathe SR, Goh SH, Ma D, Goh EL, et al. Enhanced differentiation of neural progenitor cells into neurons of the mesencephalic dopaminergic subtype on topographical patterns. Biomaterials. 2015;43:32-43.
[96] Wittenbrink I, Hausmann A, Schickle K, Lauria I, Davtalab R, Foss M, et al. Low-aspect ratio nanopatterns on bioinert alumina influence the response and morphology of osteoblast-like cells. Biomaterials. 2015;62:58-65.
[97] Stroka KM, Konstantopoulos K. Physical Biology in Cancer. 4. Physical cues guide tumor cell adhesion and migration. Am J Physiol-Cell Ph. 2014;306:C98-C109.
[98] Lam RHW, Sun YB, Chen WQ, Fu JP. Elastomeric microposts integrated into microfluidics for flow-mediated endothelial mechanotransduction analysis. Lab Chip. 2012;12:1865-73.

[99] Grazioli A, Alves CS, Konstantopoulos K, Yang JT. Defective blood vessel development and pericyte/pvSMC distribution in alpha 4 integrin-deficient mouse embryos. Dev Biol. 2006;293:165-77.
[100] Rahman A, Tseng Y, Wirtz D. Micromechanical coupling between cell surface receptors and RGD peptides. Biochem Bioph Res Co. 2002;296:771-8.
[101] Lee S, Hong J, Lee J. Cell motility regulation on a stepped micro pillar array device (SMPAD) with a discrete stiffness gradient. Soft Matter. 2016.
[102] LaCroix AS, Rothenberg KE, Hoffman BD. Molecular-Scale Tools for Studying Mechanotransduction. Annu Rev Biomed Eng. 2015;17:287-316.
[103] Jerrell RJ, Parekh A. Cellular traction stresses mediate extracellular matrix degradation by invadopodia. Acta Biomater. 2014;10:1886-96.
[104] Wong ST, Teo SK, Park S, Chiam KH, Yim EK. Anisotropic rigidity sensing on grating topography directs human mesenchymal stem cell elongation. Biomech Model Mechanobiol. 2014;13:27-39.
[105] Wu J, Wu X, Lin F. Recent developments in microfluidics-based chemotaxis studies. Lab Chip. 2013;13:2484-99.
[106] Tong ZQ, Balzer EM, Dallas MR, Hung WC, Stebe KJ, Konstantopoulos K. Chemotaxis of Cell Populations through Confined Spaces at Single-Cell Resolution. Plos One. 2012;7.
[107] Ridley AJ, Schwartz MA, Burridge K, Firtel RA, Ginsberg MH, Borisy G, et al. Cell migration: Integrating signals from front to back. Science. 2003;302:1704-9.
[108] Ikezoe Y, Fang J, Wasik TL, Shi M, Uemura T, Kitagawa S, et al. Peptide-Metal Organic Framework Swimmers that Direct the Motion toward Chemical Targets. Nano Lett. 2015;15:4019-23.
[109] Jun I, Jeong S, Shin H. The stimulation of myoblast differentiation by electrically conductive sub-micron fibers. Biomaterials. 2009;30:2038-47.
[110] Jeong SI, Jun ID, Choi MJ, Nho YC, Lee YM, Shin H. Development of electroactive and elastic nanofibers that contain polyaniline and poly(L-lactide-co-epsilon-caprolactone) for the control of cell adhesion. Macromol Biosci. 2008;8:627-37.
[111] Lizundia E, Meaurio E, Laza JM, Vilas JL, Leon Isidro LM. Study of the chain microstructure effects on the resulting thermal properties of poly(L-lactide)/poly(N-isopropylacrylamide) biomedical materials. Mater Sci Eng C Mater Biol Appl. 2015;50:97-106.
[112] Zhang Z, Liu S, Xiong H, Jing X, Xie Z, Chen X, et al. Electrospun PLA/MWCNTs composite nanofibers for combined chemo- and photothermal therapy. Acta Biomater. 2015;26:115-23.
[113] Ortiz R, Moreno-Flores S, Quintana I, Vivanco M, Sarasua JR, Toca-Herrera JL. Ultra-fast laser microprocessing of medical polymers for cell engineering applications. Mater Sci Eng C Mater Biol Appl. 2014;37:241-50.
[114] Schmidt RC, Healy KE. Effect of avidin-like proteins and biotin modification on mesenchymal stem cell adhesion. Biomaterials. 2013;34:3758-62.
[115] Costa P, Gautrot JE, Connelly JT. Directing cell migration using micropatterned and dynamically adhesive polymer brushes. Acta Biomater. 2014;10:2415-22.
[116] Guarnieri D, De Capua A, Ventre M, Borzacchiello A, Pedone C, Marasco D, et al. Covalently immobilized RGD gradient on PEG hydrogel scaffold influences cell migration parameters. Acta Biomater. 2010;6:2532-9.

[117] Miller JS, Shen CJ, Legant WR, Baranski JD, Blakely BL, Chen CS. Bioactive hydrogels made from step-growth derived PEG-peptide macromers. Biomaterials. 2010;31:3736-43.
[118] Cavalcanti-Adam EA, Volberg T, Micoulet A, Kessler H, Geiger B, Spatz JP. Cell spreading and focal adhesion dynamics are regulated by spacing of integrin ligands. Biophys J. 2007;92:2964-74.
[119] Ribeiro MC, Tertoolen LG, Guadix JA, Bellin M, Kosmidis G, D'Aniello C, et al. Functional maturation of human pluripotent stem cell derived cardiomyocytes in vitro--correlation between contraction force and electrophysiology. Biomaterials. 2015;51:138-50.
[120] Ossola D, Amarouch MY, Behr P, Voros J, Abriel H, Zambelli T. Force-controlled patch clamp of beating cardiac cells. Nano Lett. 2015;15:1743-50.
[121] Takahashi H, Okano T. Cell Sheet-Based Tissue Engineering for Organizing Anisotropic Tissue Constructs Produced Using Microfabricated Thermoresponsive Substrates. Adv Healthc Mater. 2015;4:2388-407.
[122] Boudou T, Legant WR, Mu A, Borochin MA, Thavandiran N, Radisic M, et al. A microfabricated platform to measure and manipulate the mechanics of engineered cardiac microtissues. Tissue Eng Part A. 2012;18:910-9.
[123] Shachar M, Tsur-Gang O, Dvir T, Leor J, Cohen S. The effect of immobilized RGD peptide in alginate scaffolds on cardiac tissue engineering. Acta Biomater. 2011;7:152-62.
[124] Aung A, Bhullar IS, Theprungsirikul J, Davey SK, Lim HL, Chiu YJ, et al. 3D cardiac mutissues within a microfluidic device with real-time contractile stress readout. Lab Chip. 2016;16:153-62.
[125] Marsano A, Conficconi C, Lemme M, Occhetta P, Gaudiello E, Votta E, et al. Beating heart on a chip: a novel microfluidic platform to generate functional 3D cardiac microtissues. Lab Chip. 2016;16:599-610.
[126] Fleischer S, Dvir T. Tissue engineering on the nanoscale: lessons from the heart. Curr Opin Biotech. 2013;24:664-71.
[127] Amano Y, Nishiguchi A, Matsusaki M, Iseoka H, Miyagawa S, Sawa Y, et al. Development of vascularized iPSC derived 3D-cardiomyocyte tissues by filtration Layer-by-Layer technique and their application for pharmaceutical assays. Acta Biomater. 2016.
[128] Zhang D, Shadrin IY, Lam J, Xian HQ, Snodgrass HR, Bursac N. Tissue-engineered cardiac patch for advanced functional maturation of human ESC-derived cardiomyocytes. Biomaterials. 2013;34:5813-20.
[129] Ahn S, Deravi LF, Park SJ, Dabiri BE, Kim JS, Parker KK, et al. Self-organizing large-scale extracellular-matrix protein networks. Adv Mater. 2015;27:2838-45.
[130] Chan V, Jeong JH, Bajaj P, Collens M, Saif T, Kong H, et al. Multi-material bio-fabrication of hydrogel cantilevers and actuators with stereolithography. Lab Chip. 2012;12:88-98.
[131] Tanaka Y, Morishima K, Shimizu T, Kikuchi A, Yamato M, Okano T, et al. Demonstration of a PDMS-based bio-microactuator using cultured cardiomyocytes to drive polymer micropillars. Lab Chip. 2006;6:230-5.
[132] Simon-Yarza T, Rossi A, Heffels KH, Prosper F, Groll J, Blanco-Prieto MJ. Polymeric electrospun scaffolds: neuregulin encapsulation and biocompatibility studies in a model of myocardial ischemia. Tissue Eng Part A. 2015;21:1654-61.

[133] Rai R, Tallawi M, Frati C, Falco A, Gervasi A, Quaini F, et al. Bioactive electrospun fibers of poly(glycerol sebacate) and poly(epsilon-caprolactone) for cardiac patch application. Adv Healthc Mater. 2015;4:2012-25.
[134] Bhaarathy V, Venugopal J, Gandhimathi C, Ponpandian N, Mangalaraj D, Ramakrishna S. Biologically improved nanofibrous scaffolds for cardiac tissue engineering. Mater Sci Eng C Mater Biol Appl. 2014;44:268-77.
[135] Xu Y, Patnaik S, Guo X, Li Z, Lo W, Butler R, et al. Cardiac differentiation of cardiosphere-derived cells in scaffolds mimicking morphology of the cardiac extracellular matrix. Acta Biomater. 2014;10:3449-62.
[136] Fleischer S, Feiner R, Shapira A, Ji J, Sui XM, Wagner HD, et al. Spring-like fibers for cardiac tissue engineering. Biomaterials. 2013;34:8599-606.
[137] Adzima BJ, Kloxin CJ, DeForest CA, Anseth KS, Bowman CN. 3D Photofixation Lithography in Diels-Alder Networks. Macromol Rapid Comm. 2012;33:2092-6.
[138] Duan X-M, Sun H-B, Kaneko K, Kawata S. Two-photon polymerization of metal ions doped acrylate monomers and oligomers for three-dimensional structure fabrication. Thin Solid Films. 2004;453-454:518-21.
[139] Fraysse B, Weinberger F, Bardswell SC, Cuello F, Vignier N, Geertz B, et al. Increased myofilament Ca2+ sensitivity and diastolic dysfunction as early consequences of Mybpc3 mutation in heterozygous knock-in mice. J Mol Cell Cardiol. 2012;52:1299-307.
[140] Jacot JG, McCulloch AD, Omens JH. Substrate stiffness affects the functional maturation of neonatal rat ventricular myocytes. Biophys J. 2008;95:3479-87.
[141] Qian W, Zhang Y, Chen W. Capturing Cancer: Emerging Microfluidic Technologies for the Capture and Characterization of Circulating Tumor Cells. Small. 2015;11:3850-72.
[142] Itzhaki I, Maizels L, Huber I, Zwi-Dantsis L, Caspi O, Winterstern A, et al. Modelling the long QT syndrome with induced pluripotent stem cells. Nature. 2011;471:225-9.
[143] Moretti A, Bellin M, Welling A, Jung CB, Lam JT, Bott-Flugel L, et al. Patient-Specific Induced Pluripotent Stem-Cell Models for Long-QT Syndrome. New Engl J Med. 2010;363:1397-409.
[144] Zhang SS, Hong S, Kleber AG, Lee LP, Shaw RM. A micropatterning approach for imaging dynamic Cx43 trafficking to cell-cell borders. FEBS Lett. 2014;588:1439-45.
[145] Xiao Y, Zhang B, Liu H, Miklas JW, Gagliardi M, Pahnke A, et al. Microfabricated perfusable cardiac biowire: a platform that mimics native cardiac bundle. Lab Chip. 2014;14:869-82.
[146] Wang G, McCain ML, Yang L, He A, Pasqualini FS, Agarwal A, et al. Modeling the mitochondrial cardiomyopathy of Barth syndrome with induced pluripotent stem cell and heart-on-chip technologies. Nat Med. 2014;20:616-23.
[147] Stohr A, Friedrich FW, Flenner F, Geertz B, Eder A, Schaaf S, et al. Contractile abnormalities and altered drug response in engineered heart tissue from Mybpc3-targeted knock-in mice. J Mol Cell Cardiol. 2013;63:189-98.
[148] Merkulov S, Chen X, Chandler MP, Stelzer JE. In vivo cardiac myosin binding protein C gene transfer rescues myofilament contractile dysfunction in cardiac myosin binding protein C null mice. Circ Heart Fail. 2012;5:635-44.

[149] Jiang J, Burgon PG, Wakimoto H, Onoue K, Gorham JM, O'Meara CC, et al. Cardiac myosin binding protein C regulates postnatal myocyte cytokinesis. Proc Natl Acad Sci U S A. 2015;112:9046-51.
[150] Yu B, French JA, Carrier L, Jeremy RW, McTaggart DR, Nicholson MR, et al. Molecular pathology of familial hypertrophic cardiomyopathy caused by mutations in the cardiac myosin binding protein C gene. J Med Genet. 1998;35:205-10.
[151] Rodriguez ML, Graham BT, Pabon LM, Han SJ, Murry CE, Sniadecki NJ. Measuring the contractile forces of human induced pluripotent stem cell-derived cardiomyocytes with arrays of microposts. J Biomech Eng. 2014;136:051005.
[152] Hayakawa T, Kunihiro T, Ando T, Kobayashi S, Matsui E, Yada H, et al. Image-based evaluation of contraction-relaxation kinetics of human-induced pluripotent stem cell-derived cardiomyocytes: Correlation and complementarity with extracellular electrophysiology. J Mol Cell Cardiol. 2014;77:178-91.
[153] Zhang GQ, Wei H, Lu J, Wong P, Shim W. Identification and characterization of calcium sparks in cardiomyocytes derived from human induced pluripotent stem cells. Plos One. 2013;8:e55266.
[154] Lundy SD, Zhu WZ, Regnier M, Laflamme MA. Structural and functional maturation of cardiomyocytes derived from human pluripotent stem cells. Stem Cells Dev. 2013;22:1991-2002.
[155] McCain ML, Sheehy SP, Grosberg A, Goss JA, Parker KK. Recapitulating maladaptive, multiscale remodeling of failing myocardium on a chip. P Natl Acad Sci USA. 2013;110:9770-5.
[156] Schaefer JA, Tranquillo RT. Tissue Contraction Force Microscopy for Optimization of Engineered Cardiac Tissue. Tissue Eng Part C Methods. 2016;22:76-83.
[157] You J, Moon H, Lee BY, Jin JY, Chang ZE, Kim SY, et al. Cardiomyocyte sensor responsive to changes in physical and chemical environments. J Biomech. 2014;47:400-9.
[158] Beussman KM, Rodriguez ML, Leonard A, Taparia N, Thompson CR, Sniadecki NJ. Micropost arrays for measuring stem cell-derived cardiomyocyte contractility. Methods. 2015.
[159] Taylor RE, Kim K, Sun N, Park SJ, Sim JY, Fajardo G, et al. Sacrificial layer technique for axial force post assay of immature cardiomyocytes. Biomed Microdevices. 2013;15:171-81.
[160] Chan V, Park K, Collens MB, Kong H, Saif TA, Bashir R. Development of miniaturized walking biological machines. Sci Rep. 2012;2:857.
[161] Galior K, Liu Y, Yehl K, Vivek S, Salaita K. Titin-Based Nanoparticle Tension Sensors Map High-Magnitude Integrin Forces within Focal Adhesions. Nano Lett. 2016;16:341-8.
[162] Hinson JT, Chopra A, Nafissi N, Polacheck WJ, Benson CC, Swist S, et al. Titin mutations in iPS cells define sarcomere insufficiency as a cause of dilated cardiomyopathy. Science. 2015;349:982-6.
[163] Flashman E, Redwood C, Moolman-Smook J, Watkins H. Cardiac myosin binding protein C: its role in physiology and disease. Circ Res. 2004;94:1279-89.
[164] Lux M, Andree B, Horvath T, Nosko A, Manikowski D, Hilfiker-Kleiner D, et al. In vitro maturation of large-scale cardiac patches based on a perfusable starter matrix by cyclic mechanical stimulation. Acta Biomater. 2016;30:177-87.

[165] Jeon H, Kim E, Grigoropoulos CP. Measurement of contractile forces generated by individual fibroblasts on self-standing fiber scaffolds. Biomed Microdevices. 2011;13:107-15.
[166] Mathur A, Ma Z, Loskill P, Jeeawoody S, Healy KE. In vitro cardiac tissue models: Current status and future prospects. Adv Drug Deliv Rev. 2016;96:203-13.
[167] Huebsch N, Loskill P, Mandegar MA, Marks NC, Sheehan AS, Ma Z, et al. Automated Video-Based Analysis of Contractility and Calcium Flux in Human-Induced Pluripotent Stem Cell-Derived Cardiomyocytes Cultured over Different Spatial Scales. Tissue Eng Part C Methods. 2015;21:467-79.
[168] Green EM, Wakimoto H, Anderson RL, Evanchik MJ, Gorham JM, Harrison BC, et al. A small-molecule inhibitor of sarcomere contractility suppresses hypertrophic cardiomyopathy in mice. Science. 2016;351:617-21.
[169] Hirt MN, Werner T, Indenbirken D, Alawi M, Demin P, Kunze AC, et al. Deciphering the microRNA signature of pathological cardiac hypertrophy by engineered heart tissue- and sequencing-technology. J Mol Cell Cardiol. 2015;81:1-9.
[170] Tham YK, Bernardo BC, Ooi JY, Weeks KL, McMullen JR. Pathophysiology of cardiac hypertrophy and heart failure: signaling pathways and novel therapeutic targets. Arch Toxicol. 2015;89:1401-38.
[171] Schaaf S, Shibamiya A, Mewe M, Eder A, Stohr A, Hirt MN, et al. Human engineered heart tissue as a versatile tool in basic research and preclinical toxicology. Plos One. 2011;6:e26397.
[172] Zhang YS, Khademhosseini A. Seeking the right context for evaluating nanomedicine: from tissue models in petri dishes to microfluidic organs-on-a-chip. Nanomedicine. 2015;10:685-8.
[173] Mandegar MA, Huebsch N, Frolov EB, Shin E, Truong A, Olvera MP, et al. CRISPR Interference Efficiently Induces Specific and Reversible Gene Silencing in Human iPSCs. Cell Stem Cell. 2016;18:541-53.
[174] Rho Y, Aissou K, Mumtaz M, Kwon W, Pecastaings G, Mocuta C, et al. Laterally Ordered Sub-10 nm Features Obtained From Directed Self-Assembly of Si-Containing Block Copolymer Thin Films. Small. 2015;11:6377-83.
[175] Sun W, Parowatkin M, Steffen W, Butt HJ, Mailander V, Wu S. Ruthenium-Containing Block Copolymer Assemblies: Red-Light-Responsive Metallopolymers with Tunable Nanostructures for Enhanced Cellular Uptake and Anticancer Phototherapy. Adv Healthc Mater. 2015.
[176] Hu H, Gopinadhan M, Osuji CO. Directed self-assembly of block copolymers: a tutorial review of strategies for enabling nanotechnology with soft matter. Soft Matter. 2014;10:3867-89.
[177] Gu X. Self-Assembly of Block Copolymers by Solvent Vapor Annealing, Mechanism and Lithographic Application. Thesis. 2014.
[178] Park S-M, Rettner CT, Pitera JW, Kim H-C. Directed Self-Assembly of Lamellar Microdomains of Block Copolymers Using Topographic Guiding Patterns. Macromolecules. 2009;42:5895-9.
[179] Xia H, Wang J, Tian Y, Chen QD, Du XB, Zhang YL, et al. Ferrofluids for fabrication of remotely controllable micro-nanomachines by two-photon polymerization. Adv Mater. 2010;22:3204-7.

[180] Zhang Y-L, Chen Q-D, Xia H, Sun H-B. Designable 3D nanofabrication by femtosecond laser direct writing. Nano Today. 2010;5:435-48.
[181] Li W, Muller M. Defects in the Self-Assembly of Block Copolymers and Their Relevance for Directed Self-Assembly. Annu Rev Chem Biomol Eng. 2015;6:187-216.
[182] Hamad EM, Bilatto SE, Adly NY, Correa DS, Wolfrum B, Schoning MJ, et al. Inkjet printing of UV-curable adhesive and dielectric inks for microfluidic devices. Lab Chip. 2016;16:70-4.
[183] Sochol RD, Sweet E, Glick CC, Venkatesh S, Avetisyan A, Ekman KF, et al. 3D printed microfluidic circuitry via multijet-based additive manufacturing. Lab Chip. 2016.
[184] Melchiorri AJ, Hibino N, Best CA, Yi T, Lee YU, Kraynak CA, et al. 3D-Printed Biodegradable Polymeric Vascular Grafts. Adv Healthc Mater. 2016;5:319-25.
[185] Bai W, Ross CA. Functional nanostructured materials based on self-assembly of block copolymers. Mrs Bull. 2016;41:100-7.
[186] Majewski PW, Yager KG. Latent Alignment in Pathway-Dependent Ordering of Block Copolymer Thin Films. Nano Lett. 2015;15:5221-8.
[187] Cochran EW, Garcia-Cervera CJ, Fredrickson GH. Stability of the gyroid phase in diblock copolymers at strong segregation. Macromolecules. 2006;39:2449-51.
[188] Lambooy P, Russell TP, Kellogg GJ, Mayes AM, Gallagher PD, Satija SK. Observed frustration in confined block copolymers. Phys Rev Lett. 1994;72:2899-902.
[189] Yabu H, Higuchi T, Jinnai H. Frustrated phases: polymeric self-assemblies in a 3D confinement. Soft Matter. 2014;10:2919-31.
[190] Sun YS, Wang CT, Liou JY. Tuning polymer-surface chemistries and interfacial interactions with UV irradiated polystyrene chains to control domain orientations in thin films of PS-b-PMMA. Soft Matter. 2016.
[191] Sun Z, Chen Z, Zhang W, Choi J, Huang C, Jeong G, et al. Directed Self-Assembly of Poly(2-vinylpyridine)-b-polystyrene-b-poly(2-vinylpyridine) Triblock Copolymer with Sub-15 nm Spacing Line Patterns Using a Nanoimprinted Photoresist Template. Adv Mater. 2015;27:4364-70.
[192] Gu X, Gunkel I, Hexemer A, Russell TP. Solvent vapor annealing of block copolymer thin films: removal of processing history. Colloid and Polymer Science. 2014;292:1795-802.
[193] Campbell IP, He C, Stoykovich MP. Topologically Distinct Lamellar Block Copolymer Morphologies Formed by Solvent and Thermal Annealing. ACS Macro Letters. 2013;2:918-23.
[194] Pitet LM, Alexander-Moonen E, Peeters E, Druzhinina TS, Wuister SF, Lynd NA, et al. Probing the Effect of Molecular Nonuniformity in Directed Self-Assembly of Diblock Copolymers in Nanoconfined Space. ACS nano. 2015;9:9594-602.
[195] Kubo T, Parker JS, Hillmyer MA, Leighton C. Characterization of pattern transfer in the fabrication of magnetic nanostructure arrays by block copolymer lithography. Appl Phys Lett. 2007;90.
[196] Malinauskas M, Farsari M, Piskarskas A, Juodkazis S. Ultrafast laser nanostructuring of photopolymers: A decade of advances. Physics Reports. 2013;533:1-31.
[197] Hribar KC, Soman P, Warner J, Chung P, Chen S. Light-assisted direct-write of 3D functional biomaterials. Lab Chip. 2014;14:268-75.

[198] Zhao W, Rovere T, Weerawarne D, Osterhoudt G, Kang N, Joseph P, et al. Nanoalloy Printed and Pulse-Laser Sintered Flexible Sensor Devices with Enhanced Stability and Materials Compatibility. ACS nano. 2015;9:6168-77.
[199] Kuladeep R, Jyothi L, Alee KS, Deepak KLN, Rao DN. Laser-assisted synthesis of Au-Ag alloy nanoparticles with tunable surface plasmon resonance frequency. 2012
.
[200] Morozova OB, Yurkovskaya AV. Modulation of the Rate of Reversible Electron Transfer in Oxidized Tryptophan and Tyrosine Containing Peptides in Acidic Aqueous Solution. J Phys Chem B. 2015;119:140-9.
[201] Roy S, Das TK. Study of Interaction Between Tryptophan, Tyrosine, and Phenylalanine Separately with Silver Nanoparticles by Fluorescence Quenching Method. Journal of Applied Spectroscopy. 2015;82:598-606.
[202] Kim JE, Larson BC, Pomponio JR, Shafaat HS, Kim RH, Leigh BS, et al. Electron and proton transfer from tyrosine and tryptophan residues in azurin. Abstr Pap Am Chem S. 2014;248.
[203] Tang RZ, Li HX, Liu YC, Zhang P, Cao XY, Wang WF. Laser Flash Photolysis Study on Electron Transfer Oxidation Reaction of Tryptophan or Tyrosine with Triplet State Vitamin K-3. Acta Phys-Chim Sin. 2012;28:213-6.
[204] Zhang MT, Hammarstrom L. Proton-Coupled Electron Transfer from Tryptophan: A Concerted Mechanism with Water as Proton Acceptor. J Am Chem Soc. 2011;133:8806-9.
[205] Bayle C, Siri N, Poinsot V, Treilhou M, Caussé E, Couderc F. Analysis of tryptophan and tyrosine in cerebrospinal fluid by capillary electrophoresis and “ball lens” UV-pulsed laser-induced fluorescence detection. J Chromatogr A. 2003;1013:123-30.
[206] Aubert C, Mathis P, Eker APM, Brettel K. Intraprotein electron transfer between tyrosine and tryptophan in DNA photolyase from Anacystis nidulans. P Natl Acad Sci USA. 1999;96:5423-7.
[207] Kracht S, Messerer M, Lang M, Eckhardt S, Lauz M, Grobety B, et al. Electron transfer in peptides: on the formation of silver nanoparticles. Angew Chem Int Ed Engl. 2015;54:2912-6.
[208] SONG Q-H, GUO Q-X, YAO S-D, LIN N-Y. Comparison of intermediates of tryptophan, tyrosine and their dipeptide induced by UV light and SO.¡. 2002.
[209] Bucher DB, Kufner CL, Schlueter A, Carell T, Zinth W. UV-Induced Charge Transfer States in DNA Promote Sequence Selective Self-Repair. J Am Chem Soc. 2016;138:186-90.
[210] Lee D, Paeng D, Park HK, Grigoropoulos CP. Vacuum-free, maskless patterning of Ni electrodes by laser reductive sintering of NiO nanoparticle ink and its application to transparent conductors. ACS nano. 2014;8:9807-14.
[211] Zenou M, Ermak O, Saar A, Kotler Z. Laser sintering of copper nanoparticles. Journal of Physics D: Applied Physics. 2014;47:025501.
[212] An K, Hong S, Han S, Lee H, Yeo J, Ko SH. Selective Sintering of Metal Nanoparticle Ink for Maskless Fabrication of an Electrode Micropattern Using a Spatially Modulated Laser Beam by a Digital Micromirror Device. Acs Appl Mater Inter. 2014;6:2786-90.
[213] Joo SJ, Hwang HJ, Kim HS. Highly conductive copper nano/microparticles ink via flash light sintering for printed electronics. Nanotechnology. 2014;25:265601.

[214] Son Y, Yeo J, Ha CW, Hong S, Ko SH, Yang DY. Fabrication of submicron-sized metal patterns on a flexible polymer substrate by femtosecond laser sintering of metal nanoparticles. Int Conf Manip Manu. 2012:326-9.